

Alexander Aab

Air Shower Signal Shape Analysis

A New Method to Separate Ultra-High-Energy
Photons from Cosmic Rays



Air Shower Signal Shape Analysis

A New Method to Separate Ultra-High-Energy
Photons from Cosmic Rays

Alexander Aab

© Alexander Aab 2020

Air Shower Signal Shape Analysis

- A New Method to Separate Ultra-High-Energy Photons from
Cosmic Rays

Thesis, Radboud University Nijmegen

viii + 226 pages; illustrated, with bibliographic references and summaries
in English, Dutch, German and Russian

ISBN 978-94-028-1946-5

Cover design by Alexander Aab

Printed in the Netherlands by Ipskamp Drukkers, Enschede

Air Shower Signal Shape Analysis

A New Method to Separate Ultra-High-Energy Photons from Cosmic Rays

PROEFSCHRIFT

ter verkrijging van de graad van doctor
aan de Radboud Universiteit Nijmegen
op gezag van de rector magnificus prof. dr. J.H.J.M. van Krieken,
volgens besluit van het college van decanen
in het openbaar te verdedigen op
dinsdag 10 maart 2020,
om 14:30 uur precies

door

Alexander Aab

geboren op 12 augustus 1984
te Krasnogorsk (USSR)

PROMOTOR

Prof. dr. S.J. de Jong

COPROMOTOR

Dr. C.W.J.P. Timmermans

MANUSCRIPTCOMMISSIE

Prof. dr. J.R. Hörandel (voorzitter)

Dr. C.F. Galea

Prof. dr. O. Scholten

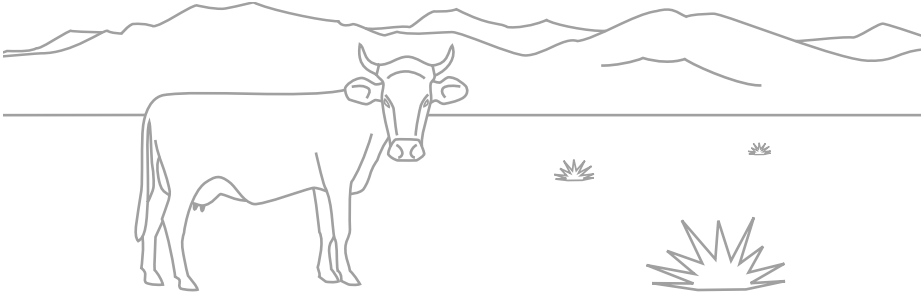
University of Groningen

Contents

1. Introduction	1
2. Cosmic rays and air showers	5
2.1. Cosmic rays	5
2.1.1. History of cosmic ray physics	6
2.1.2. Energy spectrum	8
2.1.3. Sources and acceleration	10
2.1.4. Propagation	14
2.2. Extensive air showers (EAS)	15
2.2.1. Heitler model	15
2.2.2. Air shower components	17
2.2.3. Longitudinal profile	20
2.3. Mass composition puzzle	22
2.3.1. Finding photons	24
3. Pierre Auger Observatory	27
3.1. Surface Detector (SD)	31
3.1.1. Auger Muons and Infill for the Ground Array (AMIGA)	33
3.2. Fluorescence Detector (FD)	34
3.2.1. High Elevation Auger Telescopes (HEAT)	36
3.2.2. Monitoring of the atmospheric conditions	37
3.3. Auger Engineering Radio Array (AERA)	39
3.4. Event reconstruction	41
3.4.1. Event reconstruction with SD	43
3.4.2. Hybrid event reconstruction	51
4. Air shower simulation and reconstruction	55
4.1. Air shower simulation with CORSIKA	56
4.1.1. Thinning procedure	59
4.1.2. Parallelization	61
4.2. Detector simulation and EAS event reconstruction with <u>Offline</u>	62
4.2.1. Detector simulation	63
4.2.2. EAS event reconstruction	66

4.2.3. Module sequence file	66
4.3. Set of air shower simulations used for analysis	68
5. Mass composition parameters	71
5.1. Existing observables	72
5.2. New approach: Time Probability Density Function (TPDF)	80
6. Generation of TPDF models	87
6.1. TPDF model definition	87
6.1.1. Uncertainties	90
6.2. TPDF model generation	94
6.3. TPDF model interpolation	95
6.4. TPDF confidence interval	96
7. Analysis of TPDF parameters obtained from simulated EAS	101
7.1. Primary particles differences	103
7.2. Simulation energy differences	109
7.3. Inclination angle differences	114
7.4. CORSIKA version differences	114
7.5. High-energy interaction model differences	122
7.6. Increased number of secondary muons	123
7.7. Thinning impact	130
8. Evaluation of the TPDF models	137
8.1. Correction of the reconstructed energy	137
8.2. Signal strength and number of triggered SD stations	142
8.3. Definition of testing ranges	148
8.4. Gamma cut definition	149
8.5. Gamma cut testing on simulations	158
9. Results of the TPDF application on data	161
9.1. Data selection	161
9.2. Reconstruction range and quality cuts	163
9.3. Gamma ray candidates	168
9.4. Characteristics of selected gamma ray candidate events	169
9.5. Comparison to gamma ray candidates of other studies	173
10. Conclusions	175

11. Outlook	177
11.1. AugerPrime	177
11.2. Possible TPDF improvements	179
Bibliography	183
A. Hardware and software versions	195
A.1. Hardware used	195
A.2. Software used	195
B. Steering file examples and command descriptions	196
C. Module sequence files	200
D. $\Lambda_{\gamma,p}$ histograms and graphs	202
Glossary of abbreviations	206
Summary	209
Samenvatting	213
Zusammenfassung	217
Резюме	221
Acknowledgements	225



Introduction

Many sources in the universe are known to produce particles of different nature and energy and emit them out into space. The closest source to the Earth is our Sun. Every moment it emits particles, such as photons, neutrinos, electrons, protons and heavier nuclei in a wide spectrum of energy. Some of them we can analyze by measuring their *direct* interactions with detectors, e.g. visible light or radio signals with telescopes. Other particles we can observe *indirectly*, from their interactions with the Earth's atmosphere, e.g. the solar wind (charged particles) as northern light. Next to solar particles, particles from farther sources of (extra)galactic origin also arrive at Earth. While photons from these sources (e.g. star light) are known from time immemorial, the existence of extraterrestrial charged particles (*cosmic rays*, CR) was discovered first in the beginning of the 20th century. CR are high-energetic particles of different nature, traveling close to the speed of light. Within a century a large number of experiments have measured various parameters of the cosmic rays, e.g. their energies, flux, and arrival directions. Physicists are curious to understand where these particles are being produced (*source*) and how their *acceleration* works. Also the *propagation* through the universe and the (extra)galactic magnetic fields, which deflect the charged particles, are of major interest.

When high-energetic particles reach the Earth's atmosphere, they collide with the air atoms (*interaction*) and produce *air showers*. The flux of the so called *ultra-high-energy cosmic rays* (UHECR) with energies above an EeV (10^{18} eV) is below 1 particle per km² per year. This flux

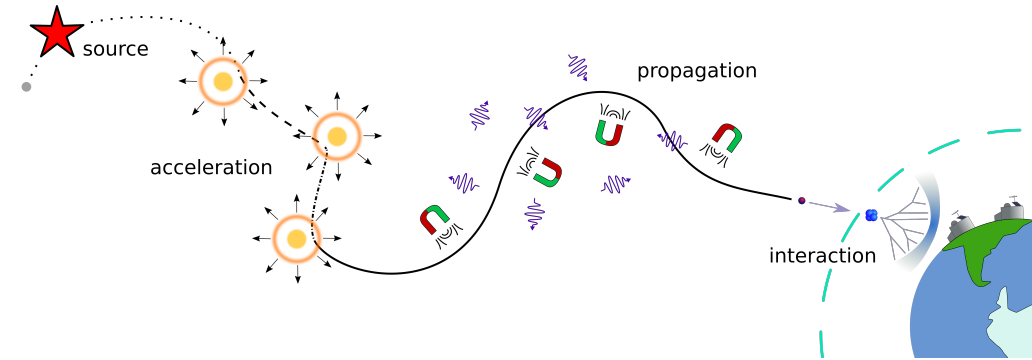


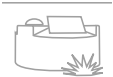
Figure 1.1.: Schematic picture of a cosmic ray which propagates from the source to the Earth and induces an air shower.

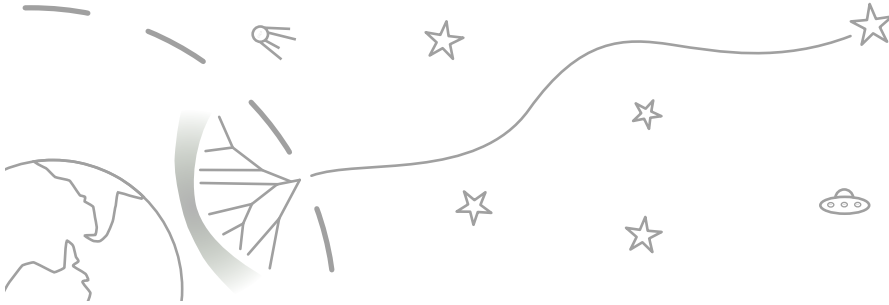
makes direct detection unfeasible, whereas the detection and analysis of the air showers offer access to study the very rare UHECR. Figure 1.1 is a schematic view of a cosmic ray traveling through the universe from its production and acceleration towards the Earth and producing an air shower by interacting with the atmosphere.

The air showers can reach several kilometers in diameter at ground and can be measured with different kinds of detectors. Besides the studies of the astrophysics of cosmic rays, air showers can also be used to test and improve the models describing the interactions between particles at the highest available energy. To understand where the cosmic rays were produced and how they were accelerated, it is essential to know their chemical or *mass composition*. This is not directly accessible, but can be deduced from the air shower properties. Especially the search for neutral particles, like *gamma rays* (photons), at the highest energies is of interest given that they are not bent by the (extra)galactic magnetic fields and point back to their origins.

The work presented in this thesis focuses on the properties of the air showers measured with the surface detectors of the Pierre Auger Observatory. A technique to evaluate the nature (type) of the primary particle through the longitudinal shape of the air shower it induces as recorded in a time trace of the surface detector will be presented and exploited in a search for *ultra-high-energy gamma rays* (UHEGR). In Chapter 2 the his-

tory of the discoveries and the physics of cosmic rays and air showers are presented. In addition, possible sources and the propagation through space as well as the focus of this work toward the mass composition analysis and the search for photons are discussed. The Pierre Auger Observatory, which provided the data for this thesis, is explained in Chapter 3. Besides the different detector types also the reconstruction algorithms are described. Air shower simulations have been performed to better understand the signals measured by the detectors. The simulation programs that were used to create the air shower and the detector simulations are presented in Chapter 4. Chapter 5 gives an overview of the existing analyses with different approaches for the mass composition studies of the Pierre Auger Collaboration. In addition, a new approach is introduced and the definition of the Time Probability Density Function (TPDF) is given, which will be used to distinguish the different types of cosmic rays. In Chapter 6 the generation of the TPDF parameterizations is described including the discussion of the uncertainties. The differences of the TPDF parameterizations obtained from different air shower simulations are presented in Chapter 7. The preparations for the application on measurements and the definition of the testing ranges are described in Chapter 8. Also the criteria for identifying air showers induced by a photon are defined there, followed by the testing of the TPDF method on air shower simulations. In Chapter 9 the results of the application of the TPDF method on events measured by the Pierre Auger Observatory are summarized. In Chapter 10 the final conclusions of this thesis are presented. Finally, the outlook of Chapter 11 provides an insight into the possible further use of the developed tools and their improvements. Also the ongoing upgrade of the Pierre Auger Observatory, AugerPrime, will be discussed there.





Cosmic rays and air showers

Cosmic rays of (extra)galactic origin permanently penetrate the Earth's atmosphere. When they interact with atmospheric nuclei and their energy is sufficiently high, they produce cascades of secondary particles - the air showers. These air showers can be used to study the very rare cosmic rays at the highest energies.

2.1. Cosmic rays

Cosmic rays are by definition charged particles with an extraterrestrial origin, traveling through space with relativistic speeds before reaching the Earth. Their energy range, as observed by several experiments, spans more than eleven orders of magnitude. Due to the rapidly decreasing flux as a function of energy, different kinds of detection strategies have to be applied to measure CR, as will be discussed in Chapter 3.

Our knowledge about the mechanisms behind the production and the propagation of the cosmic rays is very limited, especially for the UHECR. We study them carefully to obtain insight into the acceleration mechanisms and the physics of their sources, as well as improve our knowledge about particle interactions at highest energies and the propagation through the space in view of the presence of magnetic fields and cosmic particle backgrounds. These studies may give us a hint of physics beyond the Standard Model.



Figure 2.1.: Victor Franz Hess in the gondola of his balloon in 1912. Adapted from [1].

2.1.1. History of cosmic ray physics

Cosmic rays were discovered about 100 years ago. In 1912 Viktor Hess performed balloon experiments (Figure 2.1) to measure the ionizing radiation with increasing altitude, up to 5 km [3]. The unexpected result was, that after an initial decrease, the radiation started to increase again at larger altitude. Hess' conclusion was that the origin of this phenomena must come from above. In the years 1913-14 Werner Kolhörster repeated Hess' experiments up to 9 km altitude and could confirm his results [4]. Figure 2.2 displays the measurements of Hess and Kolhörster. With the discovery of the cosmic rays the questions of where they originate from and what mechanisms can accelerate them to the measured energies came up and scientists try to find answers to those questions ever since.

Besides for astronomy, cosmic ray experiments are also used for particle and nuclear physics. The positron and the muon were both discovered by studying cosmic rays. In the 1930's several scientists, among them



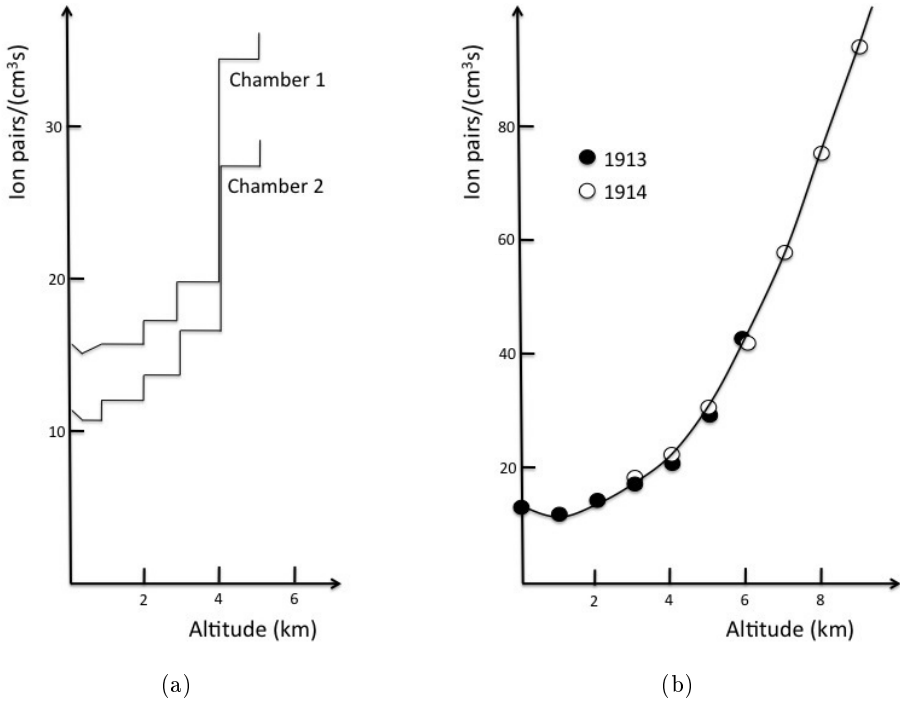


Figure 2.2.: Results of the balloon experiments by V. Hess (a) and W. Kolhörster (b). Adapted from [2].

Pierre Auger, working with cosmic rays, discovered that detectors placed at some distance to each other were triggered at almost the same time. The conclusion was that these detections are caused by particles that have a common origin in the atmosphere and belong to the same structure, called an air shower, a cascade of particles initiated by a cosmic ray when interacting with the atmosphere (Section 2.2). After analyzing the data in 1939, Auger estimated that the cosmic rays creating these air showers must have an energy of at least 10^{15} eV [5]. In fact Hess and Kolhörster were measuring the particles of air showers and not directly the cosmic rays. Also the increasing flux with altitude in their measurements can be explained by the development characteristics of air showers, where their number of particles reaches its maximum at several kilometers altitude and afterward start to decrease while proceeding toward the ground (Section 2.2.3).

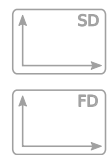
2.1.2. Energy spectrum

Since the discovery of cosmic rays, their energy spectrum has been measured by several experiments. The differential flux J of all particle types with energies above 10^8 eV is shown in Figure 2.3. For each decade increase in energy the number of particles is dropping by about 3 orders of magnitude. Therefore, the flux for particles with energy of 10^{11} eV which is around 1 particle per m^2 per second drops down to 1 particle per m^2 per year at 10^{16} eV and to below 1 particle per km^2 per century at energies around 10^{20} eV. The measured energies of cosmic rays at the end of the energy spectrum are many orders of magnitude higher than that of the particles in the beams of current particle accelerator experiments, like the Large Hadron Collider (LHC) at CERN, Geneva [6]. This fact makes cosmic rays the only candidates to study particle interactions at the highest energies, until much more powerful accelerators come into existence.

The flux can approximately be described with the power law:

$$J \sim E^{-\alpha} \quad , \quad (2.1)$$

with an overall spectral index α with a value close to 3. There are several characteristic energy regions where the spectral index changes. The feature at around $10^{15.5}$ eV, where the spectrum becomes slightly steeper, is called *the knee* and is already known for more than 50 years [8]. This energy is assumed to be the maximum for proton acceleration processes within our galaxy. At two orders of magnitude higher energy ($10^{17.5}$ eV) the spectrum steepens again. This is called *the second knee* and is, in analogy to the first one, supposed to be the maximum galactic acceleration energy for heavy nuclei [9]. Around $10^{18.7}$ eV the spectrum becomes slightly less steep and α changes to a smaller value. This region is called *the ankle* and its origin is assumed to be the change of the cosmic rays origins to primarily extra-galactic sources [10] as the galactic magnetic fields are too weak to trap the particles above this energy. Nevertheless, the cause of this feature is still an open question. One hypothesis proposes the ankle to be due to a dip in the pair production cross section [11], another due to photo-disintegration of heavy nuclei close to their sources [12], yet another proposes the need for an additional galactic source at the end of the galactic spectrum [13]. The end of the energy spectrum is marked by a sharp drop of the flux around 10^{20} eV. Both features, the ankle



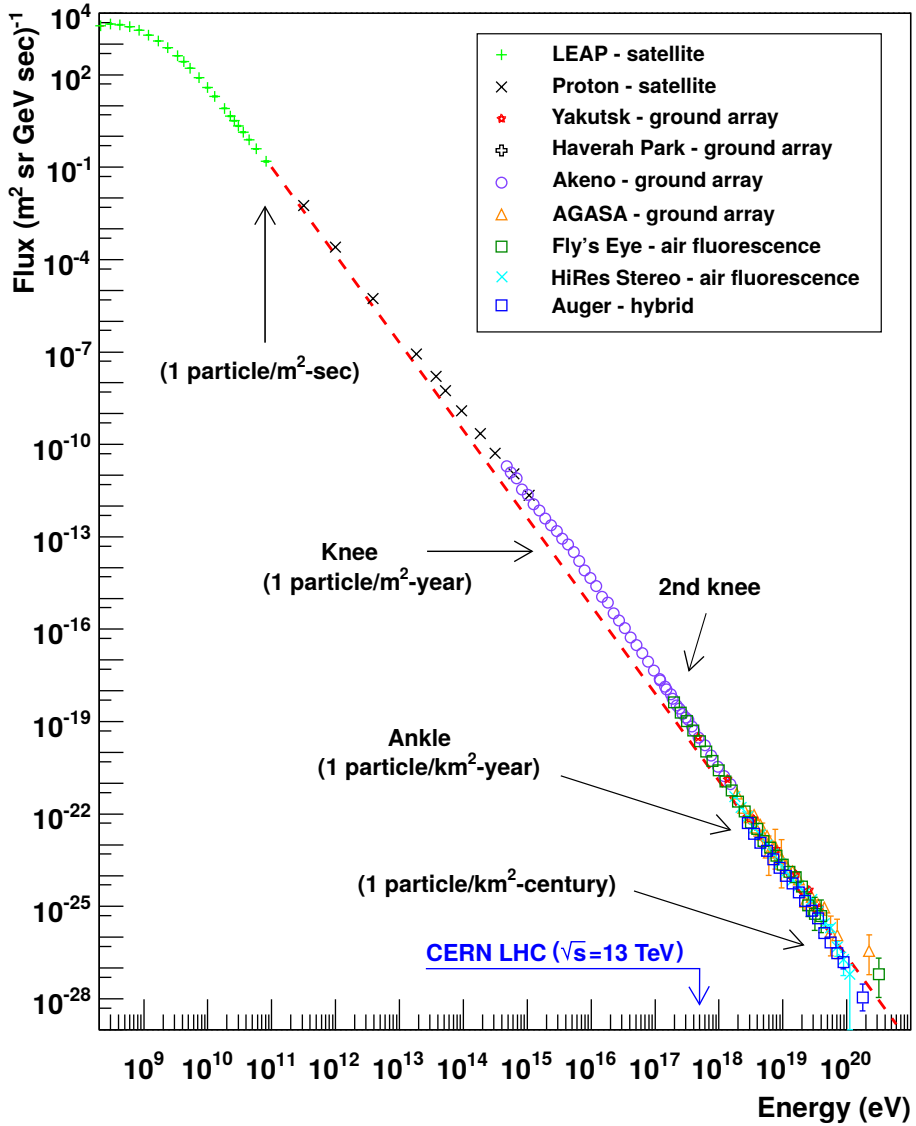


Figure 2.3.: The all-particle cosmic ray energy spectrum. The dashed red line indicates a power law with $\alpha = -2.8$. For comparison the LHC collision energy of $\sqrt{s} = 13$ TeV is shown for a proton cosmic ray colliding on a nucleon of an atmospheric gas molecule. Adapted from [7].

and the steep drop, are better visible when plotting the flux multiplied by E^3 (Figure 2.4). There are two favored hypotheses for the cause of this apparent end of the spectrum [14]. The *maximum rigidity scenario* (Figure 2.5(a)) postulates a maximum charge dependent energy, to which the particles can be accelerated. Hence, the cosmic rays at the end of the energy spectrum would consist of heavier particles due to their higher charge. In the *photo-disintegration scenario* (Figure 2.5(b)) the mass composition at the highest energies is light and the sharp drop is formed by the GZK cut-off, which will be discussed in Section 2.1.4.

2.1.3. Sources and acceleration

The origin of cosmic rays at the highest energies (above 10^{17} eV) is still unknown and is one of the main topics of the ongoing studies in astroparticle physics. Currently, two big observatories are operating at these energies, the Pierre Auger Observatory since 2004 [16] and the Telescope Array (TA) since 2008 [17]. Even though an origin of the UHECR could not be unambiguously identified yet, some scenarios for sources could be ruled out based on the data taken with these observatories. In particular the top-down models, where cosmic rays at ultra-high-energies are produced by interactions and decays of heavy, hypothetical particles are disfavored [14] compared to the bottom-up models, in which cosmic rays are produced with low energies and are accelerated afterwards.

The main mechanism to accelerate cosmic rays to the observed energies is assumed to be *Fermi acceleration* [18]. Originally postulated by Enrico Fermi in 1949 and elaborated in the 1970's, it describes how particles gain energy through scatterings on turbulent magnetic fields in shock fronts of e.g. supernova remnants, active galactic nuclei (AGN) or gamma ray bursts (GRB). This assumption naturally leads to an inverse power law energy spectrum.

In 1984 Anthony M. Hillas proposed a criterion for the maximum energy E , that can be obtained from an acceleration region with size L , the magnetic field strength B and the velocity of the magnetic shock βc [19]:

$$E[\text{EeV}] < \frac{1}{2} B[\mu\text{G}] \cdot L[\text{kpc}] \cdot Z \cdot \beta \quad . \quad (2.2)$$

Particles with higher charge can gain more energy. This is indicated by the charge number Z in the equation.

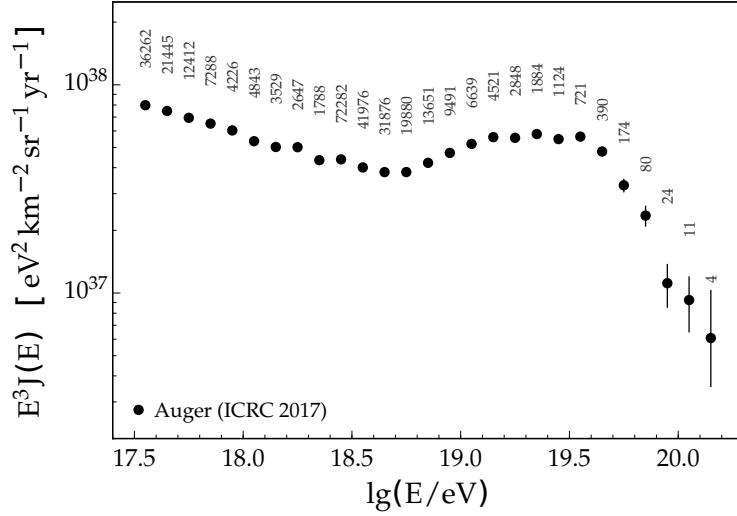


Figure 2.4.: Cosmic ray energy spectrum starting at $10^{17.5}$ eV measured with the Pierre Auger Observatory (Chapter 3). For visibility the flux was multiplied by E^3 . The numbers indicate the measured events in each energy bin. Adapted from [15].

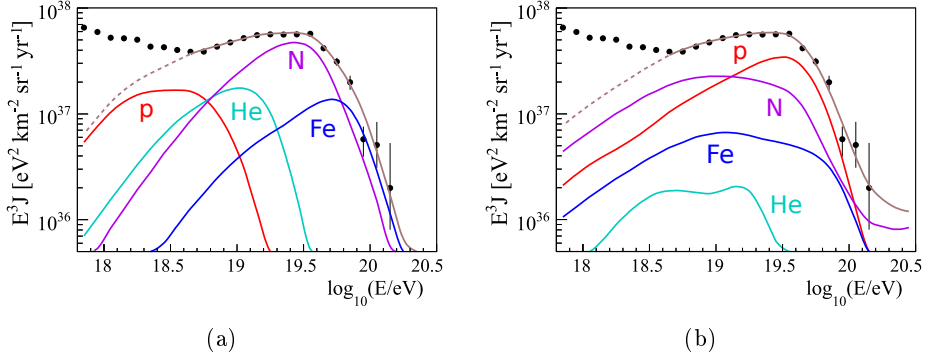


Figure 2.5.: Maximum rigidity (a) and photo-disintegration (b) scenarios for the measured energy spectrum (black dots). Four different particle types are fitted as parts of the total composition (brown line): proton (red), helium (cyan), nitrogen (purple) and iron nuclei (blue). Adapted from [14].

Based on this criterion the Hillas plot for ultra-high-energy cosmic rays is constructed (Figure 2.6). As shown in the diagram, several possible sources for the observed cosmic rays are conceivable. Even though the anisotropy studies have not yet found any clear evidence for a correlation between the arrival directions of cosmic rays and the known objects from existing catalogs [20], e.g. the Swift AGNs (Figure 2.7), a dipole was found in the data (Figure 2.8) [21], indicating that the sources of the cosmic rays are to be found outside our galaxy.

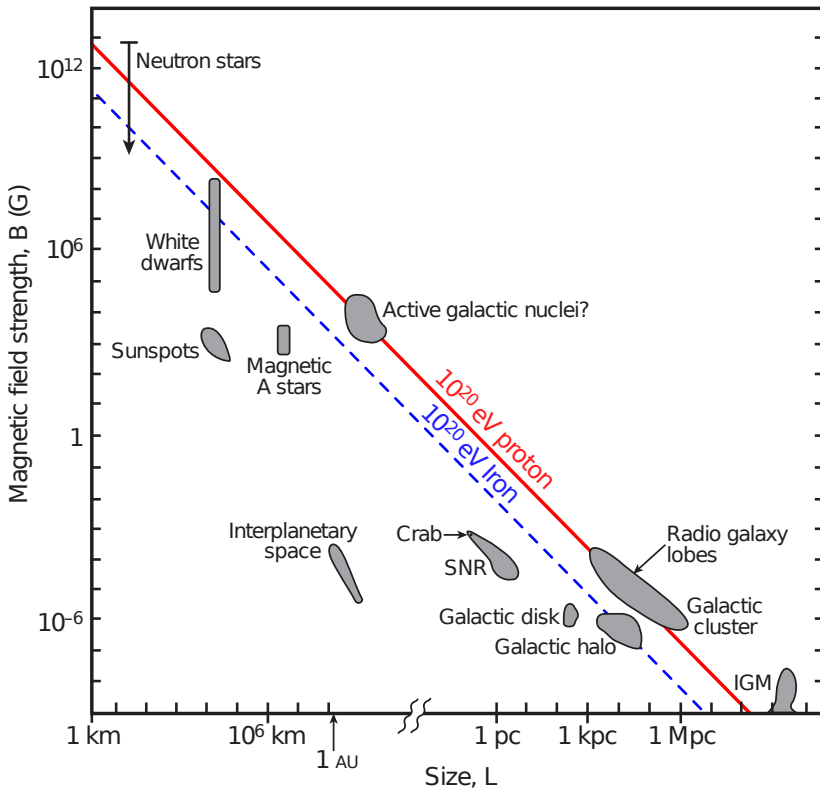


Figure 2.6.: Hillas plot for different astronomic objects. The two lines indicates which size and magnetic field are necessary to accelerate a given particle type to an energy of 10^{20} eV. Only objects above the lines are plausible. Adapted from [22].

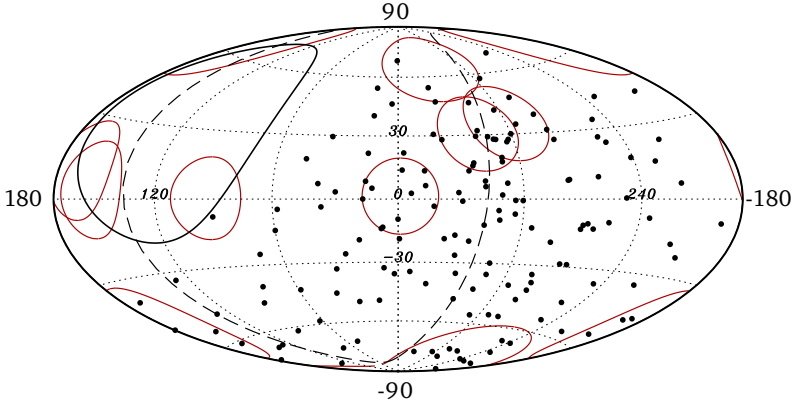


Figure 2.7.: Events with $E \geq 58 \text{ EeV}$ (black dots) measured by the Pierre Auger Observatory in galactic coordinates. Red circles of 18° radius represent Swift AGNs, brighter than 10^{37} W ($10^{44} \text{ erg s}^{-1}$) and closer than 130 Mpc. Adapted from [20].

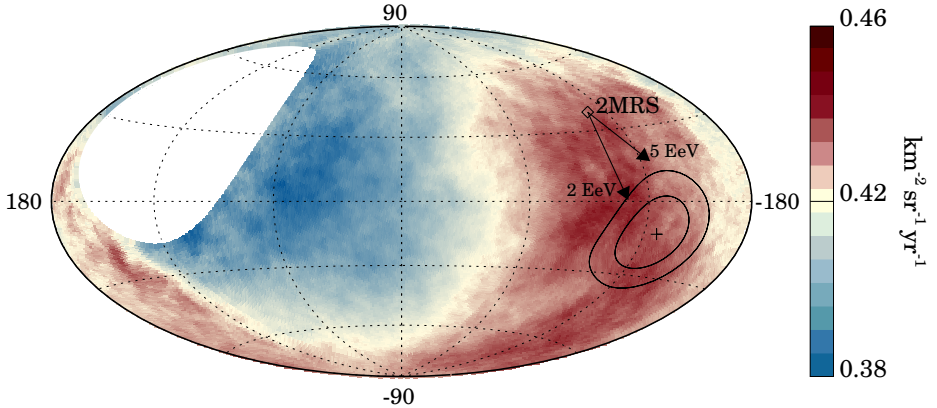


Figure 2.8.: Sky map of the flux of cosmic rays with $E \geq 8 \text{ EeV}$ measured by the Pierre Auger Observatory in Galactic coordinates, smoothed with a 45° top-hat window. The measured dipole direction is marked by the cross, with the contours of 68% and 95% confidence level regions. The dipole in the 2MRS galaxy distribution is indicated, together with the expected deflection of particles with $E/Z = 2 \text{ EeV}$ and 5 EeV for a particular Galactic magnetic field model. Obtained from [21].

2.1.4. Propagation

On their way through the universe the cosmic rays interact with the cosmic microwave (CMB) and the infrared photon (IR) backgrounds.

In case of protons a Δ^+ resonance may be created in these interactions that decays into a proton and a neutral pion or a neutron and a positive pion:

$$p + \gamma_{\text{CMB}} \rightarrow \Delta^+ \rightarrow p + \pi^0 \quad , \quad (2.3)$$

$$\rightarrow n + \pi^+ \quad . \quad (2.4)$$

This effect becomes energetically possible above energies of $5 \cdot 10^{19}$ eV and shortens the attenuation length for ultra-high-energy protons to less than 100 Mpc at 10^{20} eV. This suppression of the flux is called the GZK-limit, named after Kenneth Greisen, Georgiy T. Zatsepin and Vadim A. Kuzmin [23] [24]. Another loss that limits the attenuation length is due to the pair production, dominant below $7 \cdot 10^{19}$ eV (Figure 2.9(a)).

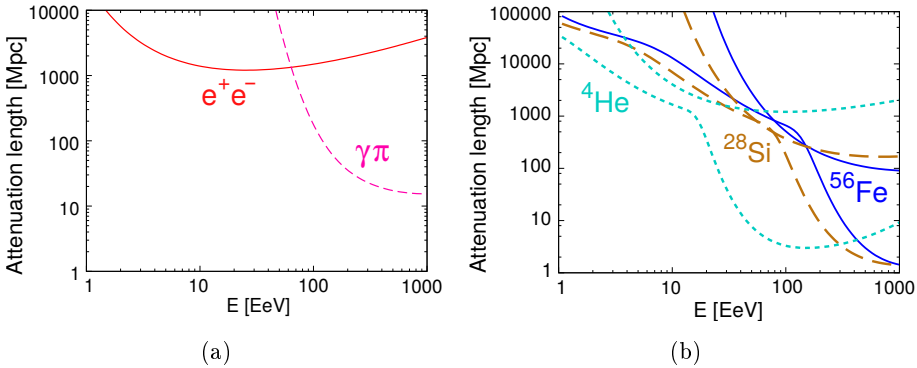


Figure 2.9.: Attenuation lengths for protons (a) and heavier nuclei (b). Note the different scale on vertical axis. In (b) the upper lines are due to pair production and the lower due to photo-disintegration. Adapted from [25].

For heavier nuclei the dominant process for limiting the attenuation length when interacting with the CMB and IR photons is the photo-disintegration, where the nuclei split into lighter fragments. Pair production causes also an energy loss, although the attenuation length is much larger. Both processes depend on the energy and mass of the CR (Figure 2.9(b)).

Because of these limitations the sources for UHECR are assumed to be nearby on the intergalactic distance scale. Apart from this, cosmic rays are also deflected by the (extra)galactic magnetic fields. This fact leads to the main difficulty in searching for the sources of the UHECR, the arrival directions of the charged particles do not necessarily point back toward their origins. The magnitude of the deviation depends on their charge as well as on their energy. Hence, protons (beside neutral particles, like photons) with ultra-high-energies and relative small attenuation lengths for cosmic scales, point back most accurately to their sources.

2.2. Extensive air showers (EAS)

When particles with sufficiently high energies collide, a bunch of new particles is produced. Similar processes are studied in collider experiments. The impact of a cosmic or a gamma ray (*primary particle*) on the Earth's atmosphere can be seen as a fixed target experiment. Particles created from the interaction of the cosmic or gamma ray with the atmospheric nuclei are directed toward the Earth's surface and are called *secondary particles*. They hit other air nuclei, thereby producing a new bunch of secondaries and hence forming a cascade of billions of particles. An *air shower* is created. Those with a width of several kilometers, created by UHECR or UHEGR, are called *extensive air showers* (EAS).

2.2.1. Heitler model

The first simple description to explain the behavior of an electromagnetic cascade was provided by Homi J. Bhabha and Walter Heitler in 1937 [27]. In their model a cascade is formed through the repeated two-body splitting of the parent particle, either via e^+e^- pair production or one-photon bremsstrahlung mechanism. This process is illustrated in Figure 2.10(a).

Each new step of splitting is performed after the particles travel a distance

$$d = \lambda_r \cdot \ln 2 \quad , \quad (2.5)$$

with *radiation length* λ_r . In this model the number of particles is doubled at each step. After n steps the total number of particles is $N = 2^n$, each of them with energy $E = E_0/2^n$, where E_0 is the energy of the primary gamma ray. The augmentation stops when the energy of the newly generated particles drops below the critical energy E_c^{em} , beneath which neither pair production nor bremsstrahlung can be performed. In air $E_c^{em} = 85 \text{ MeV}$. From this moment on, the number of particles in the air shower starts to decrease as many electrons and positrons are absorbed.

The interaction processes within a hadronic air shower are more complicated, although they can be modeled similar to the Bhabha's and Heitler's approach for the electromagnetic air showers. The creation of an air shower initiated by a hadron, can be approximated by steps of length

$$l = \lambda_i \cdot \ln 2 \quad , \quad (2.6)$$

with *interaction length* λ_i for strongly interacting particles. After travers-

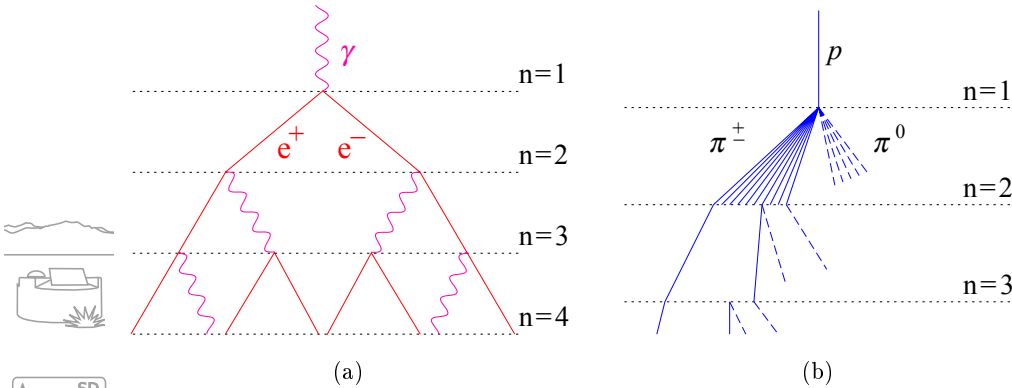


Figure 2.10.: Sketch of the Heitler model for an electromagnetic air shower (a) and its extrapolation to a hadronic air shower (b). Adapted from [26].

ing one layer of air with fixed thickness l the hadrons interact and produce N_{ch} charged pions (π^\pm) and $\frac{1}{2} N_{ch}$ neutral pions (π^0) [26]. The π^\pm either travel further and interact with another air nuclei, producing the next bunch of new particles, or decay into muons and neutrinos at early stages in the air shower development, where the air density is low, before they have a chance to interact. Once the critical energy E_c^π is reached, the charged pions also decay, as the decay probability becomes larger than the one for subsequent interactions. The neutral pions π^0 always decay immediately into two photons and start electromagnetic air showers. A model of an air shower initiated by a hadron (here proton) can be seen in Figure 2.10(b). A more detailed description of the models for electromagnetic and hadronic air showers can be found in [26].

2.2.2. Air shower components

The Heitler model for electromagnetic air showers and its adaption for the hadronic air showers are simplified, however they provide adequate approximations. In order to obtain a more detailed description of a real air shower computer simulations are performed (Chapter 4). It is clear that even in the electromagnetic air showers initiated by a photon hadrons and muons are present. Moreover, in the hadronic interactions not only pions are produced. Particularly at the start of the air shower, where the cosmic ray hits the atmospheric nuclei, the energy is going into heavier particles, that decay sometimes directly into pions. A slightly more elaborate schematic view of air shower components is shown in Figure 2.11.

The particles that appear in an air shower, can be divided into three main groups: the *electromagnetic component*, containing electrons, positrons and photons, the *muonic component*, containing muons and (mainly muon) neutrinos and the *hadronic component* with all the hadrons.

The relative sizes of these components depend on the nature of the primary particle, with the biggest difference between photon and hadron initiated air showers. The simulated number of particles from each component for a specific air shower initiated by a proton as well as their densities as function of distance to the air shower axis are illustrated in Figure 2.12.

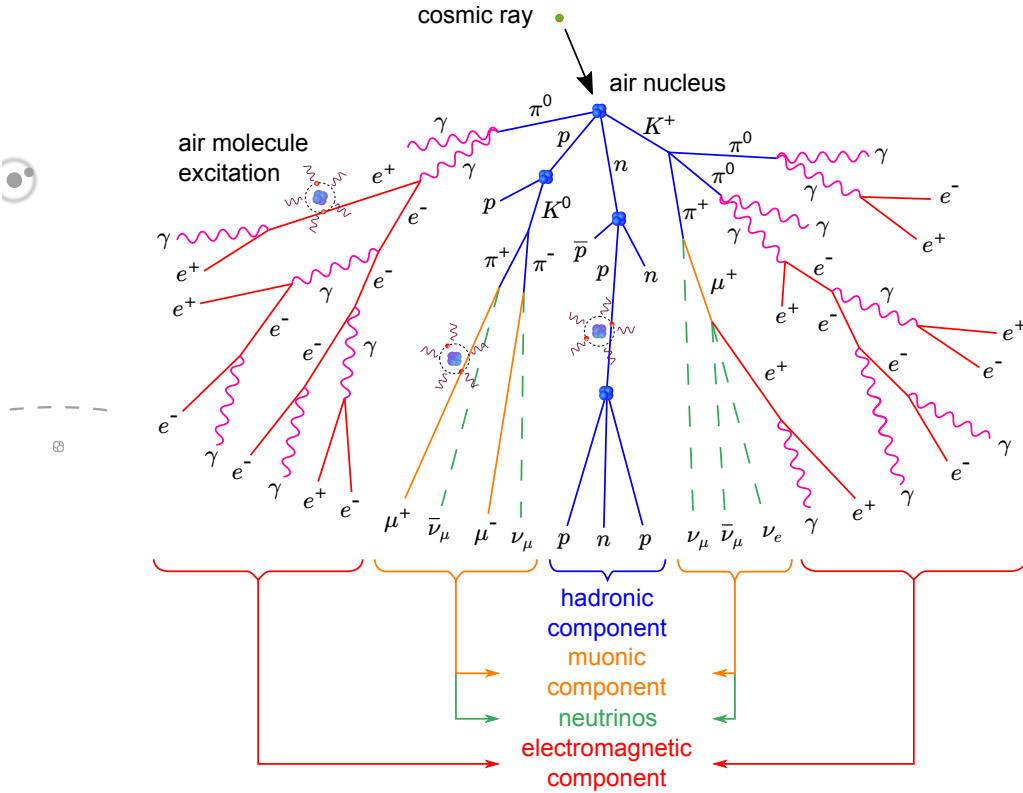


Figure 2.11.: Sketch of the different components of an air shower.

Electromagnetic component

The biggest part of an air shower in terms of the number of particles is the electromagnetic component, that consists of photons, electrons and positrons. The number of electrons and positrons is two orders of magnitude larger than the muonic component and three orders of magnitude larger than the hadronic component. The number of photons is roughly three and four orders of magnitude larger than the muonic and the hadronic components, respectively.

The electromagnetic part is constantly fed by the hadronic and muonic components, but loses the low energetic particles again. On the other hand, electrons, positrons and photons hardly feed the hadronic and never feed the muonic parts of the air shower. The low energy electrons and

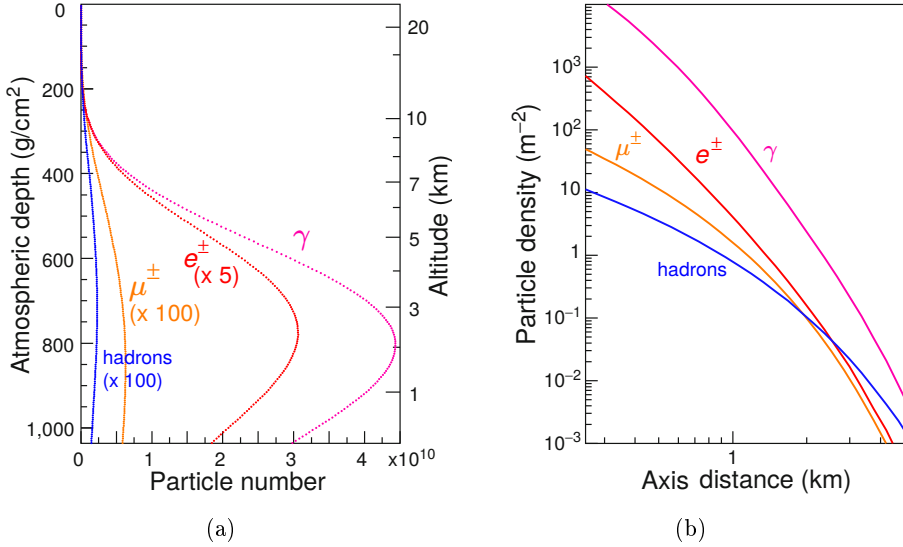


Figure 2.12.: Simulation of the single particles in an vertical air shower with proton as primary particles and energy of 10^{19} eV. Photons, electrons and positrons were traced down to an energy of 0.25 MeV and hadrons and muons to an energy of 0.1 GeV. Number of particles of the individual shower components as function of the atmospheric depth (a). Particle density for the observation level at an atmospheric depth of 875 g/cm² (b), corresponding to the vertical depth of the Pierre Auger Observatory [16]. Adapted from [28].

positrons get absorbed by the air molecules on which the photons scatter and lose a fraction of their energy by exciting the atoms. This leads to a dying-out of the electromagnetic component after reaching the point where the energy of the particles is, on average, equal to the critical energy E_c^{em} (Section 2.2.1). Therefore, the measurable electromagnetic component depends on the path of the air shower through the atmosphere before reaching the detector. In particular, there is a big difference in the measurable number of particles from the electromagnetic component for vertical and inclined air showers with the same energy and the same height of the first interaction.

Muonic component

Within an air shower the muons are produced from decays of pions and kaons, together with neutrinos. After their creation the muons hardly interact with air nuclei and almost all of them reach the ground and can be detected. A small number of lower energy muons decay into electrons and positrons (and neutrinos) before they hit the ground and contribute to the electromagnetic component of the air shower.

The neutrinos interact very weakly with the air nuclei and almost never with the detectors at ground, making the interactions very unlikely. They carry away energy, which is missing in the reconstruction of air shower properties.

Due to the fact that the muons barely interact during their way towards the ground they form the front of the air shower and are likely to trigger the detectors first. The number of muons changes slowly as a function of the inclination angle and the height of the first interaction. However, the number of muons does depend strongly on the energy and the nature of the primary particle (Chapter 5).

Hadronic component

At the first collision between a cosmic ray and an air nucleus a large number of hadronic secondaries are created. Roughly one half of the energy is converted into mainly pions and kaons and the other half is carried away by a leading particle. Although any EAS is quickly dominated by the electromagnetic part of the air shower, the early hadronic interactions influences the fraction of hadrons and specifically also the fraction of muons close to the air shower axis. Hence, these fractions are a handle to distinguish different primary particles.

2.2.3. Longitudinal profile

The air shower development is a continuous progression of interactions between secondaries and air nuclei. The interaction length of each step is therefore a function of the amount of air the air shower has traversed. This quantity is the so called *slant depth* X and is used to compare air showers traveling through different paths and thereby encountering different air density profiles. The slant depth can be expressed as the air density ρ integrated along the path of the air shower from the height h in the

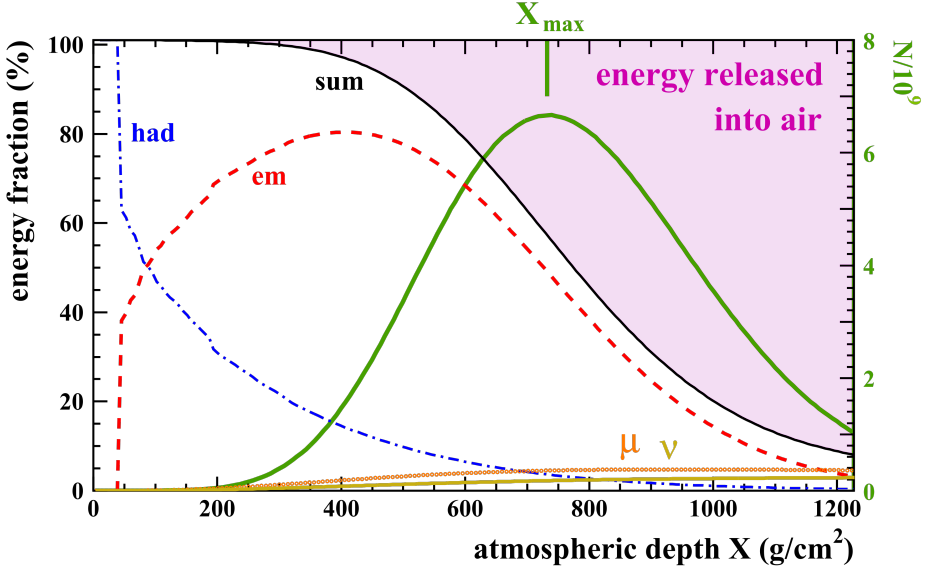


Figure 2.13.: Longitudinal profile for different components of a proton initiated air shower with energy of 10^{19} eV and the total number of particles (green line). The energy fraction above the sum of air shower particles (black line) is released into the air. Adapted from [29].

atmosphere to infinity:

$$X(h) = \int_h^\infty \rho(h') dh' \quad . \quad (2.7)$$

In the previous Section 2.2.2 it was mentioned that the contributions of the air shower components evolve differently. As an example the energy fraction in the different components as function of X for a specific air shower is presented in Figure 2.13. When the air shower contains a large number of secondaries, the energy released into the air is proportional to this number. The total number of particles as function of the slant (or atmospheric) depth is shown in green. As described above, at a certain depth the number of produced secondaries reaches its maximum and starts to decrease again. This coincides with the maximum energy release into the atmosphere. That point is called *depth of air shower maximum* X_{\max} [30] and is an important quantity for the air shower analysis (Chapter 5).

2.3. Mass composition puzzle

The exploration of the origins of cosmic rays at ultra-high-energies and their paths through the universe requires the knowledge of their mass composition. Unfortunately the nature of the primary particles is not a directly accessible quantity from indirect measurements.

Several kinds of particles may be considered as candidates for primary particles. For practical purposes six categories are identified, four for hadrons: protons, helium, C-N-O and iron nuclei, and one each for photons and neutrinos.

The protons are known to be the lightest and most common hadronic element in the universe. Iron is the heaviest element that can be produced in the fusion process of a star and has the highest charge of the elements present in a significant amount. The helium and C-N-O (carbon-nitrogen-oxygen) groups represent the elements in between these two extrema. Note that in the Heitler model the differences in X_{\max} scale as $\ln(A)$, with A the atomic mass.

As shown by simulations (Chapter 4), X_{\max} and its spread $\sigma_{X_{\max}}$ turn out to be differentiating features between air showers initiated by different types of cosmic rays. Therefore, these quantities are widely used for mass composition studies (Chapter 5). In Figure 2.14 the slant depths of simulated air showers with iron nucleus (blue) and proton (red) primary particles are shown. In terms of X_{\max} there are two important features in this plot. First of all the maxima of the distributions for air showers initiated by a proton appear at larger atmospheric depths (i.e. lower in the atmosphere), compared to air showers induced by iron nuclei. The second outcome is the spread of the X_{\max} values, $\sigma_{X_{\max}}$, which is much larger for proton induced air showers compared to air showers induced by iron nuclei. These two features can be used to distinguish between the different hadronic primary particles.

Both the Pierre Auger Observatory [16] and the Telescope Array (TA) Collaboration [17] are equipped with detectors that measure the slant depth of the air showers, and thus X_{\max} , directly. At the highest energies, above 10^{19} eV, the results of these observatories may seem in contradiction. This can be observed in Figure 2.15. The results of the Pierre Auger Observatory suggest that the mass composition is changing towards heavier nuclei at the highest energies [30], whereas Telescope Array

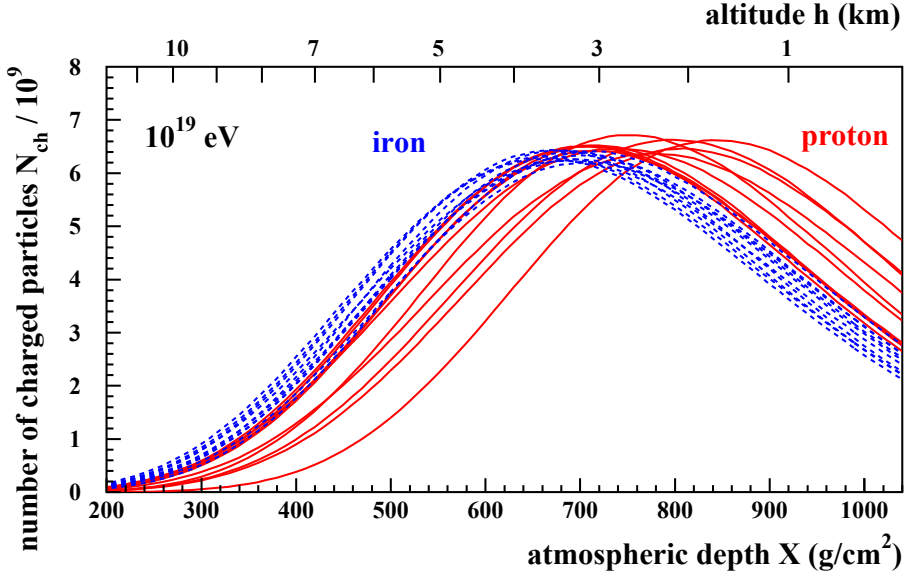


Figure 2.14.: Air shower development as a function of atmospheric depth for simulated air showers induced by protons (red lines) and iron nuclei (blue lines). Adapted from [29].

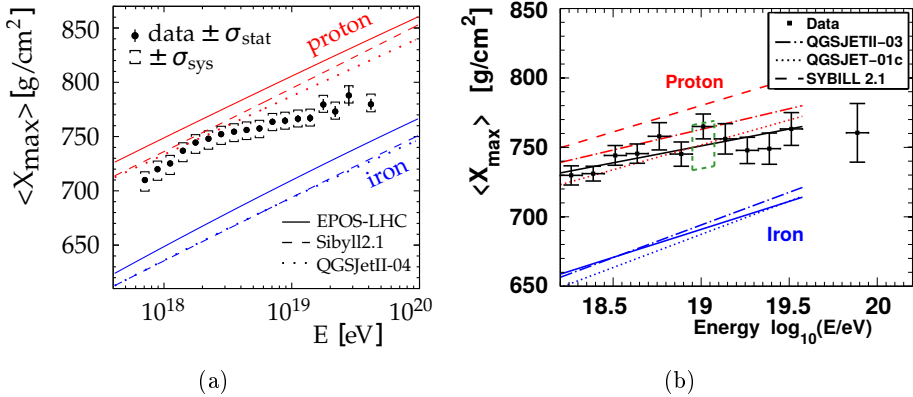


Figure 2.15.: X_{\max} measurements by the Pierre Auger Observatory (a) and the Telescope Array Collaboration (b), in comparison to the simulation prediction with different models for proton and iron nucleus as primary particles. Adapted from [31].

results suggest that the mass composition stays light [32]. However, the results cannot be compared directly due to the fact that the data from TA includes detector effects, whereas the Pierre Auger Observatory results have been unfolded for them. The data is indeed in agreement, as shown by the joint task force that applied the Telescope Array analysis to the measurements from the Pierre Auger Observatory, resulting in a similar outcome [31]. The different conclusions of the two collaborations are based upon different simulation codes and different hadronic interaction models used by the two groups.

Apart from the X_{max} analyses various other studies including different parameters were performed to investigate the mass composition of the cosmic rays (Chapter 5).

2.3.1. Finding photons

To find and study the sources of cosmic rays, neutral particles are a complementary tool. The relevant difference for high-energy particle astrophysics between hadrons and neutral particles, such as photons and neutrinos, is their charge. Charged particles are deflected by the magnetic fields in the galaxies and the inter-galactic space. The amount of deflection depends on their energy and charge. On the other hand the direction of photons and neutrinos is not affected by these magnetic fields. This implies that photons and neutrinos will point to their origin (discarding effects of deflection by masses, e.g. black holes), in contrast to protons and iron nuclei.

Neutrinos are only weakly interacting and their interaction with other particles is extremely rare. Ultra-high energy neutrinos, which are of a main interest in astrophysics, are either produced directly at the astrophysical objects and therefore called astrophysical neutrinos or via interactions of cosmic rays with CMB photons during the propagation in the universe and therefore called cosmogenic neutrinos. The detection of neutrinos is normally very difficult, but at ultra-high energy their cross section grows to produce a sizable probability for interactions in dense media. This may enable dedicated observatories, such as the IceCube Neutrino Observatory [34] and the Giant Radio Array for Neutrino Detection (GRAND) [35] to record a significant number of events and open the field of neutrino astronomy. Searches for neutrinos are also performed at the Pierre Auger Observatory [15].

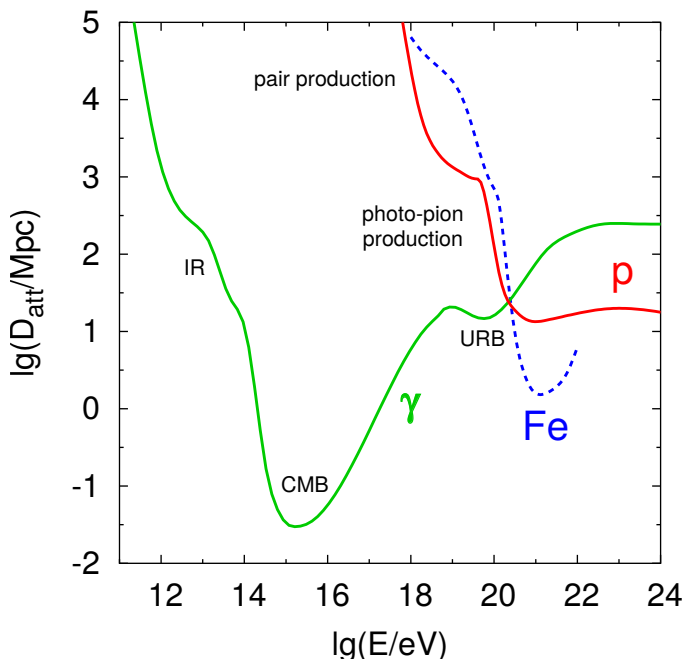


Figure 2.16.: Energy attenuation length of gamma rays for interactions with infrared (IR), cosmic microwave (CMB) and universal radio (URB) backgrounds. In addition the attenuation length for protons and iron nuclei are shown. Adapted from [33].

The second type of relevant neutral particles is the photon. At lower energies photons are mass-produced in many cosmic objects and are widely used in astronomy at different wavelengths: visible light, radio, UV, IR or gamma rays. Between 10^{15} eV and 10^{17} eV the universe is opaque for photons due to their resonant pair production cross section with the CMB (Figure 2.16). However, above 10^{17} eV the attenuation length increases rapidly again and the cosmic horizon of these gamma rays becomes many Mpc once more. The rapidly changing UHE gamma ray horizon in fact provides interesting complementary information once their detection efficiency is sufficiently high. At energies above 10^{18} eV photons are expected as decay products of the interactions of ultra-high-energy cosmic rays with the CMB. For example, UHE gamma rays are tracers of the GZK

process (Section 2.1.4), in which neutral pions subsequently decay into pairs of ultra-high-energy photons [15]. UHEGR may also emerge directly at the sources of UHECR and more exotically from the decay of ultra-heavy particles or ultra-high-energy neutrino annihilations in the Z-burst scenario, from topological defects or super-heavy dark matter (top-down models) [33]. At energies above 10^{15} eV photons have not been identified yet, upper limits for their flux could be set, constraining the top-down models. See Figure 2.17 for the limits above an energy of 10^{18} eV.

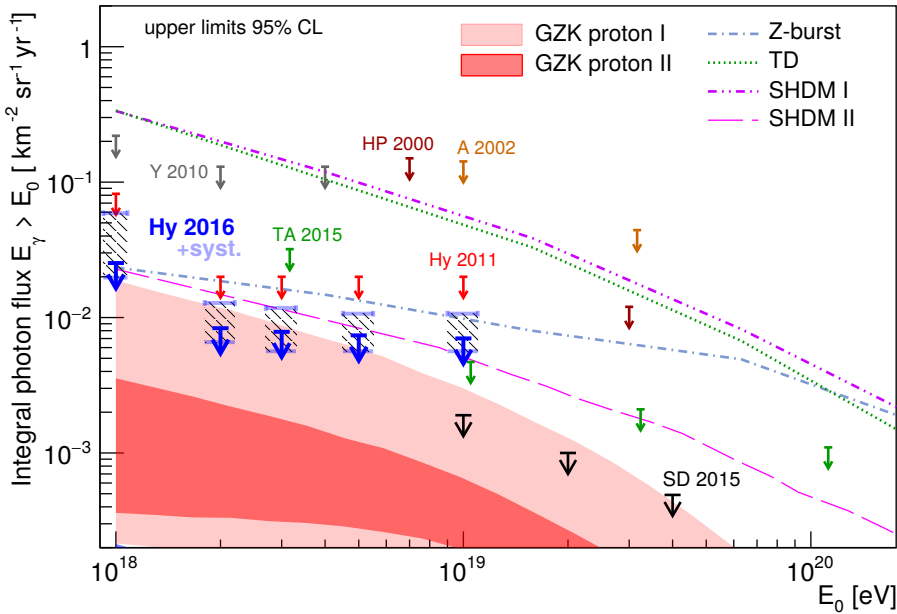
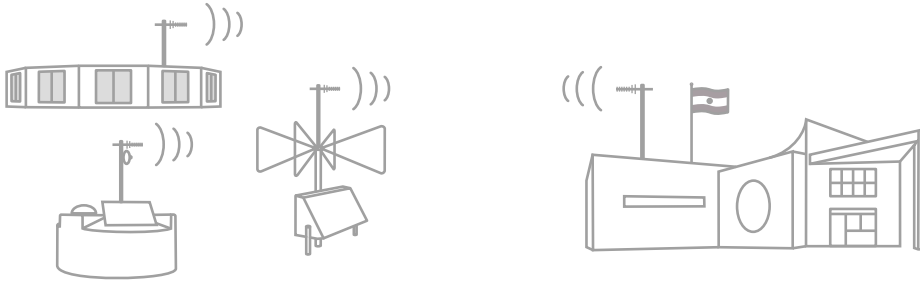


Figure 2.17.: Upper limits on integral photon flux from Pierre Auger Observatory (SD, Hybrid), Telescope Array (TA), Yakutsk (Y), AGASA (A) and Haverah Park (HP). Red shaded regions are the predictions from GZK-based models, whereas the lines represent some top-down models (Z-burst, topological defects, super-heavy dark matter). Adapted from [15].



Pierre Auger Observatory

Many different experiments were built in the past to study the characteristics of the cosmic rays. The design of a particular experiment has to be adapted to its specific task. For instance the energy spectrum of the cosmic rays has to be taken into account. As mentioned in Section 2.1, the flux measured at Earth is decreasing with energy. This has to be compensated for by exposure to be able to get reasonable results. Two different methods are used: a *direct* and an *indirect* cosmic ray measurement technique. The measurements are called direct whenever the particles of interest (cosmic rays) are interacting directly with the detector, whereas the indirect methods are measuring secondary particles produced in the interactions of the primary particle outside of the detector (e.g. air showers).

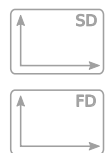
For energies up to 10^{15} eV the flux of cosmic rays is high enough to perform direct measurements, like balloon [36] or satellite [37] experiments. These experiments have to be outside of the Earth's atmosphere to avoid the interaction of the cosmic rays with the atmosphere. Above this energy the direct measurements become inefficient, as the flux drops below 1 particle per m^2 per day. The detectors for direct measurements have to be large or run for a long period of time. Large detectors are not only more expensive themselves, but bringing them high in the atmosphere by balloon or satellite becomes extremely expensive, or even impossible. To evade this inconvenience indirect techniques have to be performed at higher energies. As described in Section 2.2, ultra-high-energetic cosmic

rays produce extensive air showers (EAS) when colliding with the Earth's atmosphere. An EAS consists of billions of particles and has a spread of up to many square kilometers on the Earth's surface. By analyzing only a fraction of the secondary particles from the air showers, the properties of the cosmic rays can be reconstructed and used for further studies.

The largest astroparticle experimental setup built so far is the Pierre Auger Observatory (PAO) [16]. It is placed in the Pampa Amarilla near the town of Malargüe in Argentina and was designed to measure extensive air showers, initiated by cosmic rays with energies above $10^{18.5}$ eV.

The observatory covers an area of 3000 km^2 and is comprised of several detectors: the Surface Detector (Section 3.1), the Fluorescence Detector (Section 3.2) and the Auger Engineering Radio Array (Section 3.3). The Surface and the Fluorescence Detectors started to take data in 2004 and are fully operational since 2008. Auger Engineering Radio Array is data taking since 2011. In addition two extensions were installed, namely Auger Muons and Infill for the Ground Array (Section 3.1.1) and High Elevation Auger Telescopes (Section 3.2.1). The different detectors are working independently and provide both redundant and complementary data of the EAS. This allows to cross-calibrate the detectors, reduce the uncertainties of the measurements and to study systematic effects and detector resolutions. An overview of the Pierre Auger Observatory is given in Figure 3.1. Pictures of the individual stations of the three main detectors are shown in Figure 3.2.

The location of the observatory was chosen to fulfill several conditions. The observation height of the Surface Detector of 1400 m above the sea level corresponds to an atmospheric depth of 875 g/cm^2 [16] and leads to a higher number of secondary particles reaching the ground detectors compared to sea level. In the region where the observatory was built there is only one city, Malargüe, with a population of about 20,000 inhabitants resulting in relatively low light pollution. In addition, the dry climate with few clouds in that region makes the fluorescence light detection more efficient. At the same time Malargüe provides the necessary infrastructure for building and maintaining the observatory. The area where the observatory was built is nearly flat. This minimizes reconstruction corrections and associated uncertainties for the ground based detectors, which are spread over thousands of square kilometers.



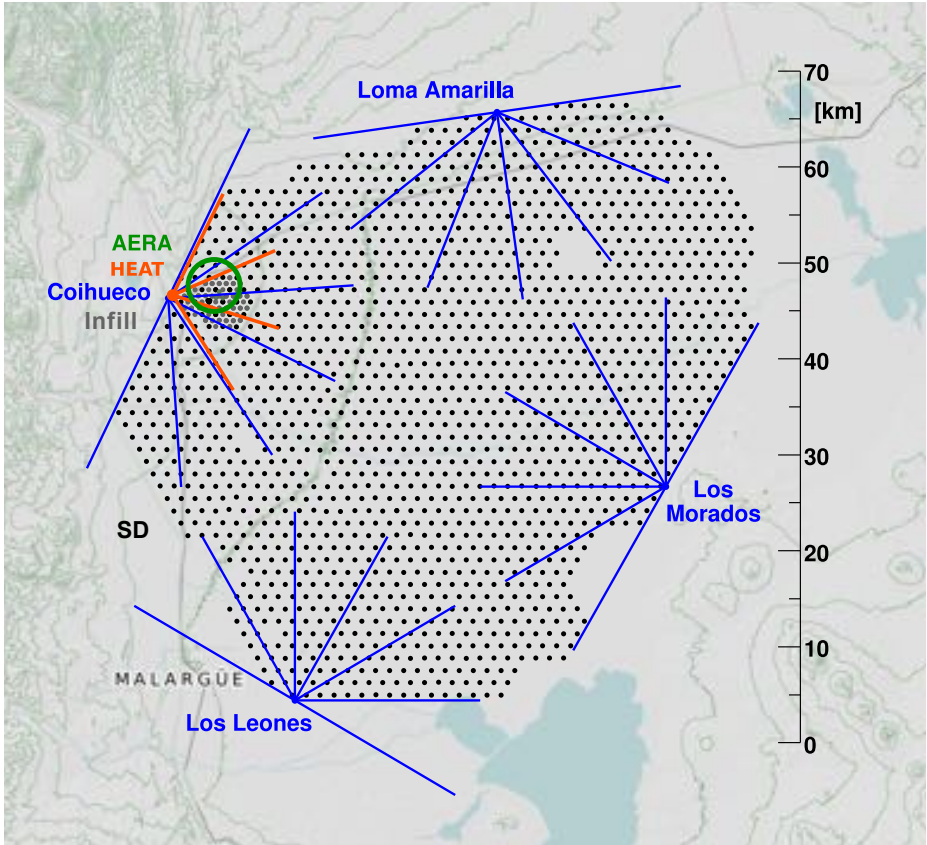


Figure 3.1.: Overview of the area of the Pierre Auger Observatory. The black dots mark the positions of SD stations, 4 FD sites are named and shown in blue, with the HEAT extension in orange. The lines represent the azimuthal field of view of each telescope. In addition, close to the Coihueco fluorescence detector, the dense SD infill array of the AMIGA extension is shown in gray, together with the AERA area in green. Adapted from [38].



(a)



(b)



(c)

Figure 3.2.: Pictures of a SD station (a), a FD housing with 6 telescopes (b) and an AERA station (c) of the Pierre Auger Observatory.

3.1. Surface Detector (SD)

A fraction of the secondary particles produced in the EAS cascade reaches the Earth's surface and forms the so called *footprint* at ground. The detection and the analysis of the secondary particles by detectors measuring the footprint, can be used to study the properties of the primary particle. For the Pierre Auger Observatory the *Surface Detector* (SD) was build to sample the secondaries at ground. It is an array of over 1600 particle detectors distributed in the pampa, covering a total area of 3000 km² [39]. They are arranged in a *regular array* of a triangular grid with a spacing of 1.5 km. The regular array is fully efficient for EAS with energies above 10^{18.5} eV.

Each particle detector consists of a cylindric tank, filled with 12 t of purified water. The water is contained in a diffusively reflective Tyvek liner inside the plastic tank. The charged particles of an air shower penetrating the water tank are traveling faster than the local speed of light and create (Vavilov-)Cherenkov radiation [40]. The reflective liner optimizes the collection of the Cherenkov light by the 3 photomultiplier tubes (PMTs) looking down into the water [39]. A cut-away view of a Surface Detector station is illustrated in Figure 3.3.

The signal produced in the PMT from the collected Cherenkov light is amplified through multiple dynodes and is provided to a 10 bit *flash analogue to digital converter* (FADC) in two gain levels. One is taken from the anode and the other from the last dynode, inverted and multiplied by a factor of 32 to extend the dynamic range for measured signals. Hence, for SD stations far away from the impact point of the *air shower axis* at ground (*air shower core* position) the amplified signal is used, to get a better separation from the background noise, whereas the amplified signal of the SD stations close to the air shower core can be saturated. In that case the anode output is used.

The signals of the two gain levels are digitized by the FADC with a combined dynamic range of 15 bits and a sampling frequency of 40 MHz, corresponding to a time bin size of 25 ns. Several SD stations measure the particles of one EAS simultaneously. Their signals are sent via the communications antenna to the *Central Data Acquisition System* (CDAS) [41] that provides the SD coincidence triggers (Section 3.4.1) to distinguish the measurements of air showers from background. To compare the trigger time of the detections, each Surface Detector station has its own GPS

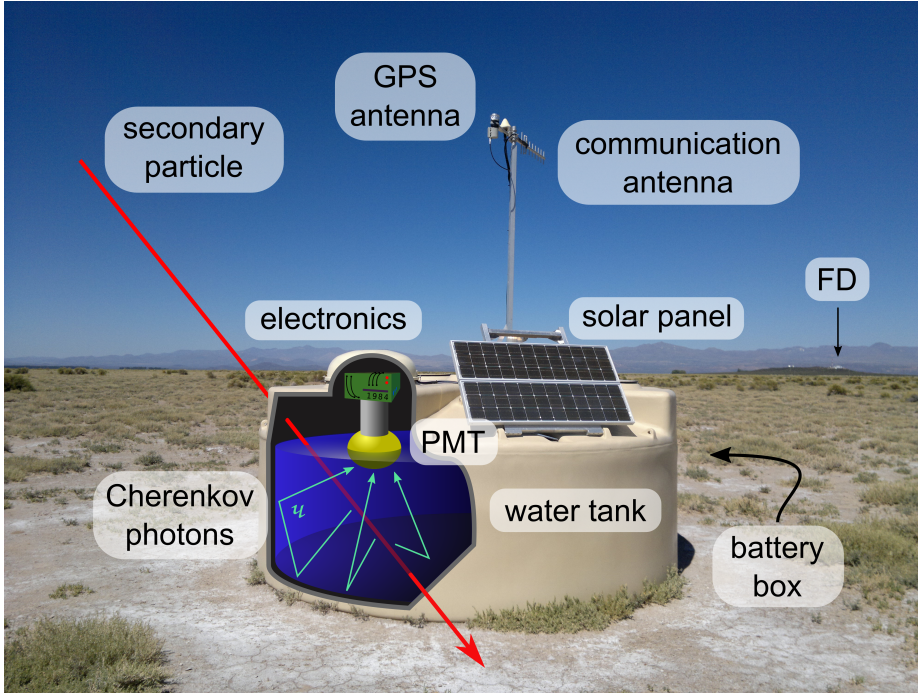


Figure 3.3.: A SD station. On top of the tank are the solar panel and the GPS and communications antennas located. The red line represents a particle going through the water and producing Cherenkov photons (cyan).

antenna. The time resolution from the GPS signal is about 10 ns [42]. On top of each SD station a solar panel is mounted to charge the battery placed on the side in the battery box. Thus, the Surface Detector stations operate continuously and autonomously.

At some locations, so-called *twin* stations are installed. These are additional identical stations, placed 11 m apart from the main one. In case two additional stations are placed the constellation is called *triplet*. The measurements at almost the same position allow to study the detector resolution and the sampling fluctuations in an air shower [42].

3.1.1. Auger Muons and Infill for the Ground Array (AMIGA)

In the western part of the Surface Detector area, close to the Coihueco fluorescence telescopes, the *Auger Muons and Infill for the Ground Array* (AMIGA) is located [43]. It is an extension of the SD and consists of two components.

The first one consists of 61 additional Surface Detector stations in the so called *infill array* of 25 km^2 , where the spacing on the triangular station grid is reduced to 750 m [44] (Figure 3.4(a)), which is half of the spacing in the regular array. This decreases the energy threshold by one order of magnitude, thus allows to detect EAS with energies above $10^{17.5} \text{ eV}$ with full efficiency. The additional stations in the infill area are identical to the ones in the regular grid with the same set of triggers. Therefore, they could easily be integrated into the readout procedure.

The second component of the AMIGA extension consists of underground muon detectors, which are placed at a depth of 2.3 m in the ground, corresponding to an additional slant depth of approximately 540 g/cm^2 [44]. The idea is to measure the muon component of an air shower by shielding the detector with a thick layer of soil, which eliminates the electromagnetic part by stopping the electrons, positrons and

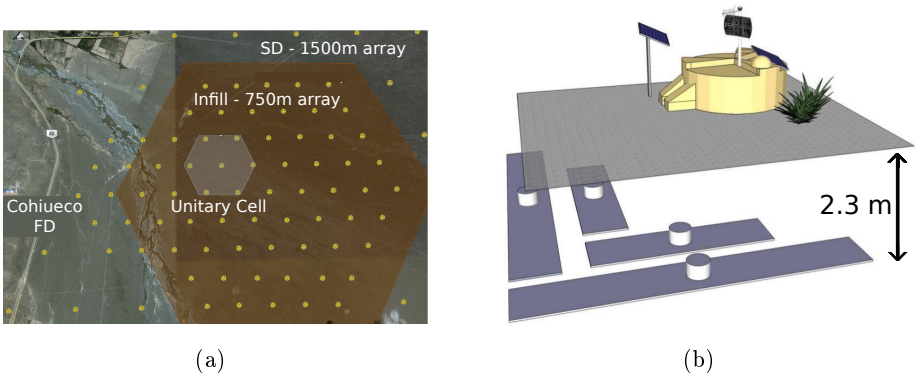


Figure 3.4.: The unitary cell equipped with AMIGA modules inside the infill array (a) and a sketch of a SD station and AMIGA muon detector modules (b) at 2.3 m underground. Adapted from [44] and [45].

photons before they can reach the detector. Most muons will pass through the soil layer, due to their small cross section and can thus be measured with good efficiency and high purity. A muon detector consists of four panels, two of which cover an area of 10 m^2 each and the other two cover 5 m^2 each (Figure 3.4(b)). Each panel contains 64 scintillator strips using a 64 channel silicon photomultiplier (SiPM) for the readout. The signals from the muons passing through the scintillator, are digitized and, using a field-programmable gate array (FPGA), are sent to the corresponding SD station. From there the signal of the underground detector is sent together with the SD signal to the CDAS.

The two parts of the AMIGA setup measure the total and the muonic components of an air shower to provide a better understanding of the air shower content at the ground level.

3.2. Fluorescence Detector (FD)

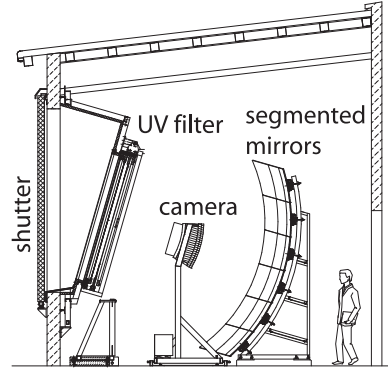
The secondary particles produced during the propagation of the air shower cascade excite the air molecules on their way downward. The molecules, mainly nitrogen, fall back in their ground state by emitting fluorescence light. The amount of this light is directly proportional to the total path length of all particles traveling through the air at a certain patch of the sky. By measuring the fluorescence light the longitudinal profile of an air shower is accessible. Parameters like energy and X_{max} can be reconstructed from the longitudinal profile. Also the direction of the air shower axis and therefore the arrival direction of the primary particle (cosmic or gamma ray) can be detected by measuring the trace of the fluorescence light.

At the Pierre Auger Observatory, the *Fluorescence Detector* (FD) was built to measure the fluorescence light produced by an air shower [46]. The FD consists of 24 telescopes at 4 sites, surrounding the area of the Surface Detector. The FD is fully efficient for air showers above the entire Surface Detector area with energies above 10^{19} eV .

The four telescope stations, Coihueco, Loma Amarilla, Los Morados and Los Leones, contain 6 telescopes each, located in individual bays in a semi-circular building. They overlook the surface area with a field of view for individual telescopes of $30^\circ \times 30^\circ$, starting at 1.5° in elevation. The combined azimuthal view angle of the 6 telescopes at one site is 180° . Each

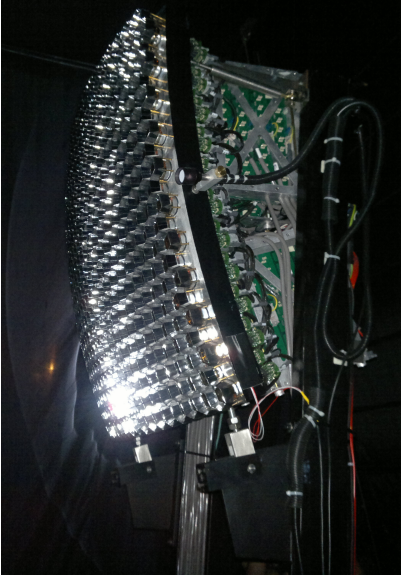


(a)

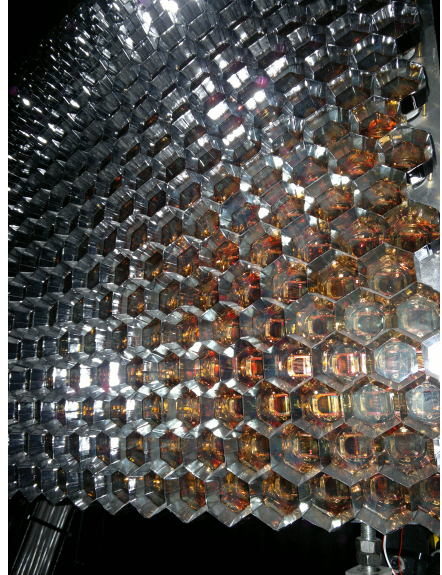


(b)

Figure 3.5.: A FD housing with opened shutters during maintenance (a) and a sketch of a FD bay interior (b). Adapted from [16].



(a)



(b)

Figure 3.6.: Pictures of the FD PMT camera (a) with the PMT grid (b).

fluorescence telescope bay houses a window with an UV filter, a concave segmented mirror and a camera [46]. The UV filter absorbs the visible light to reduce the background noise from light pollution, while the light in the UV band between 290 nm and 410 nm passes towards the mirror. This light contains all the relevant wavelength bands of the fluorescence light emitted by molecular nitrogen. The mirror focuses the incoming light towards the camera containing 440 PMTs, which are arranged in a grid of 22 rows and 20 columns. Winston cones with a frontal hexagonal shape, mounted in front of each PMT maximize the light yield. To protect the sensitive PMTs from the day light, the bays are screened by shutters, that close automatically when the light becomes too bright. One FD housing with opened shutters is shown in Figure 3.5(a), a schematic view of one FD bay in Figure 3.5(b) and a PMT camera in Figure 3.6. The segmentation of the mirror and the individual PMTs of the camera allow to follow the trajectory of the EAS.

The downside of the FD is that the fluorescence light produced by an air shower is much fainter than even the moon light. To be able to detect it from several kilometers away, the environment has to be very dark. Another disadvantage is that the field of view from the telescope to the air shower need to be unobscured, i.e. without clouds. Therefore the FD telescopes can operate only in clear, moonless nights, leading to an uptime of about 13% of the total operation time of the observatory [46].

3.2.1. High Elevation Auger Telescopes (HEAT)

Similar to the SD infill of the AMIGA extension, the FD was also extended towards a lower energy threshold. An additional fluorescence detector station, the *High Elevation Auger Telescopes* (HEAT) [47], was built close to the Coihueco site and it overlooks the infill area of the denser array of SD stations. HEAT contains 3 shelters with one telescope each (Figure 3.7), similar to the telescopes of the main FD stations, with the same field of view. The shelters can be tilted upwards to change the elevation angle of the telescopes. The maximum elevation angle is 30° and combined with the fluorescence telescopes of Coihueco, the elevation range of the field of view is extended to almost 60° . That leads to measurements of a larger fraction of the longitudinal profile in case the air shower is nearby and X_{\max} is at a large elevation. This allows the detection of less energetic air showers with energies above 10^{17} eV [47].



Figure 3.7.: HEAT shelters in the horizontal position for maintenance.

3.2.2. Monitoring of the atmospheric conditions

The interpretation of the fluorescence light measurements requires good knowledge of the weather conditions. The yield of the fluorescence light produced by the secondaries depends on the atmospheric conditions along the trace of the air shower cascade, which may vary at any given time. In addition, the fluorescence photons on their way toward the telescope can be scattered by the air molecules or the aerosols in the air. Finally, clouds can either absorb the fluorescence light or scatter it towards the telescopes, leading to a distortion of the longitudinal profile and incorrect results.

To monitor the atmospheric conditions several instruments are used (Figure 3.8), providing measurements in fixed time intervals [48]. Atmospheric variables, such as temperature, air pressure and relative humidity are measured in five minute intervals by five weather stations, one at the center of the SD array and one at each of the four FD sites. To determine the conditions at higher altitudes and to construct the atmospheric profiles, 261 balloon-based radiosondes have been launched [48]. They monitored the air conditions from August 2002 until December 2008. Based on

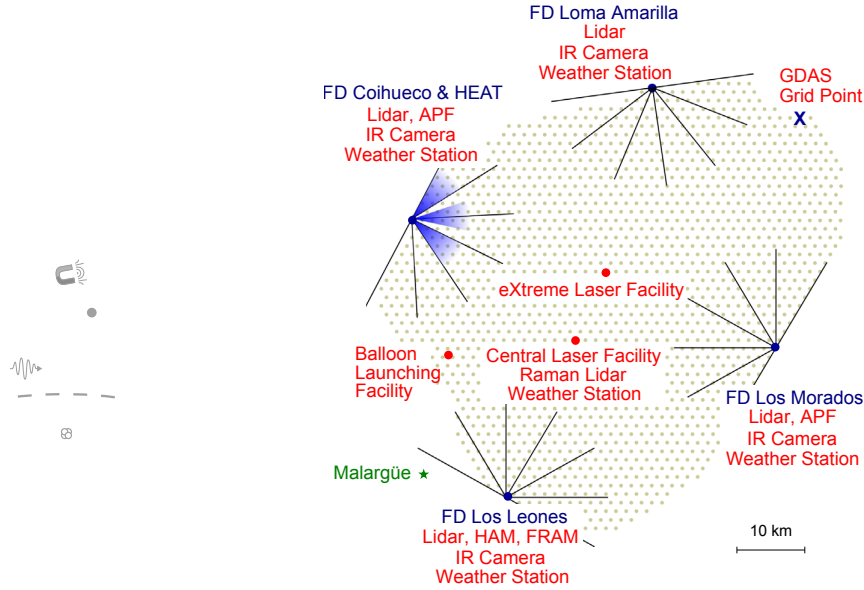
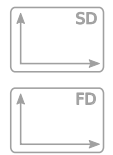


Figure 3.8.: The atmospheric conditions monitoring systems at the Pierre Auger Observatory. Grey dots represent the SD stations and the lines the field of view of FD telescopes. In red the different monitoring systems are indicated. Adapted from [48].

these measurements monthly average models were created and the measurements were used to evaluate the data of the *Global Data Assimilation System* (GDAS) for the region of the Pierre Auger Observatory [49]. The GDAS data provide models on a 3-hour base that are used for the analysis of the FD measurements.



While the atmospheric state variables can be modeled on average, the aerosol levels have to be continuously monitored, due to their change on short time scales. For instance, the amount of dust in the atmosphere can increase rapidly by the wind or decrease by a rain shower. The measurements of the vertical optical depth of aerosols are performed using the *Central Laser Facility* (CLF) and the *eXtreme Laser Facility* (XLF) [48]. They both are located near the center of the SD array and shoot every 15 minutes sets of laser beams vertically into the night sky. The laser light is

recorded by the FD telescopes and is used to compare the measurements to the clear nights with negligible aerosol influence to estimate vertical optical depth of aerosols as a function of the height. Besides these technique *Light Detection And Ranging* (LIDAR) facilities were built close to each FD site [50]. These work independently from the FD by shooting and measuring their own laser rays under different angles outside the field of view of the FD. In addition to the GDAS models, targeted measurements of the atmospheric conditions are performed with LIDAR shortly after events of special interest, like the ones with the highest energies [50].

The LIDAR systems are also used to detect the clouds and estimate their height above the detector area. When a cloud is hit by the laser, the light is widely backscattered and the cloud can be identified in the data. Repeating this measurements under different inclination angles helps to calculate the height of the cloud. In order to monitor the more global cloud coverage of the sky, infrared cameras are used, installed at each FD site. In the μm spectra, at which the IR cameras operate, the clouds can be easily distinguished as warm structures on the cold background night sky. The IR measurements provide the estimation of the cloud coverage for each pixel of the fluorescence telescopes.

The disturbances due to clouds on the fluorescence light and the longitudinal profile, are in general difficult to recover, thus the time periods where part of the FD field of the view area is covered by clouds are usually excluded from the data.

3.3. Auger Engineering Radio Array (AERA)

In the air shower cascade propagating downwards to the Earth's surface, charged particles, such as muons and electrons, are continuously produced and accelerated. This induces radio emission, based on two effects. One involves the geomagnetic field and is therefore called the *geomagnetic effect* [52]. Particles of opposite charge, electrons and positrons, are accelerated in opposite directions under the influence of the Lorentz force. The other effect is the so called *Askarian effect* and is caused by the creation of a dipole along the air shower axis [53]. The secondary particles knock out electrons from the air molecules during the propagation, leaving the positive charged ions behind. Both effects superimposed form the radio signal, with a significant component in the MHz band.

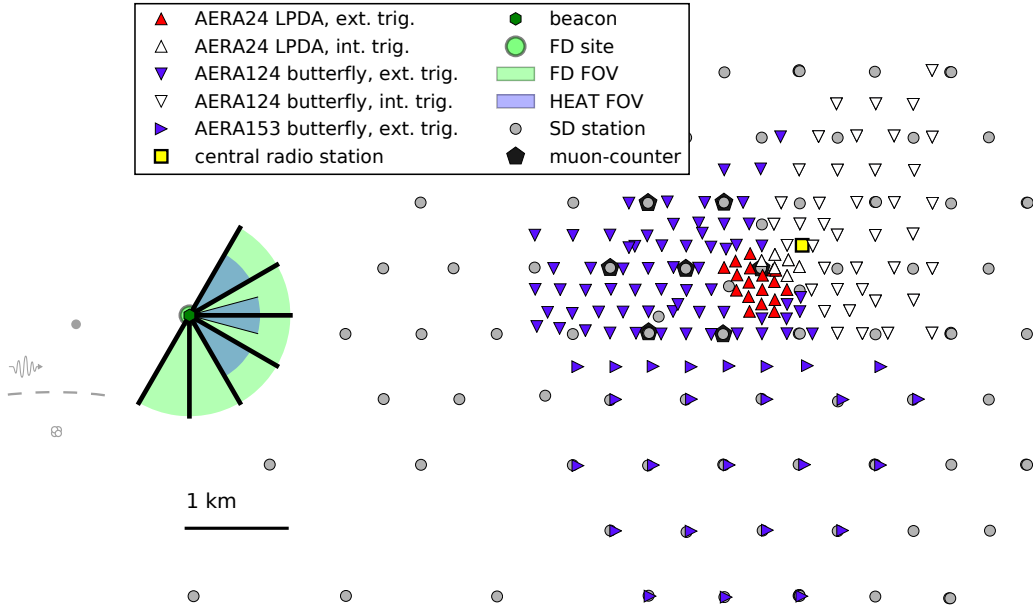


Figure 3.9.: Map of AERA stations close to the Coihueco site. Beside the AERA detectors marked as different triangles, also a fraction of SD stations (gray circles), the AMIGA array (black pentagons), and the FD and HEAT stations with their fields of view (FOV) are illustrated. Obtained from [51].

At the Pierre Auger Observatory different setups for the measurements of the radio signals were tested in the late 2000's, culminating in the *Auger Engineering Radio Array* (AERA), that started construction in 2010 and is taking data since 2011 [54]. AERA consists of radio antennas, which are placed in an area of 17 km^2 at the infill area of the Surface Detector, close to the Coihueco FD station. Their positions are chosen to optimize the measurement of EAS with energies above 10^{17} eV .

The radio detector stations have been deployed with two different types of antenna and two different types of electronics leading to four different

station types [55]. The *Logarithmic Periodic Dipole Antennas* (LPDA) were installed during the AERA-I phase in 2010, followed by the *Butterfly* antennas during the AERA-II phase in 2013. The position of the antennas varies depending on their type and electronics, as can be seen in Figure 3.9. The antenna stations are designed to operate autonomously. Therefore, each station consists of, beside the signal antenna, a solar panel, electronics and a battery box. The timing information is provided by the GPS receiver, similar to the one at an SD station. To send the signal to the CDAS each AERA station is equipped with a communication antenna. The two electronic designs follow different trigger philosophies. One requires an external trigger from the SD, where the other comes with its own internal trigger either from the radio data or by using additional small scintillator detectors in the battery box [55].

3.4. Event reconstruction

To distinguish an air shower from the background noise and to reconstruct its properties as well as to obtain the parameters of the primary particle, an *event reconstruction* has to be performed.

The analysis method presented in this thesis is based on the measurements recorded by the SD stations. The FD data is used to calibrate the SD measurements and to decrease uncertainties. Therefore, the reconstruction methods of these two detector types will be presented in this chapter. The AERA data will not be used for the analysis in this thesis. The reconstruction details of AERA can be found e.g. in [55].

An air shower can be reconstructed in different ways depending on the recorded data available (excluding AERA): using only SD or combining FD and SD measurements. The events reconstructed with the FD by using information from a few SD stations are called *hybrid events*, whereas those using simultaneously the full FD and full SD reconstruction are called the *golden events*. A visualization of a golden event is shown in Figure 3.10.

For the simulation of the detectors and the reconstruction of their signals as well as the reconstruction of the measured data from SD presented in this thesis the software package Offline (Section 4.2) version v3r3p1 was used. Hence, in this chapter the values of the constants used for the reconstruction are given for this version number.

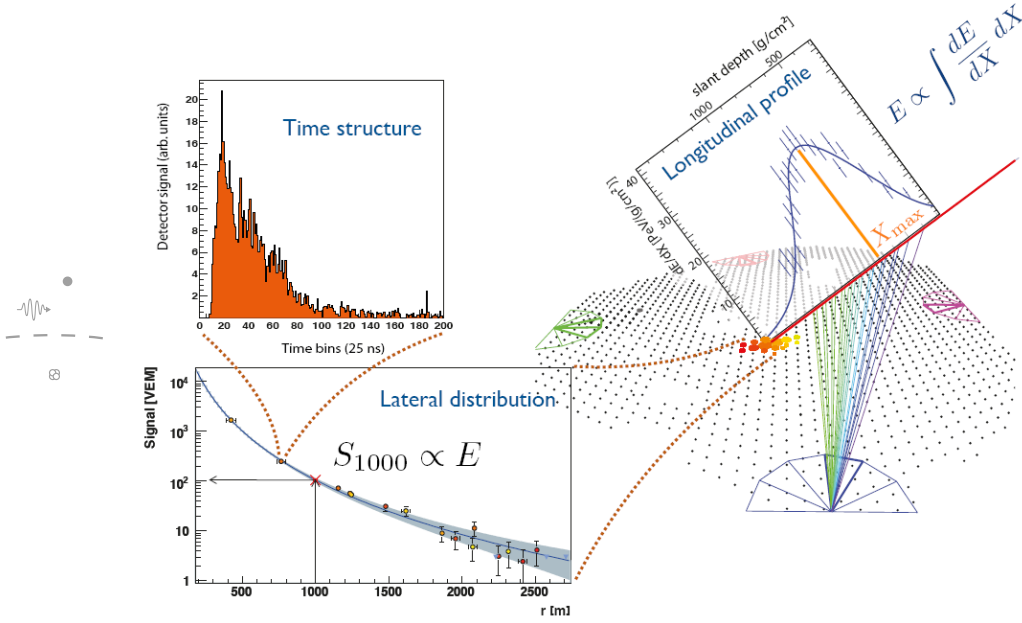
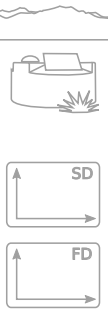


Figure 3.10.: Schematic overview of an air shower detection by both the SD and the FD. The red line marks the direction of the air shower propagating from the right hand side. The grid of gray points on the right site represents the SD stations, in which the triggered ones are colored from yellow to red. Each of them measures the time structure (top left histogram) of the air shower secondaries passing through the water tank. The signal strength of a SD station, as a function of distance to the air shower axis, reflects the lateral distribution of air shower particles (bottom left graph). The FD (bottom right) measurement of the longitudinal profile of the air shower (top right graph) is indicated through colored lines. The color code of the SD and FD signals indicates the detection time. Adapted from [56].



3.4.1. Event reconstruction with SD

Each of the Surface Detector stations samples a tiny fraction of the secondary particles arriving at the ground. The density of the secondaries at the observation level depends on the energy, inclination angle and nature of the primary particle, as well as on the distance to the air shower axis. The reconstruction of the air shower properties, and therefore of the primary particle, is only possible when combining the signals of several detector stations. The strength of the detected signal from particles traveling through the SD as seen by the PMTs depends on several parameters: the gains of the anode and the last dynode of each PMT and their ratio, the coupling of the PMT window to the water, the liner reflectivity and the water quality. To analyze the signals measured by different SD stations and to identify and study the EAS the signal strength has to be calibrated.

VEM calibration The energy deposit of the secondaries in the SD station varies from particle to particle. It depends on their path length, energy and nature. To calibrate the signal, the Cherenkov light produced by atmospheric muons from low energy air showers is used. The signal is normalized to the average signal induced by a muon traveling centrally and vertically through the water tank and is expressed in units of *Vertical Equivalent Muon* (VEM). The calibration is a continuous process. Therefore, each PMT of a given SD station measures the same signal by adjusting its gain in real time. Each SD station records several histograms and updates them permanently, e.g. a histogram with the signal produced by atmospheric muons, defining the VEM locally for each SD station. More details can be found in [57].

Triggers To separate a measurement of an air shower from background, the measurements of the Surface Detector stations have to pass 5 levels of triggers [41]. The first three are needed to record an event (Figure 3.11) and the last two select well measured air showers in the data (Figure 3.12).

The first trigger T1 is reached when the three PMTs of a SD station each have a signal S above 1.75 VEM (*threshold trigger*, TH), or at least 13 bins in 120 FADC bins are above 0.2 VEM for at least 2 PMTs (*time over threshold*, ToT). The T2 trigger is identical to the T1, with a higher threshold for TH of 3.2 VEM. These two triggers are calculated locally in each SD station to register the presence of one or more particles.

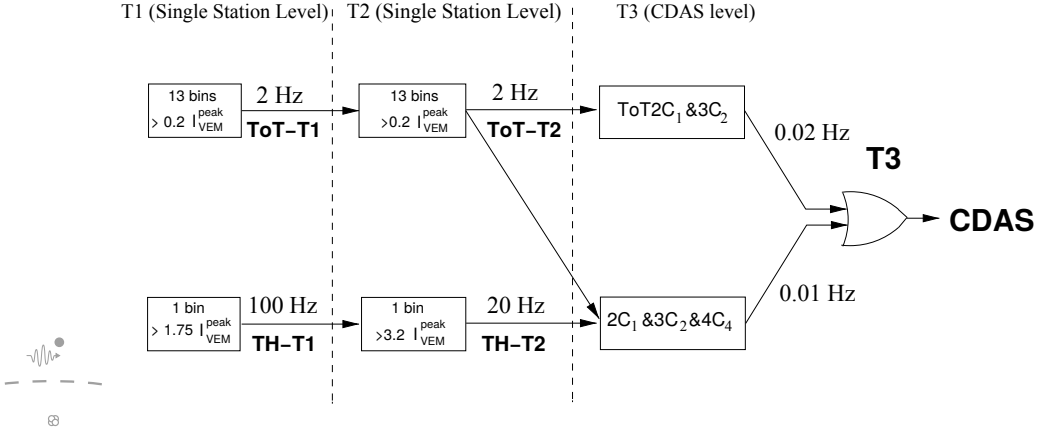


Figure 3.11.: Scheme of the local triggers T1 and T2 at one SD station and the CDAS trigger T3. Adapted from [41].

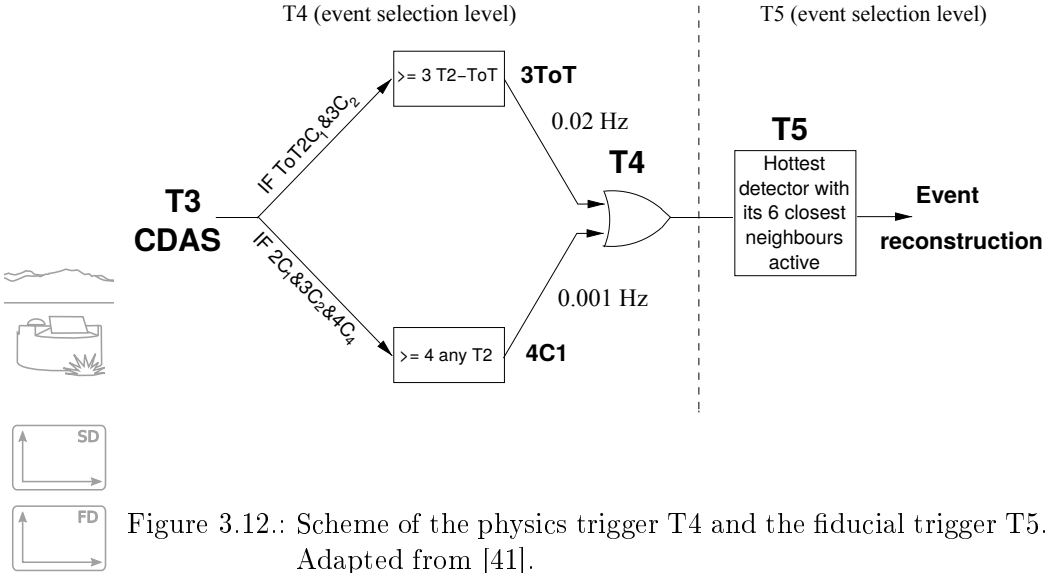


Figure 3.12.: Scheme of the physics trigger T4 and the fiducial trigger T5. Adapted from [41].

When a SD station has a T2 trigger, it sends its time stamp to the CDAS, which looks for coincidences with other SD stations within $30\,\mu\text{s}$. One possible hint of a signal from an EAS is, that three neighboring stations have a T2-ToT, two in the first ring of neighbors (crown) C1 and one in the next ring C2. This constellation is called $ToT2C_1\&3C_2$. Another possibility, where four stations have a T2 and are arranged in such a way that two are in the first ring of neighbors, the next one in the second ring and the fourth one as far as in the fourth ring, is called $2C_1\&3C_2\&4C_4$. Examples for these constellations are shown in Figure 3.13. Once one of such coincidences is found, a T3 is fired and all PMT traces of SD stations with a T1 are send to the CDAS. The efficiency of a single SD station triggers based on calculations of events that produced a T3 is above 80 % for $S \approx 5$ VEM [41].

The T3 could be caused by a coincidence of different local air showers with smaller energies. To select the events of interest, where the SD stations were triggered by one air shower with high energy, the T4 trigger is used. It checks the positions of the triggered stations and their times according to the propagation speed of an air shower. There are two T4 criteria, the 3ToT and the 4C1. The first one requires 3 neighboring SD stations in a triangular pattern, passing the T2-ToT, whereas the second looks for 4 nearby stations, passed any mode of T2. The T4 trigger also

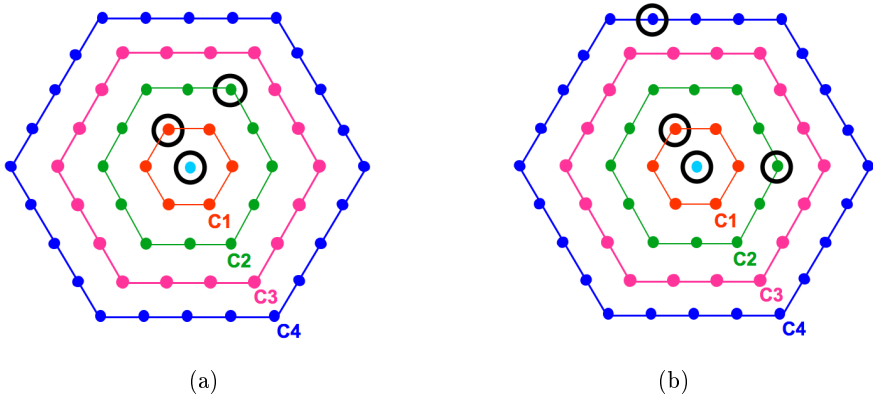


Figure 3.13.: Possible configurations for the $ToT2C_1\&3C_1$ trigger (a) and the $2C_1\&3C_2\&4C_4$ trigger (b). For description see text. Obtained from [41].

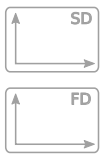
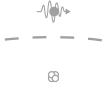
removes stations with no triggered neighbors within 3 km. The efficiency of the T4 is above 98 % [41].

The final trigger T5 is called the *fiducial trigger* and is needed to select well measured air showers. For EAS at the edge of the Pierre Auger Observatory, the reconstruction would estimate wrong properties, due to the missing SD stations inside of the footprint of the EAS, but outside of the array. Inside the fiducial area of the array non-functioning stations can also influence the quality of the measurements. Therefore, only events with a possible correct reconstruction are selected. There are different types of the T5 trigger. The strongest is the 6T5, where the SD station with the highest signal has to be surrounded by 6 other working stations in a hexagon, although not all of them need to be triggered. This trigger provides the optimal quality of measured events in terms of the air shower geometry with an efficiency above 97 % [41]. To increase the number of events for studies where the geometry is less important this criterion can be lowered to 5T5, where the central station need to be surrounded by only 5 working neighbors.

Baseline and signal region The signal from the secondaries is calculated by converting the raw FADC traces into integrated signals and thereafter into VEM units. To obtain the signal strength, the baseline of the PMT has to be taken into account. The baselines and their standard deviations for high and low gain channels of each PMT are computed for the 60 seconds interval before the signal starts, from each of the 100 Hz calibration triggers [57].

The FADC trace segment provided to the reconstruction, contains the signal on top of the baseline. The baseline is supposed to contain only the background noise. Yet, there is a bias for the time period after the signal region caused by the undershoot of the baseline after a big discharge of the PMT, especially in the high gain channel. Therefore the baseline of the signal interval is modeled with respect to the expectation of the undershoot [58].

In the first attempt to calculate the integrated signal, the amplified high gain output of the last dynode is used. In case this channel is saturated, the low gain trace of the anode is used. When both channels are saturated, likely for the SD station close to the air shower axis, a recovery of the trace is performed [59]. In Figure 3.14 the high and low gain traces of one PMT with a signal of a simulated air shower are shown.



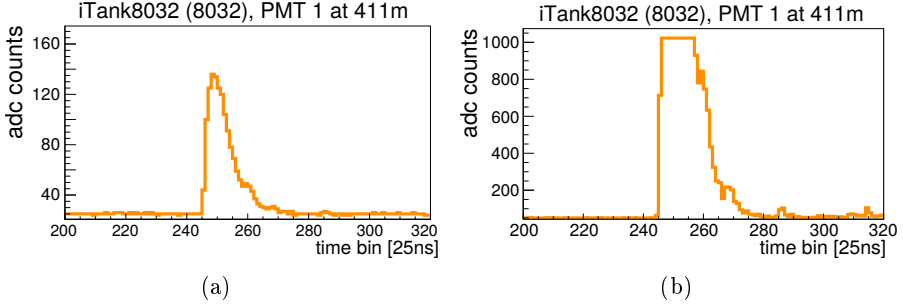


Figure 3.14.: PMT traces from anode (a) and last dynode (b) of a simulated event with $E = 10^{18.5}$ eV from a SD station at 411 m from the air shower axis. The signal of the dynode is saturated. Figure created by using the EventBrowser [60].

Event geometry Once the signals in the neighboring SD stations are identified to originate from the same EAS and the signal strength of the triggered stations is calculated, the event geometry can be reconstructed. The absolute trigger time of the SD stations determines the air shower direction. From the signal intensity the position of the air shower core as well as the total air shower energy can be estimated.

As the first approximation a *plane air shower front disk* (from now on called *air shower front*) formed by the secondaries propagating toward the Earth's surface is taken (Figure 3.15(a)). With this model a rough estimate of the air shower axis direction is calculated using the times of

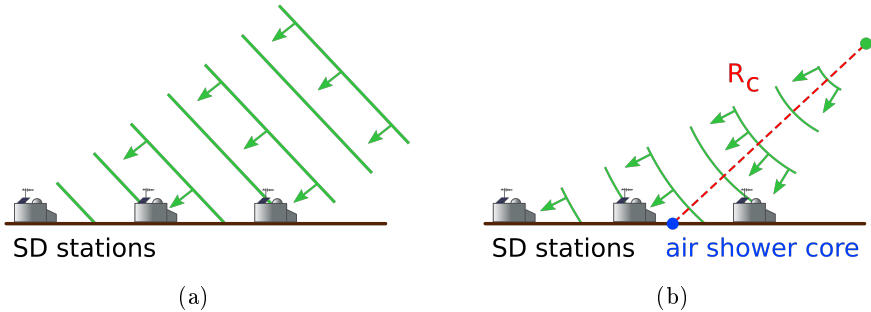


Figure 3.15.: Plane (a) and spherical (b) air shower front models.

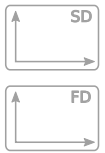
the triggered SD stations. Next, the distribution of the signal strengths from the stations as function of the distance to the air shower axis is fitted by the *Lateral Distribution Function* (LDF), which is a variation on the Nishimura-Kamata-Greisen function [61] [62]:

$$S(r) = S(1000) \left(\frac{r}{1000 \text{ m}} \right)^\beta \left(\frac{r + 700 \text{ m}}{1700 \text{ m}} \right)^{\beta+\gamma} . \quad (3.1)$$

The $S(1000)$ parameter stands for the signal strength, that would be measured at the distance of 1000 m to the air shower axis. This was found to be the optimum distance to determine the energy of the primary particle for a SD grid with a spacing of 1.5 km [63]. The fall-off of the LDF when moving away from the air shower axis is adjusted with the two parameters β and γ that were parametrized depending on the total air shower energy and the inclination angle. The LDF fit is performed by maximizing a likelihood function that uses an upper limit for the signal strength for functioning SD stations that were not triggered. From this fit the first estimation of the air shower core and the air shower size at ground are achieved, which are used for the next iteration cycle.

To evaluate the final reconstruction parameters the plane air shower front is replaced by a *curved air shower front* of an expanding sphere (Figure 3.15(b)). This approximation is assumed to be valid, given that the produced secondaries are traveling at almost the speed of light and are boosted towards the surface in the direction of the primary particle. Especially the muons practically do not interact once produced from decay of pions shortly after the first interaction, forming a sharp edge of the curved air shower front that determines the trigger time of the SD stations. The fit of the *spherical air shower front* as one variant of the curved air shower front is performed when an event consists of at least five triggered stations and yields the zenith and azimuth angles of the air shower axis, the impact time of the air shower core and a parameter called the *radius of curvature* (R_c). In case an event consists of less than five triggered SD stations, a parametrized value for R_c is used.

The radius of curvature describes the distance from the air shower core to the point along the air shower axis where the particles that form the air shower front, mainly the muons, were produced. The R_c is smaller than the distance to the point of the first interaction and is expected to depend on the nature of the primary particle (further explained in Section 5.1).



Once the curvature fit is performed, another iteration step is done, fitting the LDF with the new air shower core and air shower axis parameters. In Figure 3.16 the final fit results of the curvature fit and the LDF fit are presented for a simulated EAS.

Event energy The LDF fit yields $S(1000)$, an estimation for the total air shower energy. However, this parameter depends also on the inclination angle. To remove the inclination dependency, the *Constant Intensity Cut* (CIC) method is used [64]. It is based on the assumption that above a certain energy the cosmic ray flux is isotropic. Therefore, the number of cosmic rays is assumed to be constant as a function of $\cos^2 \theta$.

Figure 3.17(a) shows the dependency of the $S(1000)$ parameter as function of $\sec \theta$. The distribution in $x = \cos^2 \theta - \cos^2(38^\circ)$, with the reference point at 38° as the median inclination angle for the regular SD array with 1500 m spacing is fitted with a third order polynomial:

$$f_{CIC} = 1 + ax + bx^2 + cx^3 \quad , \quad (3.2)$$

where $a = 0.956 \pm 0.044$, $b = -1.625 \pm 0.086$ and $c = -1.210 \pm 0.465$ were obtained from the data [65].

By correcting the $S(1000)$ with the f_{CIC} an inclination independent signal strength can be defined as

$$S_{38} = \frac{S(1000)}{f_{CIC}(\theta)} \quad . \quad (3.3)$$

The S_{38} parameter represents the signal intensity of an air shower with an inclination angle of 38° at 1000 m from the air shower axis. The conversion from S_{38} to the total air shower energy is done with the aid of FD telescopes. For the golden events, measured and reconstructed with the SD as well as the FD, both S_{38} from SD and the calorimetric energy E_{FD} from FD are obtained. The relation between these two quantities is illustrated in Figure 3.17(b) and follows a power law:

$$E_{FD} = a \cdot (S_{38}[\text{VEM}])^b := E_{SD} \quad , \quad (3.4)$$

where $a = 0.187 \pm 0.004 \text{ EeV}$ and $b = 1.023 \pm 0.006$ [65].

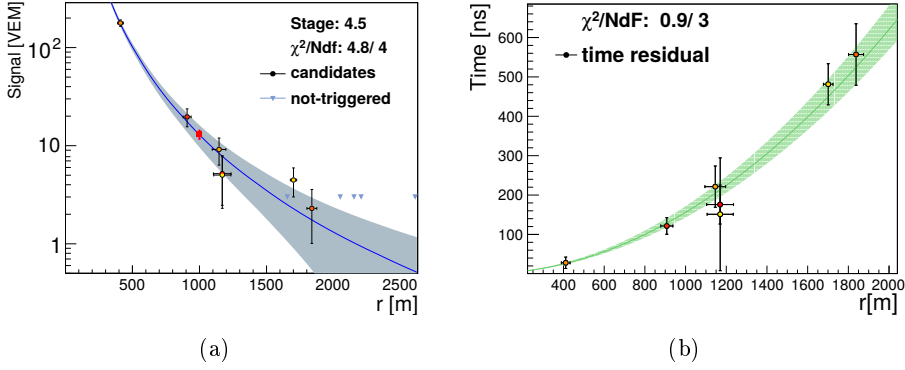


Figure 3.16.: LDF (a) and R_c (b) fits of a simulated air shower with energy of $10^{18.5}$ eV and an inclination angle of 45° . The markers represent the triggered SD stations. The color code indicates the individual trigger time. Figure created by using the EventBrowser [60].

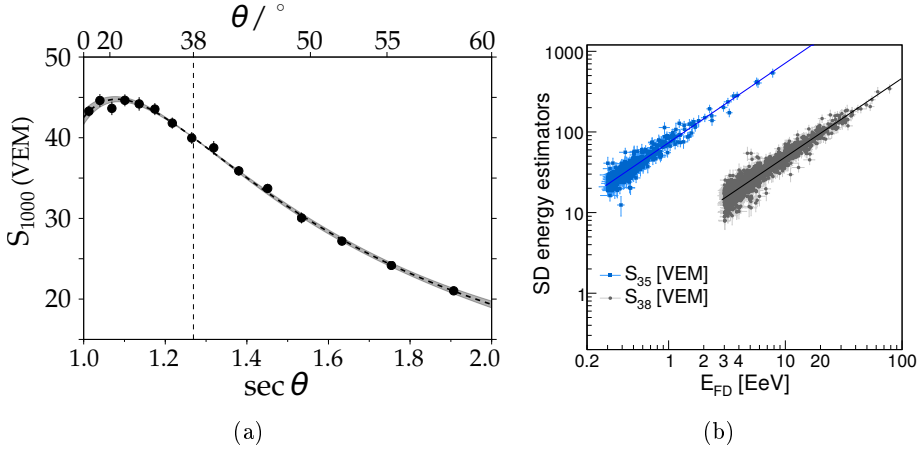


Figure 3.17.: Attenuation curve $f_{CIC}(\theta)$ with the reference angle of 38° marked as the vertical dashed line (a). SD energy calibration from hybrid events (b). The displayed calibrations are S_{38} (blue points, left) with the reference angle of 38° for the 1500 m array and S_{35} (gray points, right) with 35° for the 750 m array. Adapted from [65].

The statistical uncertainties of a and b are relatively small, of the order of a few percent. They decrease with higher energies, caused by the larger number of SD stations for high-energy events, and are limited by the event-to-event fluctuations. The main contribution to the uncertainty originates from the systematic uncertainty of the FD. Given that the calibration of the energy is done with the measurements of events with unknown composition, which is likely to be mixed, the differences between the air showers initiated by different primaries also contributes to the energy uncertainty [15]. The total energy resolution of E_{SD} for air showers with $\theta < 60^\circ$ measured with the regular array is $(15.3 \pm 0.4)\%$ [65].

3.4.2. Hybrid event reconstruction

The Fluorescence Detector stations, in contrast to the Surface Detector, measure the longitudinal profile of an air shower, in their field of view, until it reaches the Earth's surface. They also track the trajectory of an air shower during its development in atmosphere (Figure 3.18(a)).

To record an event with the FD only, a local trigger is needed. The trigger is provided by looking for the amount of detected light of neighboring pixels of the PMT camera to be above a certain threshold [46]. Once an event is identified, the geometrical reconstruction can be performed to obtain the longitudinal energy deposit profile (Figure 3.18(b)).

Geometry reconstruction From the position of the fluorescence telescope and the trace in the PMT camera (Figure 3.18(a)) the detector plane of the air shower is defined (Figure 3.19). To reconstruct the air shower axis, this information has to be combined with the timing information of at least one triggered SD station [46]. Given that another detector type is involved in the reconstruction these events are called hybrid events. For these events the air shower core location resolution is 50 m and the typical resolution for the arrival direction is 0.6° .

Longitudinal profile The longitudinal profile histogram of the energy deposit starts at high altitudes (small values of the atmospheric depth X) and goes into deeper layers toward the surface (higher values of X). At some point the energy deposit is at its maximum, before starting to decrease again. This point of atmospheric (slant) depth, where the maximum of the number of secondary particles is reached, is the X_{\max} (Section 2.2.3).

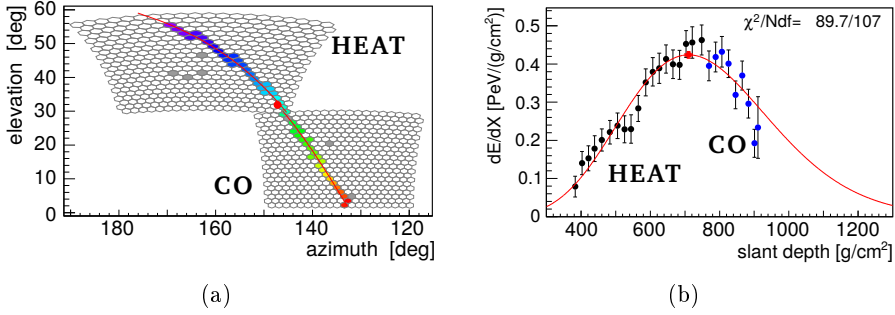


Figure 3.18.: An event with energy of $(3.7 \pm 0.1) \times 10^{17}$ eV detected by HEAT and Coihueco FD telescopes. The color code of the trace (a) indicates the detection time (blue = early, red = late). The energy deposit as function of the slant depth (b) is fitted with the Gaisser-Hillas function (eq. 3.5). Red point mark the position of X_{\max} . Adapted from [66].

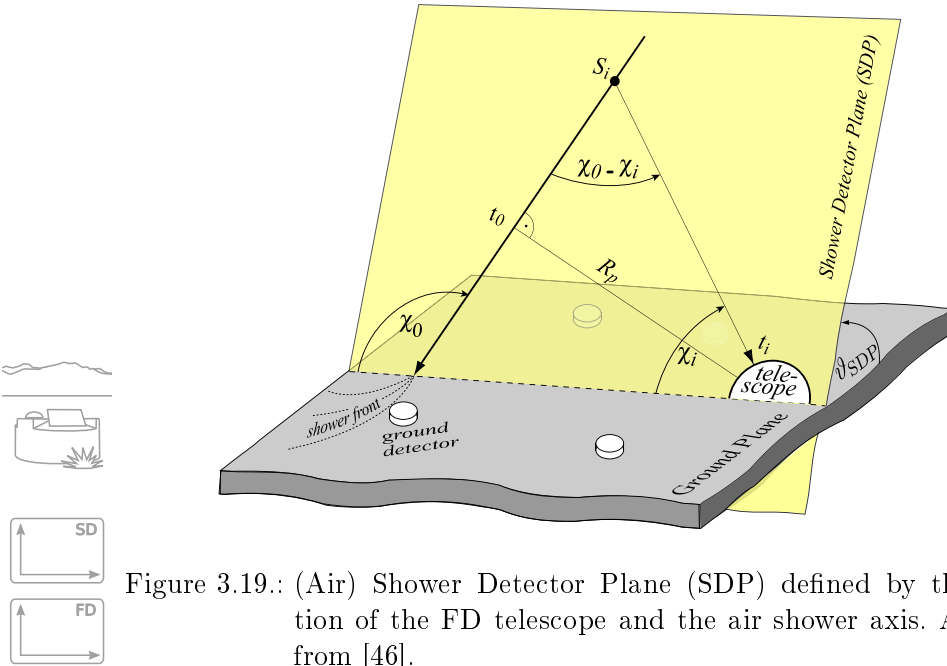


Figure 3.19.: (Air) Shower Detector Plane (SDP) defined by the position of the FD telescope and the air shower axis. Adapted from [46].

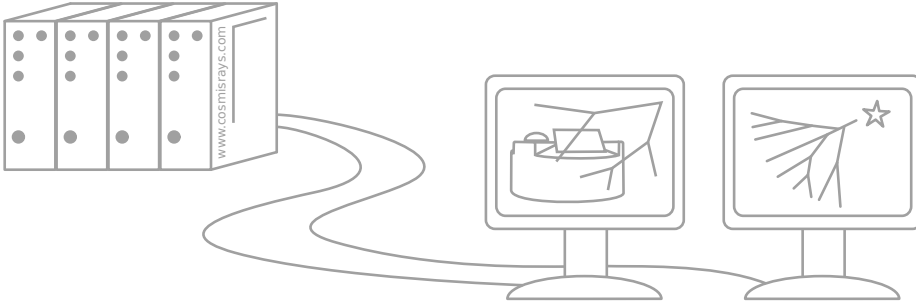
To obtain its value, the energy deposit profile is fitted with the Gaisser-Hillas function [67]:

$$f_{GH}(X) = \left(\frac{dE}{dX} \right)_{max} \left(\frac{X - X_0}{X_{max} - X_0} \right)^{\frac{X_{max} - X_0}{\lambda}} \exp \left(- \frac{X_{max} - X}{\lambda} \right), \quad (3.5)$$

where X_0 is the atmospheric depth of the first interaction of the cosmic or the gamma ray with the atmosphere and λ is the average mean free path for the secondary particles in the air shower cascade. $\left(\frac{dE}{dX} \right)_{max}$ is the differential energy deposit at the maximum of the air shower.

Calorimetric energy The main fraction of the energy from the primary particle is transferred into the electromagnetic component of an EAS and proportionally into the fluorescence light emitted during its propagation. To estimate the calorimetric energy from the longitudinal profile, the Gaisser-Hillas function (Eq. (3.5)) from Figure 3.18(b) is integrated. To take into account the missing energy carried away by neutrinos and high-energy muons, some small corrections are added. The systematic uncertainty of the FD energy estimation is about 14% [65].





Air shower simulation and reconstruction

In order to interpret the outcome of an experiment, it needs to be compared to theoretical predictions, based on knowledge of the underlying physics. Therefore, numerical simulations of the investigated process and the detector hardware response are performed using physics models, which are updated when new results become available. The simulations determine i.e. the efficiency (exposure) and selection biases of a given measurement. Furthermore, they are used to define the set-ups of future experiments.

The air shower models describe the EAS, initiated by cosmic or gamma rays, as sequences of collisions and decays of secondary particles during the propagation through the air. These interactions have been studied in several experiments and are well known up to energies of $10^{17.5}$ eV, which is the maximum energy in the frame of a fixed target cosmic ray experiment produced by the LHC [6] (Figure 2.3), the current most powerful human-made accelerator. The measured energies of the cosmic rays can be higher than that. The models for these high-energy interactions are extrapolated from measurements at lower energies. These extrapolations are blind to new interactions that appear only at higher energies. Therefore, studying EAS provides an opportunity to test theoretical predictions at energies that are not accessible under laboratory conditions.

The description of the evolution of an air shower and the prediction of the particle distribution at ground can be done in two different ways. In the *analytical method* a cascade equation is solved, whereas in the *Monte Carlo* (MC) *simulation* the numerical results are obtained through repeated random sampling of particle interactions. The MC simulations require higher computation power and take significantly longer, but they provide more realistic results, including effects of fluctuations. For the analyses of the Pierre Auger Observatory data mostly two programs are used: *CONEX* [68], including a numerical description for low-energy particle subcascades (analytical method) and MC simulations for the high-energy interactions, and *CORSIKA* (Section 4.1), a program using MC simulations down to the lowest energies.

In addition to the air shower evolution, the detector effects and their response to the secondaries of the EAS have to be understood. Hence, simulations of the detector stations and of the signal generation are performed. Similar to the EAS, these simulations can be semi-analytical or using a full MC method. For the Pierre Auger Observatory the detector simulations are incorporated in the in-house software framework called Offline (Section 4.2).

4.1. Air shower simulation with CORSIKA

One of the main air shower simulation programs used to simulate EAS is the *COsmic Ray SIMulations for KASCADE* (CORSIKA) software package [69]. It was mainly developed by a group of scientists from the Kernforschungszentrum Karlsruhe (now KIT) for the KASCADE experiment [70] in the 1990's and it has been kept up to date ever since. CORSIKA simulates the interactions of secondaries in the cascade with the air nuclei and their decays, using different interaction models for the high- and low-energy particles. This takes into account the different processes dominating or simply present in different energy regions. The transition from the high- and the low-energy ranges is at 80 GeV [69]. The interaction models are based on the knowledge of interactions measured in particle physics experiments and are updated frequently.

To start a Monte Carlo simulation a steering file has to be provided to CORSIKA. This file contains settings of the simulation options and is composed of a list of lines, each of which starts with the option identifier

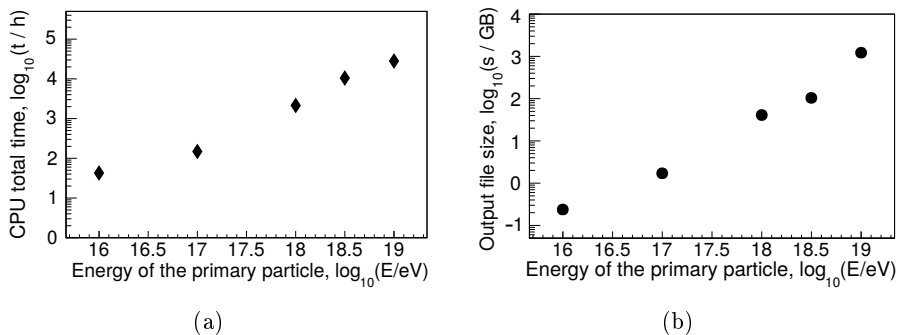


Figure 4.1.: Total CPU time in hours (a) and disk space in GB (b) needed for a single full EAS simulation. Note that the last point has a smaller inclination angle (30°), in comparison to the other simulations (45°), resulting in a higher number of particles arriving at the ground, mainly photons, electrons and positrons, which leads to a bigger output file size. At the same time this simulation is faster due to a smaller number of depth steps. The hardware specifications are listed in Appendix A.1.

followed by one or more arguments. In case an instruction for a specific option is not found, a default value is used. All steering commands and the default values can be found in the CORSIKA user's manual [71]. In Appendix B the steering files and the command descriptions are listed, used to generate the simulations for the analyses described in this thesis.

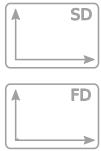
The output of the simulation is saved in a file, which contains the relevant information of the air shower properties as well as types, coordinates, arrival times and momentum vectors of all secondaries at the observation level [71]. The file size and the computation time scale roughly linear with the energy and vary also with nature and inclination angle of the simulated cosmic ray and the interaction models chosen. The energy dependence of the computation time and the output file size per event are shown in Figure 4.1. The diagrams are based on full, i.e. non-thinned simulations (Section 4.1.1) with a proton primary particle and EPOS and FLUKA as the hadronic interaction models. The full simulations are performed in parallel (Section 4.1.2) on the cluster of the high-energy physics group at the Universität Siegen. The hardware specifications and software versions are listed in Appendix A.

The file size and the computational time are becoming unmanageable for full EAS simulations with an energy close to the maximal energy measured with the Pierre Auger Observatory (10^{20} eV). To decrease the output size and the duration, different strategies have been developed and implemented in CORSIKA. One of the most used procedures is the so called *thinning*, that will be described in Section 4.1.1. Another strategy is to remove the low energetic particles (energy cut), which will barely contribute to the signal in the detectors, already during the propagation. Additionally, parts of the simulation can be done in parallel, to reduce the required wall clock time.

Hadronic models For particle energies above 80 GeV the EPOS [72] and QGSJet [73] models are commonly used to describe the hadronic interactions in EAS simulations. These models are continuously updated and tuned to the recent results from the accelerator experiments, most notably those at the LHC [6]. Both models are based on the parton-based Gribov-Regge theory [74], but differ in their implementation, which translates into slightly different predictions of the EAS properties, especially for muon production. The number of muons observed by the Pierre Auger Observatory for an EAS with an energy of 10^{19} eV is 30 % (80 %) higher than in the current EPOS-LHC (QGSJetII-04) model [75] [76]. This is an important problem, as the muons are of main interest for mass composition studies (Chapter 5).

Using the EPOS and QGSJet models affects the calculation time differently. The EPOS simulations resemble the results of the collider experiments more precisely [71], but require more CPU time.

In the low-energy region, below 80 GeV, the Monte Carlo routines from the *FLUctuating KAscade* (FLUKA) [77] package are widely used. FLUKA is based on the *Electron Gamma Shower* version 4 (EGS4) [78], that includes all the relevant electromagnetic interactions, such as the electron-positron-annihilation, pair production, bremsstrahlung, Compton, Bhabha and Møller scattering, and was extended for muon production, photonuclear and low-energy hadronic processes.



Atmosphere The EAS simulations require models for atmospheric conditions, described in Section 3.2.2. The atmosphere in these models consists of nitrogen (N_2), oxygen (O_2) and argon (Ar) with relative abundances of 78.1 %, 21.0 % and 0.9 %, respectively [71]. The influence of the

atmosphere differs for simulations with different inclination angles. Therefore the density, which varies with altitude, is modeled using 5 layers. Also seasonal variations can be taken into account for more realistic results.

In CORSIKA different atmospheric models are available. Some of them are averaged over the year, others are based on monthly averages. A world global model can be chosen or a model describing the conditions of the region of the Pierre Auger Observatory using GDAS [49].

4.1.1. Thinning procedure

The technical challenges for creating air shower simulations at the highest energies are the amount of CPU time and the huge output file size (Figure 4.1). When running the full simulation and following all secondary particles to the Earth surface, the required CPU time can easily reach several thousand hours and the output file size will be in the order of hundreds of GB for single air shower with an energy of $10^{18.5}$ eV, which is the lower bound of the energy range of interest for the Pierre Auger Observatory.

To reduce the calculation time and also the output file size the *thinning sampling algorithm* (thinning) was implemented in CORSIKA [79]. With this option, only a small fraction of the total amount of secondary particles is simulated down to the ground. At a given stage, the energy of each new created particle E_i is compared to the thinning energy threshold E_{thin} , which is expressed by the fraction ε_{thin} in comparison to the energy of the primary particle E_0 :

$$E_{thin} = \varepsilon_{thin} E_0 \quad . \quad (4.1)$$

If E_i is below E_{thin} , a survival probability p_i is calculated, depending on the energy sum of all particles with energy below E_{thin} :

$$p_i = \frac{E_i}{\sum_i E_i} \quad \text{for} \quad \sum_i E_i < E_{thin} \quad , \quad (4.2)$$

$$p_i = \frac{E_i}{E_{thin}} \quad \text{for} \quad \sum_i E_i \geq E_{thin} \quad . \quad (4.3)$$

According to this survival probability representative particles are randomly chosen for further calculations. After this random selection, the weight of the remaining secondaries is increased by a weight factor w_i ,

which is inversely proportional to p_i :

$$w_i = \frac{1}{p_i} . \quad (4.4)$$

The weight makes up for the discarded particles. A maximum weight value can be defined to avoid that a small number of representative particles cause a large influence on the outcome. Newly produced particles that would exceed this maximum weight value are excluded from thinning by the algorithm [71].

The usual process, where the energy of the particle that starts a new interaction is below the thinning energy threshold, resulting in only one representative secondary surviving the thin sampling is shown in Figure 4.2(a). In case the energy of the particle prior the interaction and consequently the energy sum of the secondary particles exceed E_{thin} , the number of remaining secondaries can be more than one. In particular, all secondaries with an energy above the thinning energy threshold are tracked for the next simulation step (Figure 4.2(b)) and the others are selected based on the survival probabilities.

For an electromagnetic cascade, where only two particles emerge from the interaction, a special case can occur where both of the secondaries survive the thin sampling. When the energy of each of both particles is below E_{thin} , but the energy of the parent particle is above this threshold, one of them is selected according to p_i , whereas the chance p_j for retaining also the other secondary is higher than 0 [79], given by

$$p_j = \sum_i p_i - 1 = \frac{\sum_i E_i}{E_{thin}} - 1 > 0 \quad \text{as} \quad \sum_i E_i > E_{thin} . \quad (4.5)$$

This is illustrated in Figure 4.2(c). Finally for the bremsstrahlung processes one particle is kept (in case of $E_i > E_{thin}$), whereas the second has also a survival probability $p_i > 0$ to remain after the thinning (Figure 4.2(d)).

Using this thin sampling procedure the CPU time and output size are reduced drastically by up to several orders of magnitude depending on thinning parameters, which helps to simulate a large number of air showers in a feasible amount of time [69]. However, several air shower properties are distorted and the thinned simulations have to be further processed to restore at least the number of secondary particles that would originate from non-thinned (full) air shower simulations.

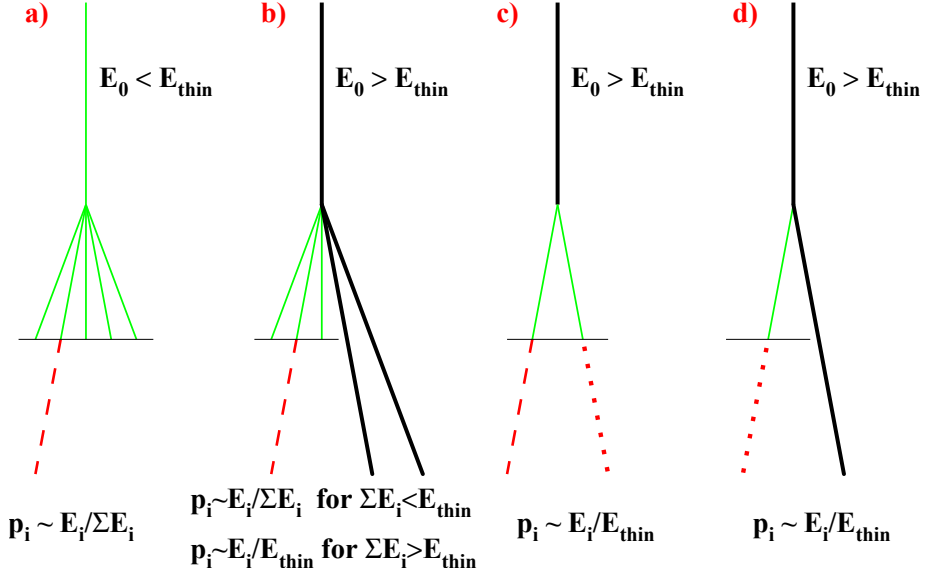


Figure 4.2.: Variations of the thin sampling algorithm implemented in CORSIKA. The horizontal line marks the thinning selection processes, with only the representative particles (dashed lines) passing through. Thick lines indicate the particles with $E_i > E_{thin}$. Dotted lines represent the possibility for additional particles to survive the thinning procedure. Adapted from [79].

4.1.2. Parallelization

To perform a full simulation and at the same time reduce the wall clock time, EAS simulations can be parallelized. In CORSIKA this option is implemented through the *OpenMPI* software [80], which uses the *Message Passing Interface* (MPI) [81]. The parallelization allows to compute the subshowers on multiple CPUs separately at the same time. In this procedure several output files are created, one for each core (minus one master core, that controls the parallelization procedure), which have to be merged at the end to receive the identical output to the non-parallelized simulations, for further analysis. This option is used to simulate the non-thinned air showers analyzed in this thesis.

4.2. Detector simulation and EAS event reconstruction with Offline

A big collaboration requires standardized software for data readout, storage, calibration, reconstruction and analysis. The Pierre Auger Collaboration has developed the *Auger Offline Software Framework* (Offline) [82], which consists of three principal parts: the *detector description*, the processing *modules* and the *event data* model (Figure 4.3). The Offline concept provides the opportunity to reconstruct the measurements and the simulations in the same way to obtain comparable results. At the same time the modules can be easily changed by users, exchanged or ordered in another way to fulfill different analysis approaches.

An event contains all the relevant informations of a single EAS (raw, calibration, reconstruction and simulation data) and acts as a repository for the communication between the modules. The information is changed by the modules that represent the different steps of the reconstruction procedure. Most of the steps can be split into self-contained tasks and are implemented as individual modules. The modules are written in C++, to benefit from the object oriented design, while the configuration of the reconstruction process is implemented in XML to provide the opportunity to change the module sequence and adjust the options without recompiling. The reconstruction procedure is controlled by a run controller and is steered through the `bootstrap.xml` file and additional XML files that contain the configurations and options used by single modules.

The detector description provides an interface for modules to receive the read-only information status of the detectors and the atmospheric conditions, that in contradiction to the event information can not be modified by the modules. The detector information, like the detector positions or their orientations is static and is stored in XML files, while data that changes with time, such as atmospheric conditions and calibration of the detectors, which varies slowly with time, due to e.g. aging, can be found in a MySQL databases.

The results of the reconstruction procedure for the simulated events and for the measured EAS are saved in the *Advanced Data Summary Tree* (ADST) file format [60]. It is based on the ROOT framework [83] and contains both the high-level quantities from the reconstruction as well as the low-level raw data.

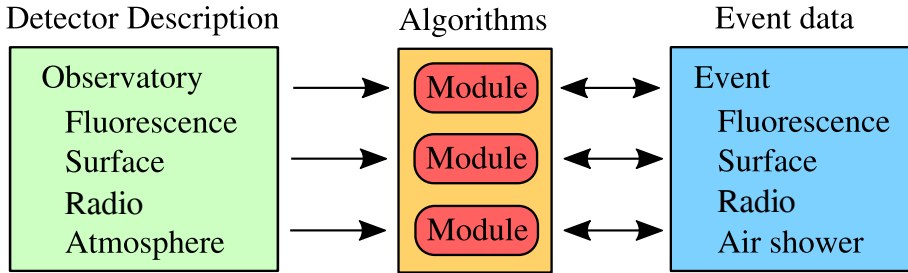


Figure 4.3.: The structure of three parts of $\overline{\text{Offline}}$. The arrows indicate which way the information can be passed. The modules can read from both detector description and the event data, but can write only into the event. Adapted from [82].

The functional principle of the main $\overline{\text{Offline}}$ modules is explained in the next section. The order of the modules is defined in the *module sequence file*, described in Section 4.2.3.

4.2.1. Detector simulation

For a comparison between the measurements from the Pierre Auger Observatory and the CORSIKA air shower simulations, the detectors have to be emulated in order to obtain their response to the secondary particles from the simulated EAS. For this purpose the properties of the individual detectors have to be well known. Also the configuration of the detectors, e.g. their relative locations has to be taken into account.

As the analysis, described in this thesis, is focused on the SD data, only the simulations of the SD stations will be discussed.

Resampling of a thinned air shower The output file of a thinned air shower contains secondary particles with weights bigger than one. The simulation of the SD station response requires a *resampling* (dethinning, unthinning) procedure [84] of these secondaries according to their weights. The resampling can be done in different ways. Figure 4.4 shows an example of the resampling process realized in $\overline{\text{Offline}}$. First a *sampling region* is defined around each SD station. For all particles hitting this region a number of clones is generated according to their weights of same nature with the same energy, direction and arrival time. Next, the number of

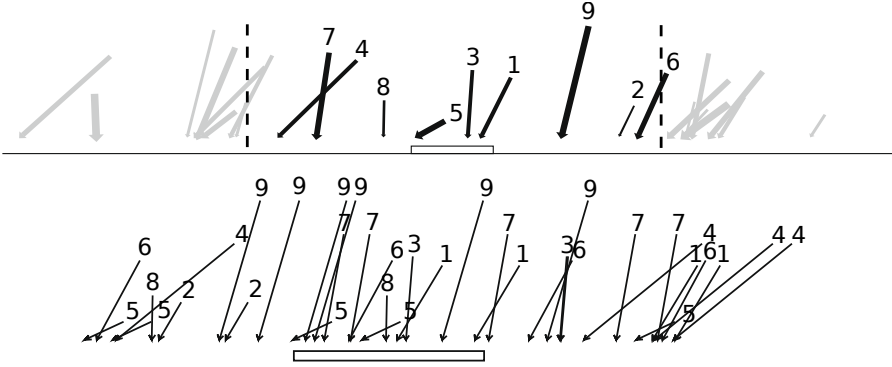
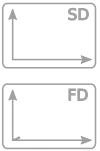


Figure 4.4.: Top: sampling region around the SD station (rectangle in the middle) is delimited by the dashed lines. The weighted particles within this area are represented by the black arrows with length proportional to their energy and width proportional to their weight. Bottom: generated clones of the particles within the sampling region. Adapted from [84].

particles of each type falling into the detector is calculated according to a Poisson distribution with the resampled weight w_r . The effective SD tank area in this process is modeled for each particle individually as function of its direction (Figure 4.5(a)).

After the resampling, the simulation of the ground detectors is performed in the same way as done for simulations without thinning. While the number of particles at the ground can be restored quite well for thinned air shower simulations through resampling, their spatial and temporal distributions are deformed in comparison to non-thinned EAS simulations. Also the fractions of the different particle types at the surface differ between non-thinned and thinned air shower simulations. All this distorts the signals in the detectors and adds uncertainties to the reconstructed parameters, which may lead to biased results.



SD detector simulation The simulation of the signal created by one SD station is split into subroutines and realized by a series of several modules. They simulate the interactions of the secondary particles with the physical setup of the SD station, thereby simulating Cherenkov photons, the

propagation and reflections of these photons through the water tank, the PMT response and the electronic chain until the signal is sent to CDAS. A more complete description of the modules involved will be given in Section 4.2.3.

The interaction of the particles with the SD can be described in two ways similar to the approach for the complete EAS simulation. Either a full simulation is done, which provides the result closest to the real detector, but requires a broader knowledge of the components of the SD and consumes more computational power. Or, alternatively, estimations from tabulated values are used as functions of the secondary particle properties in different gradations. The advantages of this method, in comparison to the full simulation, are the negligible computing power and fast access to the results. The full simulation of the interaction of the secondaries with a SD station, is realized by a module based on the

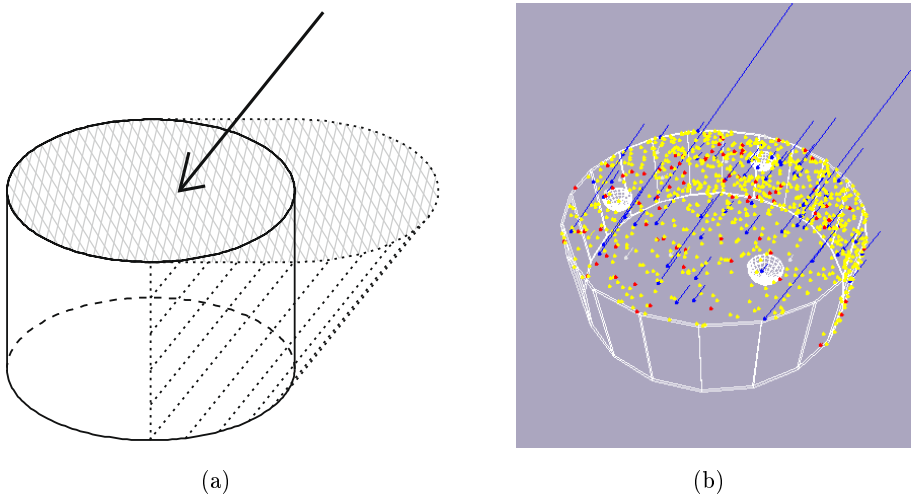


Figure 4.5.: Example of the calculation of the effective SD tank area (a) (shaded area at the top) with the direction of the incoming particle represented by the arrow. Adapted from [84]. SD station response simulation (b) with the particles hitting the tank. Photons are indicated in yellow, electrons and positrons in red and muons in blue. Figure created by using the EventBrowser [60].

Geometry and Tracking 4 (GEANT4) [85] toolkit. It emulates the behavior of the traversing particles through the different materials and propagates Cherenkov light through the water tank reflecting on the inner liner until it reaches one of the PMTs. Figure 4.5(b) illustrates a step in the SD station response simulation.

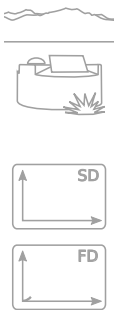
4.2.2. EAS event reconstruction

The second main purpose of the Offline framework, beside the detector simulation, is the event reconstruction, that was described in Section 3.4.1 and Section 3.4.2, with individual tasks organized in modules. The event reconstruction calculates the properties of the analyzed EAS and is applied to the measured data and the simulations in the same way. Hence, data and simulation results can be directly compared.

4.2.3. Module sequence file

The order of the steps done by modules, is defined in `ModuleSequence.xml`, which is written in XML. The description of several modules is given in [86] (SD), [87] (FD) and can be found in general in [88]. The module sequence files (Appendix C) used in this thesis for the analysis of the simulated and measured events will be explained in the following.

At first the data of the simulated or measured EAS have to be read from file into the event structure. This is done by the `EventFileReaderOG` module, with file name and simulation type defined in `EventFileReader.xml`. This module resides in a loop that controls how many events (EAS) are read from the file. For simulated air showers it is usually one per file, while for the measurements the files contain several EAS for a specific time period. When reconstructing a simulated air shower, the next loop allows to use an air shower more than once to increase the statistics. In `EventGeneratorOG`, the event time and the air shower core location are generated for the simulated EAS. The core can be placed randomly or at a fixed position inside the area that represents the observatory. This is specified in the `EventGenerator.xml` file. The next step is to loop over the secondary particles. Inside this loop the `CachedDirectInjector` module is used in case of non-thinned EAS simulations, and the `CachedShowerRegeneratorOG` module for its thinned counterpart, to simulate which secondaries hit the detector. The first



module moves the particles directly into the detector simulation, whereas the latter resamples them first (dethinning) by distributing the clones over the effective tank area of an SD station [84]. The full simulation of the SD stations is done with the GEANT4 toolkit implemented in the `G4TankSimulatorOG` module. After looping over the particles, the detector output and the data taking chain are emulated. First, the simulated detector calibration is loaded by the `SdSimulationCalibrationFillerOG` module followed by the simulation of the electronic chains of all SD stations, including the response of the PMTs (`SdPMTSimulatorOG`), the FADC signal (`SdFilterFADCSimulatorMTU`), the baseline and noise (`SdBaselineSimulatorOG`), the local triggers (`TankTriggerSimulatorOG`) and the GPS time (`TankGPSSimulatorOG`). Next, the CDAS trigger is emulated by the `CentralTriggerSimulatorXb` and the event is built by the `CentralTriggerEventBuilderOG` and the `EventBuilderOG` modules. Finally, the `EventCheckerOG` rejects events with missing SD stations as described in Section 3.4.1.

The steps up to this point are only required to be performed in case of simulated EAS (except reading the air showers). The modules listed below are applied to the measured EAS, starting with the checks of the event and the detectors, to sort out wrongly working stations which would bias the subsequent event reconstruction. The modules `SdPMTQualityCheckerKG` and `SdBadStationRejectorKG` discard malfunctioning stations and the modules `TriggerTimeCorrection` and `SdStationPositionCorrection` apply known corrections to the triggers and the positions of the SD stations in case they are off the grid. `SdSignalRecoveryKLT` tries to recover the signals of saturated SD stations.

After the measured events are cleaned, or for the simulated EAS an emulation of the readout chain has been done, the reconstruction of the air shower parameters is performed. The `SdCalibratorOG` module calibrates the signals from the SD for the analysis. `SdEventSelectorOG` prepares the events for the air shower reconstruction modules coming next by checking for the trigger criteria and removing stations with signals that do not belong to the EAS, such as lightning strikes or isolated SD stations. For simulated events the `SdMonteCarloEventSelectorOG` module takes care of the additional simulated SD stations that do not belong to the regular SD grid. `SdPlaneFitOG` performs a first estimation for the arrival direction (Section 3.4.1, Figure 3.15(a)). The results from this module are used in the `LDFFinderKG` to calculate the parameters of the LDF,

first using a plane fit and in the next iteration step using a curved front (Figure 3.15(b)), by also fitting the radius of curvature R_c (Section 5.1). In case of data events from the measurements, some corrections are applied to the energy estimation in the `EnergyCalculationPG` module based i.a. on the measurements of the weather conditions. After the reconstruction of the air shower properties is done, the event is checked with the `SdEventPosteriorSelectorOG` module for errors. Finally the event parameters are written to disk into an ADST file by `RecDataWriterNG`, with the options defined in `EventFileExporter.xml`.

4.3. Set of air shower simulations used for analysis

For the analysis described in this thesis several thousands EAS simulations have been created using CORSIKA on the computer cluster of the high-energy physics (HEP) group at the Universität Siegen. The list of hardware specifications and software versions can be found in Appendix A.

Almost all air showers that were simulated earlier for other analyses were produced with the thinning algorithm (Section 4.1.1). This allows to simulate a large number of events, although it comes with a smearing of the particle arrival times, leading to an increase of the uncertainties. To investigate this effect both thinned and non-thinned shower simulations were produced. The following settings were used for the simulations:

- Primary particle: photon (γ), proton (p), iron nucleus (Fe)
- Energy E_{sim} : 10^{18} eV, $10^{18.5}$ eV, 10^{19} eV and $10^{19.5}$ eV (only thinned)
- Inclination angle θ_{sim} : 0° , 15° , 30° , 45° , 60°

The CORSIKA parameters for the simulations were as following:

- Non-thinned, thinned: $\varepsilon_{thin} = 10^{-6}$
- CORSIKA versions: 7.4005, 7.5600
- High-energy interaction models: EPOS-LHC, QGSJetII-04
- Low-energy interaction model: FLUKA 2011.2c-4

For each set of parameters 20 air showers were simulated with the thinning algorithm. They were split into two sets of 10 simulations each for further use. However, due to the requirements on CPU time and storage space only a few non-thinned EAS simulations are created. Three sets with 10 EAS each for proton, iron nucleus and photon primaries at a fixed energy $E = 10^{18.5}$ eV, zenith angle $\theta = 45^\circ$ and with the EPOS hadronic interaction model. For these parameter sets the statistics are comparable to those of the thinned simulations. For all other configurations of inclination angles, energies of 10^{18} eV and $10^{18.5}$ eV and the EPOS hadronic interaction model only one non-thinned air shower was simulated per set. At 10^{19} eV only 2 non-thinned EAS simulations were performed, with $\theta = 30^\circ$ and the EPOS model, one with proton and one with iron nucleus as the primary particle. Using the QGSJet hadronic interaction model only three simulations were created, one per primary particle type with $E = 10^{18.5}$ eV and $\theta = 45^\circ$.

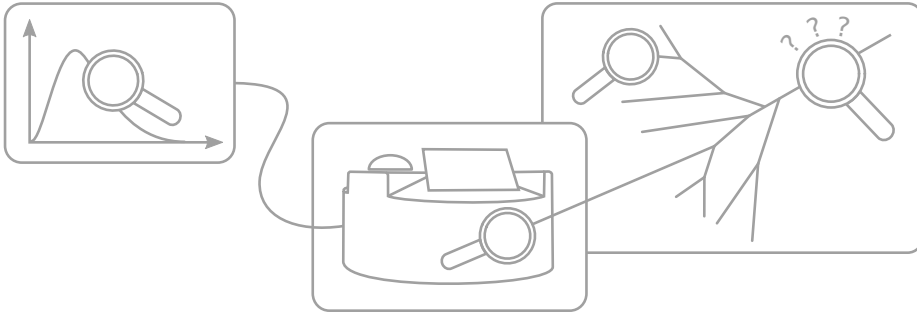
To reduce the required wall clock time the code was parallelized for the non-thinned air shower simulations (Section 4.1.2). In this process several bugs in the code of CORSIKA version 7.4005 were found that affect simulations with a photon primary particle. Therefore, the photon non-thinned EAS simulations are generated only with CORSIKA version 7.5600, which does not show these problems. The thinned simulations with a photon primary particle are also available with CORSIKA version 7.4005. Most of non-thinned simulation with proton and iron nucleus primaries including the one at 10^{19} eV were performed using CORSIKA version 7.4005.

The EAS simulations are used as an input for the detector simulation with Offline (Section 4.2), version v3r3p1.

In the next chapters the data will be confronted with simulations for the three types of primary particle which will be called *proton*, *iron* (nucleus) and in case of the photon *gamma* (ray), to avoid confusion between the words proton and photon, which only differ by one character. Although historically only the charged particles were defined as cosmic rays, gamma rays are also included in the following for reasons of simplification, e.g. when cosmic ray mass or nature of cosmic rays are mentioned. A new general term could be used in the future: *cosmic miscellaneous rays*. The air shower particles are referred to as *primary* (particle) and *secondaries* for secondary particles.

000000





Mass composition parameters

Ultra-high-energy cosmic and gamma rays carry information about their origin and propagation. There are three quantities of the primary particles that can be measured and help to understand where the cosmic and gamma rays were produced and how they propagated. These quantities are the energy, direction and nature (type) of the primary particle.

With the FD the calorimetric energy of EAS, and thus of the primary particle, can be measured directly. From the geometry, the time delays of the triggered SD stations and the FD angular measurements, the air shower axis is determined. This measurement unveils the arrival direction of the primary particle. However, this information is incomplete for studying the origin of cosmic rays. The missing part is the particle type. As described in Section 2.3 the nature of cosmic rays affects the relation between the direction of their source and their arrival directions at Earth, because the influence of the (extra)galactic magnetic fields depends on their charge. In this chapter the existing methods and a new approach are presented to determine the nature of the cosmic rays.

One big challenge in the analysis of UHECR is statistics. The SD provides the highest uptime and largest collection area of all detectors types of the Pierre Auger Observatory. Therefore the focus of the analysis in this thesis will be on this detector type.

5.1. Existing observables

Several techniques were developed to get a handle on the mass composition of cosmic rays from different air shower parameters. In this section some observables are described that are used by the Pierre Auger Collaboration to determine the particle type of cosmic rays. The observables are based on the differences in the development of EAS initiated by different primaries. They are studied using air shower simulations. Figure 5.1 illustrates the simulated trajectories of secondary particles in the Earth's atmosphere of EAS started by different primaries. These pictures provide an impression about the differences in the air shower development. Especially, the air showers started by a gamma differ greatly from the hadron initiated air showers by the numbers of muons and hadrons.

Depth of air shower maximum (X_{\max}) In Section 2.2.3 the development of an EAS was discussed. Figure 2.13 shows the change in the number of particles along the trajectory that the air shower follows on its way to the surface. The maximum of this distribution, the depth of air shower maximum X_{\max} , marks the point where the air shower reaches its maximum number of secondary particles. X_{\max} is measured in terms of the amount of atmosphere traversed, thus its units are g/cm^2 . Therefore, this quantity is independent from the inclination angle, but depends on other air shower properties like the point of first interaction of the cosmic rays with Earth's atmosphere and on the fractions between different types of secondaries, which contribute to the variation of X_{\max} for different primaries as is depicted in Figure 2.14. X_{\max} has a good separation power between primary particles (Figure 5.2(a)). Although it can be directly measured using the FD (Chapter 3.4.2) the mass of the primaries cannot be distinguished for an individual EAS due to the event-to-event fluctuations, but must be inferred statistically from the distribution of X_{\max} from multiple measurements [30]. From this distribution the parameters $\langle X_{\max} \rangle$ (mean of the X_{\max} distribution) and $\sigma_{X_{\max}}$ (see next paragraph) can be studied and compared to an average mass composition of the cosmic rays. Unfortunately, the fraction of X_{\max} measurements is limited to the uptime of the FD, which is only around 13% [46]. Therefore attempts were made to reconstruct X_{\max} from the SD data, e.g. in [89].

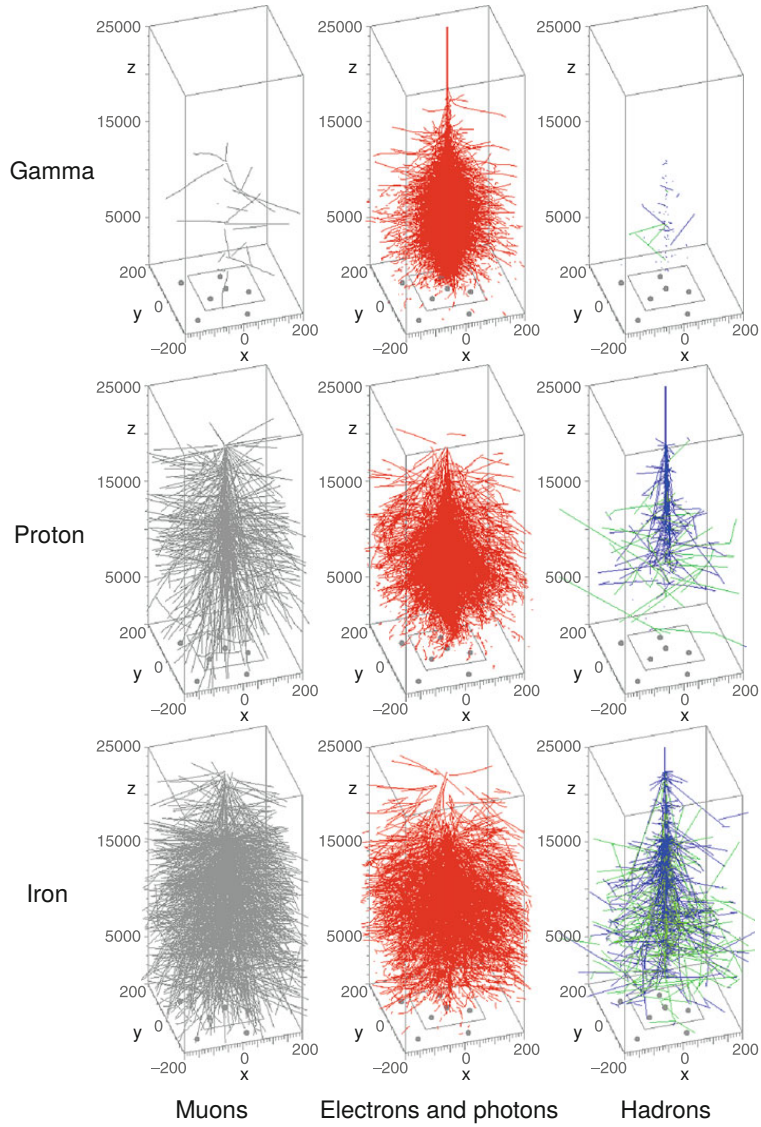


Figure 5.1.: Simulated trajectories of muons (left), EM particles (center) and hadrons (right) from EAS with gamma (top), proton (middle) and iron (bottom) primary particles with $E = 10^{13}$ eV. Adapted from [28].

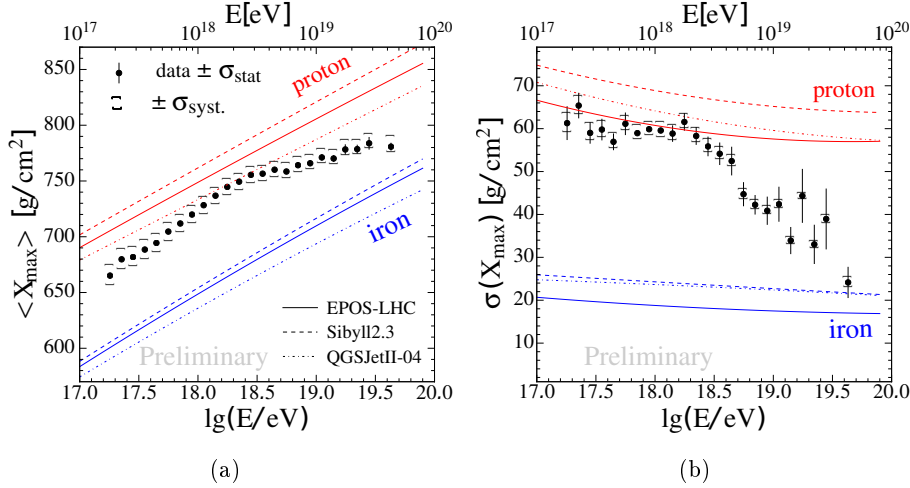
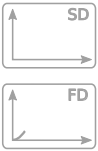


Figure 5.2.: $\langle X_{\max} \rangle$ and $\sigma_{X_{\max}}$ measurements of the Pierre Auger Observatory in comparison with theoretical predictions. Adapted from [15].

Spread of the depth of air shower maximum ($\sigma_{X_{\max}}$) The air shower profiles shown in Figure 2.14 provide more information about their primaries. The magnitude of the event-to-event fluctuations of X_{\max} also depends on the nature of the primary particles [90]. This parameter is called *the spread of the depth of air shower maximum* $\sigma_{X_{\max}}$. As can be seen in Figure 5.2(b), it has a good discrimination power for distinguishing between different primaries and is expected to decrease with the increasing number of nucleons A of the primary and to increase with its interaction length. Like the average depth of air shower maximum, the $\sigma_{X_{\max}}$ parameter must be inferred from the distribution of an ensemble of air showers and it shares the limitation of the FD uptime with the X_{\max} measurement.



Number of muons (N_{μ}) One remarkable distinguishing feature between EAS initiated by different types of particles is their *number of muons* N_{μ} . As mentioned in Section 2.2.2, muons are produced in decays of charged pions and kaons, which originate from collisions of hadrons

with air nuclei. Hence, EAS initiated by protons or iron nuclei are muon-rich, whereas air showers started by a gamma are muon-poor (Figure 5.1). From the Heitler model of hadronic air showers (Section 2.2.1) N_μ can be estimated:

$$N_\mu = A \left(\frac{E/A}{E_c^\pi} \right)^\beta, \quad (5.1)$$

where A is the cosmic ray mass, E its energy, E_c^π the critical energy for pions to decay into muons and $\beta \approx 0.9$ [91].

The advantage of N_μ is that it's almost independent of the inclination angle and X_{\max} of the EAS. This is due to the fact that many of the muons are produced early in the air shower and most survive until reaching the detectors at ground, whereas the other air shower components change with the slant depth as shown in Figure 2.13 (note the energy fraction on the y -axis corresponding to the number of particles). Unfortunately, despite the fact that the muons arrive first, the EM particles smear the signal in the SD so much, that N_μ cannot be measured directly. To solve this inconvenience very inclined air showers can be studied [91], or the muon and EM signal can be separated using nearby placed separate detectors with different sensitivity to muons and EM particles. Such extensions to the SD are the AMIGA underground detectors that are shielded from EM particles by a layer of soil (Section 3.1.1), and the Scintillator Surface Detectors (SSD) that are installed on the existing SD stations for the AugerPrime upgrade (Section 11.1).

Muon production depth (MPD) and X_{\max}^μ Another approach to determine the nature of the cosmic rays that is related to the muonic component is the *muon production depth* (MPD) [92]. It describes the atmospheric depth X^μ at which the individual muons were produced. The MPD is modeled from the arrival time information of the SD and simulations of the muon distribution in EAS, resulting in a inclination angle dependent distribution. This distribution is fitted with the Gaisser-Hillas function [67], similar to the longitudinal profile (Section 3.4.2), thus yielding the maximum of the MPD, X_{\max}^μ , as a mass composition sensitive parameter. This observable is strongly correlated to X_{\max} , mainly through the depth of first interaction of the cosmic rays with the Earth's atmosphere [92]. Unluckily, the estimation of X_{\max}^μ also strongly depends on the hadronic interaction models used in the air shower simulations. This

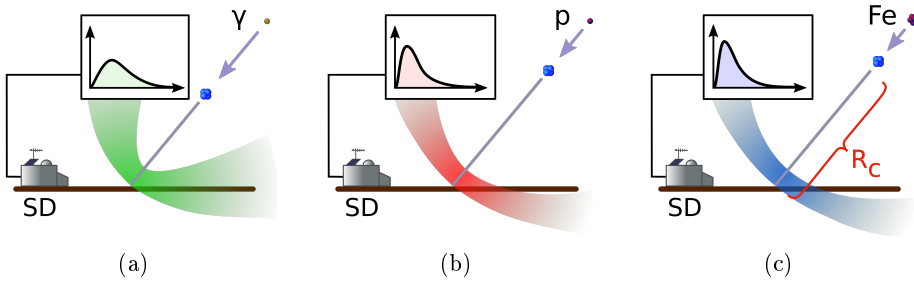


Figure 5.3.: Air shower front models for gamma (a), proton (b) and iron (c) primaries. The illustrated differences are the point of first interaction, R_c , the thickness of the air shower front and the time traces detected by the SD stations (signal shapes).

makes this variable for the time being more useful to improve the interaction models at the highest energies than to separate cosmic rays of different nature. Another problem of the MPD is the discrepancy between the number of muons in simulations and data (Section 4.1), which adds additional uncertainty.

Radius of Curvature (R_c) During the propagation through the atmosphere an EAS has the shape of a curved air shower front with a variable thickness that depends on the distance to the air shower axis and grows with the radius. The upward part of the disk is diffuse, due to particles that were produced under higher angles. However, the front downward part is well defined and is formed mainly by the muons. From the simplest assumption that the air shower front is formed from one point close to the point of the first interaction of the cosmic ray with the atmosphere, it follows that it should be curved as part of a sphere. This sphere has a radius which is defined by the curvature when an air shower hits the ground and is called the radius of curvature R_c [93]. In reality the air shower front geometry is more complicated due to the overlap of the curved shapes with different radii originating from different production heights of the secondaries. Therefore, the radius of curvature in the spherical model indicates a lower point of first interaction than in reality is the case.

As described in Section 3.4.1, R_c is used in the reconstruction process to obtain the impact time and core position from the measurements with the SD. R_c depends, among others, on the height of the first interaction, the total distance the air shower travels until reaching the detectors and the spread of the EAS [93]. Figure 5.3 shows a schematic view of the air shower fronts for different primaries.

R_c has a good separation power for distinguishing several types of cosmic rays and can be reconstructed for the full statistics of the SD measurements. However the calculation of this parameter from a few SD stations is one-sided biased due to the detected arrival time distribution: one SD station, primarily a station far away from the shower axis, could by chance be missed by the first particles of the air shower front and measure only later ones. In this scenario, R_c would be biased towards a smaller value, because no time can be measured that is smaller (leading to a bigger R_c) than the one of the first particles arriving at ground. To counter this bias *time variation models* [94] are used. These models describe how the most probable air shower arrival time depends on the time of the first measured particle, the number of particles in the detector and the air shower geometry.

Rise time (T_{50}) Due to the different compositions of the secondaries (N_μ , N_e , N_γ) and different geometries (R_c , air shower front thickness), EAS initiated by different types of primaries also have different signal time development as obtained from the PMTs in the SD stations (Figure 5.3). Based on this consideration another mass composition parameter was constructed. It is called the *rise time* T_{50} or $t_{1/2}$ and is the time between 10% and 50% of the total integrated signal of one SD station during the signal time interval [95]. T_{50} was found to depend on the average number of nucleons in the primary particle and it benefits from the almost continuous uptime of the SD. However, it is conceivable that different time traces can lead to the same T_{50} value, which makes this parameter ambiguous. Primarily far away from the air shower core, where the signal seen by the SD becomes spiky due to low statistics, T_{50} can be misleading.

Asymmetry factor and $(\sec \theta)_{\max}$ The inclination of the EAS presents additional challenges for the reconstruction task. It has to be taken into account that the air shower front is curved and expands continuously. More-

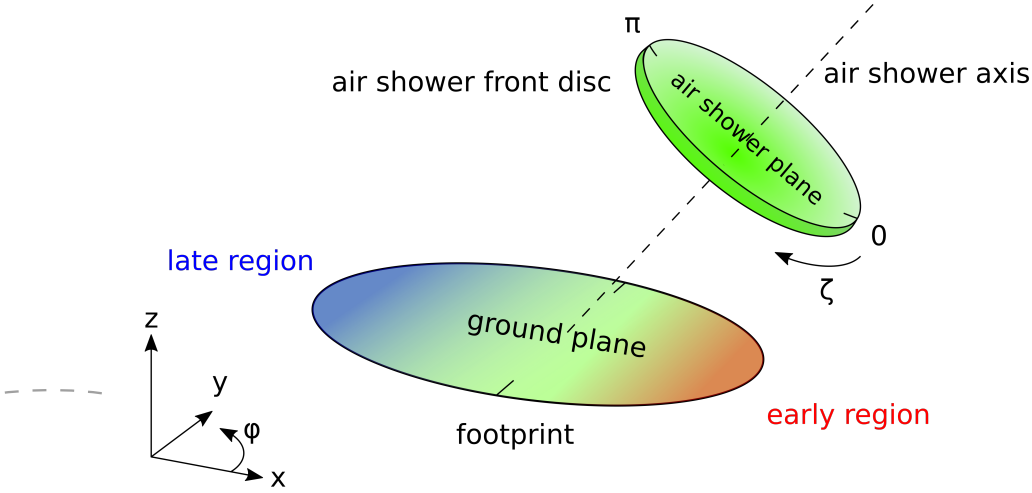


Figure 5.4.: Definition of the early and late regions of the footprint. Note the different definitions of the angles ϕ and ζ .

over the particle components vary differently with time and the varying densities of the atmospheric layers change the conditions for the propagation of particles depending on their paths. In particular the number of muons barely changes with the longitudinal distance that an air shower propagates toward the ground, whereas the electrons, positrons and photons can be captured or interact, leading to a decrease in their numbers for an air shower that is traversing a lot of atmosphere. This results in differently evolving signals in the so called *early region* ($|\zeta| < \frac{\pi}{2}$, more vertical arrival directions, particles arrive relatively early after they have been made) and *late region* ($|\zeta| > \frac{\pi}{2}$, more horizontal arrival directions, particles arrive relatively late after they have been made) of the air shower footprint [96]. Figure 5.4 shows the definition of ζ in the *air shower plane* (a plane perpendicular to the air shower axis).

The assumption that the differences between the early and late regions depend on the primary particle was confirmed by comparing the average rise time $\langle t_{1/2}/r \rangle$, weighted with the distance to the air shower axis as function of the polar angle ζ [96], which provides the relative orientation within the air shower.

The rise time distribution can be fitted with

$$\langle t_{1/2}/r \rangle = a + b \cos \zeta + c \cos^2 \zeta \quad (5.2)$$

and the parameters are combined into the *asymmetry factor* $b/(a + c)$. This asymmetry factor depends on the inclination angle θ of the EAS. The behavior of the asymmetry factor as function of atmospheric depth, measured by $\sec \theta$ was studied. The position of the maximum asymmetry $(\sec \theta)_{\max}$ was found to vary with energy, but also to provide a good discrimination power between hadronic primaries [96].

Surface signal parameter (S_b) Another attempt of using signals from the SD proposes the S_b parameter [97]. It is based on the weighted sum of signals depending on their distances to the air shower axis:

$$S_b = \sum_{i=1}^N \left[S_i \times \left(\frac{r_i}{r_0} \right)^b \right] \quad , \quad (5.3)$$

where S_i are the total signals of all N triggered SD stations, r_i their distances to the air shower axis and r_0 a reference distance of 1000 m. The parameter b adjusts the weighting and was found to maximize the discrimination power at the value of $b = 3$. Similar to the rise time S_b does not take into account the signal profile. Thus, different constellations of secondary fractions could result in the same S_i values.

Signal ratio parameter (F_γ) Specifically for the photon search the signal ratio parameter F_γ was proposed [98]. It is defined as the ratio between the reconstructed signals S_{1000} (Section 3.4.1), once using the regular procedure for hybrid events ($S_{1000|Hybrid}$) and once with parameters optimized for gamma induced air showers ($S_{1000|\gamma}$) [99]:

$$F_\gamma = \frac{S_{1000|\gamma}}{S_{1000|Hybrid}} \quad . \quad (5.4)$$

F_γ was found to have a good discrimination power when combining it with X_{\max} . However, thereby the advantage of using the full SD statistics is lost.

5.2. New approach: Time Probability Density Function (TPDF)

Most SD observables described above only use one observable for each SD station, mostly a function of the total signal value, ignoring the measured arrival trace distribution of the secondaries. Only T_{50} uses the time structure but condenses it into only one parameter. The new approach described below uses the entire signal (time) trace to gain more information about the internal structure of an air shower in view of the mass composition of cosmic rays. The time differences between the SD stations, as used for the R_c parameter are not included in the present analysis, but could be added as a mostly independent piece of information in the future (Chapter 11).

The air shower front reaching the ground contains several secondary particle types (muons, electrons, positrons, photons, etc.). The SD detector response differs slightly for the different types of secondary particles and also depends on their energies and paths through the detector. Muons mostly traverse the water tank losing only a fraction of their energy, while photons, electrons and positrons are showering and may be (almost) completely absorbed in the SD tank. Muons generally also arrive first at the SD and thus form the air shower front, while photons, electrons and positrons usually arrive later, because of the many scattering processes they and their ancestors were involved in. Thus the arrival time profile is expected to be characteristic for different primary particles. The arrival time pattern also depends on the EAS energy and inclination angle. To analyze the differences of the SD time traces (signal shapes) an empirical function that describes the arrival time profile will be presented in the next section.

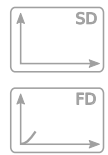


Figure 5.5 shows the time distribution of the electromagnetic and muonic components of the secondary particles reaching the ground at the air shower plane with $t_{core} = 0$ s. These distributions are taken from non-thinned simulations. It can be observed that there is a big difference between the numbers of muons (blue curves) created in a EAS with a proton (left column) and one with a gamma primary (right column). It can also be seen that the ratio between muons and electrons is changing with distance (from top to bottom). At distances to the air shower axis

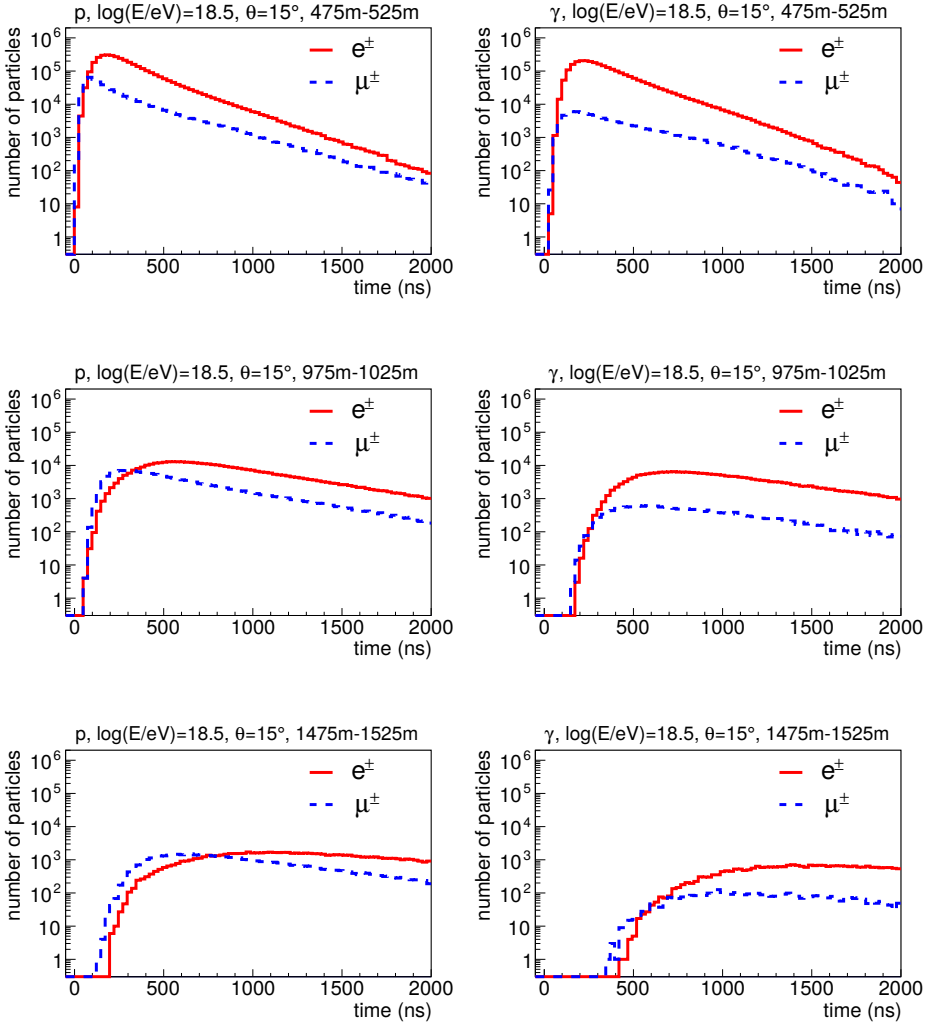


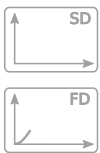
Figure 5.5.: Arrival time distributions of the secondaries in the air shower plane at SD observation level with distances r to the air shower axis of 475 m – 525 m (top), 975 m – 1025 m (middle) and 1475 m – 1525 m (bottom) of the electromagnetic and muonic components from non-thinned simulated air showers with proton (left column) and gamma (right column) primaries, with $E = 10^{18.5}$ eV and $\theta = 15^\circ$.

between 475 m and 525 m, the number of muons at the maximum of the arrival time distribution is 10 (50) times smaller than the number of electrons and positrons for proton (gamma) induced air showers. At larger distances the maxima for proton induced air shower are comparable in height, whereas for gamma induced EAS they are still different by a factor 10. Note that it is not possible to compare these histograms directly to the signal response from the SD stations because the energy deposit for muons is less than for electrons and photons, although they have higher energies when reaching the Earth surface.

One can also see from Figure 5.5 that for proton induced air showers (left column) the muon signal has a large component at early times, especially near the air shower axis. This is due to muons from pion production in the early stage of the air shower, where the pions decay before interacting. The muon production in gamma air showers (right column) is due to pion production all along the air shower, where only a small, more or less constant fraction of the pions decay before having an interaction.

To compare the measurements of real air showers with theoretical predictions, EAS simulations have been created with CORSIKA (Section 4.3). In the output files of these simulations the secondary particles at the ground level (SD observation level) are stored. Among other properties of the secondaries their type is saved, which allows to distinguish the different components. It was already mentioned that muons play an important role and define the steepness of the rise of the arrival time profile. Therefore, the muon time distribution at ground is taken to construct a function that fits the arrival time profile.

In a pure muon time distribution from a non-thinned EAS simulation with a proton primary in Figure 5.6 several characteristics can be observed. The shape begins with a very steep rise up to a maximum followed by an approximately exponential fall-off. The maximum represents the highest number of the secondaries arriving in the same time interval, whereas particles that are late form the tail of the distribution. The time distribution can be understood as the longitudinal cross section through the air shower front.



The muon time distribution in Figure 5.6 has roughly quadratic exponential rise and a linear exponential fall-off. A function that fits this distribution should be exponential, depend on the position of the maximum and have a least one parameter to adjust the tail. Several standard functions were tested for different distances to the air shower axis, e.g.

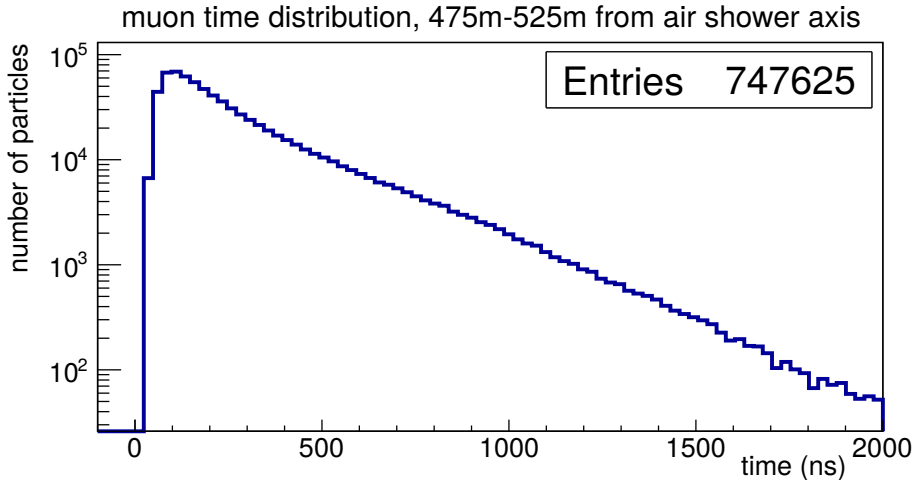


Figure 5.6.: Arrival time distribution of muons at ground, in a 475 – 525 m ring to the air shower axis. The simulated EAS was initiated by a vertical proton with an energy of $10^{18.5}$ eV.

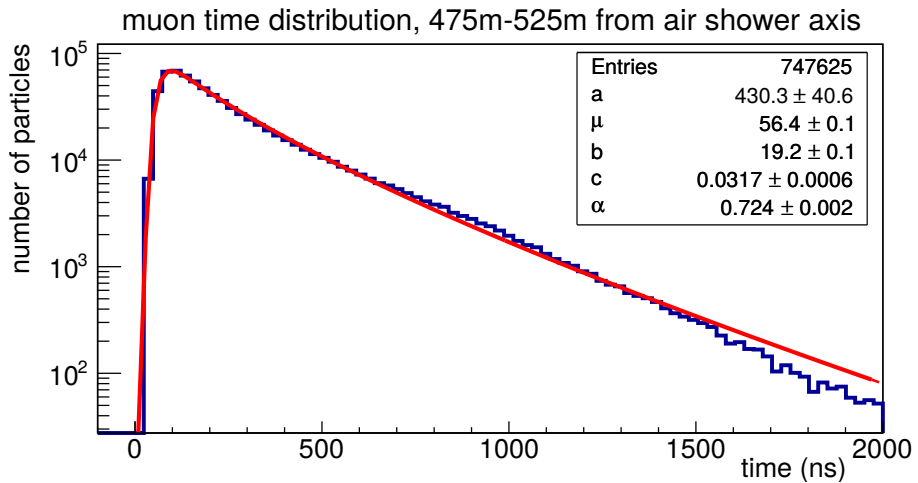


Figure 5.7.: Arrival time distribution of muons at ground (blue histogram), in a 475 – 525 m ring to the air shower axis. The simulated EAS was initiated by a vertical proton with an energy of $10^{18.5}$ eV. The red line is a fit using the function of Eq. (5.5). The fit parameters are displayed in the box.

Landau and Log-normal functions. None of these could satisfactorily fit the arrival time distribution. Especially closer to the air shower axis all of the functions either missed the true position of the maximum or could not properly fit the tail. Empirically, a double exponential function was found to fit the time profile:

$$f(t) = 10^a \cdot e^{-\left(e^{-\left(\frac{t-\mu}{b}\right)} + c \cdot t^\alpha\right)}, \quad (5.5)$$

where a defines the amplitude, b is related to the steepness of the rising part, μ is related to the position of the maximum and α and c are parameters describing the tail. The need for two tail parameters arises from the fact that the exponential slope is changing its inclination shortly after the maximum. In Figure 5.7 the function from Eq. (5.5) is fitted to the muon time distribution of Figure 5.6. The main features of the arrival time profile are well described: the rise, the maximum and the tail with a slope change after the maximum. The extreme tail is not so well fitted, but concerns only very few particles and is not relevant for the time trace analysis in this thesis.

Next, it is essential to prove that this function still works on the PMT traces recorded by the SD. Different particle types contribute differently to the total signal seen by the PMTs. Also the different paths through the tank modify the shape. Finally, the detector and electronic resolutions smear the signal.

To study this behavior the simulated air showers were fed into the Surface Detector simulation and signal reconstruction algorithms of Offline (Section 4.2). On the averaged time traces of the SD the function from Eq. (5.5) was fitted. It still describes the main characteristics of the time trace well, although there is a difference between the SD time trace and the pure muon time distribution. The tail of the SD time trace is almost exactly exponential without a change of exponential slope, due to the contribution of the EM particles and the detector resolution. Hence, the tail parameter α can be dropped, resulting in the final function that will be used for the analysis in this thesis:

$$f(t) = 10^a \cdot e^{-\left(e^{-\left(\frac{t-\mu}{b}\right)} + c \cdot t\right)}. \quad (5.6)$$

The double exponential function in Eq. (5.6) is named the *Time Probability Density Function* (TPDF) and has 4 free parameters, which

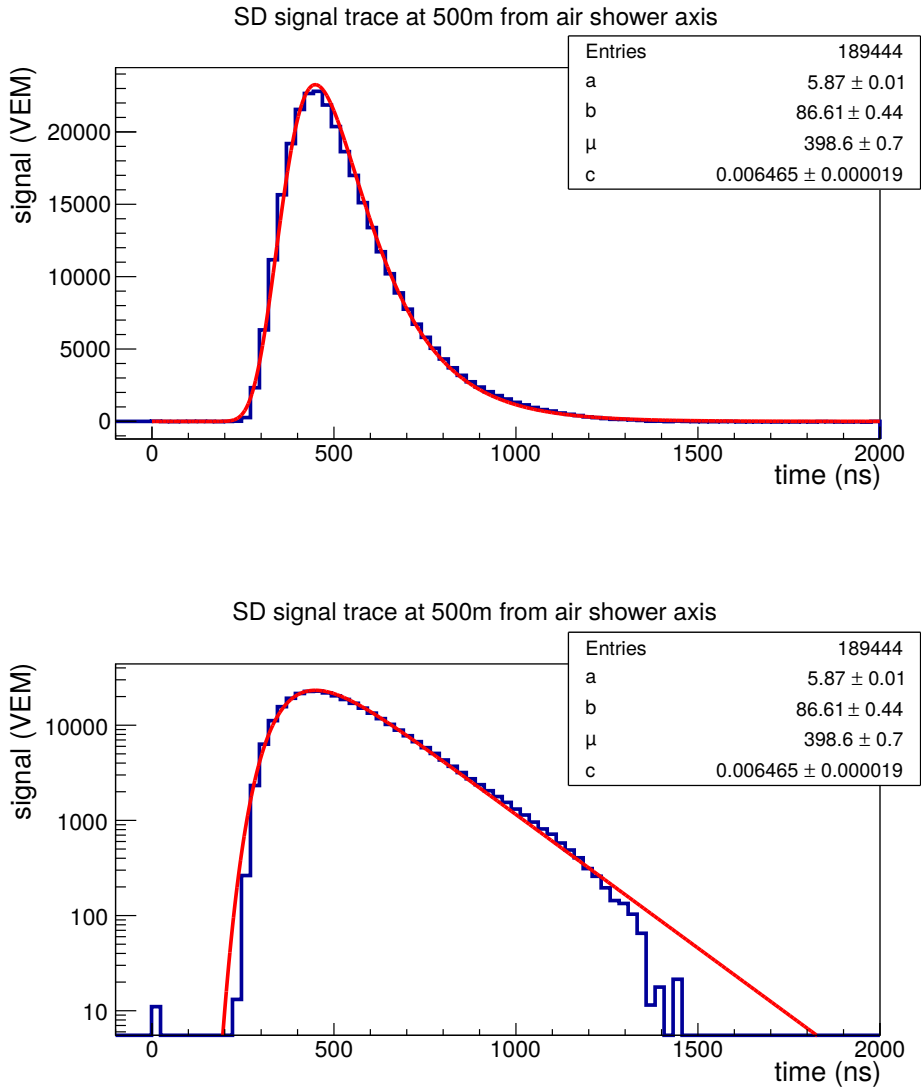
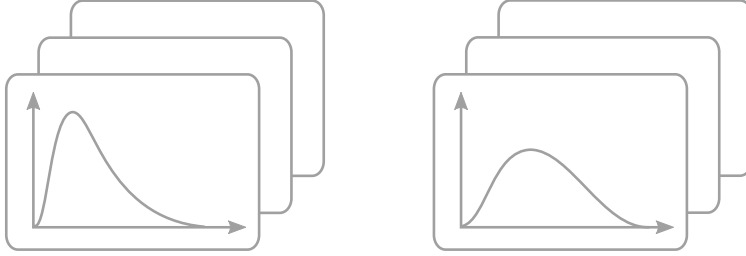


Figure 5.8.: Sum of time traces from 360 SD stations at 500m to the air shower axis. The simulated EAS was initiated by a vertical proton with an energy of $10^{18.5}$ eV. On the sum of time traces Eq. (5.6) was fitted. The top and the bottom graphs are identical except the logarithmic y -axis of the bottom one.

reflect the different features of the arrival time profile. Parameter a is the normalization parameter and depends on the total number of particles in the arrival time distribution and their energy deposit in the SD, b describes the steepness of the rising edge and the behavior up to the maximum, μ is related to the position of the maximum and c describes the slope of the exponential tail. Figure 5.8 shows the TPDF fitted to the sum of time traces of an SD simulation. It should be noted that the SD signals, within the signal region of the FADC trace, were shifted here and in the following before applying the TPDF algorithm by an offset of 250 ns to monitor potential errors i.a. in the algorithm finding the start time. Also the pure particle arrival time distributions without the SD simulation could be evaluated with this offset. This was done primarily to monitor the non-thinned simulations of air showers.

• 





Generation of TPDF models

In the previous chapter the TPDF (Time Probability Density Function) was introduced. In this chapter the TPDF model generation procedure will be described, followed by the definition of the TPDF confidence interval for the models. The TPDF models will be applied to the data (Chapter 9) to identify the nature of the primary particles and to distinguish between cosmic rays and gamma rays.

6.1. TPDF model definition

Using the TPDF ansatz (Section 5.2) the SD time traces are fitted individually. The measured SD events that pass the T5 trigger condition (Section 3.4.1) contain measurements of several SD stations at various distances to the air shower axis that belong to the same EAS. The TPDF is applied to all triggered SD stations. As the SD time trace changes with the distance of the SD station to the air shower axis (Figure 6.1), the TPDF parameters will also change. Furthermore, the parametrization of the TPDF also depends on the energy, nature and inclination angle of the primary particle. For inclined air showers ($\theta > 0^\circ$) the distribution of secondary particles in the footprint also varies with the polar angle ζ (Figure 5.4). In the air shower plane, the particle fractions in the air shower front vary due to the different paths through the atmospheric layers and the differences increase with the inclination of the EAS.

In particular, the ratio between the muonic and the EM components changes due to the differences in the number of interactions with the atmosphere. While the number of muons remains almost unchanged, EM particles interact with air molecules causing a spatial and temporal dispersion resulting in a wider distribution of their arrival times at ground in the late region.

All the above effects affect the signals of the SD stations, depending on their orientation with respect to the air shower axis. To extract the information about the nature of the primary particle that initiated a given EAS, the changes of the TPDF fit results for SD stations at different distances to the air shower axis and orientations in the footprint will be combined into TPDF models. For this purpose the first half of the thinned simulation set mentioned in Section 4.3 is used.

Ring separation The output files of the air shower simulations are divided into many smaller files, each containing information about the secondary particles in one ring of 50 m width at different distances to the air shower axis. The rings in the air shower plane correspond to ellipses at the ground plane of the footprint for inclined EAS (Figure 6.2).

For the analysis of the changes in the SD time trace as a function of distance to the air shower axis the TPDF is fit to the sum of the time traces of all SD stations placed in each ring. For vertical air showers the SD signals at a certain distance will vary only due to the statistical fluctuations, whereas for the inclined air showers the ζ dependency will cause an additional distortion. Thus, the rings need to be divided further into ζ segments.

Ring segment separation To study the ζ dependency for the inclined air showers each ring is divided into 360 segments of 1° width (Figure 6.2) in the air shower plane. From the TPDF fitted on time traces of the simulated SD stations placed in the middle of each segment the TPDF parameters can be analyzed individually as function of ζ . For each parameter 360 individual values are obtained and fitted with the following function:

$$f(\zeta) = j + k \cdot \cos(\zeta) \quad , \quad (6.1)$$

where j defines an offset and k the amplitude of the cosine function. It should be noticed here, that the geometry definitions of CORSIKA and Offline differ by 90° with an additional shift of 4.23° that arises



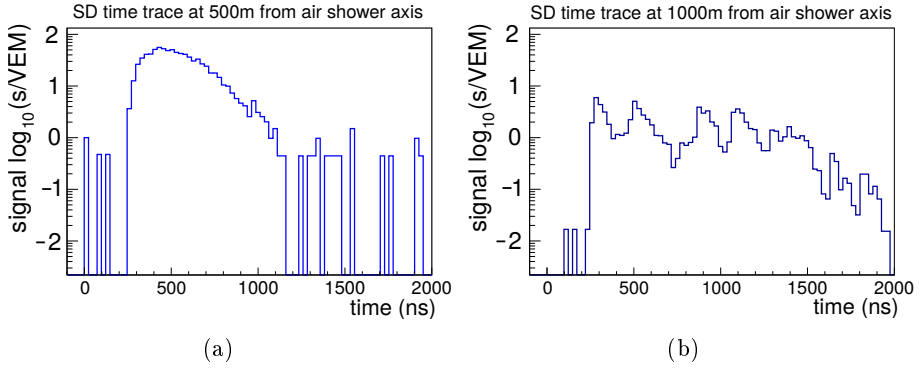


Figure 6.1.: Time traces of one SD station at 500 m (a) and one at 1000 m (b) to the air shower axis for a simulated EAS with vertical proton primary and energy of $10^{18.5}$ eV.

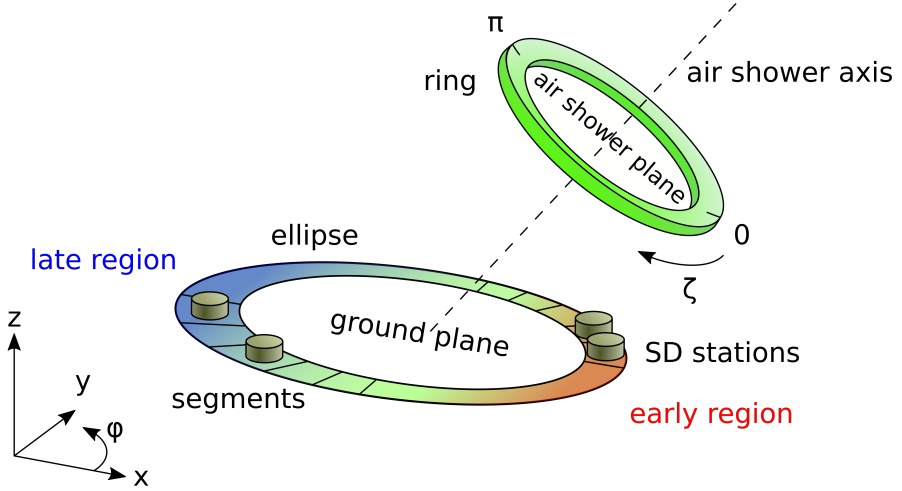


Figure 6.2.: Schematic view of the separation of the footprint into ellipses (rings in the air shower plane) and into segments in which the SD stations are simulated.

from the axis orientation differences between CORSIKA and Offline. In CORSIKA the x -axis points towards the magnetic north and the y -axis towards the west. In Offline the x -axis points towards the east and the y -axis towards the geometrical north. Hence, for the reconstruction of the measured events the magnetic field orientation at the location of the Pierre Auger Observatory has to be taken into account. Furthermore the magnetic field orientation and strength change slightly over time. However, this effect is not taken into account for the reconstruction.

Fit minimization The TPDF fit (Eq. (5.6)) is performed on the SD time traces using the log-likelihood method, whereas the $f(\zeta)$ fit (Eq. (6.1)) is done with a χ^2 minimization on the individual TPDF parameters using values determined from the statistical event-to-event fluctuations. The maximization of the likelihood of the TPDF fit and the minimization of the χ^2 of the $f(\zeta)$ fit are performed using the numerical minimization program MINUIT [100], implemented in the ROOT framework [83] version 5.34/36, with the MIGRAD minimization routines.

Minimal signal strength The number of particles measured in a SD station is decreasing with the distance to the air shower axis (Figure 2.12). As a consequence only a few secondaries hit the SD stations at larger distances, leading to a spiky signals (Figure 6.1). The fit of the TPDF then becomes difficult to interpret, because this function assumes only one maximum with an exponential tail, whereas the measured signal can have several maxima caused by a few individual particles. To prevent misinterpretations only SD stations with signals higher than 5 VEM will be taken into account.

6.1.1. Uncertainties

When comparing a measured SD time trace to the TPDF models, the uncertainties that arise from the simulations of the EAS and the detectors, the event-to-event and SD sampling fluctuations and the event reconstruction have to be taken into account. Some of these uncertainties are described below and are included in the TPDF models. Others that are described at the end of this section are not taken into account for this analysis, but could be added in future.

Included uncertainties:

- **Event-to-event fluctuations**

The CORSIKA air shower simulations used to build the TPDF models are based on the Monte Carlo method to model the interactions of the secondary particles while traveling through the atmosphere. Even with identical primary particle parameters the outcome varies event-by-event. To study these fluctuations, several air showers have been simulated for each set of initial parameters describing the primary particle using a different random number generator seed. These simulations are combined to estimate the statistical uncertainties.

- **Early-late effects**

For inclined EAS the SD signals from stations at the same distance to the air shower axis differ according to their azimuthal position around the air shower axis. To study the TPDF parameter changes, the results from the detector simulations in the 360 segments at the same distance to the air shower axis will be evaluated as a function of the polar angle ζ . The confidence interval as a function of ζ is constructed by fitting Eq. (6.1) for the upper and lower edge separately. These functions follow the trend of the main ζ function and are constructed in such a way that 68% of the mean values of the points lie between them.

- **Detector resolution**

The SD station response (Section 4.2.1) to the air showers adds another set of uncertainties to the TPDF parameters. To obtain the best estimation of the SD response the simulations are performed using GEANT4. The resulting SD signals with their uncertainties directly affect the parametrization of the TPDF parameters. Since the TPDF models are based on several simulated air showers and thus on several detector simulations these uncertainties are automatically included.

- **Event reconstruction uncertainties**

During the event reconstruction several parameters and their uncertainties are calculated from the measurements or are taken from previously generated models. For the TPDF models the relevant reconstruction parameters are the air shower core position and the inclination of the air shower axis. These parameters provide the distance from the SD stations to the air shower axis and therefore the uncertainties are propagated into the TPDF models through the reconstructions of the simulated air showers.

Uncertainties that are not taken into account:

- **Further primary particles**

For building the TPDF models only three primary particle types were simulated: protons, iron nuclei and gamma rays. Although the mass composition of the cosmic rays in reality remains unknown, there is no reason to assume that only particles of these three types arrive at the Earth. However, all other hadronic primaries are believed to initiate EAS with average characteristics, like X_{\max} or N_{μ} , in between those from proton and iron initiated air showers. In case of the search of ultra-high-energy gamma rays in the data this is not an issue, because the cases of proton and iron are thought to effectively encapsulate all hadronic primary possibilities.

- **Geometrical effects**

The TPDF analysis is based on the estimation of the SD time trace as function of the distance and ζ orientation to the air shower axis. Therefore, a projection of the detector position onto the air shower plane (Figure 6.3) was calculated by a linear shift of the detector position at ground parallel to the air shower axis to determine the distance to the axis. This is not an accurate projection according to the expanding sphere air shower model. As described in Section 5.1 this model also has its problems, thus the projection in the direction toward the R_c origin would not be correct either. The calculation of the SD position in the air shower plane mostly biases the sum of



time traces of 360 SD stations. This is due to the different angles particles arrive at in the early and late regions. However, for individual stations this bias is present in the simulations as well as in the air shower data and should not affect the testing for the different TPDF models.

- **Detector and atmospheric effects**

The simulated events were reconstructed with static environmental parameters of the SD stations. In reality the detector response varies with time, due to periodically changing conditions like day-night and summer-winter cycles [15] and detector aging [101]. These effects are difficult to simulate properly. For the data they are taken into account when calibrating the detectors. The uncertainties arising from these detector and atmospheric effects are not include in the current study.

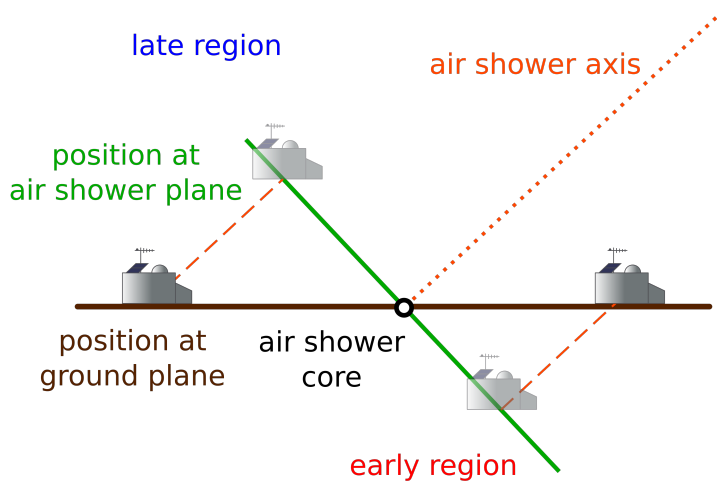


Figure 6.3.: The calculation of the distance of SD station position to the air shower axis is equal to the projection into the air shower plane. The expanding character of the air shower front is ignored.

6.2. TPDF model generation

For each parameter set of the primary particle types, energies and inclination angles, CORSIKA versions and high-energy models mentioned in Section 4.3 an individual TPDF model is generated. For each set 10 thinned and for a few sets some non-thinned air showers are simulated on which the TPDF is fitted. The TPDF models obtained from the thinned air shower simulations will be used for the mass composition analysis of the measured events, while the one based on the non-thinned EAS simulations will mainly be used for a comparison to the thinned one for validation.

Each TPDF model consists of the TPDF parametrization from 360 individual simulated SD stations for distances to the air shower axis from 575 m to 1525 m in 50 m steps. For each ring the parameterizations are available in 1° steps in ζ . The distance range on the lower side is limited due to the software boundary conditions of Offline, as the reconstruction of 360 SD stations and the large number of simulated particles, especially for the higher energy air showers, cause an overflow in the internal memory. The upper limit is chosen due to the small particle density, as was shown in Figure 2.12, and as a consequence the very small signals in the SD stations at larger distances.

During the model generation it was noticed that some of the TPDF fits failed for different reasons. Mostly, the spiky time traces are difficult to fit due to the continuous shape that is assumed for the model. Especially for more inclined air showers the differences between the time traces of the early and late regions cause problems, where the former are in general reconstructed and fitted well, the latter may have a very small number of particles. Although the total signal strength is a good discrimination parameter, some failed fits had other reasons. Therefore, the following fit quality criteria were applied. First the time traces should contain values different from zero for more than half of their bins and have a total signal above 5 VEM. The zero bins indicate a missing signal part, which is crucial mainly for fitting the tail of the distribution, and the signal threshold ensures that only SD stations with a reasonably large signals are used. Next, the maximum of the TPDF function has to be between 0 ns and 2000 ns. This removes results with arbitrary parameters where the TPDF fits failed. The maximum of the TPDF can be calculated using

the derivative of Eq. (5.6):

$$\frac{\partial}{\partial t} f(t) \stackrel{!}{=} 0 = \underbrace{f(t)}_{\neq 0} \cdot \left[-\exp\left(-\frac{t-\mu}{b}\right) \cdot \left(-\frac{1}{b}\right) - c \right] \quad (6.2)$$

$$\Rightarrow \quad t_{max} = -b \cdot \ln(bc) + \mu \quad . \quad (6.3)$$

Finally all TPDF fits with an uncertainty of the first parameter (a) larger than 1.0 are not taken into account for building the ζ function. A high uncertainty of this parameter indicates that the TPDF function could not be fitted properly. As the a parameter is the decimal power (10^a) an uncertainty of 1.0 implies an uncertainty of one order of magnitude for the TPDF function. This can happen for time traces without a clear maximum position, especially in case of almost horizontal air showers.

6.3. TPDF model interpolation

While the TPDF models are created for certain discrete energies and inclination angles of the primary particle, these parameters can take all values for the measured EAS. Thus, the TPDF parameters from different models have to be combined for testing the measured air showers. The following sequence for this procedure is used.

First the measured (reconstructed) energy of the EAS is corrected for the energy misreconstruction (which will be discussed in Section 8.1). Using the corrected energy and measured inclination angle, the four closest TPDF models from the discrete grid are determined with the closest lower and higher energies and inclination angles θ . The weights for these models are calculated based on the difference of their energies and θ to the corrected energy and measured inclination angle.

Next, according to the distances to the air shower axis and ζ orientations of each triggered SD station in the tested EAS, the TPDF parameters and their uncertainties are taken from the four closest TPDF models individually and interpolated to the estimated values with different weights. This interpolation is performed for each primary separately.

6.4. TPDF confidence interval

For data testing the individual TPDF parameter values and their confidence intervals at the positions of the SD stations have to be calculated from the TPDF models. Each TPDF parameter has a mean expectation value and a confidence interval as function of ζ angle. The parameter confidence intervals are then propagated into confidence intervals for the time trace models that are to be compared to the data.

The TPDF parameters are expected to be correlated and for proper propagation of the uncertainties their correlation factors have to be determined and taken into account. For this purpose the correlations are cal-

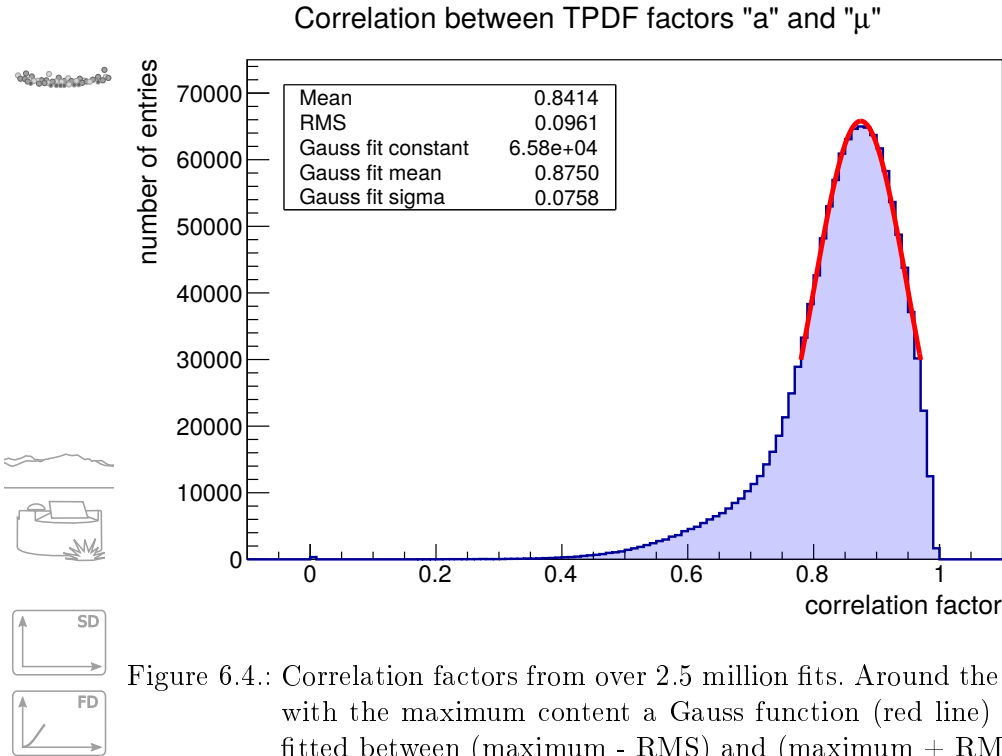


Figure 6.4.: Correlation factors from over 2.5 million fits. Around the bin with the maximum content a Gauss function (red line) was fitted between (maximum - RMS) and (maximum + RMS).

culated during the TPDF model generation procedure, when the TPDF is fitted to the SD time traces of the simulated EAS. Afterwards the individual correlation factors are stored into histograms and their most probable values are fitted using a Gauss function, as can be seen in Figure 6.4 for the correlation between a and μ . To avoid influences from failed TPDF fits during the model generation procedure, only correlation factors from simulated air showers with a minimum energy of $E = 10^{18.5}$ eV and a maximum inclination of $\theta = 45^\circ$ are taken into account. In addition, those fits that have not passed the quality cuts from Section 6.2 are discarded. The Gaussian fits on the correlation histograms provide the most probable correlation factors and are summarized in Table 6.1.

	a	b	μ	c
a	1	0.7058	0.8750	0.9648
b	0.7058	1	0.8847	0.5901
μ	0.8750	0.8847	1	0.7677
c	0.9648	0.5901	0.7677	1

Table 6.1.: Values of the most probable correlation factors of TPDF parameters.

Once the TPDF correlation factors are determined, they are included in the calculation of the confidence interval. The total squared uncertainty for each time bin is calculated as:

$$\sigma_{total}^2(t) = \sum_{i,j} \frac{\partial f(t)}{\partial p_i} \frac{\partial f(t)}{\partial p_j} \cdot \sigma_{p_i} \cdot \sigma_{p_j} \cdot corr(p_i, p_j) \quad , \quad (6.4)$$

where $corr(p_i, p_j)$ represents the correlation factors, $\frac{\partial f(t)}{\partial p}$ are the derivatives of the TPDF $f(t)$ with respect to one parameter $p = \{a, b, \mu, c\}$ and σ_p is the uncertainty of the corresponding TPDF parameter. The TPDF and their derivatives with respect to the four parameters are:

$$f(t) = 10^a \cdot e^{-\left(e^{-\left(\frac{t-\mu}{b}\right)} + c \cdot t\right)} \quad (6.5)$$

$$\frac{\partial f(t)}{\partial a} = f(t) \cdot \ln 10 \quad (6.6)$$

$$\frac{\partial f(t)}{\partial b} = f(t) \cdot \left(-\frac{t-\mu}{b^2} \cdot e^{-\left(\frac{t-\mu}{b}\right)} \right) \quad (6.7)$$

$$\frac{\partial f(t)}{\partial \mu} = f(t) \cdot \left(-\frac{1}{b} \cdot e^{-\left(\frac{t-\mu}{b}\right)} \right) \quad (6.8)$$

$$\frac{\partial f(t)}{\partial c} = f(t) \cdot (-t) \quad (6.9)$$



The confidence intervals for each TPDF parameter are constructed with separate functions for the upper and the lower bounds. They are asymmetric around the mean expectation in most cases. The widest confidence interval obtained from all combinations of TPDF parameter uncertainties is used for comparison with the tested SD time traces. Figure 6.5 shows an example of a time trace and TPDF models (no fits) for different primaries with their corresponding confidence intervals.



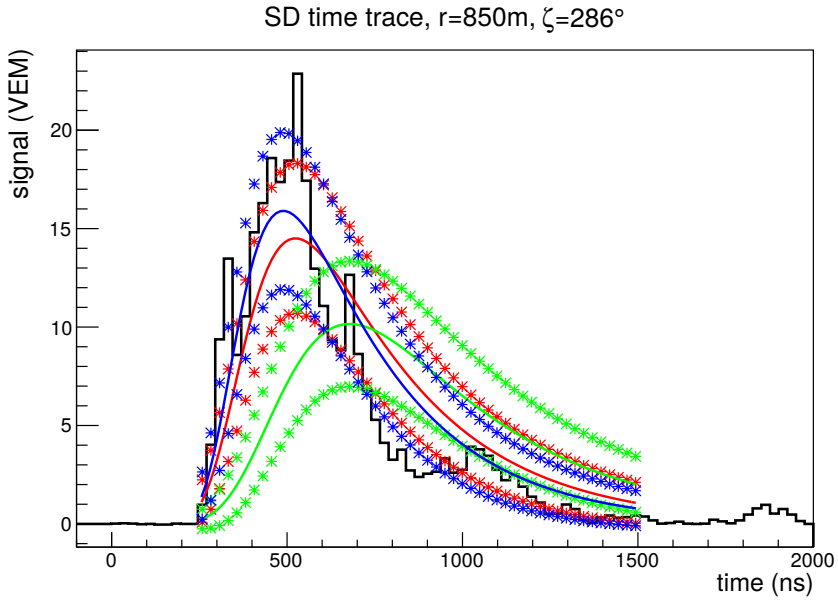
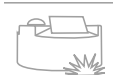
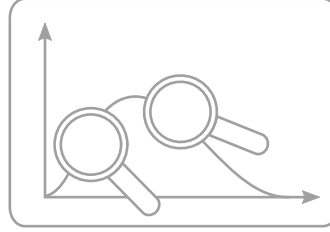
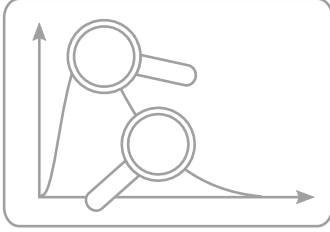


Figure 6.5.: Time trace (black line) of a single SD station at 850 m from the air shower axis and $\zeta = 286^\circ$ with interpolated TPDF models (solid color lines) and 1 sigma confidence intervals (asterisks), based on simulations with protons (red), iron nuclei (blue) and gamma rays (green).





Analysis of TPDF parameters obtained from simulated EAS

The TPDF models, mentioned in Section 6.2 are generated on air shower simulations with different input parameters and properties of the primary particle. In this chapter the analysis of the variations in the parameters of the TPDF models is described. The variations with the change of the primary particle properties, i.e. energy and inclination angle are expected. However, the differences of the TPDF parameters obtained from simulations with different simulation parameters, e.g. CORSIKA version or high-energy hadronic interaction model would indicate the uncertainty of the simulations themselves.

The analysis of the TPDF parameters is focused on their dependence on *distance* r to the air shower axis and on the *polar angle* ζ . The graphs in Figure 7.1(a) show the general trend for the fit parameters as a function of the distance r . Each point represents the mean and the standard deviation from all TPDF fits on several air shower simulations with the same simulation parameters (but other random number sequences) and primary particle properties. The second set of graphs, plotted in Figure 7.1(b), shows the results of the TPDF parameter fits as a function of the ζ angle at the same distance r displayed together with the individual standard deviations and the confidence interval covering 68 % of the individual TPDF parameters (points in Figure 7.1(b)) not taking the individual standard deviations into account.

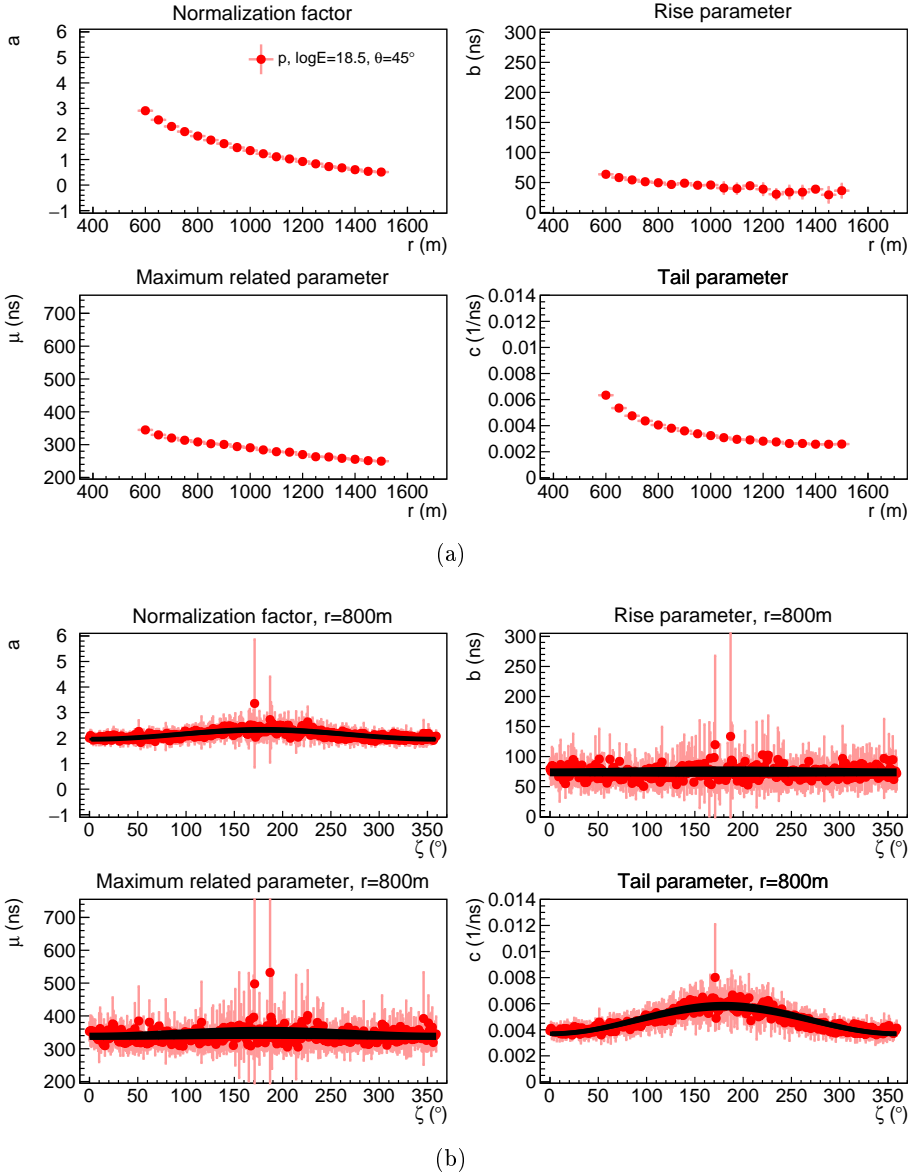


Figure 7.1.: TPDF parameters as functions of r (a) and ζ at 800m (b) to air shower axis obtained from non-thinned EAS simulations with proton primary, $E = 10^{18.5}$ eV, $\theta = 45^\circ$, EPOS and FLUKA models and CORSIKA version 7.4005. In (b) individual values with standard deviations (red) for each 1° segment and fitted ζ functions and their 68 % confidence interval (black) are shown.

Note that the TPDF parameters as functions of distance r to the air shower axis and polar angle ζ are calculated differently and therefore Figure 7.1(a) and (b) cannot directly be compared. This is also true for all following graphs and is due to the fact that the distance dependence is constructed from the *sums* of the time traces of all 360 SD stations in a ring. The time traces at the same distance r to the air shower axis are first summed and then fitted with the TPDF. The results of the TPDF fits are used to calculate the mean and the uncertainty of each point displayed in Figure 7.1(a). However, in calculating the ζ dependence, each segment of the 360 in each ring is treated separately. First the individual time trace histograms in each ζ segment are fitted with the TPDF. Next the results of the fits are used to calculate the mean and the uncertainty at each ζ angle separately. Finally the ζ function (Eq. (6.1)) and the confidence interval are fitted for each distance r (Figure 7.1(b)).

All ζ angle dependency fits have been performed for all different models. However, as the total number is large, only some of them are shown in the following sections. The air shower simulations used are all thinned, except when explicitly written. The open markers indicate TPDF parameters built on thinned EAS simulations, whereas for non-thinned simulations full markers are used. In case of proton primary red circles will be shown, for iron induced EAS blue upward triangles and for gamma primary green downward triangles will be drawn.

7.1. Primary particles differences

The TPDF approach (Section 5.2) is targeted at the discrimination of the primary particles of air showers to find ultra-high-energy gamma rays. To set criteria for estimating that a certain unknown air shower was initiated by a gamma the air shower simulations with the same energy and angular starting parameters, but different primaries, have to be compared.

Figures 7.2, 7.3, 7.4 and 7.5 show the results obtained from air shower simulations with proton, iron and gamma primaries at energies of $10^{18.5}$ eV and $10^{19.5}$ eV, and at inclination angles of 0° and 45° .

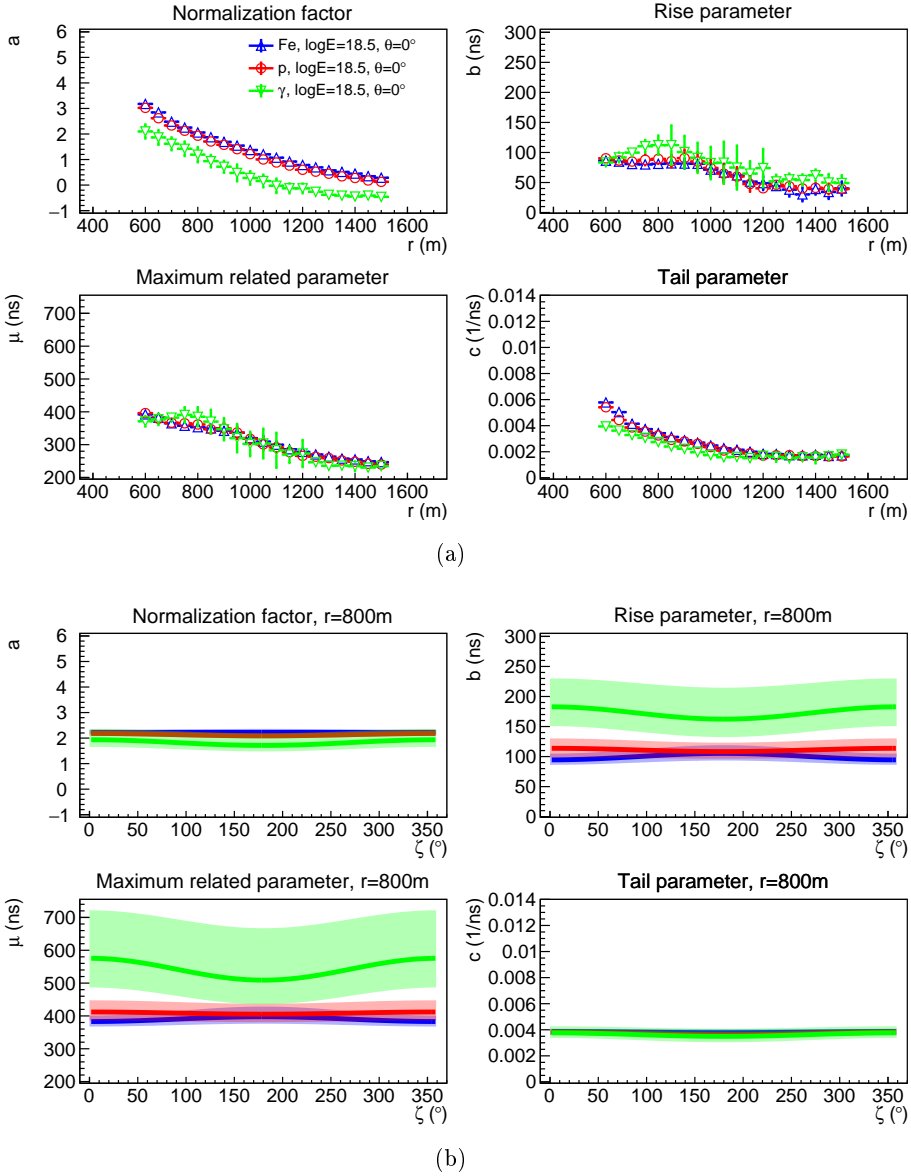


Figure 7.2.: TPDF parameters as functions of r (a) and ζ (b) for air shower simulations with iron (blue), proton (red) and gamma (green) primaries. For each primary 10 thinned simulations are used with $E = 10^{18.5} \text{ eV}$, $\theta = 0^\circ$, EPOS and FLUKA models and CORSIKA v. 7.4005. Note that the results in (a) and (b) were built differently and therefore cannot be compared directly.

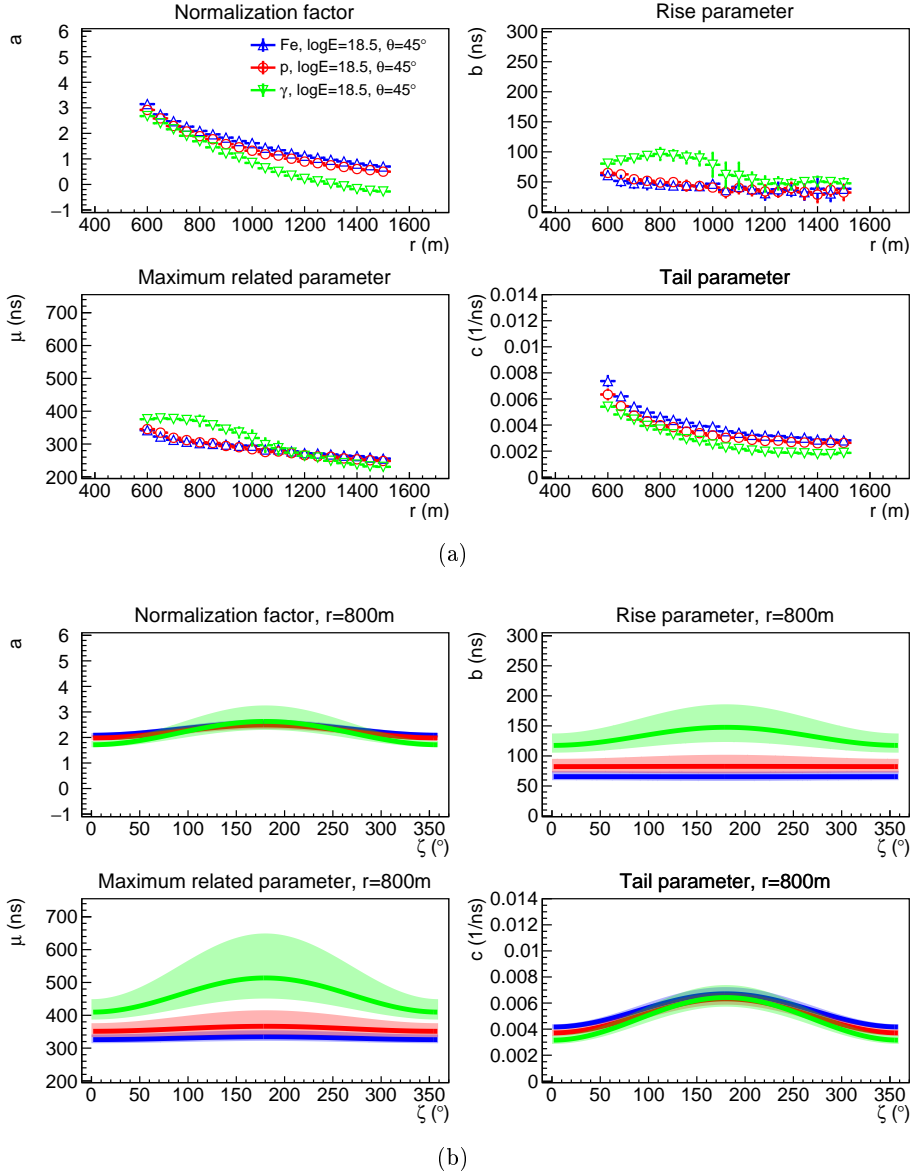


Figure 7.3.: TPDF parameters as functions of r (a) and ζ (b) for air shower simulations with iron (blue), proton (red) and gamma (green) primaries. For each primary 10 thinned simulations are used with $E = 10^{18.5}$ eV, $\theta = 45^\circ$, EPOS and FLUKA models and CORSIKA v. 7.4005. Note that the results in (a) and (b) were built differently and therefore cannot be compared directly.

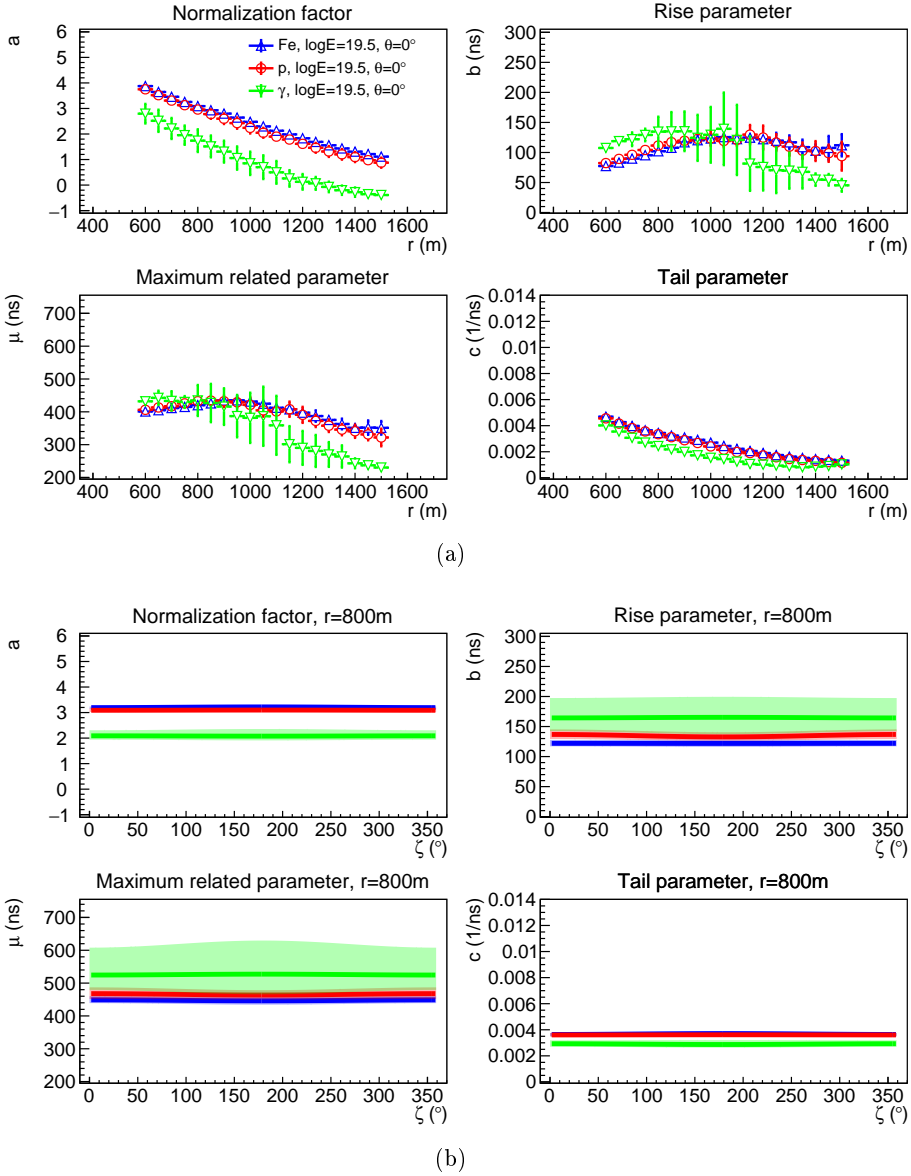


Figure 7.4.: TPDF parameters as functions of r (a) and ζ (b) for air shower simulations with iron (blue), proton (red) and gamma (green) primaries. For each primary 10 thinned simulations are used with $E = 10^{19.5}$ eV, $\theta = 0^\circ$, EPOS and FLUKA models and CORSIKA v. 7.4005. Note that the results in (a) and (b) were built differently and therefore cannot be compared directly.

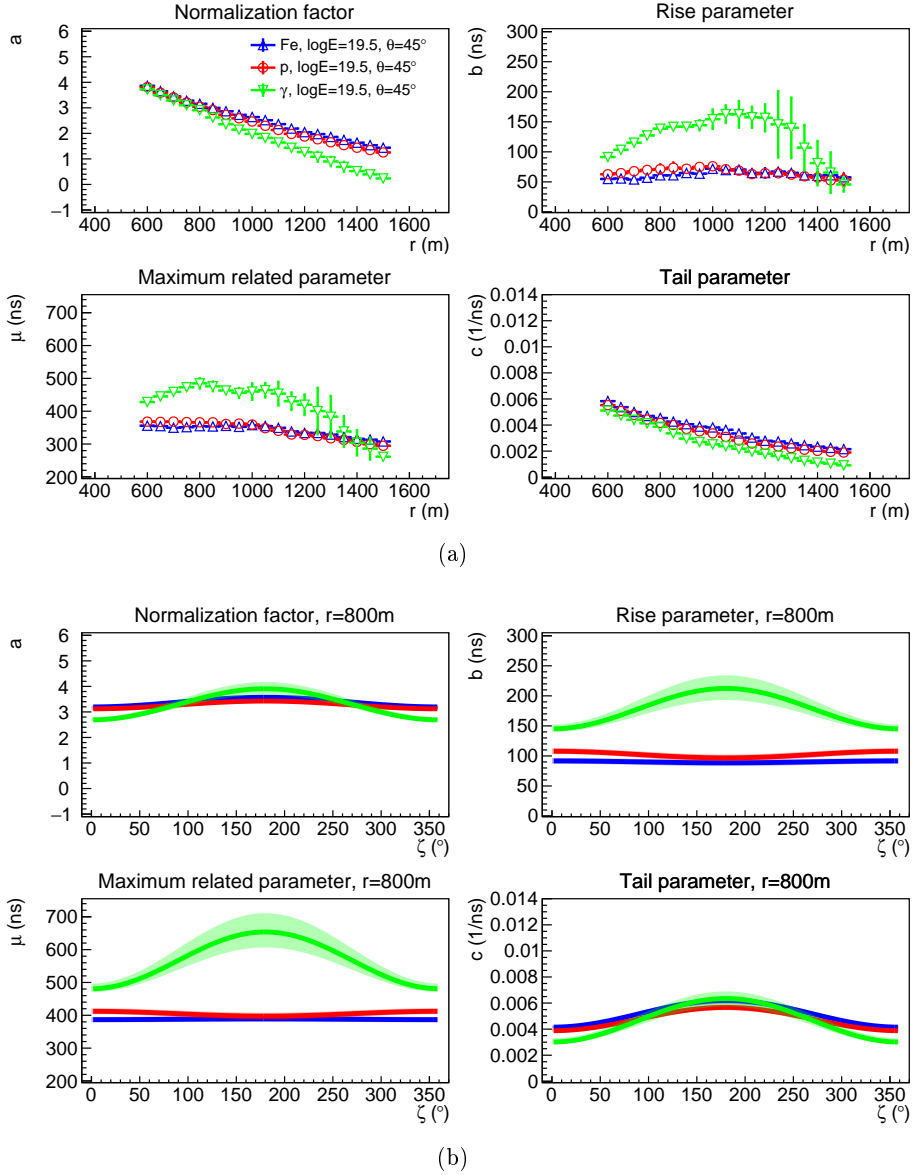


Figure 7.5.: TPDF parameters as functions of r (a) and ζ (b) for air shower simulations with iron (blue), proton (red) and gamma (green) primaries. For each primary 10 thinned simulations are used with $E = 10^{19.5}$ eV, $\theta = 45^\circ$, EPOS and FLUKA models and CORSIKA v. 7.4005. Note that the results in (a) and (b) were built differently and therefore cannot be compared directly.

By comparing the results as a function of distance r to the air shower axis (upper graphs (a)) one can see that the differences between proton and iron primaries are small, but that gamma primaries show a different behavior from the hadrons. The second observation is that the uncertainties on the TPDF parameters are much larger for the gamma TPDF model when compared to the other two. Both statements are also valid for the ζ angle dependence (lower graphs (b)). In addition, parameters from inclined air showers with gamma primaries show a larger dependency in the ζ angle than those from inclined EAS initiated by hadrons. This can be explained by the different fractions of EM and muonic components for gamma and hadron air showers (Figure 5.5). For vertical air showers, Figures 7.2 and 7.4, the a parameter in the r graphs (a), which is proportional to the number of secondaries and their energy deposit in the SD, shows a large difference between hadronic and gamma EAS simulations. This is caused mainly by the small number of muons in case of gamma air showers. Finally, the ζ graphs (b) show that the uncertainties are decreasing with increasing energy. This is due to a larger number of particles in the SD stations, leading to smoother time traces and better fits of the TPDF function.

The reason for the large uncertainties e.g. at around 1000 m from the air shower axis for the rise parameter b in Figure 7.4(a) is the so called *transition zone* where this parameter is changing for an individual air shower from near 150 ns to 50 ns. The change accomplishes rapidly within a few distance bins and highly depends on the individual statistics of the air showers. The uncertainties in the graphs depends on the value differences before and after the change and on the distances to the air shower axis where this change is happening.

In general, Figures 7.2, 7.3, 7.4 and 7.5 show that there are differences in the TPDF parameters between TPDF models constructed using the gamma and the hadron induced EAS simulations. Furthermore, these differences get larger for more inclined and more energetic air showers. This fact will be used for the search of ultra-high-energy gamma rays.

As the differences between the TPDF parameters from EAS with proton and iron primaries are relatively small, in the following only the results from TPDF models with the proton primary will be displayed as representative for hadronic primaries.

7.2. Simulation energy differences

The size of an air shower depends directly on the number of secondary particles produced during the propagation and therefore on the energy of the primary particle. The signal strengths of SD stations at a certain distance r to the air shower axis are increasing with increasing energy of the primary, thus the TPDF parameters will also change. To investigate those changes, the TPDF parameters of air showers with energies of $E = 10^{18}$ eV, $10^{18.5}$ eV, 10^{19} eV and $10^{19.5}$ eV are plotted in Figures 7.6, 7.7, 7.8 and 7.9, separately for proton and gamma primaries, for two inclination angles $\theta = 0^\circ$ and 45° .

Three of the four TPDF parameters get larger with increasing EAS energy, the normalization parameter a and the parameters defining together the steepness of the rising part and the maximum, b and μ . The tail parameter c appears to be rather stable as a function of energy. As a consequence the predictions of the SD time traces depend on the energy. The uncertainties for the time trace sums in the r graphs (a) are larger for the vertical and for the gamma initiated air showers compared to inclined EAS and those with a proton primary.

The ζ graphs (b) show a larger dependency of the ζ angle with a wider confidence interval for air showers initiated by gamma primaries. Especially, the TPDF parameters for the gamma induced EAS with an energy of $E = 10^{18}$ eV feature very wide confidence intervals, which makes a discrimination between different primaries almost impossible. However, the reconstructed energy in this case is well below 10^{18} eV (Section 8.1), therefore this is not a real problem, as air showers with such reconstructed energies will be rejected by the quality cuts.

The energy comparisons in Figures 7.6, 7.7, 7.8 and 7.9 show large uncertainties for low energy EAS in combination with high inclination angle. Higher uncertainties are also present for gamma primaries compared to hadronic primaries. The origin of this uncertainty is the lack of particles in a single SD station. In these cases the electromagnetic component of the air showers has died out, whereas there is almost no muonic component in case of gamma initiated EAS.

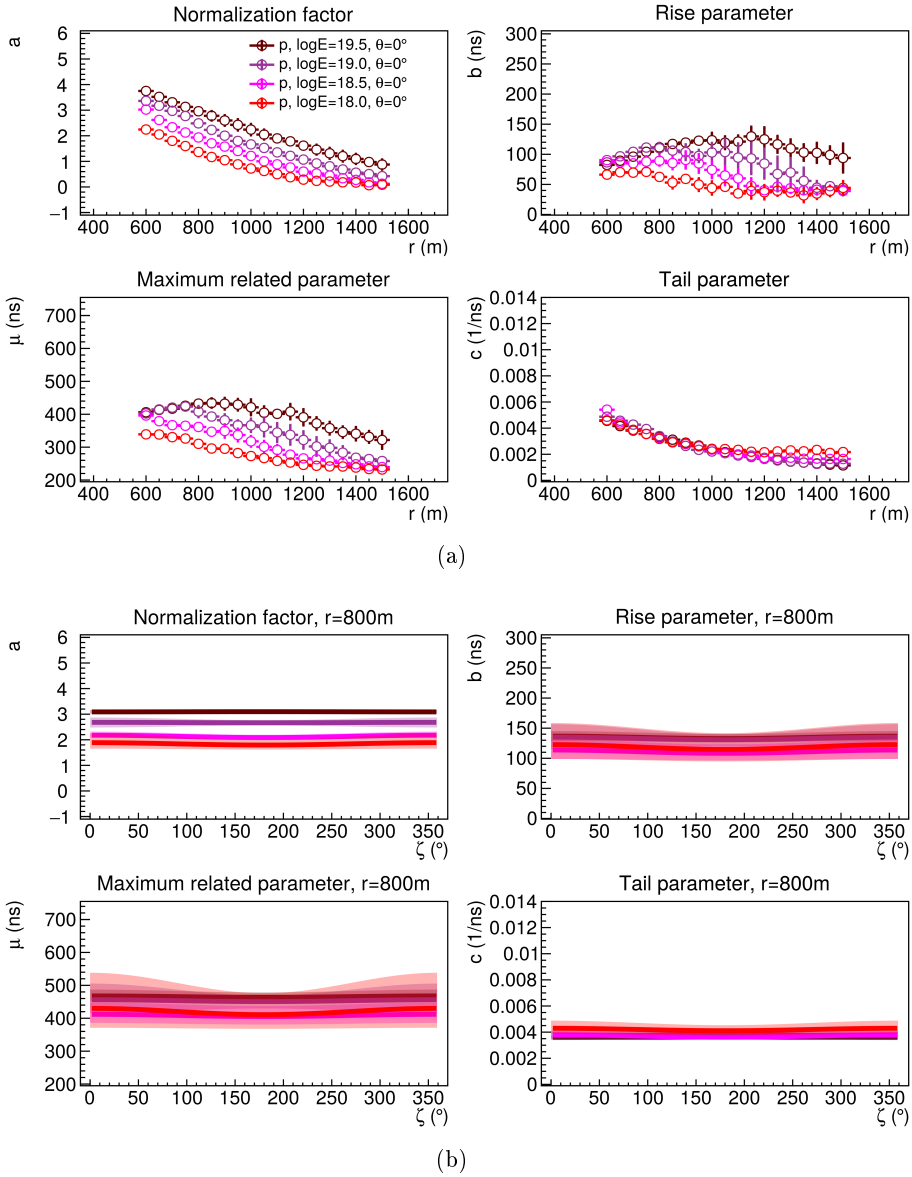


Figure 7.6.: TPDF parameters as functions of r (a) and ζ (b) for air shower simulations with different energies. For each energy 10 thinned simulations are used with proton primary, $\theta = 0^\circ$, EPOS and FLUKA models and CORSIKA version 7.4005. Note that the results in (a) and (b) were built differently and therefore cannot be compared directly.

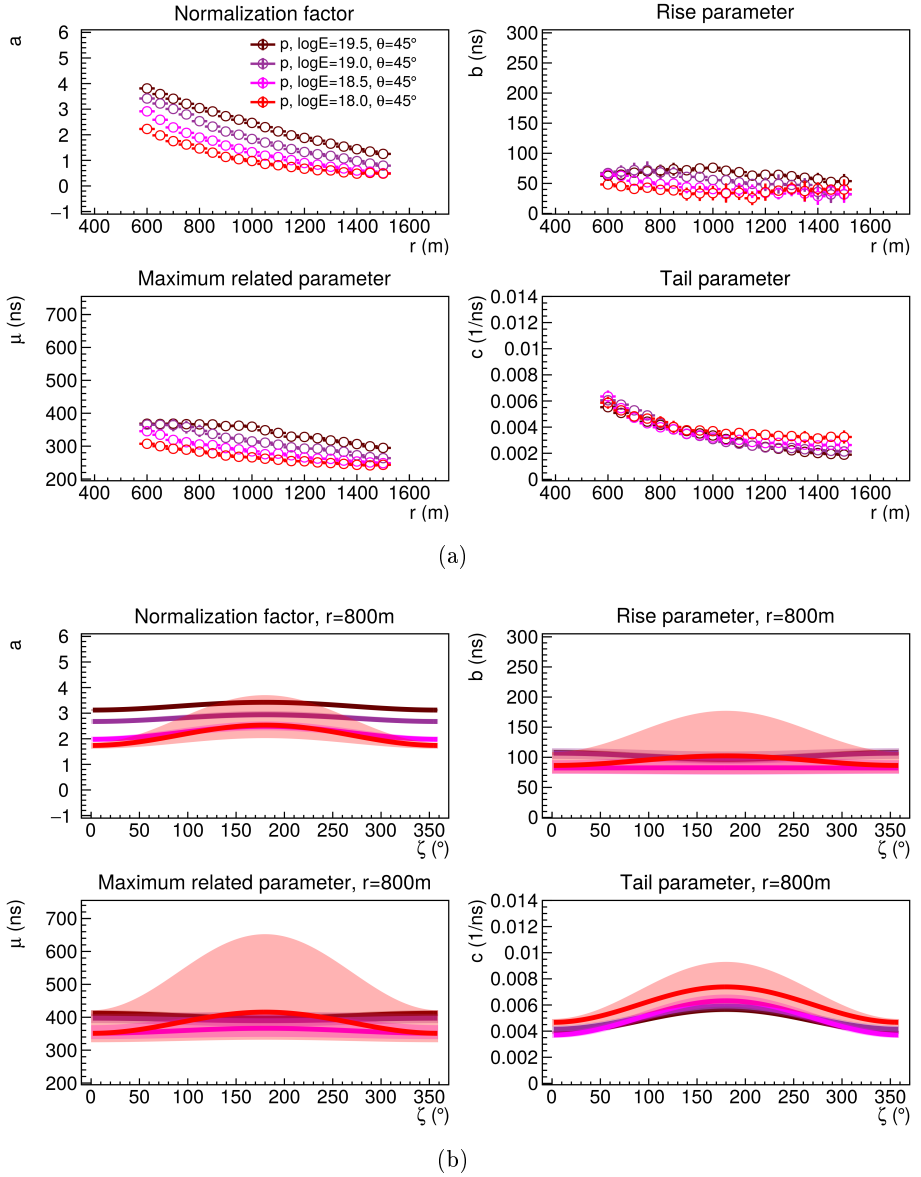


Figure 7.7.: TPDF parameters as functions of r (a) and ζ (b) for air shower simulations with different energies. For each energy 10 thinned simulations are used with proton primary, $\theta = 45^\circ$, EPOS and FLUKA models and CORSIKA version 7.4005. Note that the results in (a) and (b) were built differently and therefore cannot be compared directly.

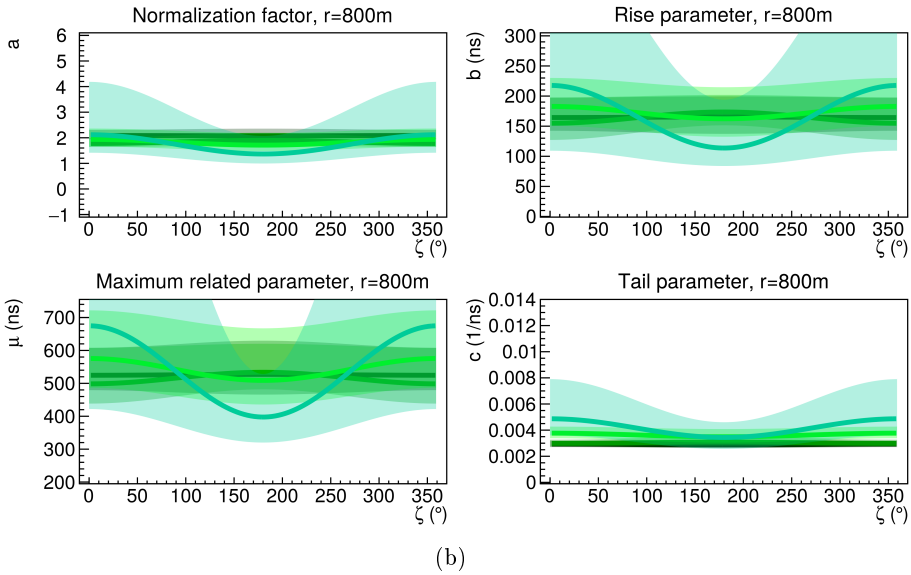
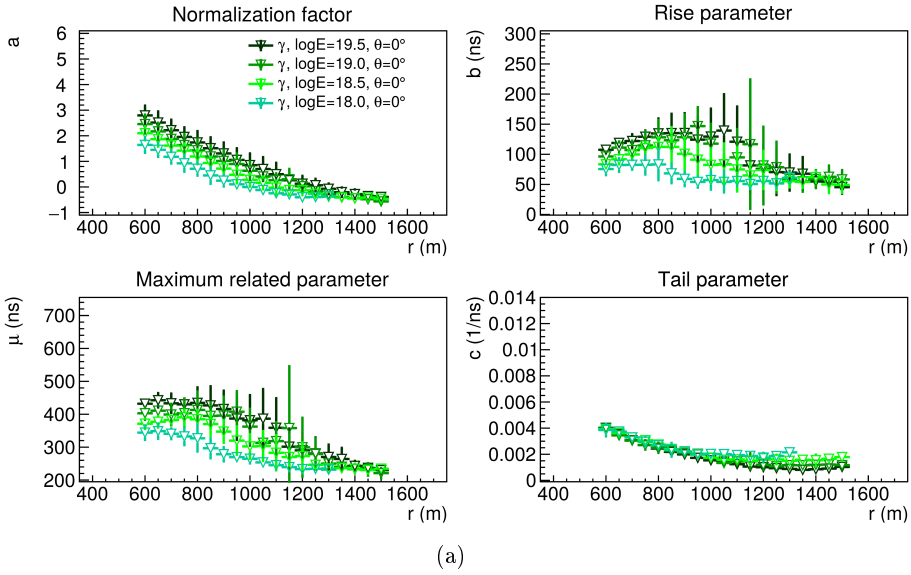


Figure 7.8.: TPDF parameters as functions of r (a) and ζ (b) for air shower simulations with different energies. For each energy 10 thinned simulations are used with gamma primary, $\theta = 0^\circ$, EPOS and FLUKA models and CORSIKA version 7.4005. Note that the results in (a) and (b) were built differently and therefore cannot be compared directly.

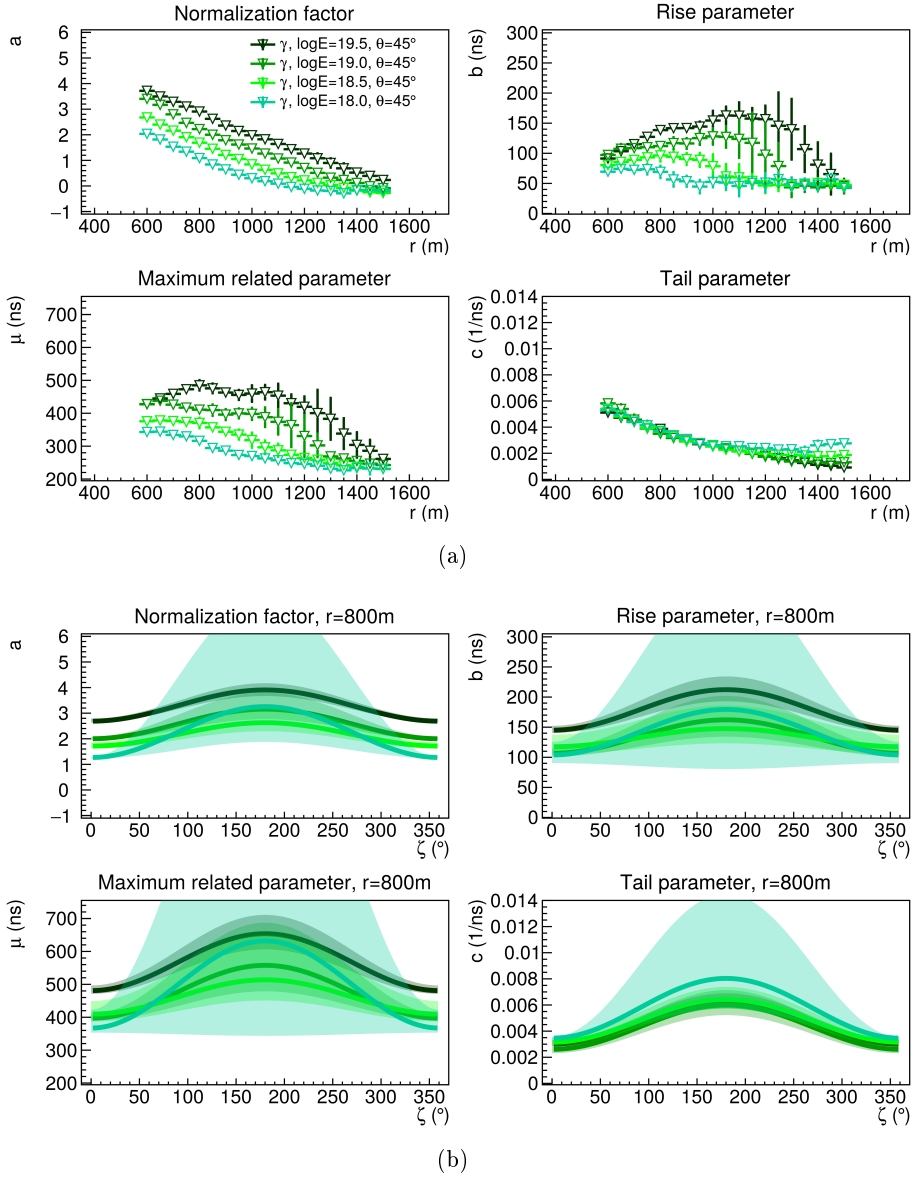


Figure 7.9.: TPDF parameters as functions of r (a) and ζ (b) for air shower simulations with different energies. For each energy 10 thinned simulations are used with gamma primary, $\theta = 45^\circ$, EPOS and FLUKA models and CORSIKA version 7.4005. Note that the results in (a) and (b) were built differently and therefore cannot be compared directly.

7.3. Inclination angle differences

While for the vertical air showers no big ζ angular differences are expected neither in the time traces nor for the TPDF parameters, for inclined air showers these differences are present and increase with the θ angle. To study this behavior the TPDF parameters from fits on the simulated air showers with inclination angles of $\theta = 0^\circ, 15^\circ, 30^\circ, 45^\circ$ and 60° are compared, separately for proton and gamma primaries, for two energies $E = 10^{18.5}$ eV and $10^{19.5}$ eV displayed in Figures 7.11, 7.12, 7.13 and 7.14.

The distance r to the air shower axis graphs (a) show that the TPDF parameters vary differently with the inclination angle θ for increasing distance r , for different primaries and as a function of primary particle energies. For proton induced air showers the tail parameter c for $\theta = 60^\circ$ is completely off from the ones of the other inclination angles for both energies, while for the EAS with gamma primaries this difference is smaller and decreases with the increase of the primary energy.

The ζ graphs (b) show the increase of the ζ angular differences and the width of the confidence intervals for more inclined EAS. This means that for lower energies and higher inclination angles it will be more difficult to differentiate air shower primaries, as the TPDF parameters cover many possible values for this case.

7.4. CORSIKA version differences

The air shower simulations used for building the TPDF models were performed using two CORSIKA versions. Therefore, a comparison of the simulations has to be done, to ensure that both simulations sets can be used for testing the unknown air showers. To analyze the differences of TPDF parameters the simulations using the two CORSIKA versions 7.4005 and 7.5600 are shown together, separately for proton and gamma primaries, for the energy of $E = 10^{18.5}$ eV and inclination angle of 45° in Figures 7.15 and 7.16. The newer CORSIKA version includes small changes e.g. several bug fixes, protection from negative energy deposits due to rare problems and the use of ρ^0 mesons instead of pions at high-energy photonuclear interactions.

The distance r graphs (a) for proton and gamma primaries show comparable TPDF parameters for EAS simulations done with both CORSIKA versions. Small differences are observed in the tail parameter c . The com-

parison indicates a steeper slope after the maximum of the time traces for simulations done with CORSIKA version 7.4005. Figure 7.10 displays 20 TPDF, 10 done with each of the CORSIKA versions. The TPDF are obtained from sums of time trace fits for the ring at 800 m to the air shower axis and confirms the behavior of the steeper slope for CORSIKA version 7.4005. Additionally, it can be observed that the spread of the TPDF is higher for these air shower simulations.

The ζ graphs (b) also confirm that behavior of the tail parameter for the EAS simulation with a proton primary. In case of gamma initiated EAS all TPDF parameters reveal a stronger dependency on the ζ angle and at the same time an increase of the confidence intervals.

However, the values obtained with both CORSIKA versions are compatible and both sets of TPDF models can be used for testing the measured air showers.

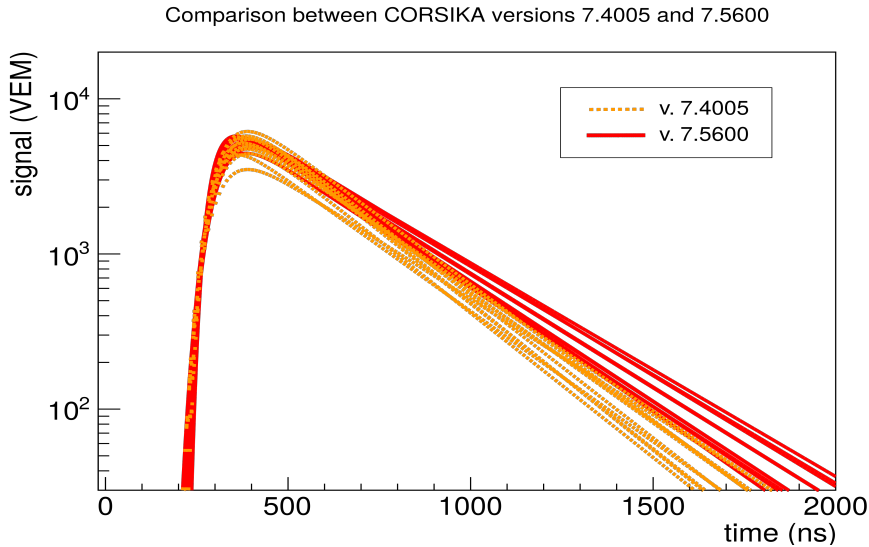


Figure 7.10.: TPDF results from fits of time trace sums (from 360 SD stations) at 800 m from the air shower axis. The SD time traces are simulated using thinned air shower simulations done with proton primary, $E = 10^{18.5}$ eV, $\theta = 45^\circ$, EPOS and FLUKA models. The orange dotted lines represent results obtained from 10 simulation done with CORSIKA v. 7.4005 and the red solid lines those 10 done with v. 7.5600.

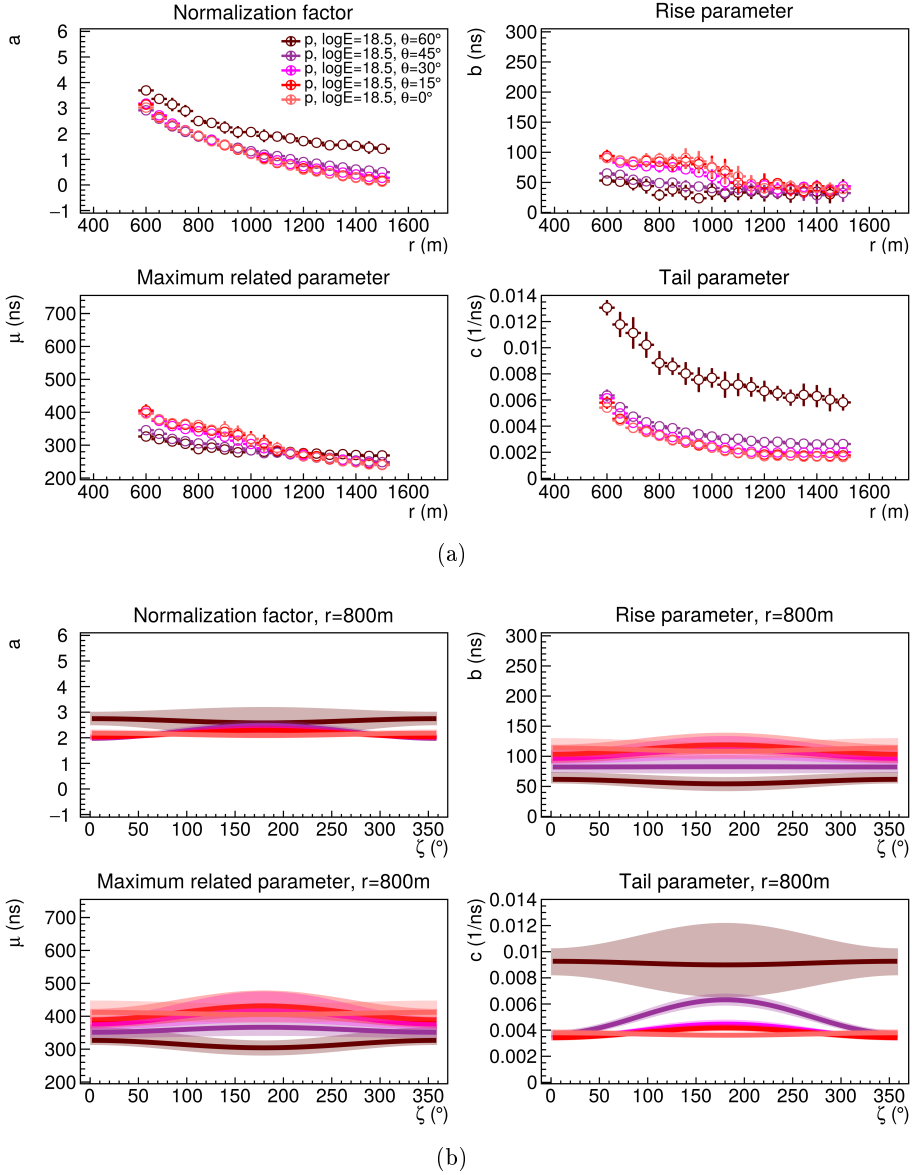


Figure 7.11.: TPDF parameters as function of r (a) and ζ (b) for air shower simulations with different inclination angles. For each θ angle 10 thinned simulations are used with proton primary, $E = 10^{18.5}$ eV, EPOS and FLUKA models and CORSIKA version 7.4005. Note that the results in (a) and (b) were built differently and therefore cannot be compared directly.

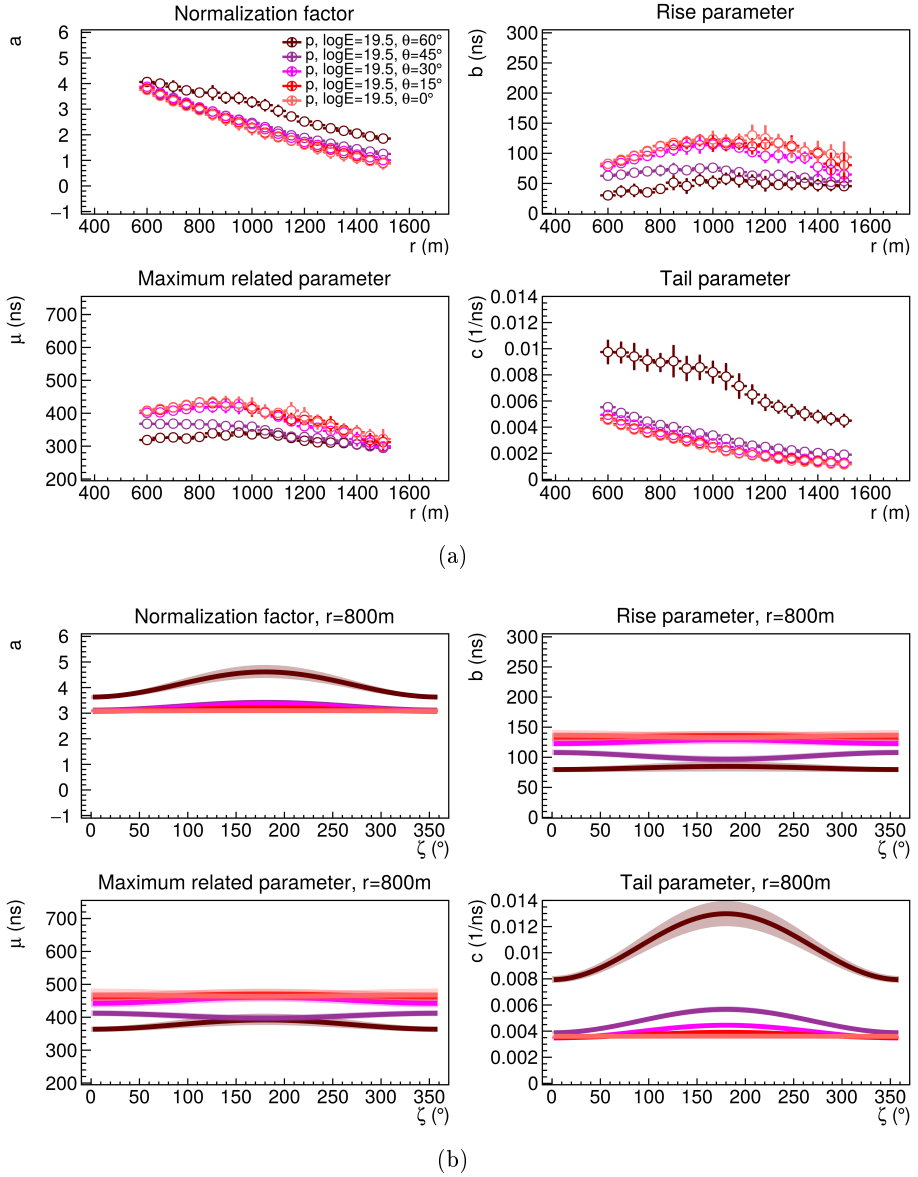


Figure 7.12.: TPDF parameters as function of r (a) and ζ (b) for air shower simulations with different inclination angles. For each θ angle 10 thinned simulations are used with proton primary, $E = 10^{19.5}$ eV, EPOS and FLUKA models and CORSIKA version 7.4005. Note that the results in (a) and (b) were built differently and therefore cannot be compared directly.

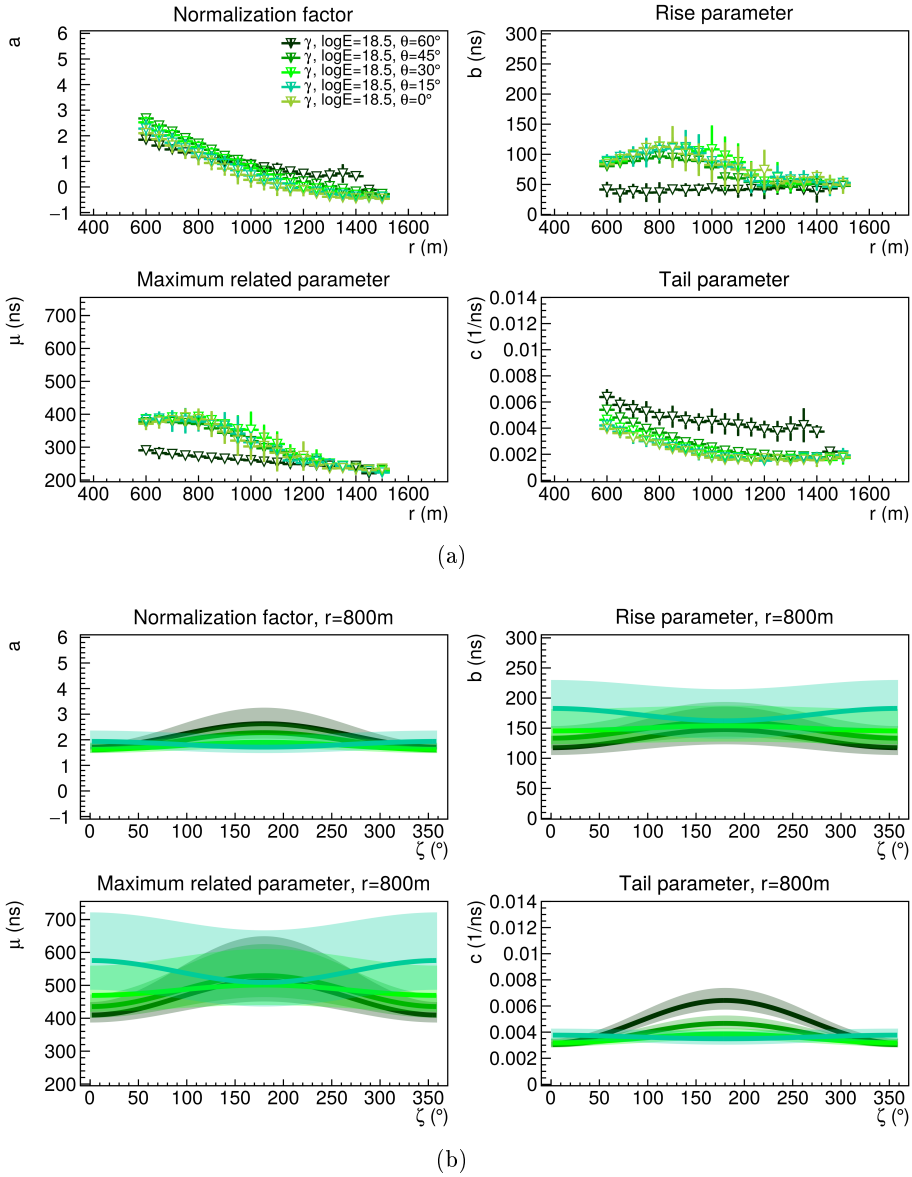


Figure 7.13.: TPDF parameters as function of r (a) and ζ (b) for air shower simulations with different inclination angles. For each θ angle 10 thinned simulations are used with gamma primary, $E = 10^{18.5}$ eV, EPOS and FLUKA models and CORSIKA version 7.4005. Note that the results in (a) and (b) were built differently and therefore cannot be compared directly.

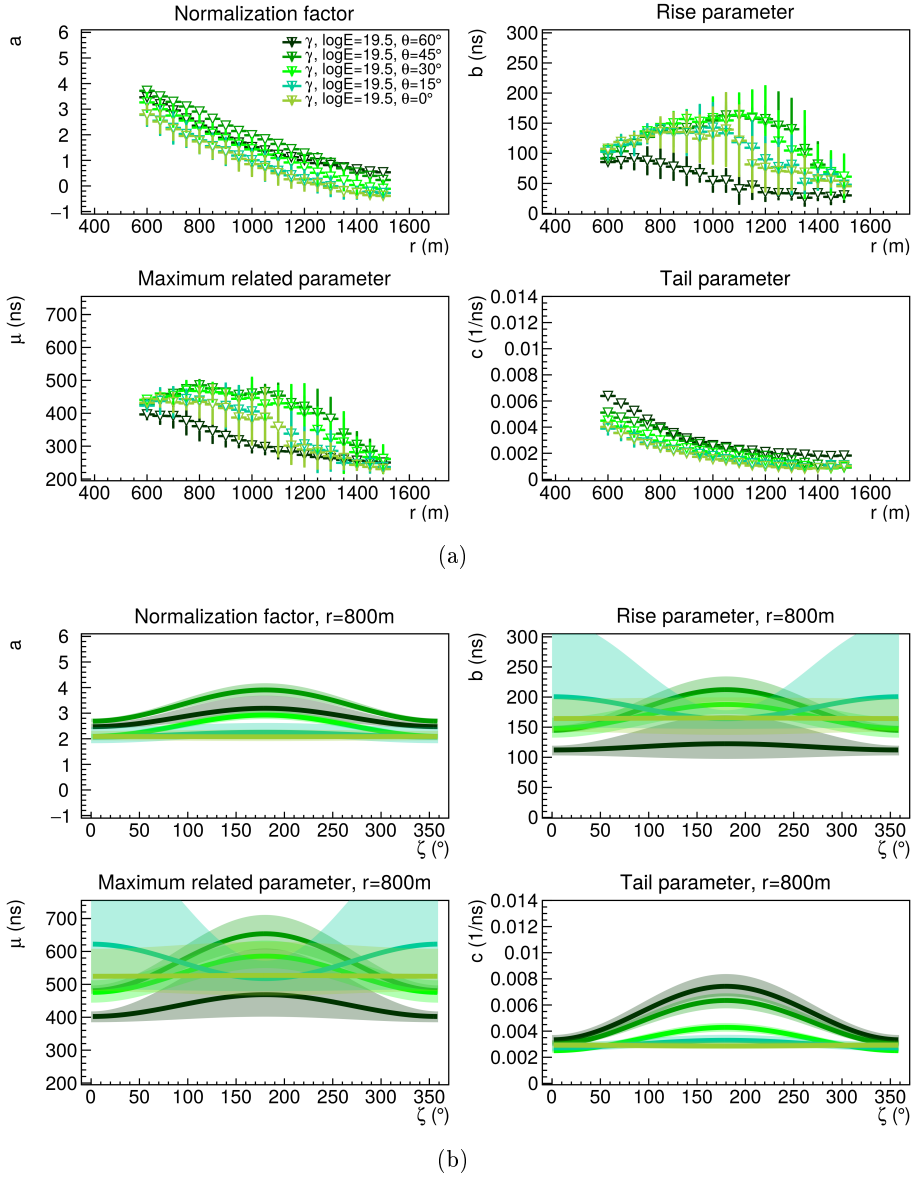


Figure 7.14.: TPDF parameters as function of r (a) and ζ (b) for air shower simulations with different inclination angles. For each θ angle 10 thinned simulations are used with gamma primary, $E = 10^{19.5}$ eV, EPOS and FLUKA models and CORSIKA version 7.4005. Note that the results in (a) and (b) were built differently and therefore cannot be compared directly.

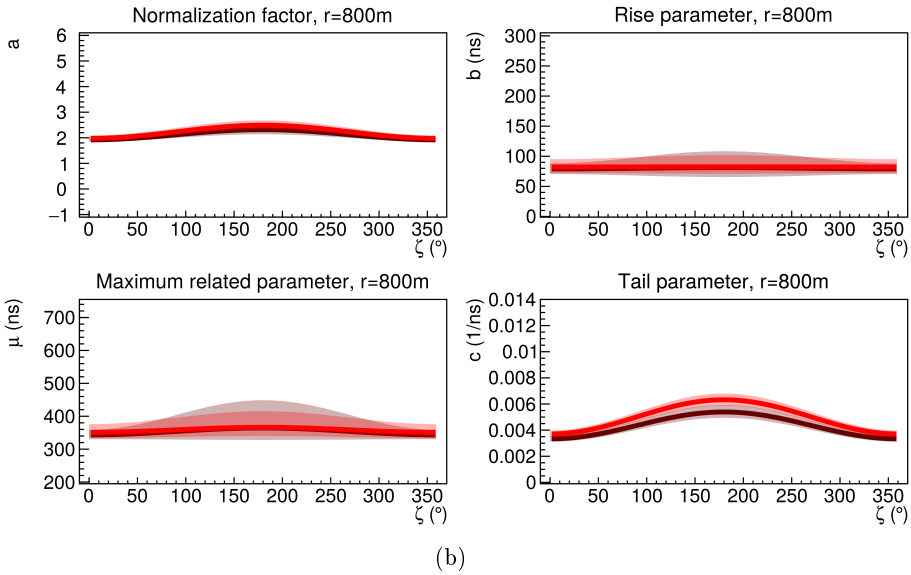
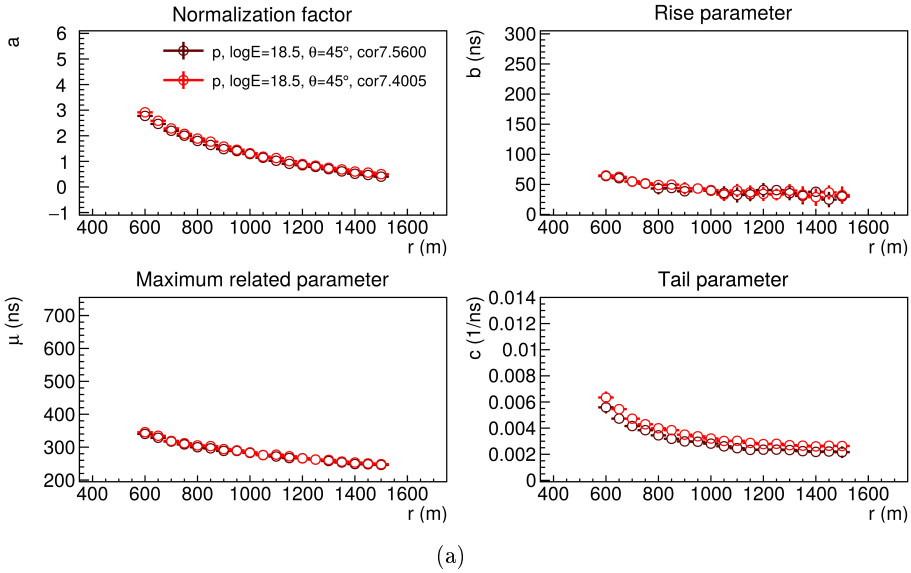


Figure 7.15.: TPDF parameters as functions of r (a) and ζ (b) for air shower simulations with different versions of CORSIKA. For each CORSIKA version 10 thinned simulations are used with proton primary, $E = 10^{18.5}$ eV, $\theta = 45^\circ$ and EPOS and FLUKA models. Note that the results in (a) and (b) were built differently and therefore cannot be compared directly.

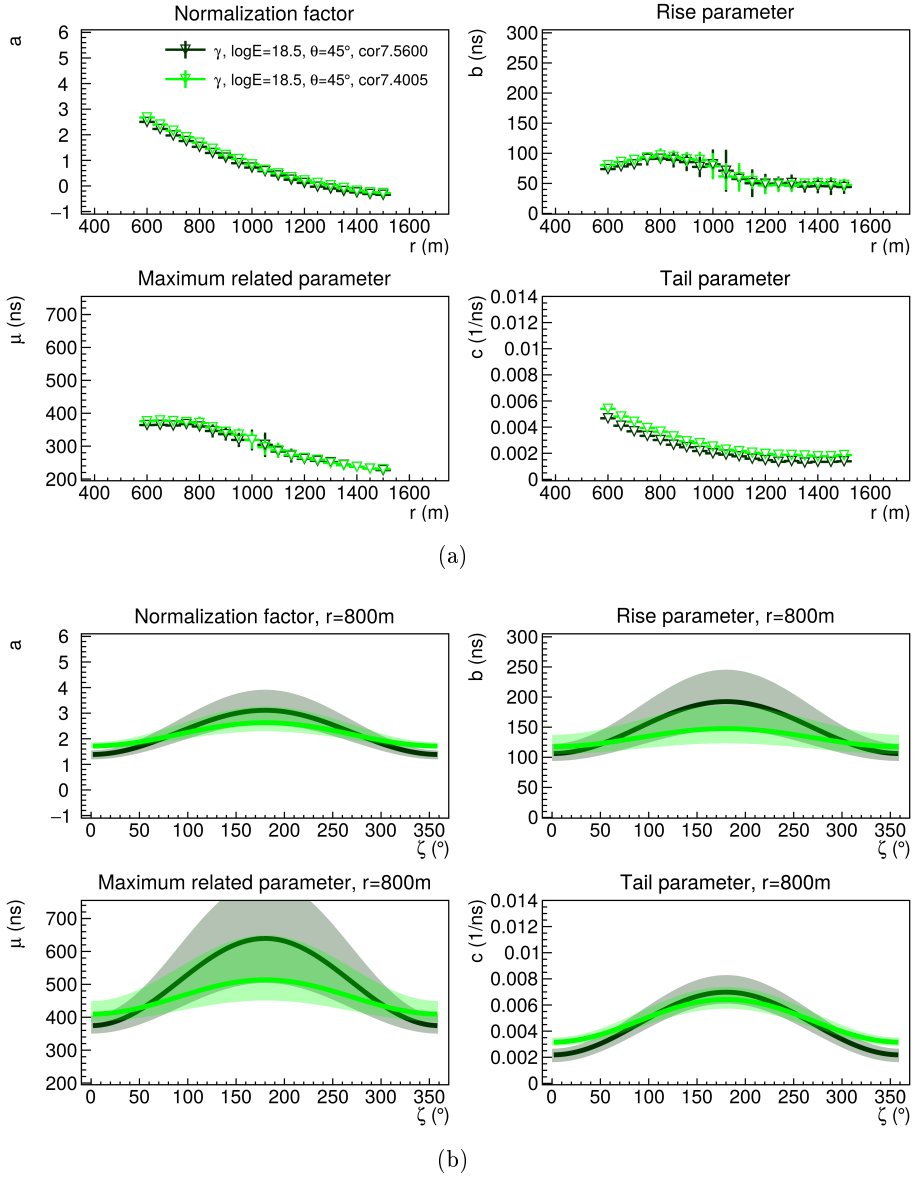


Figure 7.16.: TPDF parameters as functions of r (a) and ζ (b) for air shower simulations with different versions of CORSIKA. For each CORSIKA version 10 thinned simulations are used with gamma primary, $E = 10^{18.5}$ eV, $\theta = 45^\circ$ and EPOS and FLUKA models. Note that the results in (a) and (b) were built differently and therefore cannot be compared directly.

7.5. High-energy interaction model differences

Air showers are simulated using different interaction models, as described in Section 4.1. For the low-energy region only the FLUKA package [77] was used. In the more important high-energy region, above 80 GeV two models were used: EPOS [72] and QGSJet [73]. Both models are frequently used by the Pierre Auger Collaboration. This strategy provides a test for sensitivity of results against the interaction model that is used and a means to estimate the associated systematic uncertainty. All of the different sets of thinned air shower simulations described in Section 4.3 were created with both hadronic interaction models. In case of the non-thinned simulations, most sets were created using the EPOS model for the high-energy region.

Figure 7.17 shows that model dependence of the TPDF parameters is negligible for proton primary at $10^{18.5}$ eV and a zenith angle of 45° . The same is true at other angles and energies as well as for iron primary. Figure 7.18 shows the same for gamma primary. In this case a hint of a slight model dependence may be observed in the ζ graphs (b). However, this dependence is within the statistical uncertainty of the Monte Carlo simulations.



7.6. Increased number of secondary muons

As mentioned in Section 4.1 a muon deficit of 30 % was found in the CORSIKA simulations, which are performed using the EPOS hadronic interaction model [75] [76], with respect to data. To investigate how much this lack of muons affects the TPDF a simple test is performed. The number of muons in the CORSIKA output file is artificially increased through a loop over the particles, whereby each muon has a 30 % probability to be saved twice with unchanged parameters. The modified output files are used to construct the TPDF models following the same procedure as the original ones. This simple test will only be used to investigate if there are large systematic biases. The TPDF models based on simulations with 30 % additional muons will not be applied to the data.

The results from TPDF models with both the standard and increased number of muons are plotted together, separately for proton and gamma primaries, for non-thinned air shower simulations with energy of $10^{18.5}$ eV and for inclination angles $\theta = 0^\circ$ and 45° in Figures 7.19, 7.20, 7.21 and 7.22.

Figures 7.19 and 7.21 show that the TPDF parameters for vertical EAS with and without an increased number of muons are in good agreement. In the case of 45° inclination the TPDF parameters obtained from air shower simulations with proton primaries (Figure 7.20) and an increased number of muons are in agreement with the one with the default number of muons, while for gamma primaries (Figure 7.22) the ζ graphs reveal an increase of the uncertainties with small changes of the ζ mean fit functions. The larger uncertainties are in the late region of the EAS at $\zeta = 180^\circ$. This is likely due to the fact that the additional muons enlarge the signals in the SD stations, while distorting the time traces by increasing the muons contribution in certain bins and not smearing them.

Based on these results the conclusion is that the lack of muons in the hadronic interaction models is unlikely to have a significant impact on the TPDF parameters.

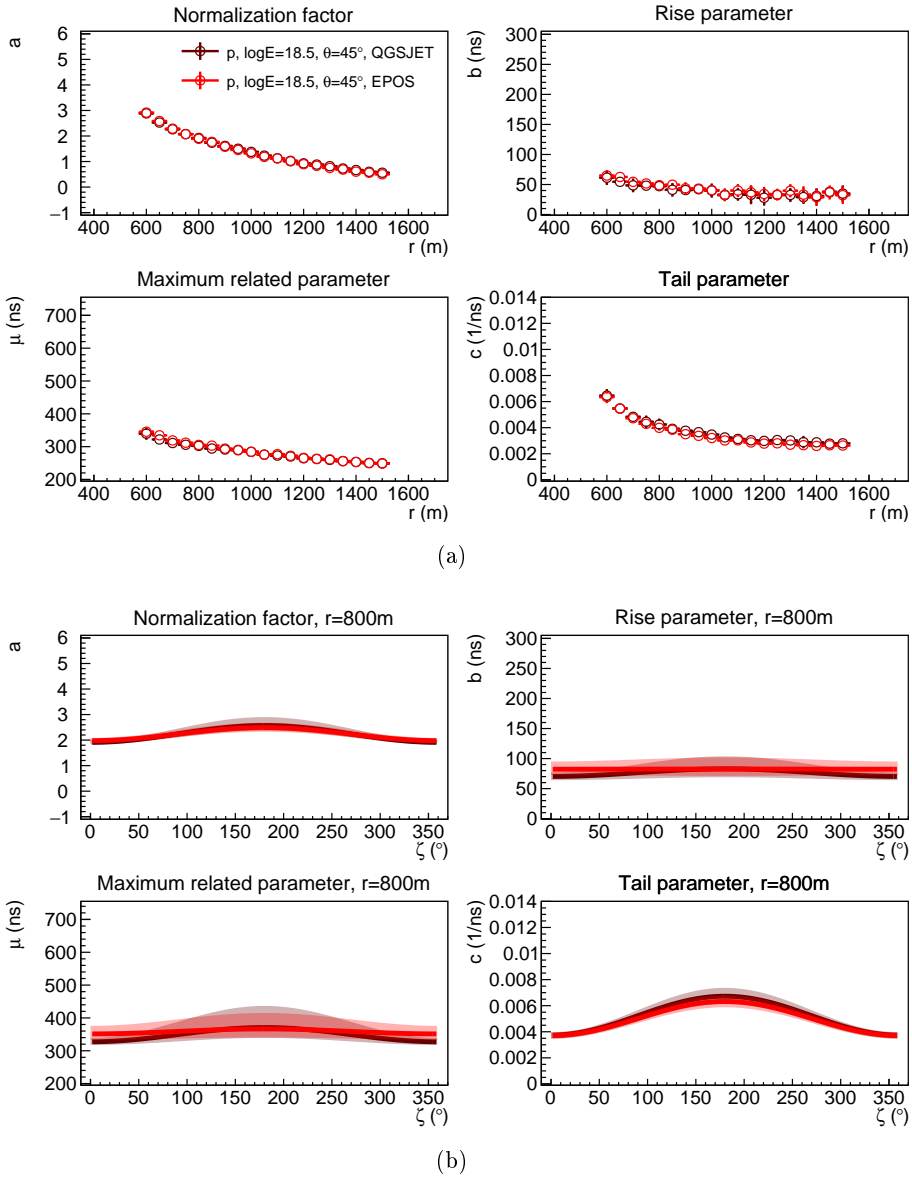


Figure 7.17.: TPDF parameters as functions of r (a) and ζ (b) for air shower simulations with different high-energy hadronic interaction models. For each model 10 thinned simulations are used with proton primary, $E = 10^{18.5}$ eV, $\theta = 45^\circ$ and CORSIKA version 7.4005. Note that the results in (a) and (b) were built differently and therefore cannot be compared directly.

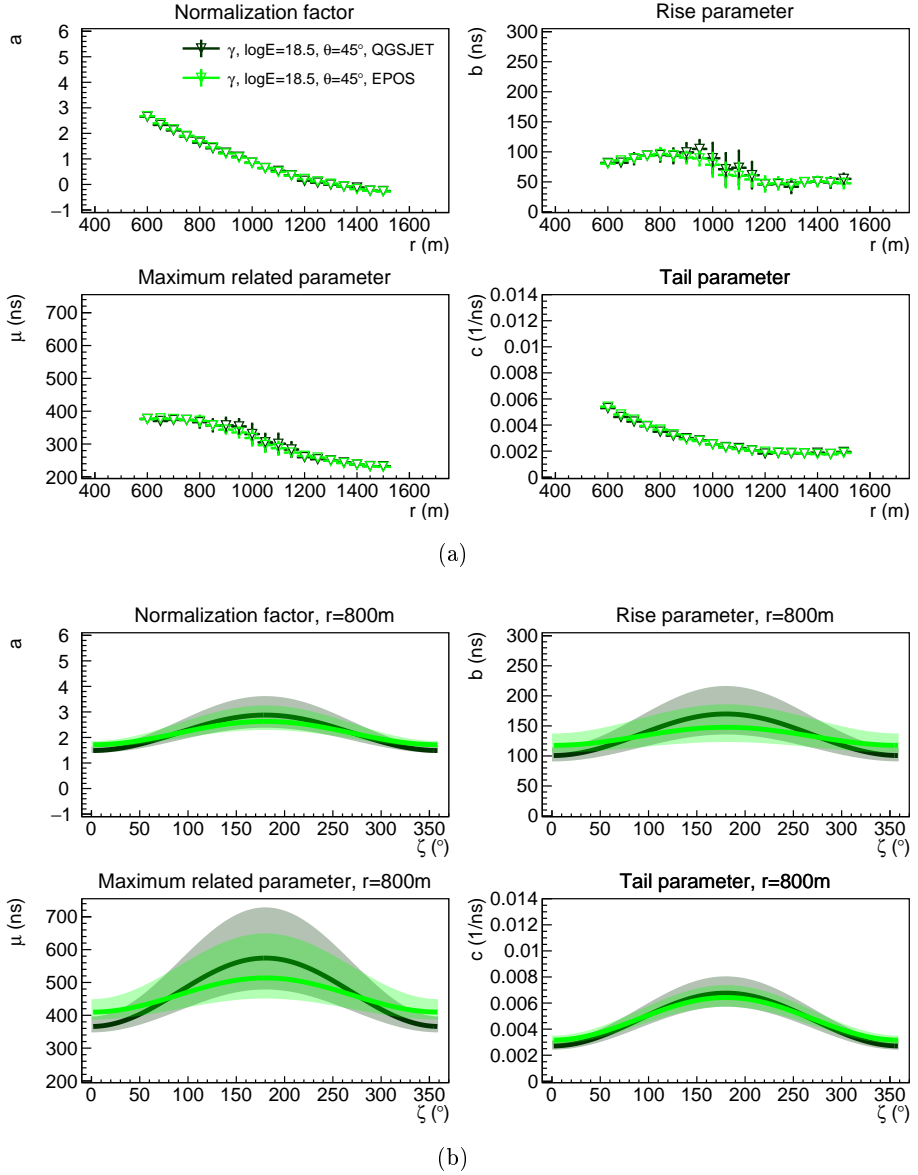


Figure 7.18.: TPDF parameters as functions of r (a) and ζ (b) for air shower simulations with different high-energy hadronic interaction models. For each model 10 thinned simulations are used with gamma primary, $E = 10^{18.5}$ eV, $\theta = 45^\circ$ and CORSIKA version 7.4005. Note that the results in (a) and (b) were built differently and therefore cannot be compared directly.

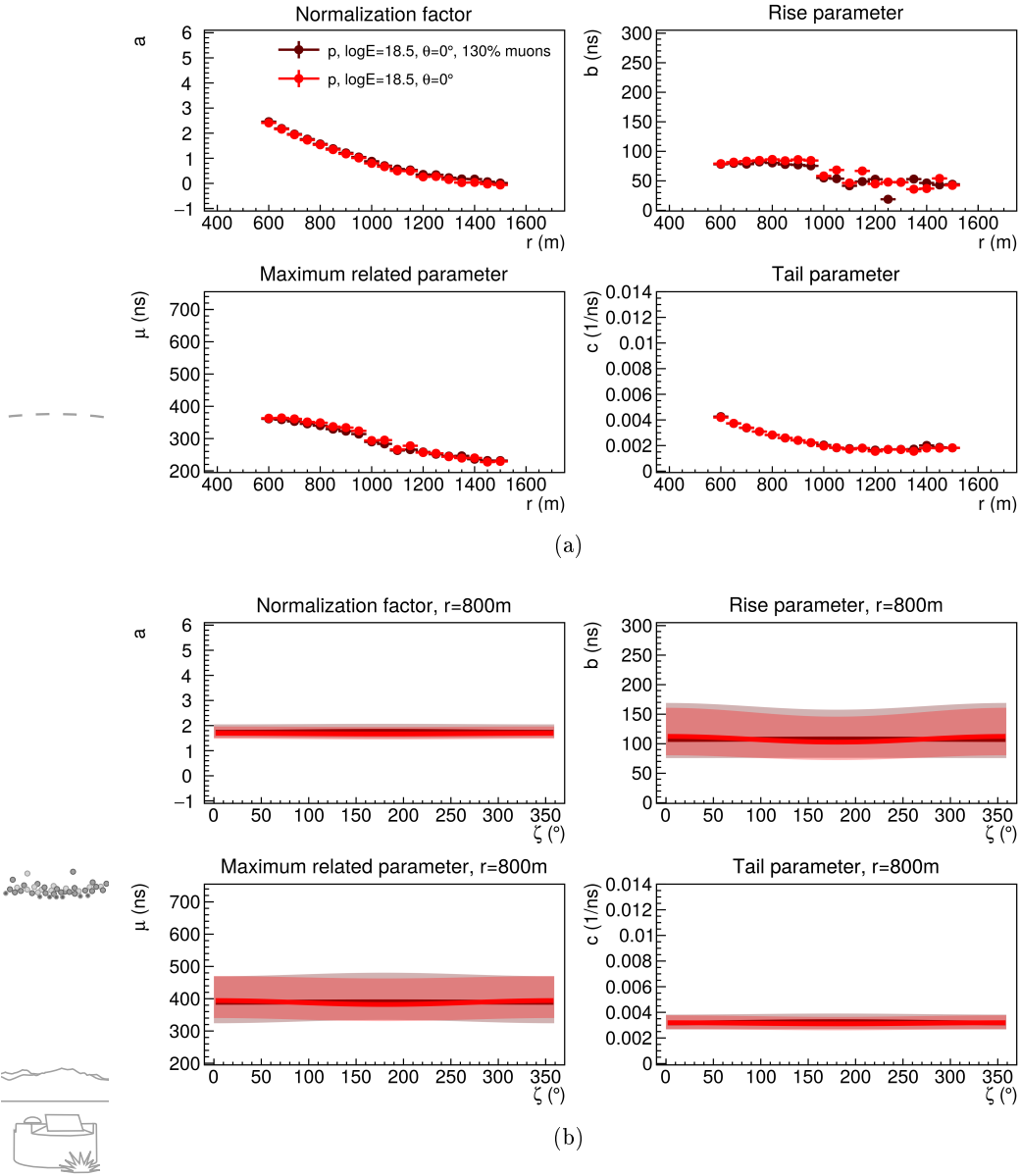


Figure 7.19.: TPDF parameters as functions of r (a) and ζ (b) for EAS simulations of default and artificially increased number of muons. In both cases 1 non-thinned simulation is used with proton primary, $E = 10^{18.5}$ eV, $\theta = 0^\circ$, EPOS and FLUKA models and CORSIKA version 7.4005. Note that the results in (a) and (b) were built differently and therefore cannot be compared directly.

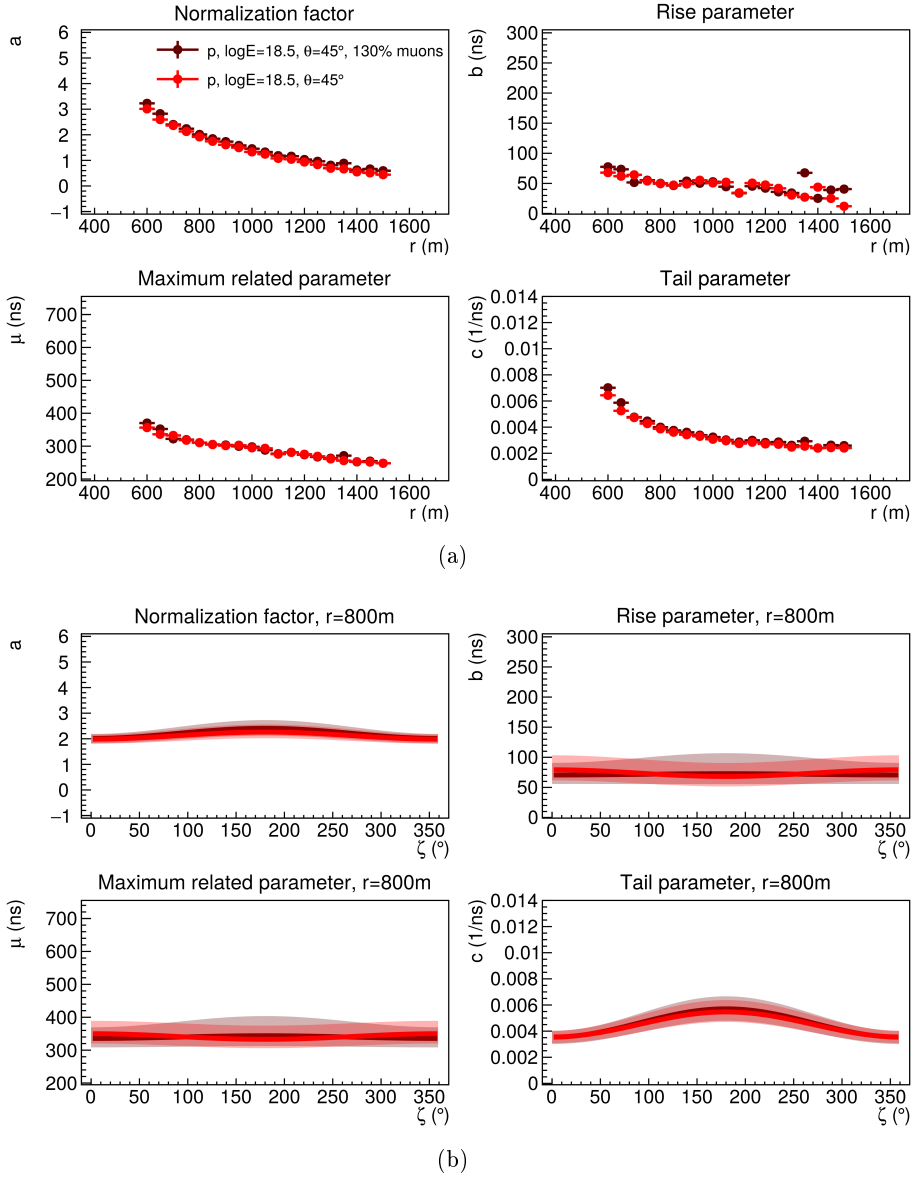


Figure 7.20.: TPDF parameters as functions of r (a) and ζ (b) for EAS simulations of default and artificially increased number of muons. In both cases 1 non-thinned simulation is used with proton primary, $E = 10^{18.5}$ eV, $\theta = 45^\circ$, EPOS and FLUKA models and CORSIKA version 7.4005. Note that the results in (a) and (b) were built differently and therefore cannot be compared directly.

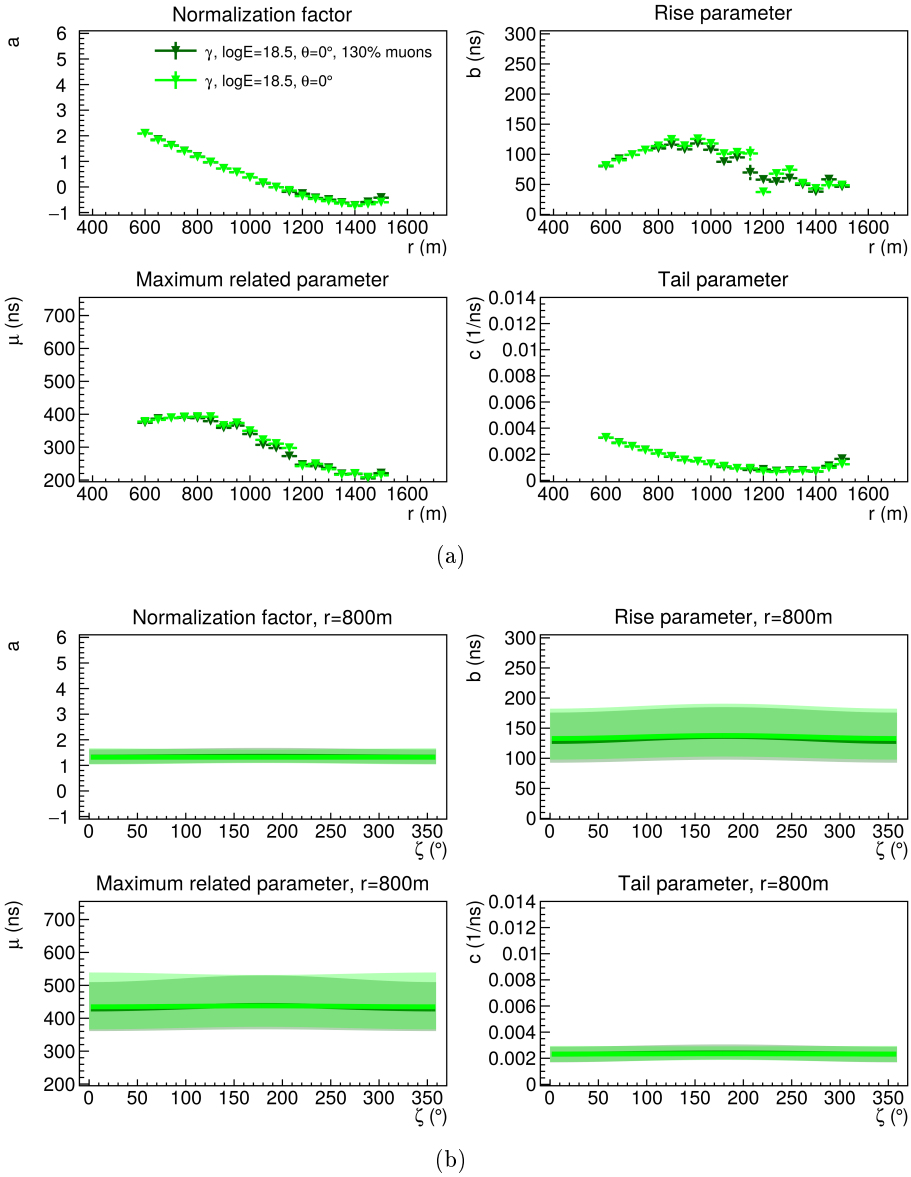


Figure 7.21.: TPDF parameters as functions of r (a) and ζ (b) for EAS simulations of default and artificially increased number of muons. In both cases 1 non-thinned simulation is used with gamma primary, $E = 10^{18.5}$ eV, $\theta = 0^\circ$, EPOS and FLUKA models and CORSIKA version 7.5600. Note that the results in (a) and (b) were built differently and therefore cannot be compared directly.

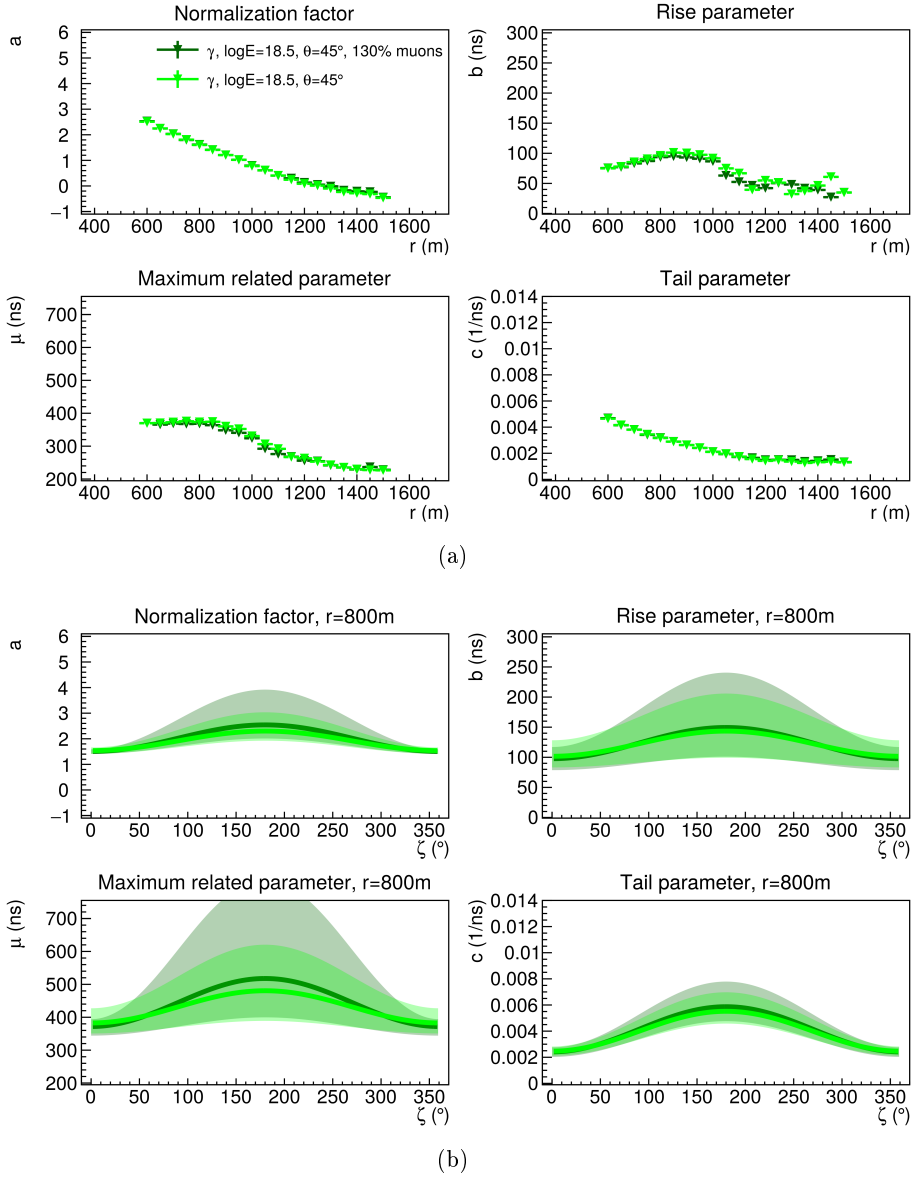


Figure 7.22.: TPDF parameters as functions of r (a) and ζ (b) for EAS simulations of default and artificially increased number of muons. In both cases 1 non-thinned simulation is used with gamma primary, $E = 10^{18.5}$ eV, $\theta = 45^\circ$, EPOS and FLUKA models and CORSIKA version 7.5600. Note that the results in (a) and (b) were built differently and therefore cannot be compared directly.

7.7. Thinning impact

The thinning algorithm (Section 4.1.1) and the resampling (dethinning) procedure (Section 4.2.1) used by the detector simulation add other sources of uncertainties in the simulated SD signal. It was shown that the number of particles after the resampling matches the number of particles in the non-thinned air shower simulation [102], although the impact on the shape of the SD signal was not studied.

As the TPDF function takes into account the structure within the air shower time development folded with the detector response the thinning and especially the dethinning procedure could cause distortions in the TPDF parameters, even though they reproduce the same number of particles. This analysis is crucial for the decision whether the thinned air shower simulations provide the same results as the non-thinned ones and therefore can be used for the search for UHEGR. In addition, the non-thinned simulations of air showers are studied to verify the proper SD station signal simulation on the thinned ones.

For three sets of simulation parameters, one each for proton, iron and gamma primary, at least 10 non-thinned EAS simulations are available. All of these are simulated with $E = 10^{18.5}$ eV and $\theta = 45^\circ$, using the EPOS and FLUKA interaction models. For simulated EAS with proton and iron primaries CORSIKA version 7.4005 was used and in case of a gamma primary version 7.5600. The results of the comparison between the TPDF model parameters based on these 10 non-thinned EAS simulations per primary particle and their 10 thinned counterparts, generated with thinning level of $\varepsilon_{thin} = 10^{-6}$ are displayed in Figures 7.23, 7.24 and 7.25 separately for the three different primaries.

In general a good agreement for all three primaries was found. Only the ζ graphs (b) for gamma induced EAS show some differences, mostly in the late region ($\zeta = 180^\circ$). These can be explained by the low number of muons in the SD stations and the amplifying effect of the thinning procedure on this fact.

During the simulation of the non-thinned air showers several problems have been found and solved, like the bug with several air shower cores in the footprint. Unfortunately, there are still remaining issues that have not been fixed, like the energy loss bug. Between thinned and non-thinned simulations created with CORSIKA version 7.4005 large differences of the

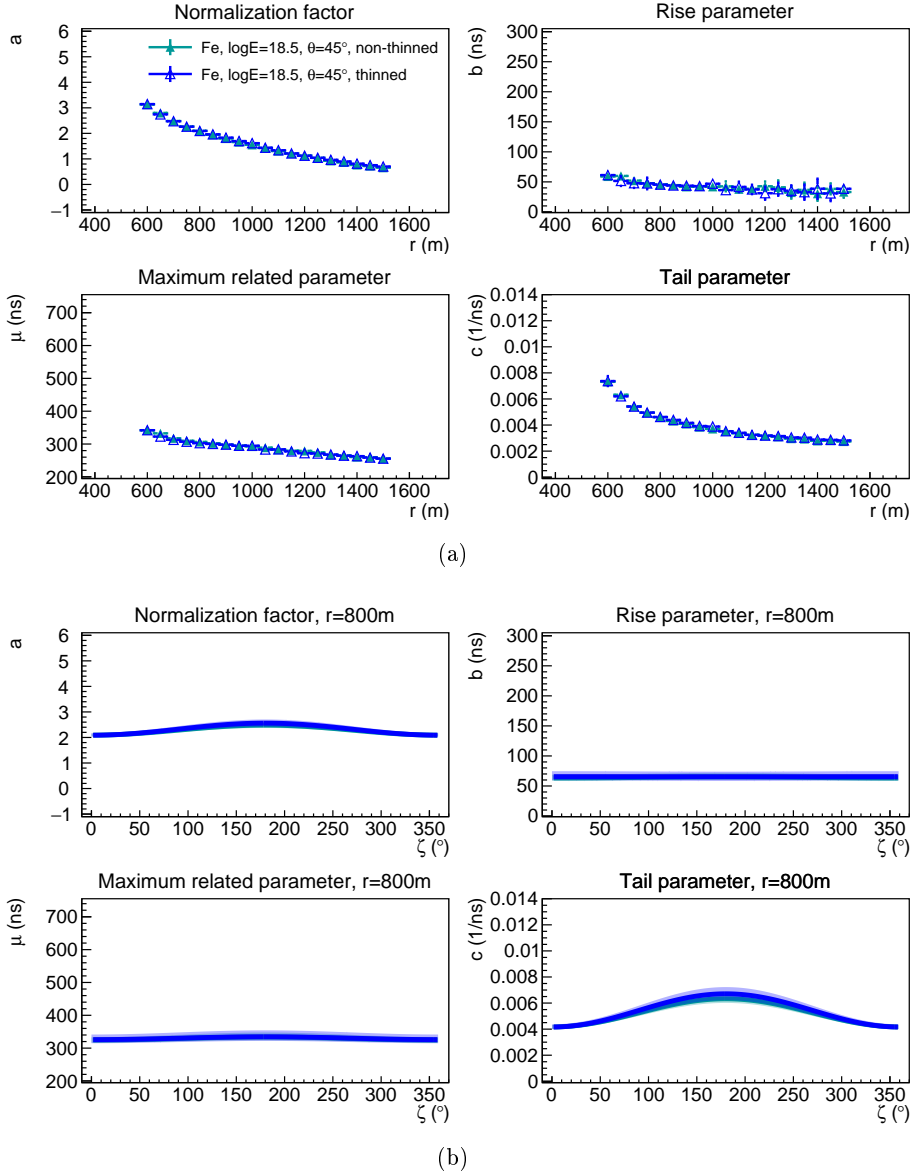


Figure 7.23.: TPDF parameters as functions of r (a) and ζ (b) for air shower simulations with and without thinning. 10 thinned and 10 non-thinned simulations are used with iron primary, $E = 10^{18.5}$ eV, $\theta = 45^\circ$, EPOS and FLUKA models and CORSIKA version 7.4005. Note that the results in (a) and (b) were built differently and therefore cannot be compared directly.

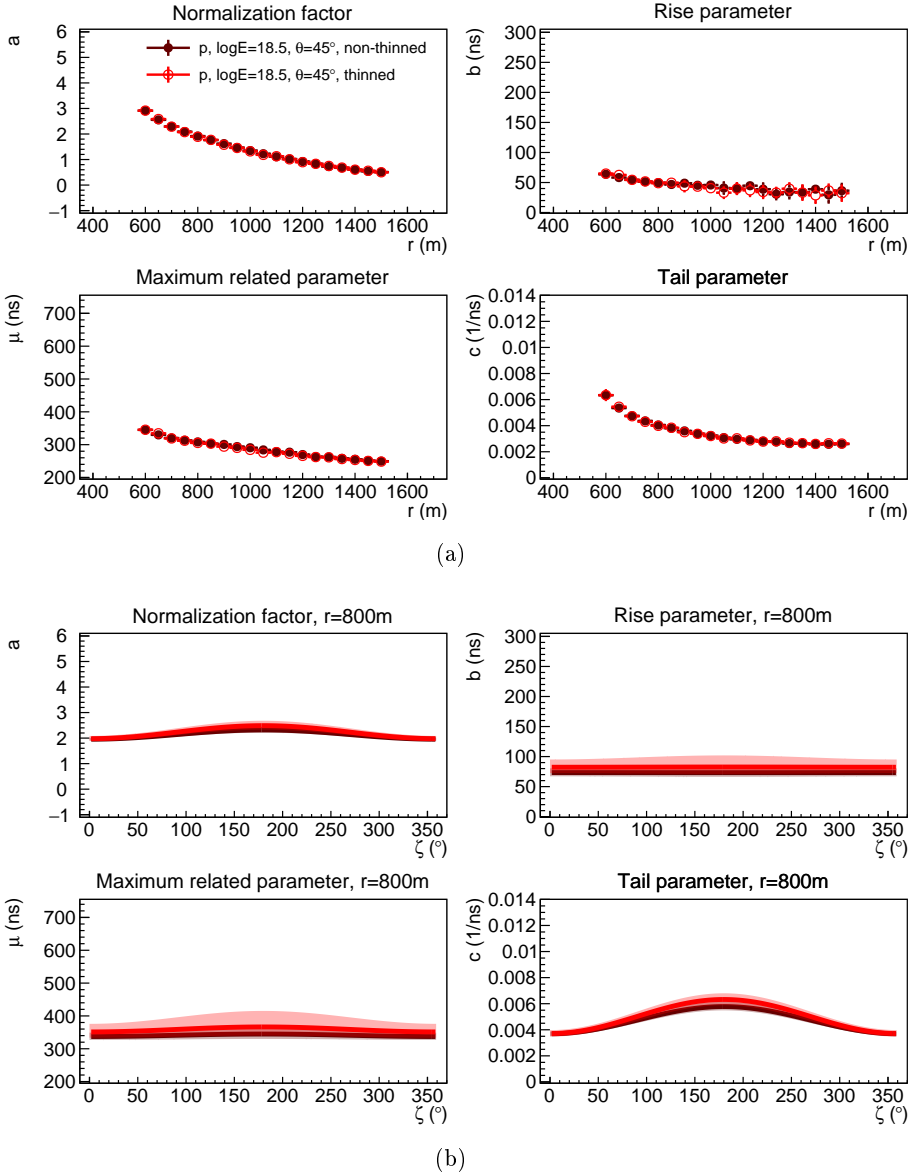


Figure 7.24.: TPDF parameters as functions of r (a) and ζ (b) for air shower simulations with and without thinning. 10 thinned and 10 non-thinned simulations are used with proton primary, $E = 10^{18.5}$ eV, $\theta = 45^\circ$, EPOS and FLUKA models and CORSIKA version 7.4005. Note that the results in (a) and (b) were built differently and therefore cannot be compared directly.

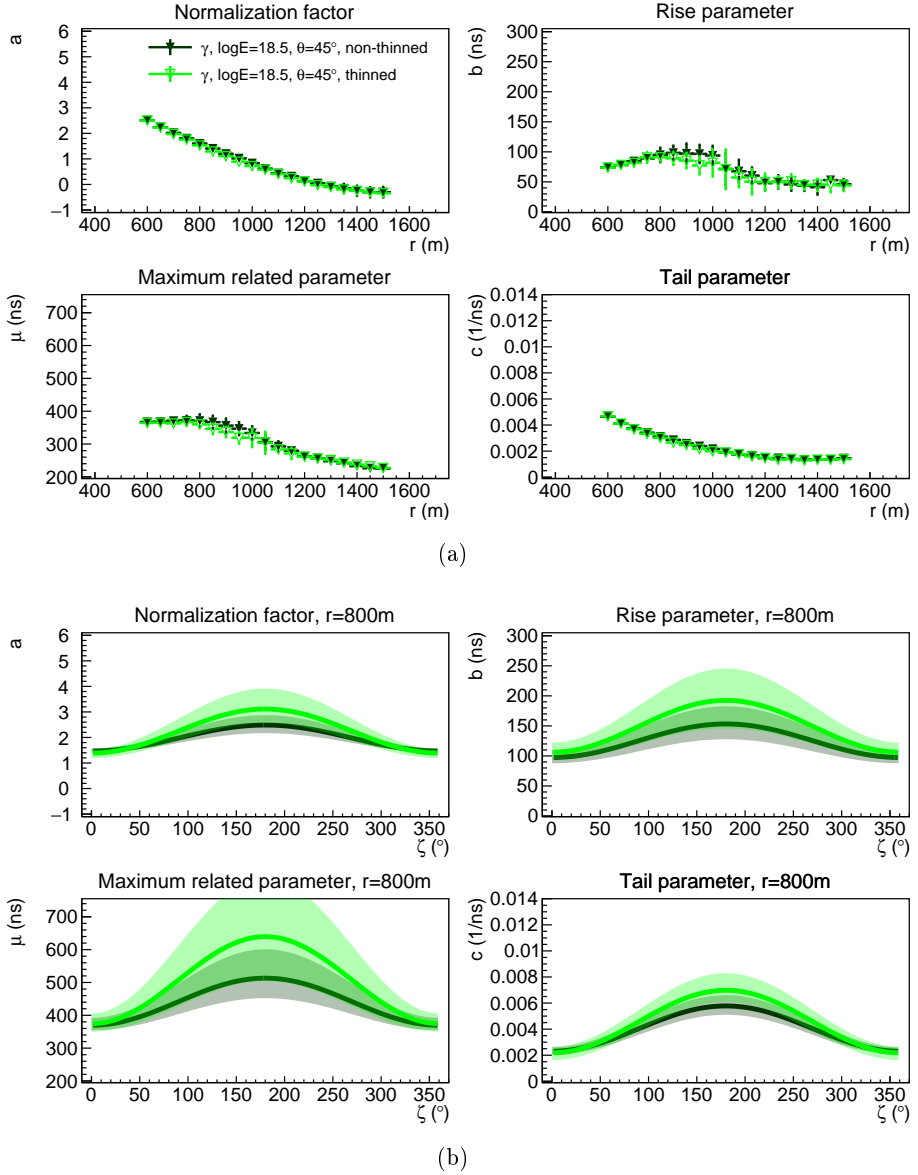
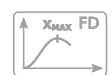


Figure 7.25.: TPDF parameters as functions of r (a) and ζ (b) for air shower simulations with and without thinning. 10 thinned and 10 non-thinned simulations are used with gamma primary, $E = 10^{18.5}$ eV, $\theta = 45^\circ$, EPOS and FLUKA models and CORSIKA version 7.5600. Note that the results in (a) and (b) were built differently and therefore cannot be compared directly.

signal heights were found, as shown in Figure 7.26. These differences in the signal height of the maximum were found in several simulations using proton and iron primaries. Note that no gamma primaries were simulated using the older CORSIKA version. Table 7.1 summarizes when this signal height difference was seen. The discrepancy of a factor of 2-3 was found for all distances to the air shower axis of the affected simulations, although the difference decreases for larger distances.



Primary	$\log(E/\text{eV})$	$\theta(^{\circ})$	high-energy interaction model	Height difference between thinned and non-thinned EAS
iron	18	0	EPOS	no
iron	18	15	EPOS	no
iron	18	30	EPOS	no
iron	18	45	EPOS	no
iron	18	60	EPOS	yes
iron	18.5	0	EPOS	yes
iron	18.5	30	EPOS	yes
iron	18.5	45	EPOS	no
iron	18.5	45	QGSII	yes
iron	18.5	60	EPOS	yes
iron	19	30	EPOS	no
proton	18	0	EPOS	no
proton	18	15	EPOS	no
proton	18	30	EPOS	no
proton	18	45	EPOS	no
proton	18	60	EPOS	no
proton	18.5	0	EPOS	yes
proton	18.5	30	EPOS	yes
proton	18.5	45	EPOS	no
proton	18.5	45	QGSII	no
proton	18.5	60	EPOS	yes
proton	19	30	EPOS	no

Table 7.1.: Sets of simulated EAS done with CORSIKA version 7.4005 where both the thinned and non-thinned simulations are available for the comparison.

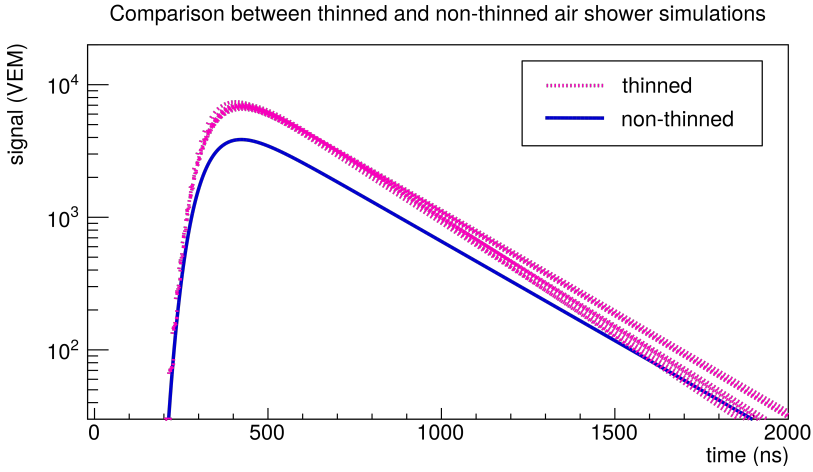


Figure 7.26.: TPDF results from fits of time trace sums (360 SD stations) at 800 m to air shower axis obtained using 10 thinned (violet dotted lines) and 1 non-thinned (blue solid line) EAS simulations, with iron primary, $E = 10^{18.5}$ eV, $\theta = 30^\circ$, CORSIKA version 7.4005 and EPOS and FLUKA models.

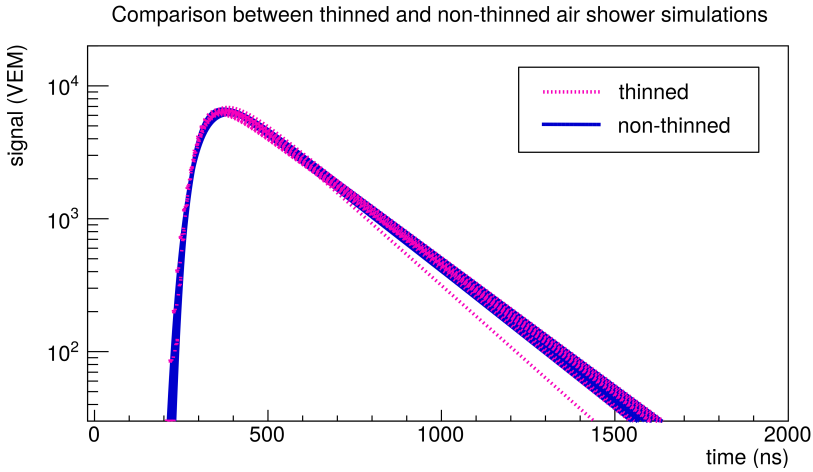
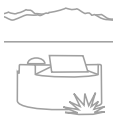
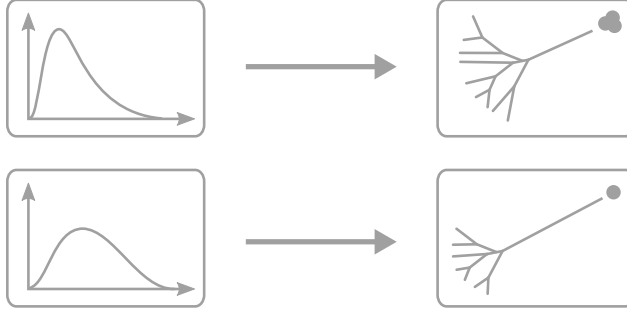


Figure 7.27.: TPDF results from fits of time trace sums (360 SD stations) at 800 m to air shower axis obtained using 10 thinned (violet dotted lines) and 10 non-thinned (blue solid lines) EAS simulations, with iron primary, $E = 10^{18.5}$ eV, $\theta = 45^\circ$, CORSIKA version 7.4005 and EPOS and FLUKA models.

The origin of these differences are the smaller SD signals that are generated by the GEANT4 simulations, which indicates that during the propagation of the particles from simulated EAS through the air some energy was lost, beyond what was expected. This is a bug that affects only the non-thinned simulations and can be inferred from the comparison between time traces for EAS using the same simulation parameters but different inclinations of e.g. $\theta = 30^\circ$ and 45° (Figures 7.26 and 7.27). The TPDF obtained from the one non-thinned air shower at the lower inclination angle (30°) shows a much lower maximum compared to the one obtained from the thinned air showers. The TPDF results from both the non-thinned and the thinned air shower simulations with higher inclination angles (45°) are in a good agreement. Due to the fact that the lower maximum from the one non-thinned simulation at $\theta = 30^\circ$ (Figure 7.26) is even lower compared to the one obtained from non-thinned EAS simulation at 45° (Figure 7.27), it can be concluded that something for the $\theta = 30^\circ$ non-thinned simulation went wrong. It should be stressed that for CORSIKA version 7.5600 no such differences were found.

Due to this bug, the EAS simulations done with CORSIKA version 7.4005 and the TPDF models based on these simulations will not be used for the application on data. Unfortunately, there is only a small number of non-thinned air shower simulations available with the newer CORSIKA version 7.5600, therefore only the thinned simulations will be used in the next steps. However, as was shown, this makes little difference for the final analysis.





Evaluation of the TPDF models

Once the TPDF models are created, they are evaluated to define the testing ranges and to test their discrimination power for the identification of specific primary particles using simulated air showers.

8.1. Correction of the reconstructed energy

For probing the nature of cosmic rays, a proper TPDF model for each primary particle type has to be chosen, depending on the total calorimetric energy E and the inclination angle θ of the air shower axis of the investigated EAS. The inclination angle can be used directly from the reconstruction as its value is quite precise, however the reconstructed total energy has to be corrected. The reconstruction of the air shower parameters through Offline (Section 3.4.1) are performed using the assumption that the air shower was initiated by a hadron. While this is true for most air showers, the development and the longitudinal profile of an air shower initiated by a gamma differ from the ones with a hadron primary. This leads to incorrect fit results and wrongly reconstructed air shower parameters of gamma induced EAS.

The inclination angle θ is calculated from the time differences and orientations of the triggered SD stations (Section 3.4.1), with the additional aid of the FD data, when available. Using a wrong assumption of the lon-

gitudinal profile, e.g. from an iron and not a gamma initiated air shower simulation, has no significant impact on the calculated inclination angle.

The total calorimetric energy is calculated from the signals of the triggered SD stations and the results of the θ reconstruction. The signal strengths depend on the air shower development. As can be seen in Figure 5.1 air showers with gamma primaries are narrower compared to those initiated by protons or iron and have a significantly smaller muon content. This leads to a wrong total energy estimation by Offline.

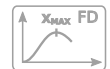
For both simulated air showers and data the reconstructed total energy will be corrected by a factor determined from this study, separately for each primary particle assumption. This corrected energy is used to determine the TPDF models that are subsequently used to probe the primary particle type of the air showers.

To investigate the discrepancy between the reconstructed total energy by Offline of the simulations with the same configuration as at the Pierre Auger Observatory and the corresponding true energy of the air shower simulations, their quantities are compared for iron, proton and gamma primaries and inclination angles $\theta = 0^\circ, 15^\circ, 30^\circ, 45^\circ$ and 60° . The results are shown in Figures 8.1, 8.2 and 8.3. For each point the value and the uncertainty are calculated for 40 random SD grid configurations with the smallest distance to the air shower axis of the closest SD station of 500m for 40 thinned air shower simulations: 10 each for 2 different high-energy hadronic interaction models and 2 different CORSIKA versions (Section 4.3). For every set of simulated primary particle, energy and inclination angle in total 1600 air shower reconstructions have been analyzed. For some inclination angles, e.g. $\theta = 0^\circ$, and especially at low energies of 10^{18} eV not all SD grid configurations could be reconstructed, e.g. due to missing trigger signals.

All energy evaluation graphs were fitted with a straight line going through the origin. The slope of the fit function indicates how much the reconstructed total energy differs from the simulated one and will be used as the *energy correction factor*:

$$\kappa_E = \frac{E_{rec}}{E_{sim}} \quad . \quad (8.1)$$

For air shower simulations with an iron primary κ_E decreases with the inclination angle from 0.94 ± 0.07 at $\theta = 0^\circ$ to 0.86 ± 0.06 at $\theta = 60^\circ$. The energies for simulated EAS induced by protons are reconstructed



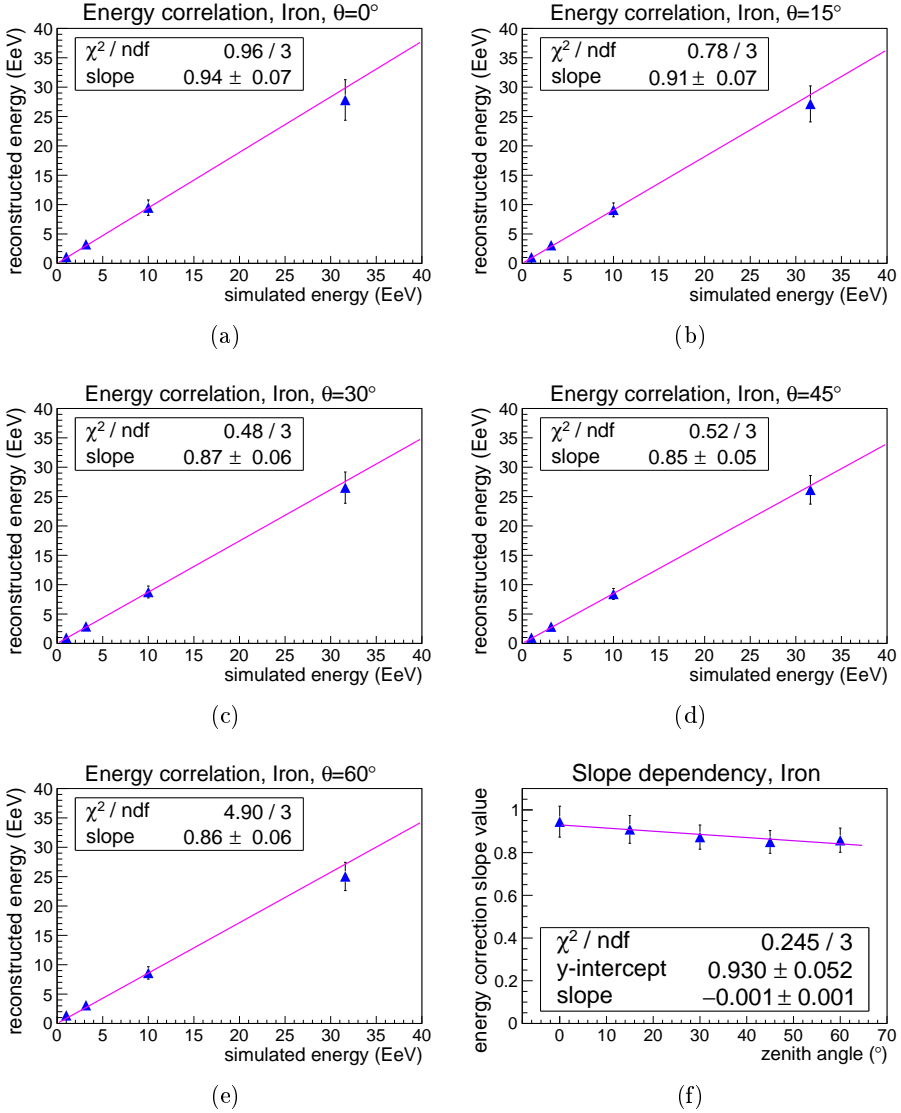


Figure 8.1.: Correlation between simulated and reconstructed energies for EAS simulations with iron primary, $E_{sim} = 10^{18}$ eV, $10^{18.5}$ eV, 10^{19} eV and $10^{19.5}$ eV and $\theta_{sim} = 0^\circ$ (a), 15° (b), 30° (c), 45° (d) and 60° (e), fitted with a straight line going through the origin. The dependence of the slope on the inclination angle θ (f), fitted by another straight line.

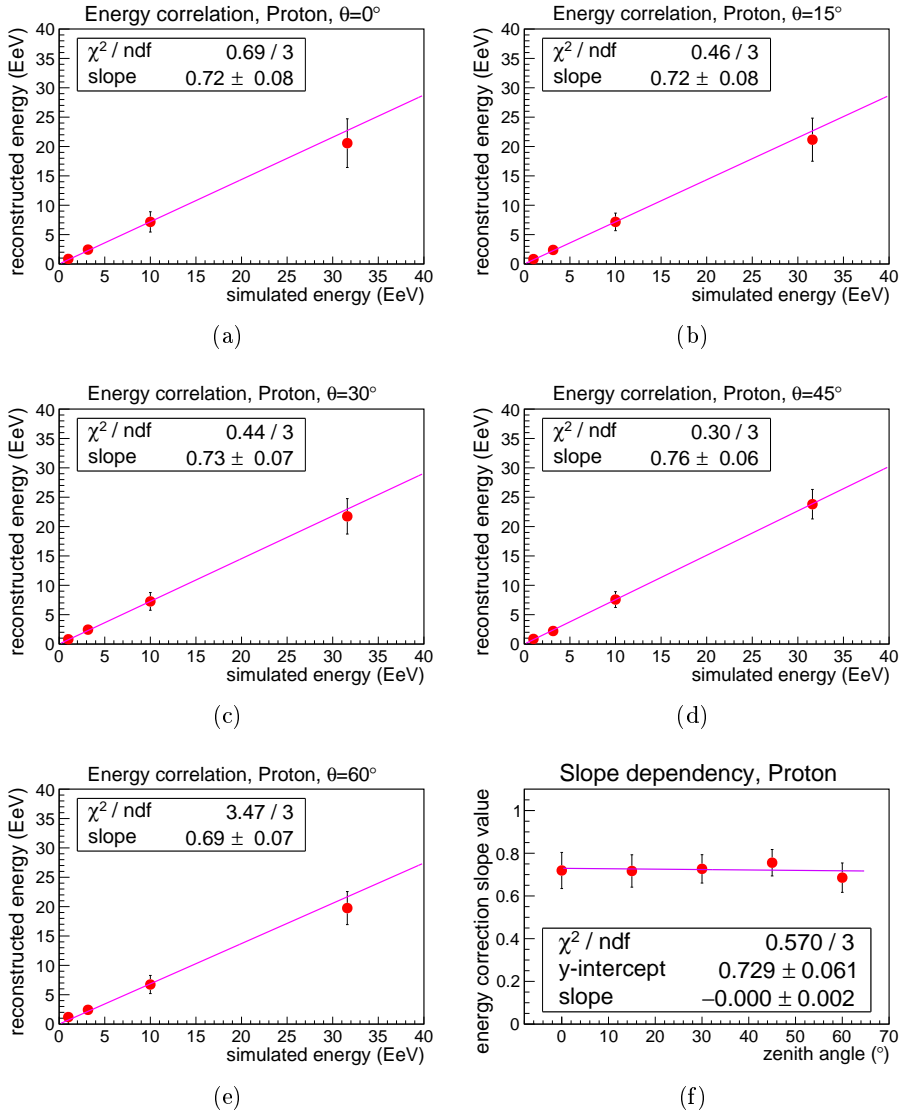


Figure 8.2.: Correlation between simulated and reconstructed energies for EAS simulations with proton primary, $E_{sim} = 10^{18} \text{ eV}$, $10^{18.5} \text{ eV}$, 10^{19} eV and $10^{19.5} \text{ eV}$ and $\theta_{sim} = 0^\circ$ (a), 15° (b), 30° (c), 45° (d) and 60° (e), fitted with a straight line going through the origin. The dependence of the slope on the inclination angle θ (f), fitted by another straight line.

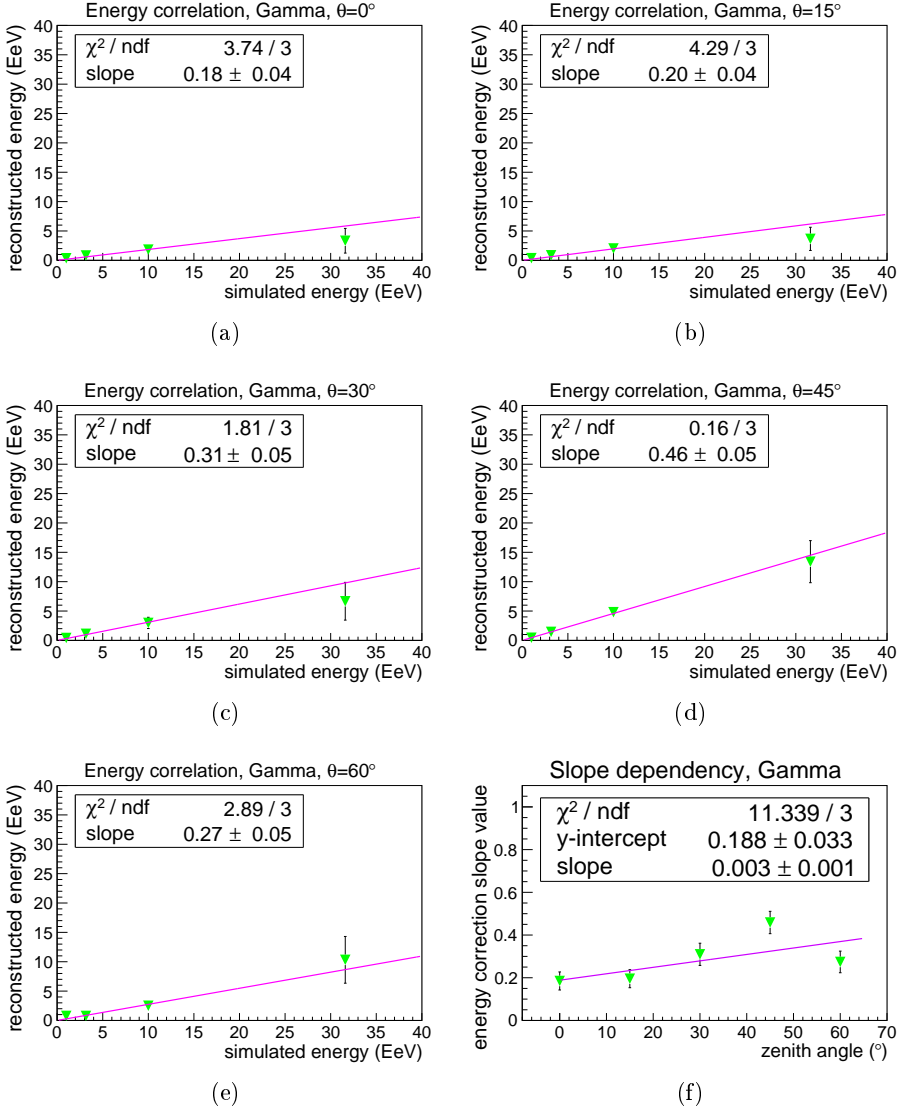


Figure 8.3.: Correlation between simulated and reconstructed energies for EAS simulations with gamma primary, $E_{sim} = 10^{18}$ eV, $10^{18.5}$ eV, 10^{19} eV and $10^{19.5}$ eV and $\theta_{sim} = 0^\circ$ (a), 15° (b), 30° (c), 45° (d) and 60° (e), fitted with a straight line going through the origin. The dependence of the slope on the inclination angle θ (f), fitted by another straight line.

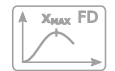
with correction factors around 0.70 for all inclination angles. The biggest discrepancy between the simulated and reconstructed total energies can be found for air shower simulations initiated by gamma primaries. The estimated energies are for all inclination angles below the half of the simulated energies, and their ratio vary from the smallest value for $\theta = 0^\circ$ with $\kappa_E = 0.18 \pm 0.04$ up to 0.46 ± 0.05 at $\theta = 45^\circ$.

As the calibration for the energy reconstruction varies with the inclination angle, an estimation for each angle is made for each primary particle. The inclination angle dependence is parametrized with a straight line (Figures 8.1(f), 8.2(f) and 8.3(f)). When comparing an air shower to a TPDF model for each particle type the reconstructed inclination angle is first used to calculate the corrected total energy separately for each model. In the next step the applicable TPDF models are determined based on the reconstructed inclination angle and the corrected energy. This means that the reconstructed energy of an air shower will be much higher for the gamma than for the hadron primary particle hypothesis.

8.2. Signal strength and number of triggered SD stations

While the reconstruction procedure by Offline requires that the total signal of a SD station is above 3 VEM, the TPDF models were created from simulated SD stations with a total signal above 5 VEM (Section 6.2). This restriction prevents problems coming from spiky time traces, but limits the distance range to the air shower axis up to where enough SD stations can be reconstructed with a signal strength above this threshold. At some distances to the air shower axis, depending on the primary particle type, energy and inclination angle, only a few out of the 360 SD stations simulated for the TPDF models are above this limit. This effect could distort the ζ function fit. Therefore, when testing an air shower, only SD stations within distances to the air shower axis where at least 180 simulated SD stations of the TPDF models with a signal above 5 VEM could be reconstructed will be used.

To study at which distances at least half of the simulated SD stations is reconstructed, the efficiency of the SD stations above the 5 VEM threshold is displayed in Figures 8.4, 8.5, 8.6 and 8.7 for each ring in the air shower plane of the TPDF models. This is done for each simulation energy and



inclination angle separately. The distance range of the rings was chosen between 575 m and 1525 m from the air shower axis using a ring width of 50 m (Section 6.2). In each ring the simulated SD stations were placed at the mean distance, e.g. at 600 m for the ring between 575 m and 625 m.

When comparing the different particle types, it should be noted that the energy of the gamma TPDF models is 3 times higher than that of protons and iron in Figures 8.4, 8.5 and 8.6. This approximately compensates the discrepancy between the reconstructed and the corrected energies (Section 8.1). As a consequence the inclination angle behavior of the efficiency is different for gamma initiated EAS compared to the ones with hadronic primaries.

Figure 8.4 shows the probability for a SD station to have a signal S at 5 VEM or higher, using simulations with $E = 10^{18}$ eV for proton (red circles) and iron (blue upward triangles) and $E = 10^{18.5}$ eV for gamma (green downward triangles) primaries. The four upper graphs (a) to (d) displaying the different inclination angles of the EAS up to $\theta = 45^\circ$ reveal that over half of all SD stations in each ring are successfully reconstructed ($S \geq 5$ VEM) up to a distance r of 825 m from the air shower axis, including the ring width. At smaller distances nearly all of the simulated SD stations in each ring can be reconstructed. After 825 m a steep decrease follows, ending at around 1225 m, where only a few SD stations have a signal above 5 VEM. In case of an inclination angle of $\theta = 60^\circ$, Figure 8.4(e), not even at the smallest available distances all SD stations could be successfully reconstructed.

In Figure 8.5 the number of successfully reconstructed stations with $S \geq 5$ VEM is shown for EAS simulations with energies of $E = 10^{18.5}$ eV for proton and iron and $E = 10^{19}$ eV for gamma primaries. The steep decrease starts at higher distances r to the air shower axis. For all EAS simulations up to $\theta = 45^\circ$ at least the half of all SD stations have a signal above 5 VEM up to 1025 m. For simulated air showers with $\theta = 60^\circ$ this is true up to 975 m.

Figure 8.6 shows the results for EAS simulations with energies of $E = 10^{19}$ eV for proton and iron and $E = 10^{19.5}$ eV for gamma primaries. It is clearly shown that the efficiency as function of distance to the air shower axis depends on the primary particle type. The number of successfully reconstructed SD stations is above half of all SD stations in the rings for at least up to 1175 m and is limited for the gamma initiated EAS simulations, even though they were simulated with a higher energy.

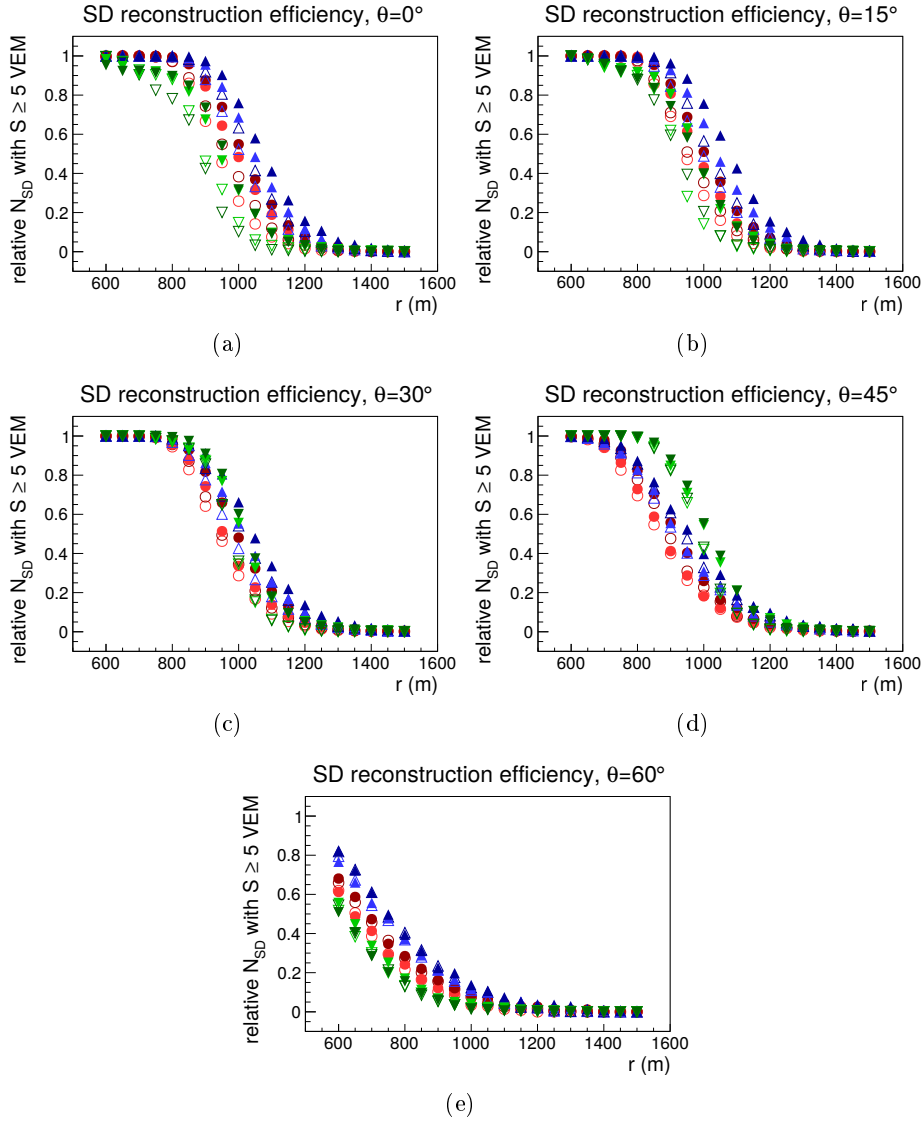


Figure 8.4.: Reconstruction efficiency of SD stations with a signal above 5 VEM as function of r for $\theta = 0^\circ$ (a), 15° (b), 30° (c), 45° (d) and 60° (e). Each graph contains points from 4 TPDF models per primary with $E = 10^{18}$ eV (gamma: $E = 10^{18.5}$ eV), EPOS (darker colors) and QGSJet (lighter colors) models and CORSIKA versions 7.4005 (open markers) and 7.5600 (full markers). Proton EAS in red, iron in blue and gamma in green.

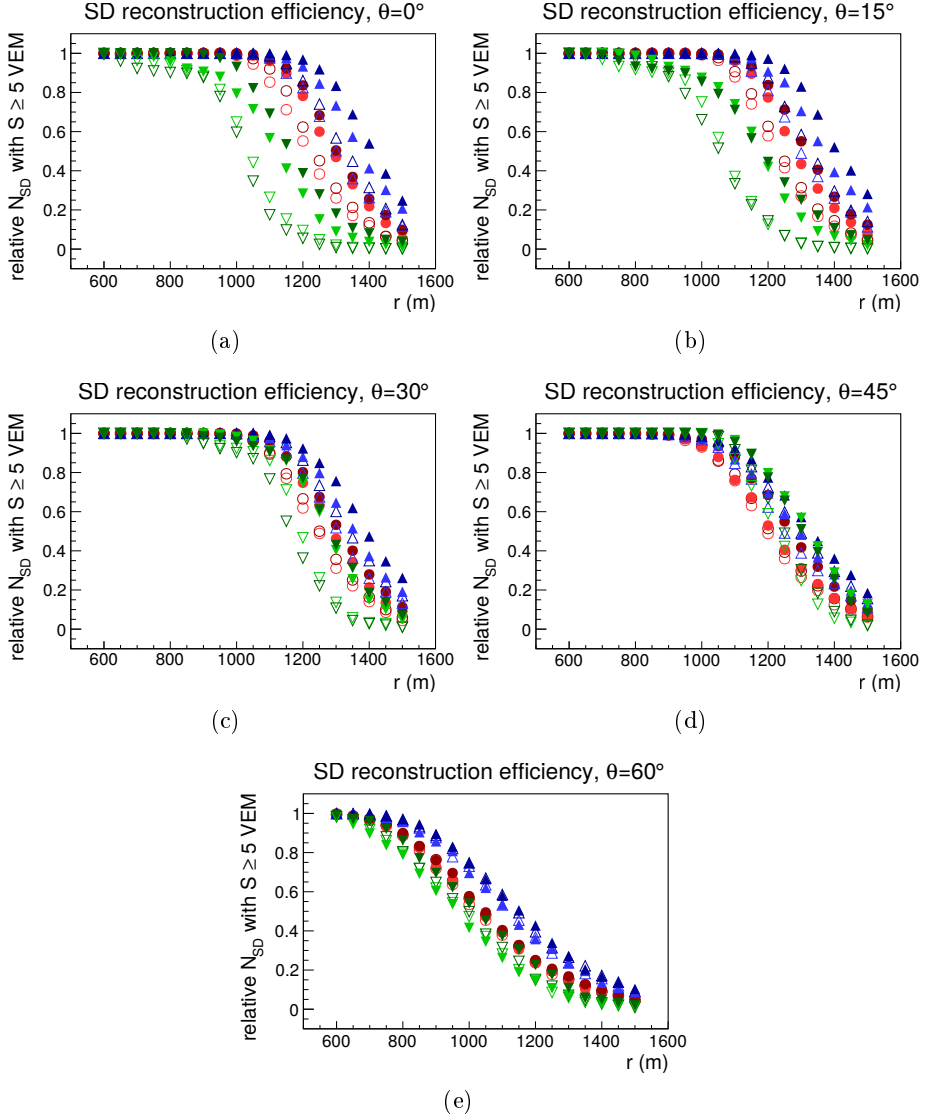


Figure 8.5.: Reconstruction efficiency of SD stations with a signal above 5 VEM as function of r for $\theta = 0^\circ$ (a), 15° (b), 30° (c), 45° (d) and 60° (e). Each graph contains points from 4 TPDF models per primary with $E = 10^{18.5}$ eV (gamma: $E = 10^{19.0}$ eV), EPOS (darker colors) and QGSJet (lighter colors) models and CORSIKA versions 7.4005 (open markers) and 7.5600 (full markers). Proton EAS in red, iron in blue and gamma in green.

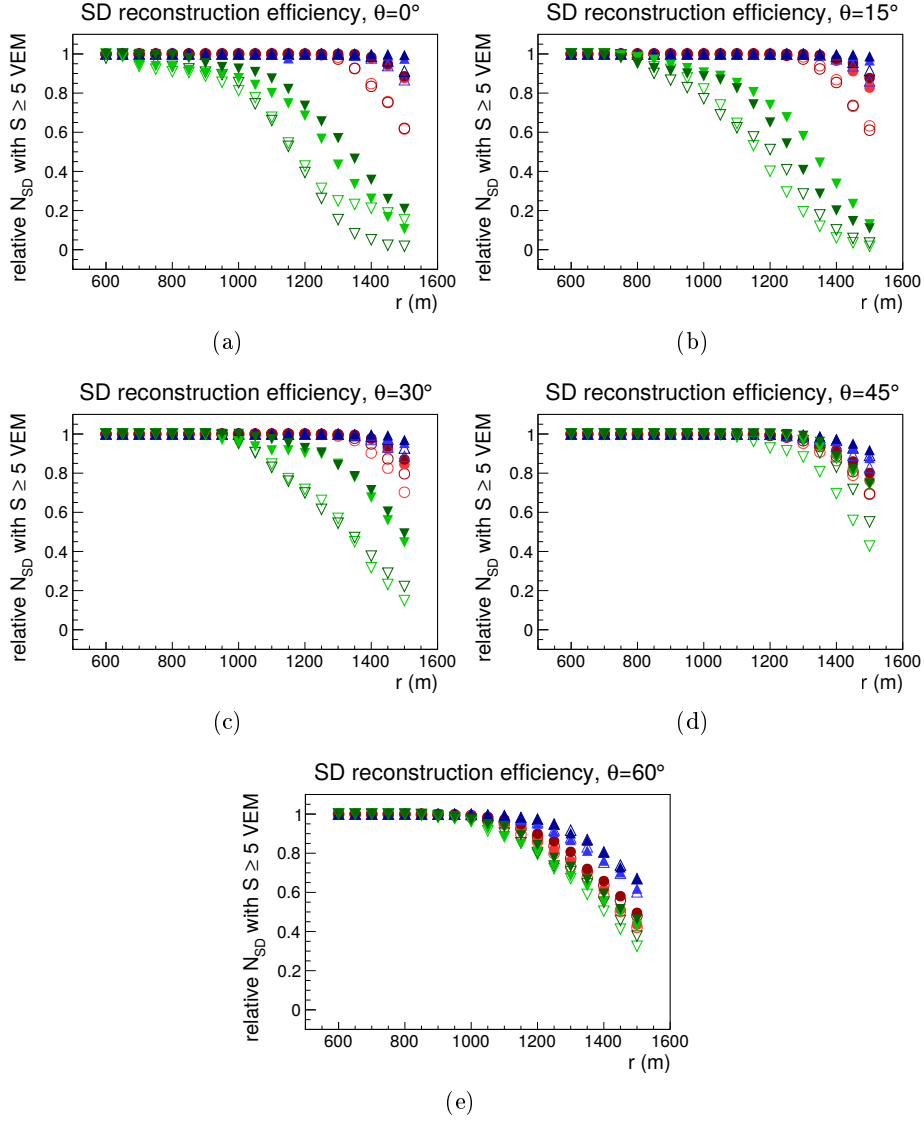


Figure 8.6.: Reconstruction efficiency of SD stations with a signal above 5 VEM as function of r for $\theta = 0^\circ$ (a), 15° (b), 30° (c), 45° (d) and 60° (e). Each graph contains points from 4 TPDF models per primary with $E = 10^{19.0}$ eV (gamma: $E = 10^{19.5}$ eV), EPOS (darker colors) and QGSJet (lighter colors) models and CORSIKA versions 7.4005 (open markers) and 7.5600 (full markers). Proton EAS in red, iron in blue and gamma in green.

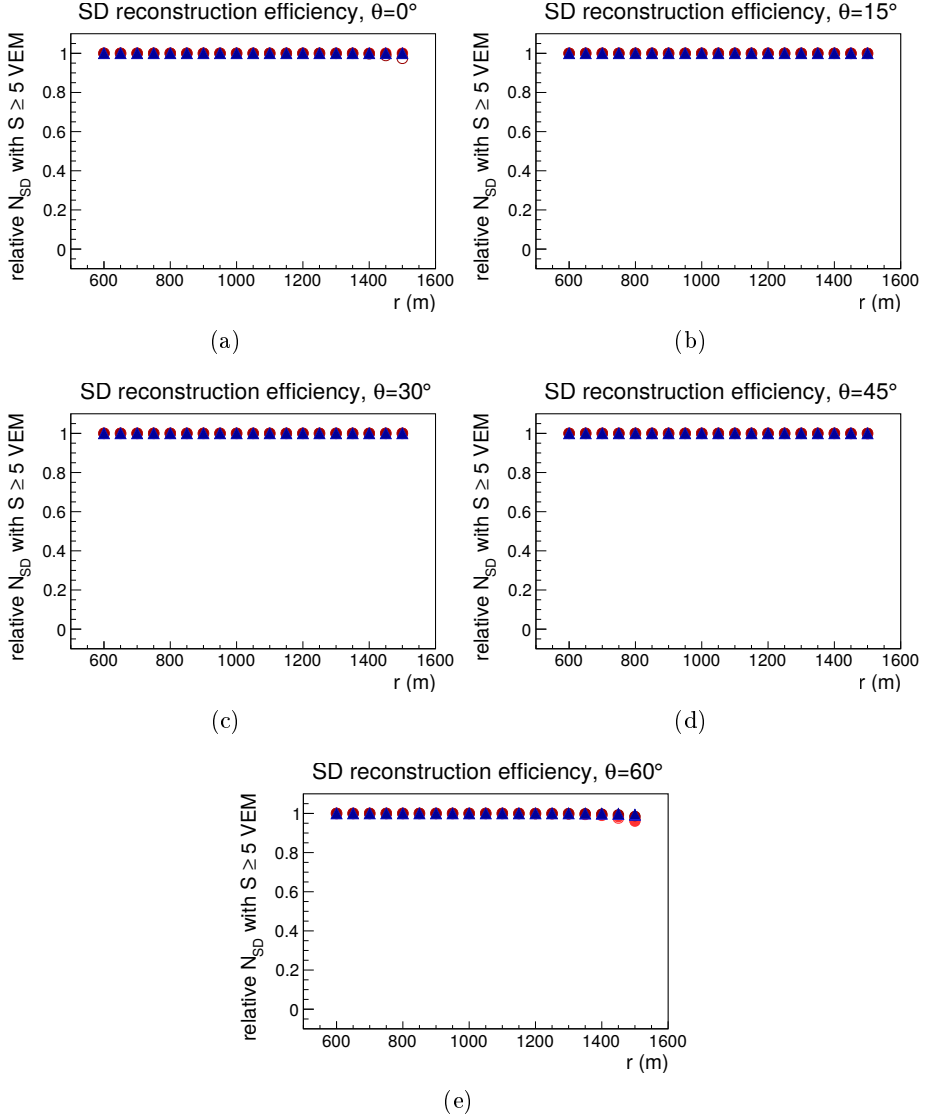


Figure 8.7.: Reconstruction efficiency of SD stations with a signal above 5 VEM as function of r for $\theta = 0^\circ$ (a), 15° (b), 30° (c), 45° (d) and 60° (e). Each graph contains points from 4 TPDF models per primary with $E = 10^{19.5}$ eV, EPOS (darker colors) and QGSJet (lighter colors) models and CORSIKA versions 7.4005 (open markers) and 7.5600 (full markers). Proton EAS in red and iron in blue.

For TPDF models with proton and iron primaries at least half of all simulated SD stations were reconstructed with $S \geq 5$ VEM for all available distances r and all inclination angles.

Finally, Figure 8.7 displays the results for EAS simulations with energy of $E = 10^{19.5}$ eV for proton and iron primaries. For all distances r to the air shower axis and all inclination angles nearly all simulated SD stations could be successfully reconstructed.

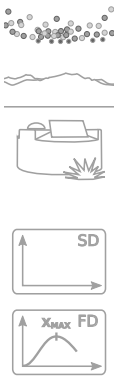
Another detail can be seen in the model dependence of the simulations. For each primary the TPDF models are created with two CORSIKA versions and two high-energy hadronic interaction models. Hence, for each distance r four points for each primary are drawn. The open markers represent the results obtained from simulations with CORSIKA version 7.4005 and the full markers those done with version 7.5600. Especially for simulated EAS with gamma primaries in Figure 8.6 the differences in the efficiencies are visible. The origin for this dependence is most probably the same as described in Section 7.7, the bug in the older CORSIKA version with the loss of some energy during the simulation of the air shower particle propagating through the air. This will be taken into account for the definition of the distance testing region in the next section and, as mentioned before, the TPDF models calculated using EAS simulations that were done with CORSIKA version 7.4005 will not be used for probing the primary particle nature.

8.3. Definition of testing ranges

Based on the results in Section 8.2 a range for the SD station distances to the air shower axis is set to make sure that an accurate prediction of the TPDF parameters was obtained. Therefore, the tested events will be divided into two different sets based on their reconstructed energy.

The first set contains EAS with reconstructed energies between $E = 10^{18}$ eV and $10^{18.5}$ eV. Here, only SD stations between 575 m and 825 m from the air shower axis will be tested. For all distances within this range at least half of all simulated SD stations in the rings were reconstructed for the TPDF models (Figure 8.4). For this set only air showers with a maximum inclination of $\theta = 45^\circ$ are tested. At higher inclination angles the SD station reconstruction efficiency is too small.

The second set of EAS contains those with reconstructed energies between $E = 10^{18.5}$ eV and 10^{19} eV. The upper limit originates from the



maximum energy of the available simulated air showers with gamma primary. The corrected energy in case of a gamma induced EAS with $E_{rec} = 10^{19}$ eV is around $E_{corr} = 10^{19.5}$ eV. The TPDF model fit parameters of such air showers can be compared to the predictions of the TPDF model parameters with $E_{sim} = 10^{19.5}$ eV. The distance range for this set is larger and ranges from 575 m up to 975 m to the air shower axis. The upper bound is limited due to the criteria of SD reconstruction efficiency to be above 50 % by the EAS with $\theta = 60^\circ$ as can be seen in Figure 8.5(e).

8.4. Gamma cut definition

The discrimination power of the TPDF method is tested on new thinned simulations with parameters mentioned in Section 4.3. Per each set of parameters 10 simulations are used. The SD signals of these simulations are used to probe different TPDF models. There are 80 different SD grid configurations created with the randomly chosen air shower core positions and azimuthal angle orientations. 20 each with 2 and with 3 SD stations within the distance ranges to the air shower axis defined for the two event sets in Section 8.3. It should be mentioned here, that especially for air shower simulations with energies less than $10^{18.5}$ eV not all of the detector simulations could be completed due to the small footprint of these air showers.

As the inclination angles are reconstructed quite accurately, all results from the air shower simulations are evaluated for $\theta = 0^\circ, 15^\circ, 30^\circ, 45^\circ$ and 60° . Furthermore, the reconstructions with 2 SD stations within the testing distance range and those with 3 SD stations are analyzed separately. Another division into 2 groups is created based on the reconstructed energy as defined in Section 8.3. The simulation with lower energies $E_{rec} < 10^{18.5}$ eV are only evaluated for θ up to 45° .

In order to test an unknown air shower with respect to the TPDF interpolated models for each of the three primary assumptions (gamma, proton and iron) a χ^2 value is calculated:

$$\chi^2 = \sum_{i=1}^n \frac{(S_{SD,i} - S_{TPDF,i})^2}{\sigma_{TPDF,i}^2} \quad , \quad (8.2)$$

with the reconstructed signal of the i -th time trace bin $S_{SD,i}$, the prediction of the TPDF model $S_{TPDF,i}$ and the uncertainty $\sigma_{TPDF,i}$, defined by

the TPDF confidence interval, as shown in Figure 6.5. The calculation of χ^2 is done for n bins of the signal trace with 25 ns sampling within the time range between 250 ns and 1500 ns. The uncertainties of the measured signal values are much smaller than the uncertainties from the TPDF models and therefore are not included in the χ^2 calculations. The lower limit of the time range is set to exclude the offset that is used to monitor whether some part of the signal was missing (Section 5.2). The upper boundary is set to limit the comparison to a region with significant signal values only.

For each χ^2 a probability p is calculated using the number of bins ($n_{bins} = 51$) minus the number of TPDF parameter ($n_{pars} = 4$). For calculation purposes the values of the probabilities are limited to the range of $-200 \leq \log(p) \leq +200$. The p values for the N SD stations within the defined distance range of one event are all multiplied to obtain the *TPDF model probability* λ for the event to be initiated by one specific primary:

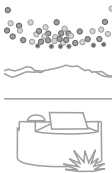
$$\lambda = \prod_{j=1}^N p_j \quad . \quad (8.3)$$

Hence, for each tested air shower three probabilities are obtained describing the compatibility with a gamma, proton and iron induced air shower simulation model. An unknown air shower is deemed to be initiated by a photon when it is compatible with a photon induced EAS model, i.e. when the *gamma TPDF model probability* λ_γ is high, whereas the probabilities for proton and iron primaries (λ_p , λ_{Fe}) are low. As the proton TPDF model prediction compared to the iron prediction is usually closer to the gamma prediction, only the proton and the gamma TPDF model probabilities are used in the following. λ_{Fe} will be displayed only for demonstration purposes.

The efficiency of the TPDF method is studied by dividing λ_γ by the *proton TPDF model probability* λ_p . Due to the small values, the logarithm is taken and the division becomes a subtraction yielding in the *primary particle discrimination variable* $\Lambda_{\gamma,p}$:

$$\Lambda_{\gamma,p} = \log_{10}(\lambda_\gamma) - \log_{10}(\lambda_p) \quad . \quad (8.4)$$

For all available air shower simulations used here this variable is calculated and the results are plotted for different inclination angles, as shown in Figure 8.8 for one simulation data set of kinematic variables. All other



histograms and graphs are provided in Appendix D. Note that there are no results for $E_{rec} < 10^{18.5}$ eV and $\theta \leq 15^\circ$ with $N_{SD} = 3$. This is due to the small upper limit of the distance range of 825 m to the air shower axis that does not allow to trigger 3 SD stations within this distance r for nearly vertical EAS.

The results of $\Lambda_{\gamma,p}$ in upper histograms in Figure 8.8 are colored green for simulations with a gamma primary, those with proton primary are shown in red and those with iron primary are in blue. Based on these histograms the sum graphs are calculated, which are displayed below the histograms. They represent the relative fractions of all $\Lambda_{\gamma,p}$ in the range between $-\infty$ and $\Lambda_{\gamma,p}^{cut}$. The green lines in the sum graphs (lower figures) indicate the *signal efficiencies* ϵ for gamma, while the red (blue) line represents the *background rejection* ρ for proton (iron), when making a cut at the $\Lambda_{\gamma,p}$ value on the horizontal axis. The definitions of ϵ and ρ are:

$$\epsilon = \frac{N_{\gamma}(\Lambda_{\gamma,p} \geq \Lambda_{\gamma,p}^{cut})}{N_{\gamma,all}} \quad (8.5)$$

$$\rho = \frac{N_p(\Lambda_{\gamma,p} < \Lambda_{\gamma,p}^{cut})}{N_{p,all}} \quad , \quad (8.6)$$

with $N_{\gamma}(\Lambda_{\gamma,p} \geq \Lambda_{\gamma,p}^{cut})$ representing all results above a threshold from gamma induced air showers and $N_p(\Lambda_{\gamma,p} < \Lambda_{\gamma,p}^{cut})$ representing all results below a threshold from proton induced EAS of all tested simulations with gamma $N_{\gamma,all}$ and proton primaries $N_{p,all}$.

The left side histogram and graph (a) in Figure 8.8 show the results for simulated EAS with 2 reconstructed SD stations (N_{SD}) and at the right side (b) are those with 3 stations within the distance r to the air shower axis ranges described in Section 8.3. The reconstructed energy interval and the inclination angle θ are written at the upper edge of each histogram and graph. In addition the simulated primary particle type and the number of reconstructed EAS are displayed.

The upper histograms show that for almost all simulated data sets with reconstructed energies below $10^{18.5}$ eV most entries are concentrated towards $\Lambda_{\gamma,p} = 0$. Especially for simulations with a gamma primary this is true. This is a consequence of the wider confidence intervals of the TPDF models at lower energies compared to the higher energies. For higher reconstructed energies ($E_{rec} \geq 10^{18.5}$ eV) the spread in the distributions is

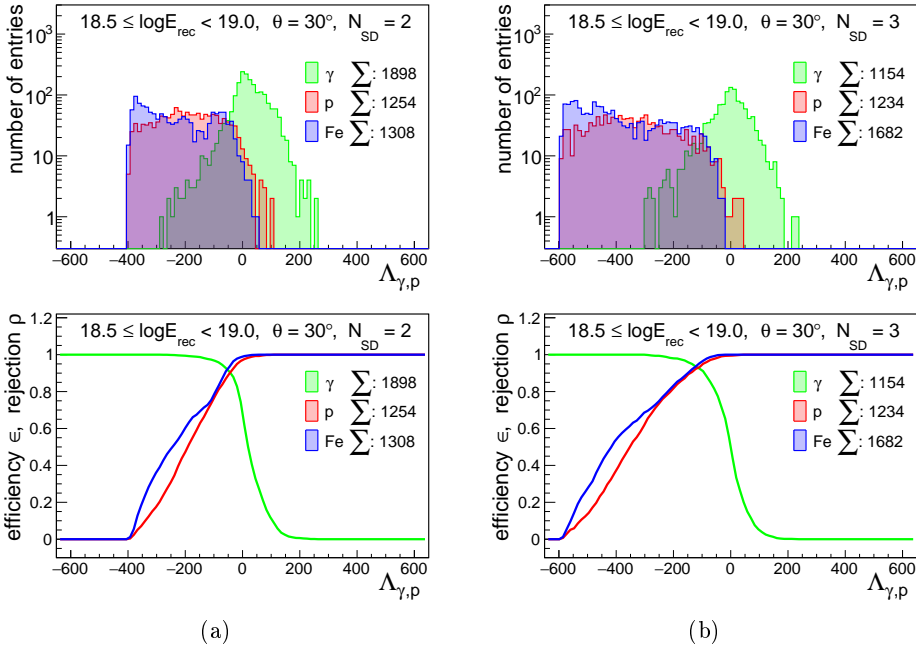


Figure 8.8.: $\Lambda_{\gamma,p}$ histograms for simulated EAS with gamma rays (green), protons (red) and iron nuclei (blue) and the corresponding signal efficiency ϵ for gamma ray EAS with background rejection ρ for proton and iron nucleus induced EAS.

larger and in case of proton and iron air shower simulations more flat or concentrated toward the lower edge. In addition, the signals in the SD stations are higher for more energetic air showers, which create more precise time traces for testing against a TPDF model.

The lower graphs show that the background rejection is above 90% for positive $\Lambda_{\gamma,p}$ for all simulated data sets, except for very inclined EAS with $\theta = 60^\circ$ and E_{rec} above $10^{18.5}$ eV. By defining a threshold at some value of $\Lambda_{\gamma,p}$ the signal efficiency and the background rejection can be obtained directly from the lower graphs. When comparing the left and right histograms it can be seen that the distributions of $\Lambda_{\gamma,p}$ for 3 SD stations are wider. This is due to the additional SD station, which adds another probability.

For a better understanding of how the signal efficiency and background rejection correlate, these two parameters (ϵ and ρ) are plotted one versus

the other in Figures 8.9, 8.10 and 8.11. At the bottom of each graph the energy range, inclination angle and number of SD stations within the testing distance range are displayed. Again, the graphs for lower energies, $N_{SD} = 3$ and $\theta = 0^\circ$ and 15° are missing due to the size of the defined distance range (Section 8.3).

When comparing the background rejections at the same signal efficiency level of e.g. 50% the best rejection is obtained for simulated air showers with $E \geq 10^{18.5}$ eV and $\theta = 30^\circ$, while the lowest background rejection is found for simulations with $E < 10^{18.5}$ eV and $\theta = 45^\circ$. As expected the background rejection at the same signal efficiency level increases with energy and the number of SD stations involved.

Another evaluation of the goodness of the TPDF method is obtained using the *merit factor* η defined as:

$$\eta = \frac{|\mu_\gamma - \mu_p|}{\sqrt{\sigma_\gamma^2 - \sigma_p^2}}, \quad (8.7)$$

with μ_γ and σ_γ^2 as the mean and the uncertainty of $\Lambda_{\gamma,p}$ for simulated EAS with a gamma primary and μ_p and σ_p^2 for simulated EAS with a proton primary. The results are displayed in Figure 8.12.

The merit factors confirm that the distinction between gamma and proton induced air showers works better at higher energies and with more SD stations involved. The best separation power of the TPDF method is at $\theta = 30^\circ$ for high energies between $E = 10^{18.5}$ eV and $10^{19.0}$ eV with both 2 and 3 selected SD stations with merit factors of 1.7 and 2.1, respectively. In general an observable is considered to have a good separation power when the merit factor is above 1.

Several *photon discrimination criteria* (*gamma cuts*) $\Lambda_{\gamma,p}^{cut}$ are defined to test the gamma compatibility of air showers with different purities by setting thresholds of background rejection ρ at 0.8, 0.9, 0.95 and 0.99. The gamma cuts are defined individually for each TPDF model available.

The reconstructed energy E_{rec} of a tested unknown air shower, together with the number of involved SD stations and the reconstructed inclination angle θ_{rec} determine which gamma cuts (at the same ρ level) of the TPDF models with the closest simulation parameters E_{sim} and θ_{sim} are used. As E_{rec} and θ_{rec} will not correspond to the simulated values, conservatively the highest gamma cuts of the selected TPDF models are used.

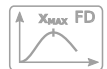
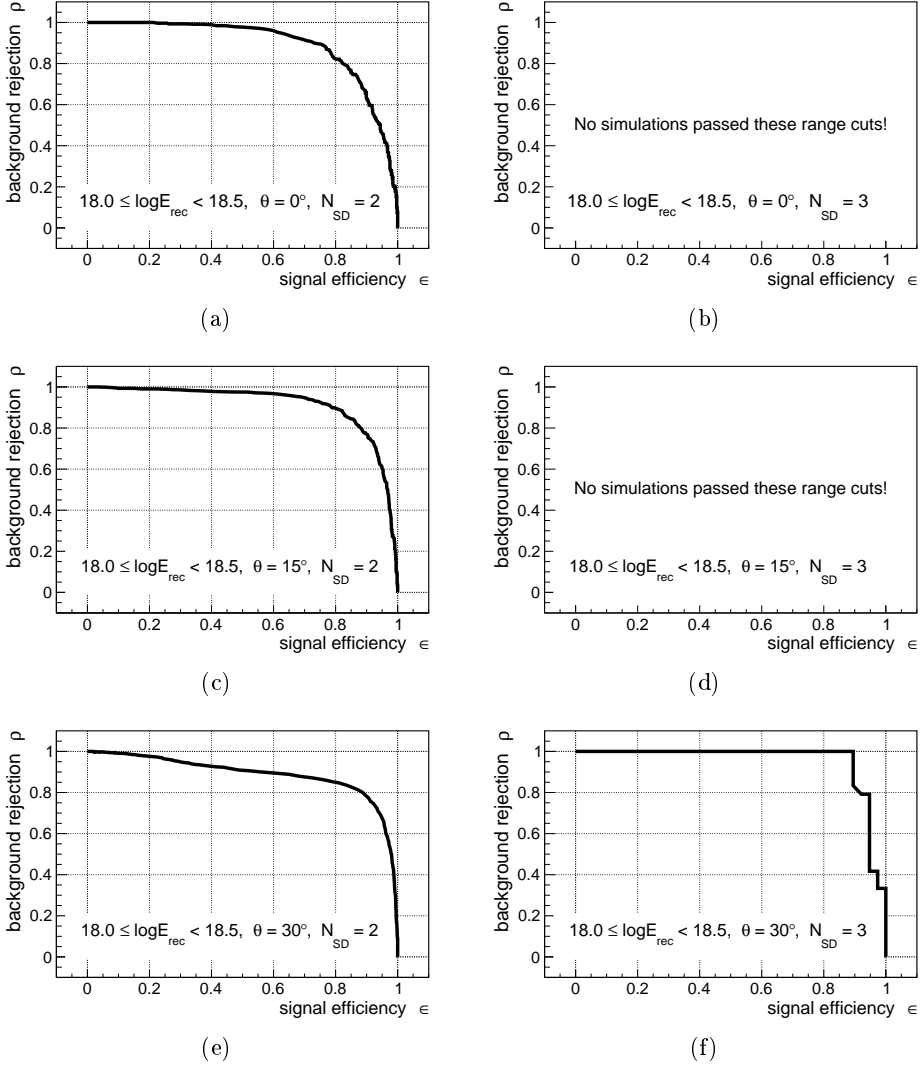


Figure 8.9.: Signal efficiency ϵ vs. background rejection ρ calculated from EAS simulations separated by the reconstructed energy. The results in the left column are with 2 reconstructed SD stations within the testing distance range and in the right column those with 3 SD stations. The different rows show the results with different inclination angles.

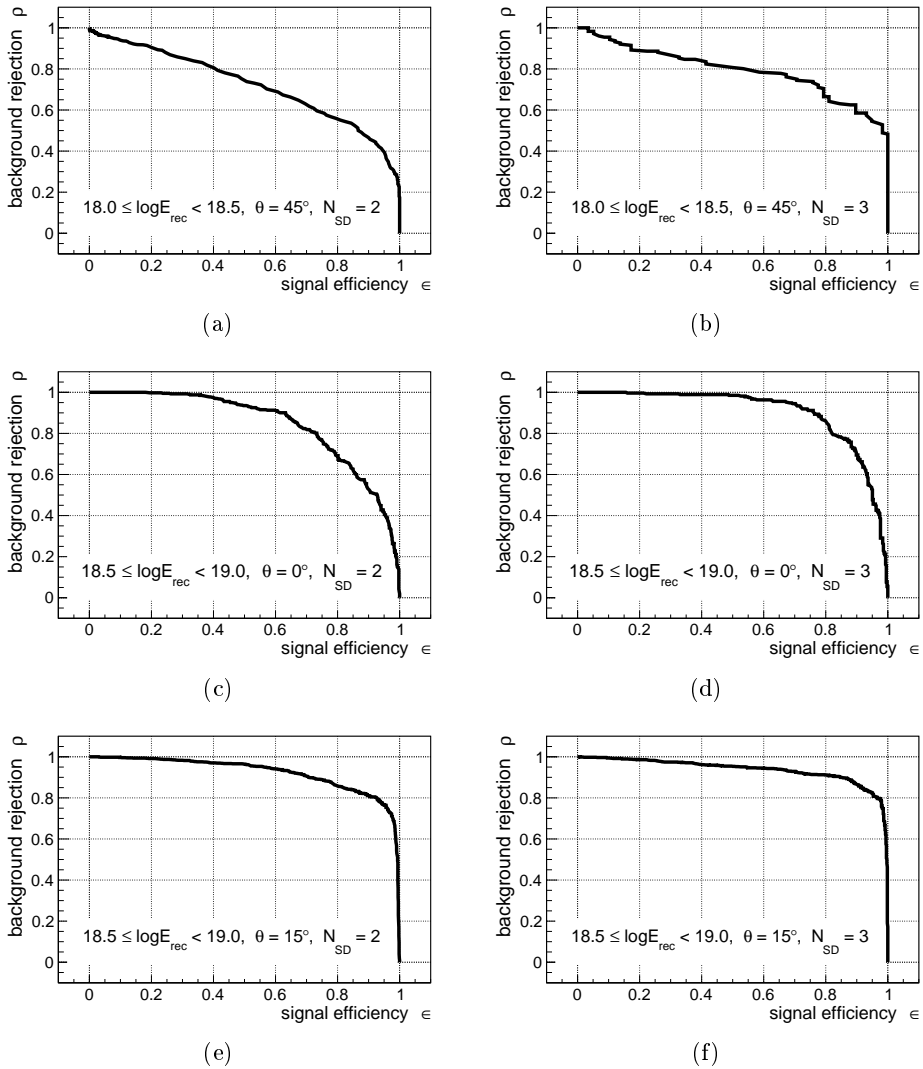


Figure 8.10.: Signal efficiency ϵ vs. background rejection ρ calculated from EAS simulations separated by the reconstructed energy. The results in the left column are with 2 reconstructed SD stations within the testing distance range and in the right column those with 3 SD stations. The different rows show the results with different inclination angles. Note that the top graphs here show results from simulations with different energies compared to the other graphs.

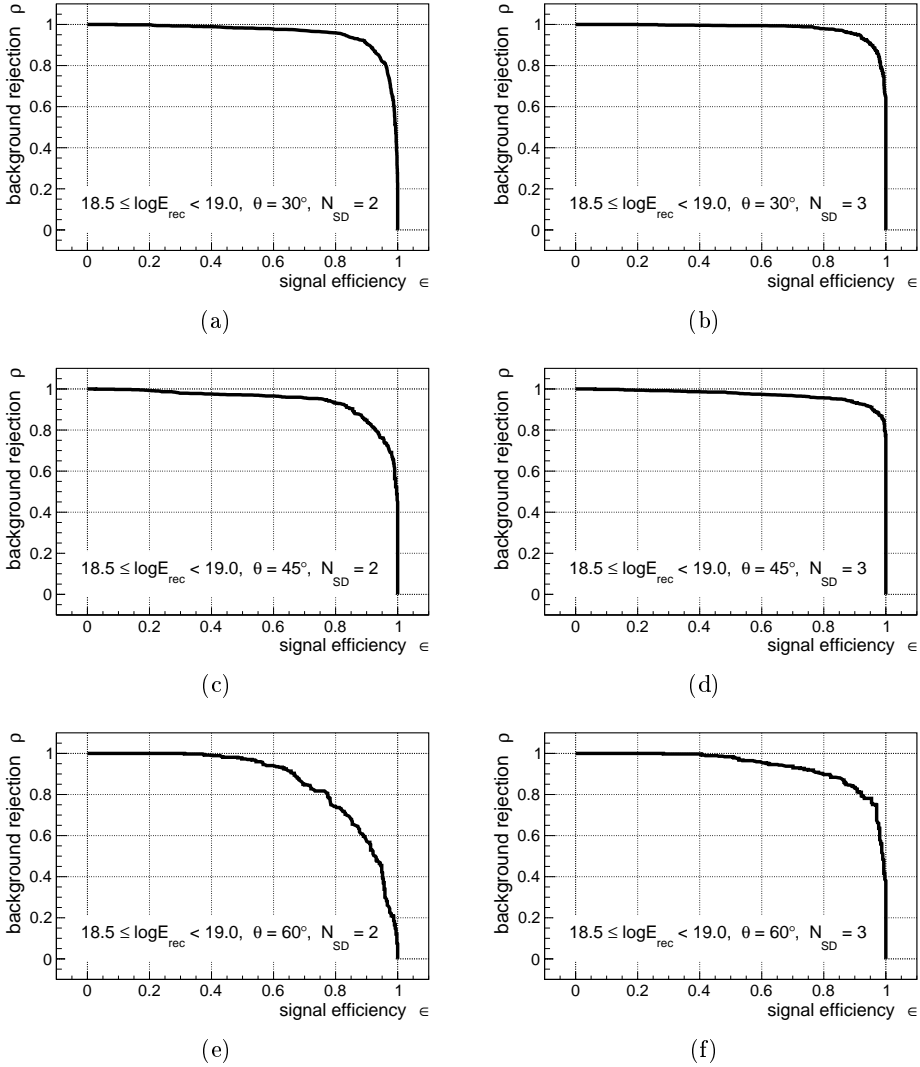
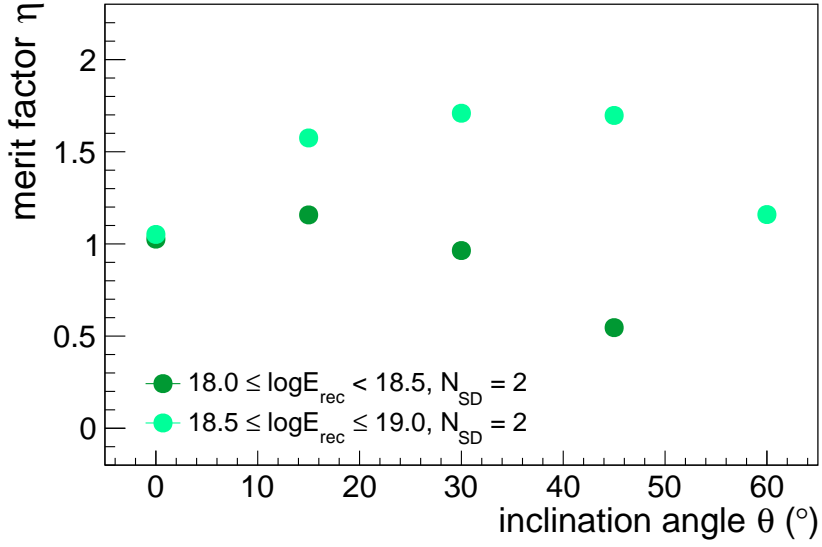
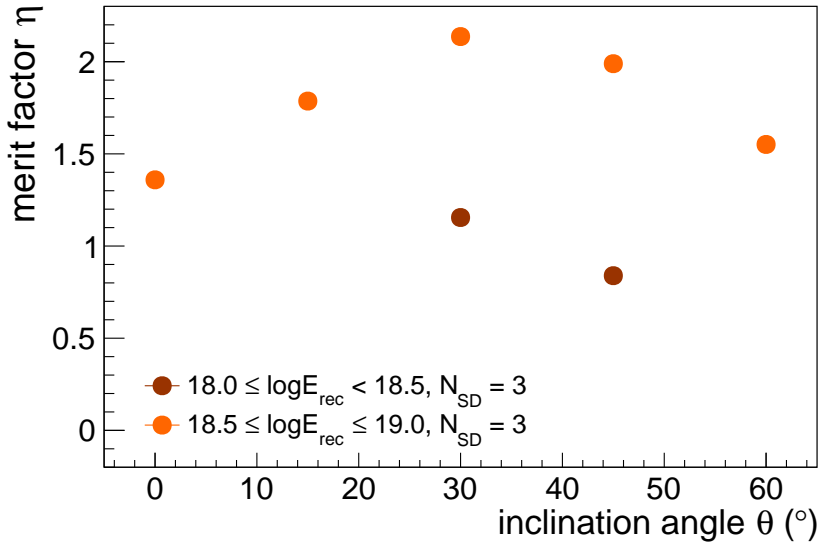


Figure 8.11.: Signal efficiency ϵ vs. background rejection ρ calculated from EAS simulations separated by the reconstructed energy. The results in the left column are with 2 reconstructed SD stations within the testing distance range and in the right column those with 3 SD stations. The different rows show the results with different inclination angles.



(a)



(b)

Figure 8.12.: Merit factors based on results from air shower simulations with 2 selected SD stations (a) and those with 3 stations (b).

As the TPDF models were created for two high-energy interaction models EPOS and QGSJet separately, different gamma cuts are defined for each model, and the tested event has to pass the gamma cuts for both models to be identified as a *gamma ray candidate*.

8.5. Gamma cut testing on simulations

After the gamma cuts are defined for the TPDF models and the domain of applicability has been determined, the sensitivity for distinguishing gamma induced EAS is tested on additional air shower simulations produced by the Pierre Auger Collaboration. These air showers were created by the group in Wuppertal with the following parameters:

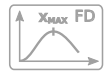
- Primary particle: gamma (γ), proton (p), iron (Fe).
- Energy $E_{sim} : 10^{18.5} \text{ eV} - 10^{20.5} \text{ eV}$
- Inclination angle $\theta_{sim} : 0^\circ - 70^\circ$ ($0^\circ - 65^\circ$ for γ)
- CORSIKA version: 7.5600
- High-energy interaction model: EPOS
- Low-energy interaction model: FLUKA
- Thinning: $\varepsilon_{thin} = 10^{-6}$

$$\begin{array}{rcccl} 18.0 & \leq & \log(E_{rec}/\text{eV}) & < & 18.5 \\ 0.0 & \leq & \theta_{rec} & \leq & 45.0 \\ 2 & \leq & N_{SD} & \leq & 3 \end{array}$$

Table 8.1.: Reconstruction range cuts for low energies (set I).

$$\begin{array}{rcccl} 18.5 & \leq & \log(E_{rec}/\text{eV}) & \leq & 19.0 \\ 0.0 & \leq & \theta_{rec} & \leq & 60.0 \\ 2 & \leq & N_{SD} & \leq & 3 \end{array}$$

Table 8.2.: Reconstruction range cuts for high energies (set II).



The total numbers of simulations for the three primary particles are: $N_{sim,Fe} = 999$, $N_{sim,p} = 8409$ and $N_{sim,\gamma} = 29988$. The tests of these simulated air showers with “unknown” primary and later also on real data are performed for EAS with reconstructed parameters within the ranges (Section 8.3) summarized in Tables 8.1 and 8.2.

From all simulated air showers (N_{sim}) only a fraction could be reconstructed (N_{rec}) within the reconstruction ranges defined above. The results of the search for gamma ray candidates in the two simulated EAS sets are summarized in Tables 8.3 and 8.4. The requirement of the number

	N_{rec}	$N_{gammalike}$			
		ρ			
		0.8	0.9	0.95	0.99
p	29	2	0	0	0
	100%	$6.9 \pm 4.9\%$	$< 8.4\%$	$< 8.4\%$	$< 8.4\%$
γ	691	578	377	176	38
	100%	$83.6 \pm 3.5\%$	$54.6 \pm 2.8\%$	$25.5 \pm 1.9\%$	$5.5 \pm 0.9\%$

Table 8.3.: Statistics of simulation set I passing the gamma cuts. In cases where no events were selected, the upper limits at a confidence level (CL) of 90% are calculated. No iron air shower simulations were available for this set.

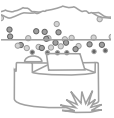
	N_{rec}	$N_{gammalike}$			
		ρ			
		0.8	0.9	0.95	0.99
Fe	91	10	5	0	0
	100%	$11.0 \pm 3.5\%$	$5.5 \pm 2.5\%$	$< 2.7\%$	$< 2.7\%$
p	705	200	116	52	1
	100%	$28.4 \pm 2.0\%$	$16.5 \pm 1.5\%$	$7.4 \pm 1.0\%$	$0.1 \pm 0.1\%$
γ	2323	1802	1528	1291	602
	100%	$77.6 \pm 1.8\%$	$65.8 \pm 1.7\%$	$55.6 \pm 1.5\%$	$25.9 \pm 1.1\%$

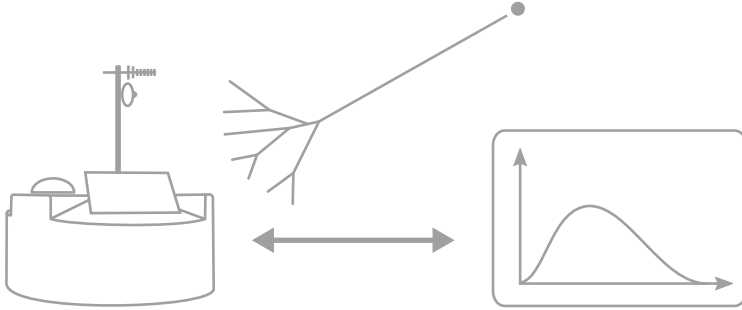
Table 8.4.: Statistics of simulation set II passing the gamma cuts. In cases where no events were selected, the upper limits at a confidence level (CL) of 90% are calculated.

of SD stations to be within a defined distance range to the air shower axis reduces the available number of tested events to about 10% of the total number of simulations. In cases where no gamma ray candidates were selected, the upper limits are displayed, calculated according to [103].

A comparison of the relative numbers passing the gamma cuts ($N_{\text{gammalike}}$) for EAS with proton and iron primaries in Table 8.4 shows that more iron air showers are cut than proton EAS at the same ρ . The numbers of EAS with proton primary left are higher compared to the expectation given at a certain ρ , e.g. 10% proton air showers left at $\rho = 0.90$, except for $\rho = 0.99$. In this case less than 0.1% of $N_{\text{rec},p}$ passed the gamma cuts. In nearly all individual cases there is marginal statistical compatibility between the number of selected proton events and the value expected based on the cut values. However, the number of selected protons at $\rho = 0.99$ in set II is too small. The upper limit at this gamma cut level is 0.6% and is below the expected value of 1%. This discrepancy results from the definition of gamma cuts on discrete distributions (Figure 8.8), the approach of use of the highest gamma cuts of the selected models, mentioned in the previous section, which is very conservative, and the small statistics of proton EAS simulations in the region of $\rho = 0.99$. This can be observed when comparing the upper and lower histograms of Figure D.3. When a set of tested EAS has an energy of $10^{18.5} \text{ eV} \leq E_{\text{rec}} < 10^{19.0} \text{ eV}$ and inclination angle of $0^\circ \leq \theta < 15^\circ$ the gamma cuts of these models are selected. The gamma cuts at $\rho = 0.99$ used would be around $\Lambda_{\gamma,p}^{\text{cut}} = 0$ (histograms in (c) and (d)). For almost vertical EAS (histograms in (a) and (b)) these would be too high gamma cuts which lead to a too small number of selected events with a proton primary.

For simulations with a gamma primary the fractions of EAS are much higher than of those with proton or iron primaries passing $\Lambda_{\gamma,p}^{\text{cut}}$. This means that the TPDF separation of air showers initiated by gammas from EAS with other primaries is confirmed to be working. Even for the highest tested background rejection of $\rho = 0.99$ still more than 5% of gamma induced and reconstructed EAS with the lower energies and more than 25% of those with higher energies have passed the gamma cuts.





Results of the TPDF application on data

Once the thresholds for optimal gamma-hadron separation are set, the TPDF models are applied to the data recorded by the Pierre Auger Observatory with the aim to find ultra-high-energy gamma rays. This analysis is similar to the tests of the simulated air showers described in the previous Section 8.5.

9.1. Data selection

At the Pierre Auger Observatory EAS are measured with different types of detectors as described in Chapter 3. The measured events are stored once a defined trigger was fired. In particular, all SD events passing the T3 trigger are saved. Among these there are some events with a bad quality that are useless for the TPDF analysis and should be discarded.

All recorded SD events were reconstructed with the same Offline version as was used for the simulation. This ensures that both simulated and measured EAS are treated in the same way. During the reconstruction some errors could occur that would lead to wrong results. To select reliably reconstructed events, which will be used to search for gamma ray candidates, SD and reconstruction cuts are applied.

First, the events that are comparable with the simulated EAS as listed in Section 4.3 have to be selected. Although the SD efficiency reaches 100% for EAS above $10^{18.5}$ eV, also air showers with smaller energies are detected by the regular array. The energy threshold is set to 10^{18} eV. The maximum inclination angle θ of the recorded EAS is set to 60° . Above this angle the reconstruction of the air shower geometry becomes more difficult, because e.g. a non-negligible part of the air shower travels horizontal and either misses the SD stations or hits several in a row. The recorded data contain also bad events due to e.g. environmental conditions or reconstruction problems. In particular lightning can cause a distortion in the SD PMT traces. Therefore, known periods of lightning are discarded from the data set. SD station components, such as the PMTs, electronics or power supply can break down and prevent the detectors from measuring the air showers correctly. Hence, periods with many SD stations with known problems (bad SD) are excluded from the reconstruction.

		N	ε
Raw sample		5 963 923	100 %
SD cut name	value		
Minimum SD energy	10^{18} eV	2 173 205	36.4 %
Maximum SD inclination angle	60°	1 928 881	88.8 %
Include lightning periods	false	1 928 881	100.0 %
Reject bad SD periods	true	1 893 550	98.2 %
T4 trigger	2	1 893 258	99.9 %
T5 trigger	0	1 664 540	87.9 %
Minimum reconstruction level	4	1 663 658	99.9 %
LDF status	4.5	1 663 652	99.9 %
Select saturated events	false	1 576 376	94.8 %
Use events with silent SD stations	false	1 574 586	99.9 %
Total number of events		1 574 586	26.3 %

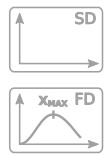
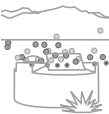


Table 9.1.: SD cuts for the data, the number of data events that passed the individual cut and their fraction comparing to the previous number.

As mentioned in Section 3.4.1 the CDAS provides two triggers, namely T4 and T5, to select well measured events. For the data selection the T4 is set to pick all the SD events and the T5 trigger value is set so that all events that passed this trigger are used. The measured SD events have to be reconstructed with Offline to calculate the air shower geometry. The reconstruction is done in steps (Section 3.4.1), where some steps require e.g. a minimum number of stations to work correctly. For the TPDF analysis the reconstructed air shower geometry properties, such as the air shower core position, estimated energy and air shower axis orientation are necessary inputs. Therefore, the minimum reconstruction level is set to include the LDF and the radius of curvature fits with the LDF status flag of 4.5. For some events where the air shower axis is close to one SD station both high and low gain channels of its PMTs are saturated. Although the reconstruction could have passed the previous cuts the SD signals of these stations need to be further prepared for the TPDF analysis. This needs to be studied in detail and is not part of this thesis. Hence, these events are excluded. Another cut removes events with silent SD stations in the range of a detected air shower where they should have a signal.

All these cuts, summarized in Table 9.1, are used to select events that can be probed with the TPDF models. This table also shows the fraction of events that pass a specific cut with respect to the previous one. At the end the total number of events passing all cuts is listed.

The number of air showers recorded by the Pierre Auger Observatory between January 2004 and December 2017 that passed all SD cuts is 1 574 586.

9.2. Reconstruction range and quality cuts

Taking the reconstruction efficiency into account and the defined ranges in Section 8.3, the preselected air showers are separated based on the reconstructed parameter range cuts from Tables 8.1 and 8.2 into two data sets, *data set I* and *data set II*, displayed in Figure 9.1. The inclination angle distribution of SD events of these two sets are displayed in Figures 9.2 and 9.3. Note that for smaller energies (data set I) only EAS up to $\theta = 45^\circ$ are tested according to the definition from Section 8.3.

Additional quality cuts are applied to these data sets.

The first cut rejects all events for which for at least one selected SD

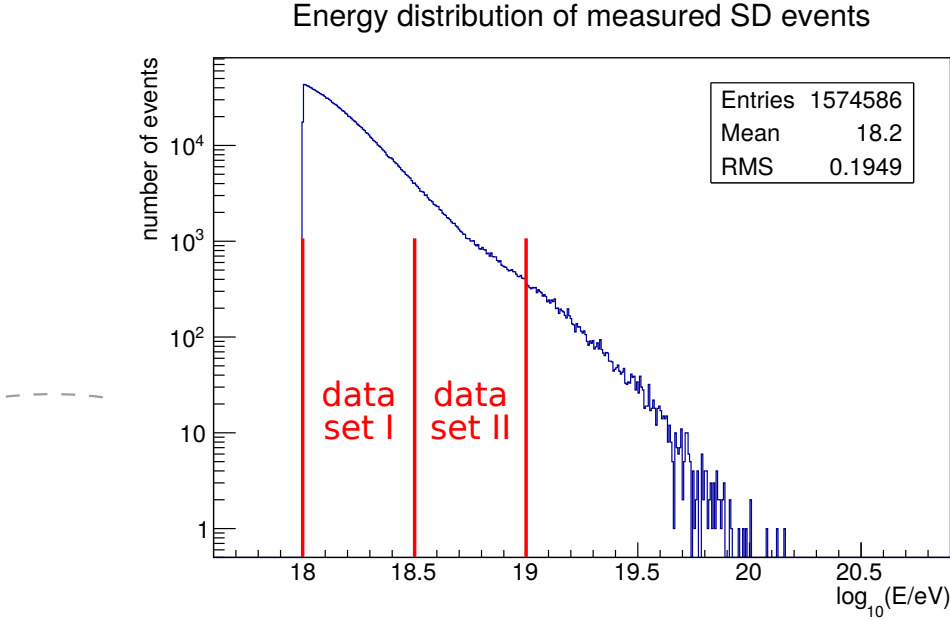
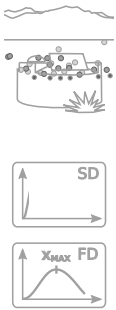


Figure 9.1.: Energy distribution of measured EAS, as selected in Section 9.1. For testing against TPDF models only events with energy in data set I and data set II will be used.

station one or more PMTs have no signal. This can be caused by several problems, e.g. the PMT is broken or the wiring is damaged. Those events are more likely to pass the gamma cuts as the total signal is reduced by the missing PMT signal.

The second cut rejects all events with a time trace with a misidentified start time. An example is shown in Figure 9.4. This can happen due to an error in the electronics as well as due to a particle unrelated to the EAS passing the water tank around the trigger time window. The misidentification of the start time can occur for one or more PMTs, depending on the cause. This effect enhances the time between time trace maximum and start time, thus making the event look more gamma-like. Therefore, events with a wrong start time are rejected. A wrong start time is recognized by using two algorithms scanning the time trace in the range between 250 ns and 750 ns. The first algorithm searches for traces with minimally 5 bins in a row with a content below 0.1 VEM and is mainly sensitive for a big



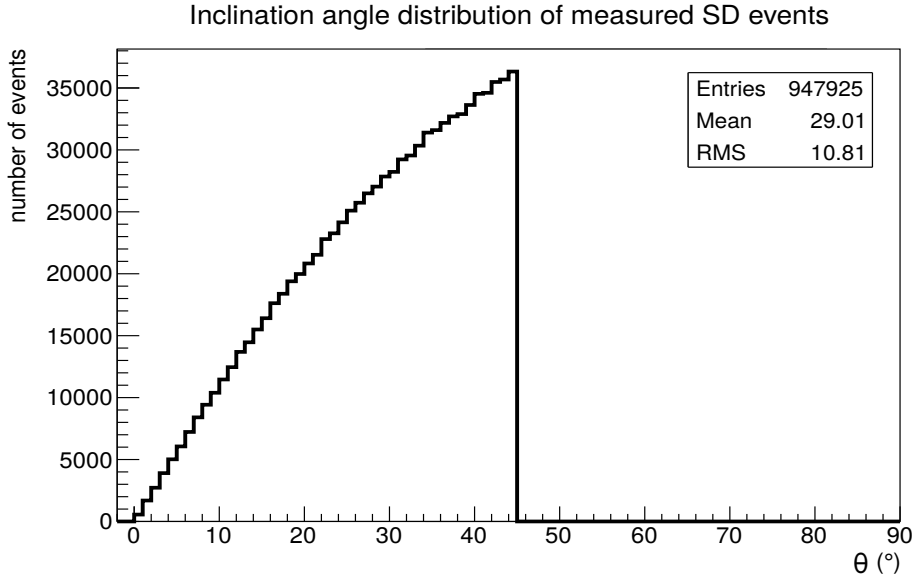


Figure 9.2.: Distribution of θ for data set I.

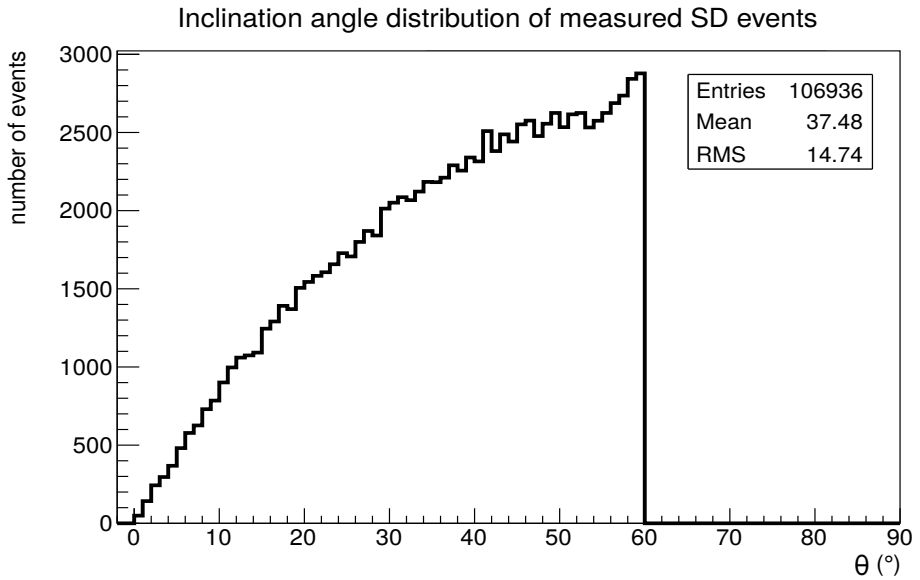


Figure 9.3.: Distribution of θ for data set II.

gap between the wrongly triggered front bin and the signal of the main air shower. The second algorithm removes events with a leading accidental particle with relative small energy that does not belong to the air shower. It searches for minimally 3 bins in a row with a decreasing signal starting at at least 1% of the total signal of the PMT time trace.

It can happen that an event has a signal from an accidental particle in front of the main air shower that has sufficient energy and is in time very close to the main signal. Those events are hard to classify as faulty events and are not removed at this stage.

The last quality cut removes all events with SD stations with a signal S lower than 5 VEM, to be consistent with the TPDF models (Section 6.1).

The numbers of events left after all range and quality cuts are applied are summarized in Tables 9.2 and 9.3. 188 435 data set I events with lower energies and 39 761 data set II events with higher energies are left, which account for 12.0% and 2.5% of all measured events by the Pierre Auger Observatory between January 2004 and December 2017.

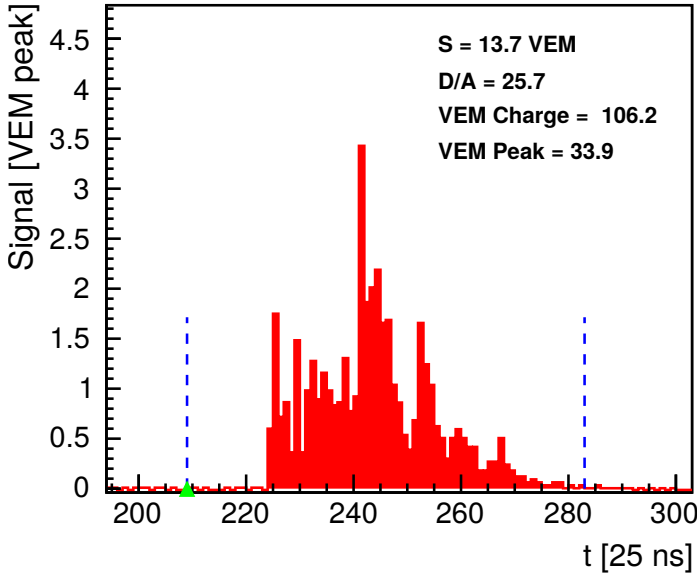


Figure 9.4.: Time trace from data event 16015959, SD station 844 with misidentified start time. The dashed vertical lines define the signal region and the green arrow the start time of the signal.

Preselected sample	1 574 586	100 %
<hr/>		
Range cuts		
$18.0 \leq \log(E_{rec}/\text{eV}) < 18.5$	1 456 095	92.5 %
$0.0^\circ \leq \theta_{rec} \leq 45.0^\circ$	947 925	65.1 %
$2 \leq N_{SD}(575 \text{ m} - 825 \text{ m}) \leq 3$	235 050	24.8 %
<hr/>		
Quality cuts		
Missing PMTs cut	189 873	80.8 %
Wrong start time cut	188 445	99.2 %
$S \geq 5.0 \text{ VEM}$	188 435	99.9 %
<hr/>		
Number of data set I testing events	188 435	12.0 %

Table 9.2.: Range and quality cuts of data set I, the number of events that passed the individual cut and their fraction comparing to the previous number.

Preselected sample	1 574 586	100 %
<hr/>		
Range cuts		
$18.5 \leq \log(E_{rec}/\text{eV}) \leq 19.0$	106 936	6.8 %
$0.0^\circ \leq \theta_{rec} \leq 60.0^\circ$	106 936	100 %
$2 \leq N_{SD}(575 \text{ m} - 975 \text{ m}) \leq 3$	52 087	48.7 %
<hr/>		
Quality cuts		
Missing PMTs cut	39 919	76.6 %
Wrong start time cut	39 801	99.7 %
$S \geq 5.0 \text{ VEM}$	39 761	99.9 %
<hr/>		
Number of data set II testing events	39 761	2.5 %

Table 9.3.: Range and quality cuts of data set II, the number of events that passed the individual cut and their fraction comparing to the previous number.

9.3. Gamma ray candidates

The data set I and II events are tested against TPDF models if they pass the gamma cuts at several background rejection thresholds as defined in Section 8.4. The result of the search for gamma ray candidates are summarized in Tables 9.4 and 9.5. Note that for some events in each set, less than 1%, the testing procedure including several fits has failed and they are discarded.

When comparing these results to Tables 8.3 and 8.4, it is clear that the numbers of events passing the gamma cuts are comparable with the scenario of only hadronic cosmic rays. For the data set II the results are even comparable with the iron EAS from Table 8.4. Therefore, there is no indication of a significant number of gamma ray candidates. It should be noted that the comparison of data to simulation expectations is completely limited by the available simulation statistics.

	N_{range}	$N_{gammalike}$			
		ρ			
		0.8	0.9	0.95	0.99
data	187 747	11 961	2 808	1 036	138
set I	100%	$6.37 \pm 0.06\%$	$1.50 \pm 0.03\%$	$0.55 \pm 0.02\%$	$0.07 \pm 0.01\%$

Table 9.4.: Numbers of tested air showers of data set I and those passed the gamma cuts.

	N_{range}	$N_{gammalike}$			
		ρ			
		0.8	0.9	0.95	0.99
data	39 371	5 116	2 084	593	14
set II	100%	$12.99 \pm 0.18\%$	$5.29 \pm 0.12\%$	$1.51 \pm 0.06\%$	$0.04 \pm 0.01\%$

Table 9.5.: Numbers of tested air showers of data set II and those passed the gamma cuts.

9.4. Characteristics of selected gamma ray candidate events

The highest threshold tested is at the background rejection ρ of 99%. The events passing this threshold are studied in more detail. From data set I events 138 air showers were classified as gamma ray candidates, which corresponds to 0.07% of all events in this set. For the data set II 14 gamma ray candidates were found, corresponding to 0.04% of all events in this set. The EAS of data set II passed the gamma cuts at 0.99 are listed in Table 9.6. Both results are comparable with the scenario that there are no gamma induced EAS.

When taking a close look into the gamma ray candidate events, some issues were found. Event 35749641 has a huge signal value in just one time trace bin. This is unlikely to originate from a particle, as only one out of

Event ID	Date	Time	$E(\text{EeV})$	$\theta(^{\circ})$	$b(^{\circ})$	$l(^{\circ})$
1207345	11. Feb 2005	06:00:13	7.55	59.70	10.89	-145.36
3528386	6. Jun 2007	15:50:36	5.09	11.52	-35.57	-126.06
3531107	7. Jun 2007	14:11:40	7.17	10.84	-57.20	-133.55
7569396	12. Apr 2009	05:08:56	3.41	58.83	60.32	29.34
13516784	3. Jan 2012	06:37:35	3.60	30.68	-20.32	-86.14
24530119	9. Dec 2013	15:21:25	7.38	56.82	38.34	-77.86
26071805	16. Mar 2014	05:00:31	5.29	59.93	-21.26	-106.19
27405165	5. Jun 2014	04:46:08	3.60	24.08	16.62	10.64
34053480	1. Aug 2015	23:21:26	5.57	57.43	16.83	-85.47
38336722	21. Jun 2016	06:32:49	4.00	41.66	14.01	3.07
38515023	4. Jul 2016	07:18:42	3.90	34.77	-81.91	2.85
41116581	12. Jan 2017	11:53:34	4.20	9.58	23.19	-21.98
44805263	7. Oct 2017	02:58:50	4.02	58.55	-48.40	147.91
45664243	6. Dec 2017	13:51:50	3.89	59.59	34.00	30.80

Table 9.6.: Events of data set II that passed the gamma cuts of $\rho = 0.99$.

The ID, arrival time, reconstructed energy E , inclination angle θ , galactic latitude b and galactic longitude l for each event are displayed. Events with some issues (see text) are highlighted.

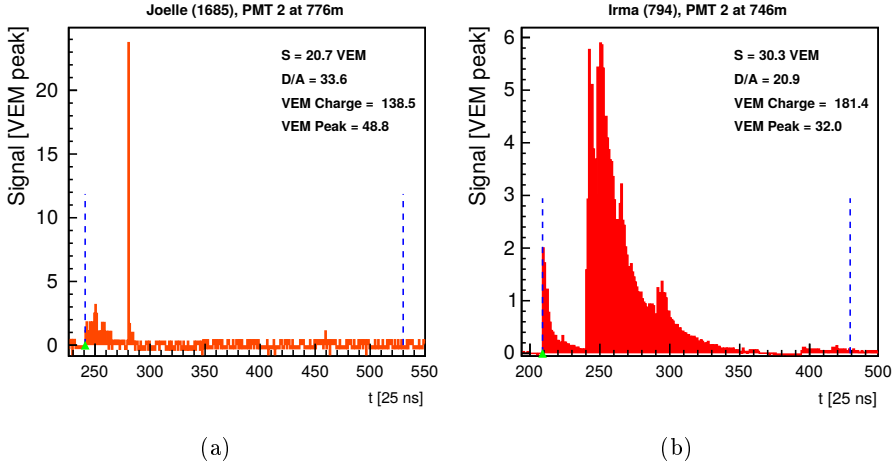


Figure 9.5.: PMT time traces of wrong events with artificial bin signal (a) and wrong start time (b). The dashed vertical lines define the signal region and the green arrow the start time of the signal.

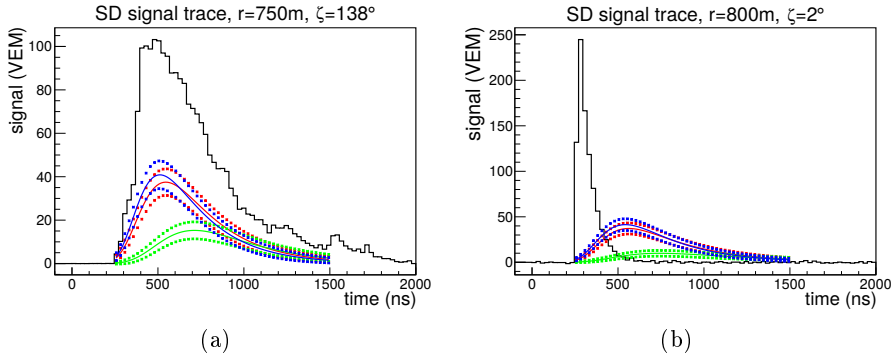


Figure 9.6.: Examples of events with too high signals (black lines) compared to interpolated TPDF models (solid color lines) and 1 sigma confidence intervals (asterisks), based on simulations with proton (red), iron (blue) and gamma (green) primaries.

three time traces has this peak and the signal decay is abnormally fast. The trace of this event is shown in Figure 9.5(a). Event 41531570 has a wrong start time, although it passed the quality cuts. This results mainly from the signal of the second PMT. The decay trace after each signal peak indicates an electronics issue, as it is slowly exponentially decreasing instead of falling back on the baseline quickly. The time trace of the second PMT of this event is shown in Figure 9.5(b).

Several issues were found in events 13744313, 20864072, 26093052, 2900001, 39712045, 44252528 of data set I, and for 3 events in data set II with IDs 3528386, 3531107, 4116581. For all of these events the time trace predicted by the TPDF models is too low compared to the measured signal for some SD stations, either for the front part of the time trace or for the whole time range. Examples are displayed in Figure 9.6. In case of some data set II events a wrong LDF fit by Offline could be identified

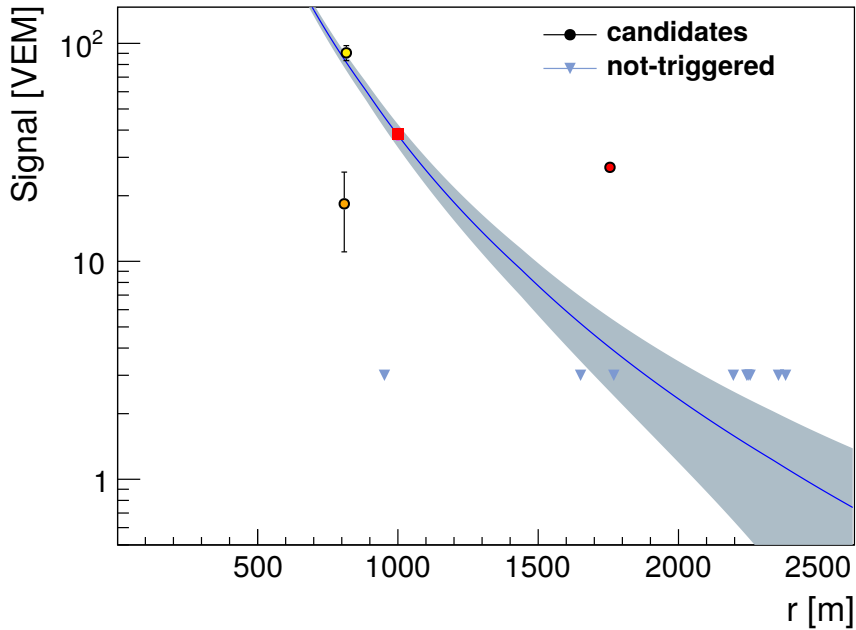


Figure 9.7.: Example of a wrong LDF fit. Note the orange and red points far from the fit line.

causing a wrong distance to air shower axis calculation. An example for event 3531107 is given in Figure 9.7.

In the data set I several events could be found with an additional peak at late times or at the very end of the tested time range of 1500 ns. They have passed the gamma cuts, because at that stage of the time trace the uncertainties of the TPDF models become small. Thus, the higher TPDF model values for a gamma primary results in a higher probability to be a gamma induced EAS. An example of a time trace from event with ID 12659312 is shown in Figure 9.8. Although such events may not be initiated by a gamma primary it is not possible to determine whether the second peak belongs to the air shower or not.

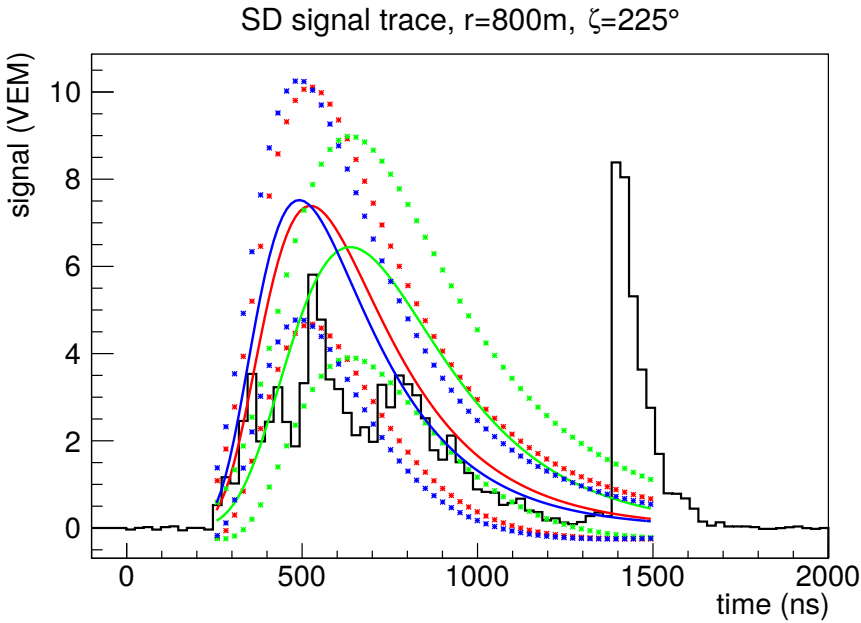


Figure 9.8.: Example of events with multiple peaks in the time traces (black line) with interpolated TPDF models (solid color lines) and 1 sigma confidence intervals (asterisks), based on simulations with proton (red), iron (blue) and gamma (green) primaries.

9.5. Comparison to gamma ray candidates of other studies

The TPDF method can be verified by a comparison with the results of other analyses that concentrated on finding gamma initiated air showers. Two such analyses were described in [99] and [104]. The first analysis uses the ratio of the energy estimator for hybrid events obtained from a gamma optimized and a standard fit, as already mentioned under “Signal ratio parameter F_γ ” in Section 5.1. The second analysis discriminates gamma ray candidates using the time trace distribution. Therefore, the second approach is close to what is done in this thesis, although the function used in [104] generally does not fit the time trace well.

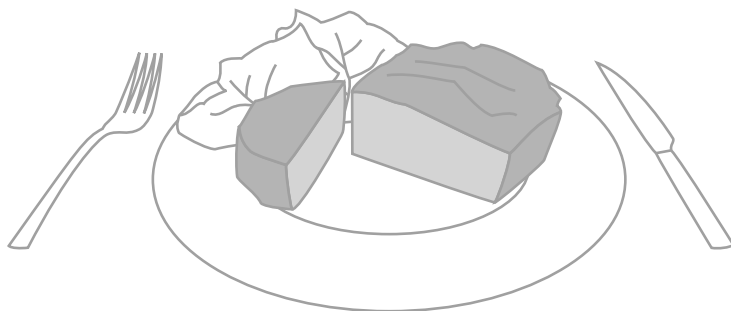
In the first analysis only 1 event passed the gamma cuts. This small number is due to the use of hybrid events and additional selection criteria. Unfortunately, this event’s reconstructed SD energy is below the range used in this thesis and no comparison is possible.

Auger ID	Event ID	Date	Time	ρ	
				0.95	0.99
80555184500	4586998	25. Feb 2008	02:24:04	-	-
81143356100	4841436	23. Apr 2008	21:19:20	✓	-
103196014500	10611670	16. Nov 2010	04:42:24	✓	-
120026705600	13516784	3. Jan 2012	06:37:35	✓	✓

Table 9.7.: Highest energy events from [104] that are also in the data set of this thesis.

In the thesis describing the second analysis 103 events with energies $10^{18.8} \text{ eV} < E_{rec}^\gamma < 10^{19.0} \text{ eV}$ and 13 events with higher energies were selected. Following that analysis we focus on the 13 high-energy events. Four of these events were found in data sets used in this thesis. 7 were rejected due to range cuts (energy, inclination angle and 2 or 3 SD stations with signals within a defined distance range to the air shower axis) and 2 due to quality cuts applied. From the 4 events in overlap with the data sample of this thesis 3 passed the $\rho = 0.95$ and only 1 also the $\rho = 0.99$ gamma cuts. The results are summarized in Table 9.7.





Conclusions

In this work the time traces measured by the Surface Detector (SD) stations (water-Cherenkov detectors) of the Pierre Auger Observatory are fitted with the newly introduced Time Probability Density Function (TPDF). The parameters obtained in these fits are used to study the mass composition of ultra-high-energy cosmic rays (UHECR), in particular for the search for ultra-high-energy gamma rays (UHEGR). In addition, comparisons of simulation results are presented for different primary particles as function of energy, inclination angle and other simulation parameters.

In Chapter 6 the description of the TPDF model building procedure is given. It is shown in Chapter 7 that the TPDF parameters vary with cosmic ray energy E and inclination angle θ , as well as with the polar angle ζ around the air shower axis, while they hardly depend on the CORSIKA simulation software versions and high-energy hadronic interaction models. Given the energy, inclination angle and polar angle the differences are maximal between gamma ray and hadron induced extensive air showers (EAS). This makes the TPDF method sensitive to discriminate air showers started by gamma rays from EAS initiated by other primary particles.

A general increase in the number of muons in the footprint, as observed in data compared to simulations, causes no large changes in the TPDF parametrization. Note that this study is performed on a small number of full, non-thinned simulations and this effect should be further verified with a larger sample.

In the comparison between thinned simulations with thinning level of $\varepsilon_{thin} = 10^{-6}$ in which only a fraction of the air shower particles are tracked and non-thinned simulations in which all particles of significant energy are tracked some small differences have been seen for the simulated EAS with a gamma ray primary particle. The ζ distributions for the non-thinned air shower simulations show a smaller confidence interval and less variation in ζ .

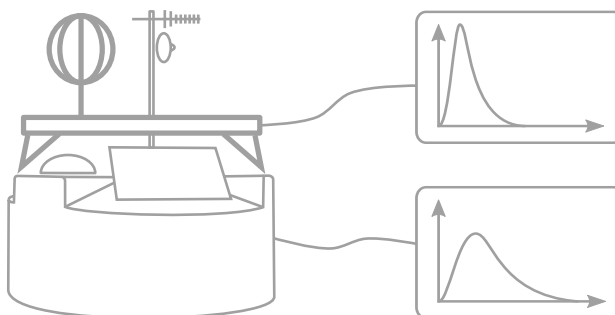
Chapter 9 concentrates on finding gamma ray induced air showers in the measured events with gamma cuts defined on simulated test samples in Chapter 8. It was shown using simulations in Section 8.5 that for a background rejection ρ (simulated air showers with proton primary particle) of 99% more than 5 % of signal events (simulated EAS with gamma ray primary particle) with lower energies ($10^{18.0}$ eV - $10^{18.5}$ eV) and more than 25 % of those with higher energies ($10^{18.5}$ eV - $10^{19.0}$ eV) pass the gamma cuts (Tables 8.3 and 8.4).

The application on the events measured by the Pierre Auger Observatory between January 2004 and December 2017 was made in the same way. The events were divided into two samples, the first with energies of $10^{18.0}$ eV $\leq E_{rec} < 10^{18.5}$ eV and inclination angles of $0^\circ \leq \theta_{rec} \leq 45^\circ$ (data set I) and the second with $10^{18.5}$ eV $\leq E_{rec} \leq 10^{19.0}$ eV and $0^\circ \leq \theta_{rec} \leq 60^\circ$ (data set II). From 187 747 successfully tested data-set-I events 138 passed the gamma cuts with $\rho = 0.99$ and from the 39 371 data-set-II events 14 passed the $\rho = 0.99$ gamma cuts. For both samples this is less than 0.1% of all events tested with the TPDF method.

The number of selected events is compatible with the expectations from hadron induced air showers as determined in Chapter 8 and therefore there is no indication of the presence of gamma ray induced EAS in the selected samples.

A closer look at the events selected as gamma ray candidates reveals that the TPDF method is sensitive to unusual events with some issues caused by electronics or physics circumstances. Especially the origin of events with a late peak after the main signal of the air shower should be studied further.





Outlook

In this chapter a short discussion of the upcoming improvement of the particle detection with the Surface Detector is given. In addition, possible improvements of the TPDF analyses are suggested.

11.1. AugerPrime

In the near future the *AugerPrime* upgrade [105] [15] [106] will be finished by the Pierre Auger Observatory. The SD stations will be modified with an additional Scintillator Surface Detector (SSD) and a spherical radio antenna on top (Figure 11.1).

This modification allows a better determination of the muonic and electromagnetic components of an air shower at the position of each SD station. This will be achieved due to the differences in the signals of the muons and the EM particles (electron-to-muon ratio), measured by the PMTs in the water tank and the SSD for air showers with small inclination angles. The additional radio antennas in combination with the water-Cherenkov detector will make the electron-to-muon ratio accessible for horizontal air showers.

The separation of the muonic signal will allow to measure the number of muons N_μ and provide a better estimation for the muon production

depth. Both parameters are of main interest for the mass composition studies and could be added to the TPDF analysis.

Additionally, the electronics of the SD stations will be upgraded. The time resolution will be improved by a factor of 3 leading to a reduction of the bin size from 25 ns to below 10 ns by increasing the Flash Analogue to Digital Converter (FADC) sampling frequency from 40 MHz to 120 MHz. In view of the mass composition studies this will lead to an improvement of time critical parameters, like R_c or T_{50} . For the TPDF analysis this will lead to a more precise time trace and decreasing uncertainties of the TPDF models. Increased raggedness of the time trace may also lead to complications when fitting the smooth TPDF model, for which solutions will have to be found.

Also a smaller PMT will be added to each SD station, that will extend the dynamic range. This will allow to use the signals of SD stations closer to the air shower axis.

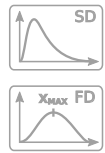
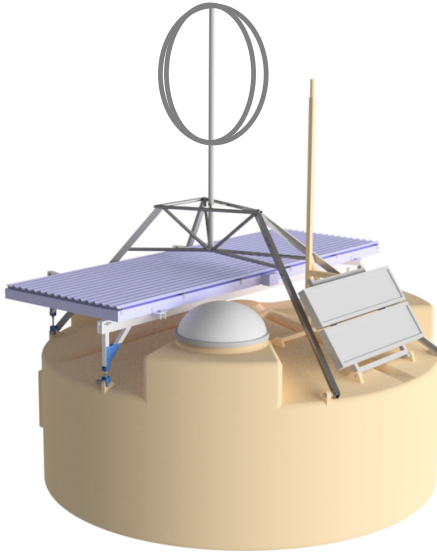


Figure 11.1.: SD station with an additional flat scintillator (SSD) on top and an additional spherical radio antenna. Adapted from [106].

11.2. Possible TPDF improvements

- **Curvature of the air shower front using the time trace maximum**

The TPDF can help to define a new curvature parameter that depends on the time trace maximum. When plotting the muon arrival time distribution of a vertical air shower as a function of distance to the air shower axis (Figure 11.2), it can be observed that the time between the impact of the air shower core ($t_{core} = 0$ s) and the arrival time of the muons increases with distance. This corresponds to the curved air shower front model (Figure 3.15) and is used to calculate R_c . Compared to the arrival times of the first muons the delays of the arrival time distribution maxima vary differently with distance to the air shower axis. This variation is used to calculate the T_{50} parameter.

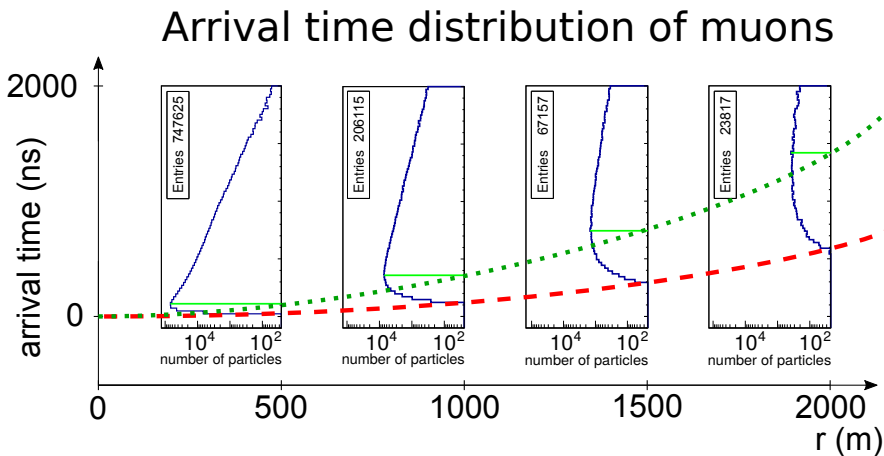


Figure 11.2.: Arrival time distributions of muons as function of distance to the air shower axis from an EAS induced by a vertical proton with an energy of $10^{18.5}$ eV. Each distribution was calculated for rings with width of 50 m at different distances. The red dashed line shows the delay of the first muons arrive at ground. The green dotted line shows the time of the highest muon densities at different distances. Green lines mark the maxima of the time distributions.

In Figure 5.5 it was shown that the time distribution maximum changes differently for different primary particles at same distance to the air shower axis. In particular, this timing of the maximum changes rapidly at the distance where the dominance of the electromagnetic component is overtaken by the muonic one. In this thesis, this behavior was only found for simulated EAS with a gamma ray primary particle. Both, this rapid change and the timing of the time trace maximum can be used for further mass composition studies. In particular, the timing of the maxima together with the absolute time of the SD stations may replace the start time of the station as is currently used for determining R_c .

• Modified ζ functions

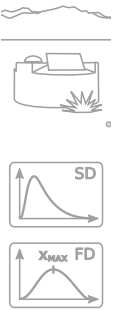
To build the TPDF models the parameters of ring segments were fitted with a ζ function (Eq. (6.1)). While this function fits quite well for most distances and air showers with different primary particles, in case of the gamma ray primary particle there are some difficulties when the muonic component starts to become the dominant contribution to the signal. For these rings the TPDF parameters of the early and late regions differ significantly. Figure 7.1(b) displays a small plateau around 180° . Here, it might be better to modify the ζ function and add an additional \cos^2 term:

$$f(\zeta)^* = j + k \cdot \cos(\zeta) + l \cdot \cos^2(\zeta) \quad . \quad (11.1)$$

• Extend the testing ranges

The main focus of this thesis was the development of the TPDF method. Some aspects, especially in case of simulations, were changing and improved during the work of this thesis, but too late to be included. The lower distance range to the air shower axis of 575 m was set due to computational limits. The range could be extended toward lower distances reducing the simulated number of SD stations. However, there are some other difficulties that have to be taken into account, e.g. the saturated PMTs.

In addition, the energy limits could be extended by simulating more air showers with higher or lower energies than used in this thesis.



Also the number of tested SD stations of the grid within the distance range to the air shower axis could be increased. While most air showers inside the tested energy range have 2 or 3 SD stations within the tested distances, there are some with more triggered SD stations that can be included in future studies, especially in case of inclined EAS.

- **Reconstruction of the saturated SD signals**

In Section 5.2 it was mentioned that the TPDF describes the main characteristics of the SD time trace well. Thus, it can be used to model the time trace of the saturated signals such as shown in Figure 3.14(b).



Bibliography

- [1] URL: <https://www.nytimes.com/2012/08/07/science/space/when-victor-hess-discovered-cosmic-rays-in-a-hydrogen-balloon.html> Accessed: 15. August, 2017.
- [2] URL: <https://commons.wikimedia.org/wiki/File%3AHessKol.jpg> Accessed: 15. August, 2017.
- [3] V. F. Hess. ‘Über Beobachtungen der durchdringenden Strahlung bei sieben Freiballonfahrten’. In: *Physikalische Zeitschrift* 13 (1912), pp. 1084–1091. URL: <https://www.mpi-hd.mpg.de/hfm/HESS/public/HessArticle.pdf>.
- [4] W. Kohlhörster. ‘Messungen der durchdringenden Strahlung bis in Höhen von 9300m’. In: *Verhandlungen der Deutschen Physikalischen Gesellschaft* 16 (1914), pp. 719–721.
- [5] P. Auger et al. ‘Extensive cosmic ray showers’. In: *Rev. Mod. Phys.* 11 (1939), pp. 288–291. DOI: 10.1103/RevModPhys.11.288.
- [6] G. Apollinari et al. ‘High Luminosity Large Hadron Collider HL-LHC’. In: *CERN Yellow Report* 5 (2015), pp. 1–19. DOI: 10.5170/CERN-2015-005.1. arXiv: 1705.08830 [physics.acc-ph].
- [7] URL: <http://www.physics.utah.edu/~whanlon/spectrum.html> Accessed: 15. August, 2017.
- [8] G. Kulikov and G. B. Khristiansen. ‘On the size spectrum of extensive air showers’. In: *J. Exptl. Theoret. Phys.* 35 (8) (1959), (441–444). URL: http://www.jetp.ac.ru/cgi-bin/dn/e_008_03_0441.pdf.
- [9] J. R. Hörandel. ‘On the knee in the energy spectrum of cosmic rays’. In: *Astropart. Phys.* 19 (2003), pp. 193–220. DOI: 10.1016/S0927-6505(02)00198-6. arXiv: astro-ph/0210453 [astro-ph].
- [10] J. Abraham et al. ‘Correlation of the highest energy cosmic rays with nearby extragalactic objects’. In: *Science* 318 (2007), pp. 938–943. DOI: 10.1126/science.1151124. arXiv: 0711.2256 [astro-ph].

- [11] V. Berezhinsky, A. Z. Gazizov and S. I. Grigorieva. ‘On astrophysical solution to ultrahigh-energy cosmic rays’. In: *Phys. Rev. D* 74 (2006), p. 043005. DOI: 10.1103/PhysRevD.74.043005. arXiv: hep-ph/0204357 [hep-ph].
- [12] M. Unger, G. R. Farrar and L. A. Anchordoqui. ‘Origin of the ankle in the ultrahigh energy cosmic ray spectrum, and of the extragalactic protons below it’. In: *Phys. Rev. D* 92.12 (2015), p. 123001. DOI: 10.1103/PhysRevD.92.123001. arXiv: 1505.02153 [astro-ph.HE].
- [13] J. R. Hörandel et al. ‘Measurement of the properties of cosmic rays with the LOFAR radio telescope’. In: *25th European Cosmic Ray Symposium (ECRS 2016) Turin, Italy, September 04-09, 2016*. arXiv: 1705.04233 [astro-ph.HE].
- [14] A. Aab et al. ‘Combined fit of spectrum and composition data as measured by the Pierre Auger Observatory’. In: *JCAP* 1704.04 (2017), p. 038. DOI: 10.1088/1475-7516/2017/04/038. arXiv: 1612.07155 [astro-ph.HE].
- [15] A. Aab et al. *The Pierre Auger Observatory: Contributions to the 35th International Cosmic Ray Conference (ICRC 2017)*. arXiv: 1708.06592 [astro-ph.HE].
- [16] A. Aab et al. ‘The Pierre Auger Cosmic Ray Observatory’. In: *Nucl. Instrum. Meth. A* 798 (2015), pp. 172–213. DOI: 10.1016/j.nima.2015.06.058. arXiv: 1502.01323 [astro-ph.IM]. URL: www.auger.org.
- [17] J. N. Matthews et al. ‘The Telescope Array Experiment’. In: *Proceedings, 32nd International Cosmic Ray Conference (ICRC 2011): Beijing, China, August 11-18, 2011*, p. 273. URL: http://inspirehep.net/record/1352289/files/v2_1306.pdf.
- [18] E. Fermi. ‘On the Origin of the Cosmic Radiation’. In: *Phys. Rev.* 75 (1949), pp. 1169–1174. DOI: 10.1103/PhysRev.75.1169.
- [19] A. M. Hillas. ‘The Origin of Ultrahigh-Energy Cosmic Rays’. In: *Ann. Rev. Astron. Astrophys.* 22 (1984), pp. 425–444. DOI: 10.1146/annurev.aa.22.090184.002233. URL: <http://articles.adsabs.harvard.edu/pdf/1984ARA%26A..22..425H>.

-
- [20] A. Aab et al. ‘Searches for Anisotropies in the Arrival Directions of the Highest Energy Cosmic Rays Detected by the Pierre Auger Observatory’. In: *Astrophys. J.* 804.1 (2015), p. 15. DOI: 10.1088/0004-637X/804/1/15. arXiv: 1411.6111 [astro-ph.HE].
- [21] A. Aab et al. ‘Observation of a Large-scale Anisotropy in the Arrival Directions of Cosmic Rays above 8×10^{18} eV’. In: *Science* 357.6537 (2017), pp. 1266–1270. DOI: 10.1126/science.aan4338. arXiv: 1709.07321 [astro-ph.HE].
- [22] P. M. Bauleo and J. Rodriguez Martino. ‘The dawn of the particle astronomy era in ultra-high-energy cosmic rays’. In: *Nature* 458N7240 (2009), pp. 847–851. DOI: 10.1038/nature07948.
- [23] G. T. Zatsepin and V. A. Kuzmin. ‘Upper limit of the spectrum of cosmic rays’. In: *Pisma Zh. Eksp. Teor. Fiz.* 4 3 (1966), pp. 78–80. URL: http://www.jetpletters.ac.ru/ps/1624/article_24846.pdf.
- [24] K. Greisen. ‘End to the cosmic ray spectrum?’ In: *Phys. Rev. Lett.* 16 (1966), pp. 748–750. DOI: 10.1103/PhysRevLett.16.748.
- [25] D. Harari, S. Mollerach and E. Roulet. ‘On the ultrahigh energy cosmic ray horizon’. In: *JCAP* 0611 (2006), p. 012. DOI: 10.1088/1475-7516/2006/11/012. arXiv: astro-ph/0609294 [astro-ph].
- [26] J. Matthews. ‘A Heitler model of extensive air showers’. In: *Astropart. Phys.* 22 (2005), pp. 387–397. DOI: 10.1016/j.astropartphys.2004.09.003.
- [27] Bhabha, H. J. and Heitler, W. ‘The Passage of Fast Electrons and the Theory of Cosmic Showers’. In: *Proceedings of the Royal Society of London A: Mathematical, Physical and Engineering Sciences* 159.898 (1937), 432–458. ISSN: 0080-4630. DOI: 10.1098/rspa.1937.0082. URL: <https://royalsocietypublishing.org/doi/pdf/10.1098/rspa.1937.0082>.
- [28] R. Engel. ‘Indirect Detection of Cosmic Rays’. In: *Handbook of particle detection and imaging, vol.1 and vol.2*. Ed. by C. Grupen and I. Buvat. 2012, pp. 593–632. DOI: 10.1007/978-3-642-13271-1_24.

- [29] M. Risse. ‘Properties of extensive air showers’. In: *Acta Phys. Polon.* B35 (2004), pp. 1787–1798. arXiv: astro - ph / 0402300 [astro-ph].
- [30] A. Aab et al. ‘Depth of maximum of air-shower profiles at the Pierre Auger Observatory. I. Measurements at energies above $10^{17.8}$ eV’. In: *Phys. Rev. D* 90.12 (2014), p. 122005. DOI: 10 . 1103 / PhysRevD.90.122005. arXiv: 1409.4809 [astro-ph.HE].
- [31] R. Abbasi et al. ‘Report of the Working Group on the Composition of Ultra High Energy Cosmic Rays’. In: *JPS Conf. Proc.* 9 (2016), p. 010016. DOI: 10 . 7566 / JPSCP . 9 . 010016. arXiv: 1503 . 07540 [astro-ph.HE].
- [32] Y. Tsunesada et al. ‘Study on mass composition of ultra-high energy cosmic rays by Telescope Array’. In: *Proceedings, 33rd International Cosmic Ray Conference (ICRC2013): Rio de Janeiro, Brazil, July 2-9, 2013*. URL: <https://galprop.stanford.edu/elibrary/icrc/2013/papers/icrc2013-0132.pdf>.
- [33] M. Risse and P. Homola. ‘Search for ultrahigh energy photons using air showers’. In: *Mod. Phys. Lett.* A22 (2007), pp. 749–766. DOI: 10 . 1142 / S0217732307022864. arXiv: astro - ph / 0702632 [ASTRO-PH].
- [34] A. Karle et al. ‘IceCube - the next generation neutrino telescope at the south pole’. In: *Nucl. Phys. Proc. Suppl.* 118 (2003), pp. 388–395. DOI: 10 . 1016 / S0920 - 5632(03) 01337 - 9. arXiv: astro - ph/0209556 [astro-ph].
- [35] J. Alvarez-Muniz et al. *The Giant Radio Array for Neutrino Detection (GRAND): Science and Design*. 2018. arXiv: 1810.09994 [astro-ph.HE].
- [36] S. Haino et al. ‘Measurements of primary and atmospheric cosmic - ray spectra with the BESS-TeV spectrometer’. In: *Phys. Lett.* B594 (2004), pp. 35–46. DOI: 10.1016/j.physletb.2004.05.019. arXiv: astro-ph/0403704 [astro-ph].
- [37] N. Tomassetti. ‘AMS-02 in space: physics results, overview, and challenges’. In: *Nucl. Part. Phys. Proc.* 265-266 (2015), pp. 245–247. DOI: 10 . 1016 / j . nuclphysbps . 2015 . 06 . 063. arXiv: 1511 . 00052 [astro-ph.HE].

-
- [38] K.-H. Kampert. ‘Ultra-High Energy Cosmic Rays: Recent Results and Future Plans of Auger’. In: *AIP Conf. Proc.* 1852.1 (2017), p. 040001. DOI: 10.1063/1.4984858. arXiv: 1612.08188 [astro-ph.HE].
- [39] I. Allekotte et al. ‘The surface detector system of the Pierre Auger Observatory’. In: *Nuclear Instruments and Methods in Physics Research A* 586 (2008), pp. 409–420. DOI: 10.1016/j.nima.2007.12.016. arXiv: 0712.2832 [astro-ph].
- [40] Cherenkov, P. A. ‘Visible emission of clean liquids by action of γ radiation’. In: *Usp. Fiz. Nauk* 93.10 (1967), 385–388. DOI: 10.3367/UfNr.0093.196710n.0385. URL: <https://ufn.ru/ru/articles/1967/10/n/>.
- [41] J. Abraham et al. ‘Trigger and aperture of the surface detector array of the Pierre Auger Observatory’. In: *Nucl. Instrum. Meth.* A613 (2010), pp. 29–39. DOI: 10.1016/j.nima.2009.11.018. arXiv: 1111.6764 [astro-ph.IM].
- [42] J. Abraham et al. ‘Properties and performance of the prototype instrument for the Pierre Auger Observatory’. In: *Nucl. Instrum. Meth.* A523 (2004), pp. 50–95. DOI: 10.1016/j.nima.2003.12.012. URL: <https://www.auger.org/index.php/document-centre/finish/99-general-information/2291-properties-and-performance-of-the-prototype-instrument-for-the-pierre-auger-observatory>.
- [43] A. Etchegoyen. ‘AMIGA, Auger Muons and Infill for the Ground Array’. In: *Proceedings, 30th International Cosmic Ray Conference (ICRC 2007): Merida, Yucatan, Mexico, July 3-11, 2007*. Vol. 5, pp. 1191–1194. arXiv: 0710.1646 [astro-ph].
- [44] A. Aab et al. ‘Prototype muon detectors for the AMIGA component of the Pierre Auger Observatory’. In: *JINST* 11.02 (2016), P02012. DOI: 10.1088/1748-0221/11/02/P02012. arXiv: 1605.01625 [physics.ins-det].
- [45] E. M. Holt. ‘The Auger Engineering Radio Array and multi-hybrid cosmic ray detection’. In: *J. Phys. Conf. Ser.* 718.5 (2016), p. 052019. DOI: 10.1088/1742-6596/718/5/052019. arXiv: 1704.07240 [astro-ph.HE].

- [46] J. Abraham et al. ‘The fluorescence detector of the Pierre Auger Observatory’. In: *Nuclear Instruments and Methods in Physics Research Section A: Accelerators, Spectrometers, Detectors and Associated Equipment* 620.2 (2010), pp. 227–251. ISSN: 0168-9002. DOI: <http://dx.doi.org/10.1016/j.nima.2010.04.023>. arXiv: 0907.4282 [astro-ph.IM].
- [47] T. H.-J. Mathes. ‘The HEAT Telescopes of the Pierre Auger Observatory - Status and First Data’. In: *International Cosmic Ray Conference* 3 (2011), p. 153. URL: <http://particle.astro.ru.nl/pub/icrc11-0761.pdf>.
- [48] J. Abraham et al. ‘A Study of the Effect of Molecular and Aerosol Conditions in the Atmosphere on Air Fluorescence Measurements at the Pierre Auger Observatory’. In: *Astropart. Phys.* 33 (2010), pp. 108–129. DOI: 10.1016/j.astropartphys.2009.12.005. arXiv: 1002.0366 [astro-ph.IM].
- [49] P. Abreu et al. ‘Description of Atmospheric Conditions at the Pierre Auger Observatory using the Global Data Assimilation System (GDAS)’. In: *Astropart. Phys.* 35 (2012), pp. 591–607. DOI: 10.1016/j.astropartphys.2011.12.002. arXiv: 1201.2276 [astro-ph.HE].
- [50] S. Y. BenZvi et al. ‘The Lidar System of the Pierre Auger Observatory’. In: *Nucl. Instrum. Meth.* A574 (2007), pp. 171–184. DOI: 10.1016/j.nima.2007.01.094. arXiv: astro-ph/0609063 [astro-ph].
- [51] C. Glaser. ‘Results and Perspectives of the Auger Engineering Radio Array’. In: *EPJ Web Conf.* 135 (2017), p. 01006. DOI: 10.1051/epjconf/201713501006. arXiv: 1609.01513 [astro-ph.HE].
- [52] F. D. Kahn and I. Lerche. ‘Radiation from Cosmic Ray Air Showers’. In: *Proceedings of the Royal Society of London Series A* 289 (1966), pp. 206–213. DOI: 10.1098/rspa.1966.0007.
- [53] G. Askaryan. ‘Excess negative charge of an electron-photon shower and its coherent radio emission’. In: *Zhur. Eksp. i Teoret. Fiz.* Vol: 41 (1961). URL: https://inspirehep.net/record/1351286/files/e_014_02_0441.pdf.

-
- [54] A. Aab et al. ‘Probing the radio emission from air showers with polarization measurements’. In: *Phys. Rev. D* 89.5 (2014), p. 052002. DOI: 10.1103/PhysRevD.89.052002. arXiv: 1402.3677 [astro-ph.HE].
- [55] S. Jansen. ‘Radio for the masses’. PhD thesis. Nijmegen U., 2016. URL: https://inspirehep.net/record/1451836/files/thesis_S_Jansen.pdf.
- [56] L. Tománková. ‘Optical Properties and Calibration of the Pierre Auger Fluorescence Detector’. PhD thesis. KIT, 2016. DOI: 10.5445/IR/1000061954.
- [57] X. Bertou et al. ‘Calibration of the surface array of the Pierre Auger Observatory’. In: *Nucl. Instrum. Meth. A* 568 (2006), pp. 839–846. DOI: 10.1016/j.nima.2006.07.066. URL: <https://core.ac.uk/download/pdf/46778349.pdf>.
- [58] Q. Luce and I. Lhenry-Yvon. *A modified baseline estimation and signal selection in FADC traces of SD dectectors within CDAS*. Pierre Auger Observatory internal paper GAP-2016-044.
- [59] M. Aglietta et al. *Recovery of saturated signals of the surface detector*. Pierre Auger Observatory internal paper GAP-2008-030.
- [60] I. Maris et al. *Data Summary Trees and Shower Visualization for Reconstructed Auger Events*. Pierre Auger Observatory internal paper GAP-2006-081.
- [61] K. Greisen. ‘The Extensive air showers’. In: *Progress in Cosmic Ray Physics* III (1956).
- [62] K. Kamata and J. Nishimura. ‘The Lateral and the Angular Structure Functions of Electron Showers’. In: *Progress of Theoretical Physics Supplement* 6 (1958), pp. 93–155.
- [63] D. Newton, J. Knapp and A. A. Watson. ‘The Optimum Distance at which to Determine the Size of a Giant Air Shower’. In: *Astropart. Phys.* 26 (2007), pp. 414–419. DOI: 10.1016/j.astropartphys.2006.08.003. arXiv: astro-ph/0608118 [astro-ph].
- [64] J. Hersil et al. ‘Observations of Extensive Air Showers near the Maximum of Their Longitudinal Development’. In: *Phys. Rev. Lett.* 6 (1961), pp. 22–23. DOI: 10.1103/PhysRevLett.6.22.

- [65] I. Valino. ‘The flux of ultra-high energy cosmic rays after ten years of operation of the Pierre Auger Observatory’. In: *PoS ICRC2015* (2016). + talk, p. 271. URL: <https://pos.sissa.it/236/271/pdf>.
- [66] A. Aab et al. *The Pierre Auger Observatory: Contributions to the 34th International Cosmic Ray Conference (ICRC 2015)*. arXiv: 1509.03732 [astro-ph.HE].
- [67] T. K. Gaisser and A. M. Hillas. ‘Reliability of the method of constant intensity cuts for reconstructing the average development of vertical showers’. In: *International Cosmic Ray Conference 8* (1977), pp. 353–357. URL: <http://articles.adsabs.harvard.edu/pdf/1977ICRC....8..353G>.
- [68] T. Bergmann et al. ‘One-dimensional Hybrid Approach to Extensive Air Shower Simulation’. In: *Astropart. Phys.* 26 (2007), pp. 420–432. DOI: 10.1016/j.astropartphys.2006.08.005. arXiv: astro-ph/0606564 [astro-ph].
- [69] D. Heck et al. *CORSIKA: A Monte Carlo code to simulate extensive air showers*. 1998. URL: <https://inspirehep.net/record/469835/files/FZKA6019.pdf>.
- [70] G. Schatz. ‘The KASCADE cosmic ray experiment’. In: *Nucl. Phys. Proc. Suppl.* 43 (1995), pp. 261–264. DOI: 10.1016/0920-5632(95)00486-S.
- [71] Heck, D. and Pierog, T. *Extensive Air Shower Simulation with CORSIKA: A User’s Guide (Version 7.5600 from August 17, 2016)*. URL: <https://www.ikp.kit.edu/corsika/>.
- [72] T. Pierog et al. ‘EPOS LHC: Test of collective hadronization with data measured at the CERN Large Hadron Collider’. In: *Phys. Rev. C* 92.3 (2015), p. 034906. DOI: 10.1103/PhysRevC.92.034906. arXiv: 1306.0121 [hep-ph].
- [73] S. Ostapchenko. ‘Monte Carlo treatment of hadronic interactions in enhanced Pomeron scheme: I. QGSJET-II model’. In: *Phys. Rev. D* 83 (2011), p. 014018. DOI: 10.1103/PhysRevD.83.014018. arXiv: 1010.1869 [hep-ph].
- [74] H. J. Drescher et al. ‘Parton based Gribov-Regge theory’. In: *Phys. Rept.* 350 (2001), pp. 93–289. DOI: 10.1016/S0370-1573(00)00122-8. arXiv: hep-ph/0007198 [hep-ph].

-
- [75] J. Espadanal, L. Cazon and R. Conceição. ‘Sensitivity of EAS measurements to the energy spectrum of muons’. In: *Astropart. Phys.* 86 (2017), pp. 32–40. DOI: 10.1016/j.astropartphys.2016.11.003. arXiv: 1607.06760 [hep-ph].
- [76] A. Aab et al. ‘Muons in air showers at the Pierre Auger Observatory: Mean number in highly inclined events’. In: *Phys. Rev. D* 91.3 (2015), p. 032003. DOI: 10.1103/PhysRevD.91.059901. arXiv: 1408.1421 [astro-ph.HE].
- [77] A. Ferrari et al. *FLUKA: A multi-particle transport code (Program version 2005)*. URL: <https://www.slac.stanford.edu/pubs/slacreports/reports16/slac-r-773.pdf>.
- [78] W. R. Nelson, H. Hirayama and D. W. O. Rogers. *The Egs4 Code System*. 1985. URL: <https://inspirehep.net/record/220592/files/slac-r-265.pdf>.
- [79] D. Heck and J. Knapp. ‘Upgrade of the Monte Carlo code CORSIKA to simulate extensive air showers with energies $> 10^{20}$ eV’. In: *Spring Meeting of the Germany Physical Society (DPG) on Particle Physics (In German) Freiburg, Germany, March 23-27, 1998*. URL: <http://bibliothek.fzk.de/zb/berichte/FZKA6097.pdf>.
- [80] URL: <https://www.open-mpi.org/> Accessed: 30. August, 2017.
- [81] URL: <http://www.mcs.anl.gov/research/projects/mpi/> Accessed: 30. August, 2017.
- [82] S. Argiro et al. ‘The Offline Software Framework of the Pierre Auger Observatory’. In: *Nucl. Instrum. Meth.* A580 (2007), pp. 1485–1496. DOI: 10.1016/j.nima.2007.07.010. arXiv: 0707.1652 [astro-ph].
- [83] R. Brun and F. Rademakers. ‘ROOT: An object oriented data analysis framework’. In: *Nucl. Instrum. Meth.* A389 (1997), pp. 81–86. DOI: 10.1016/S0168-9002(97)00048-X. URL: <https://root.cern.ch>.
- [84] Billoir, Pierre. ‘A sampling procedure to regenerate particles in a ground detector from a “thinned” air shower simulation output’. In: *Astroparticle Physics* 30 (2008), 270–285. URL: http://www.ung.si/public/pao/bibl/app_2008_pb.pdf.

- [85] R. Brun et al. *GEANT4: Detector Description and Simulation Tool*. 1994. DOI: 10.17181/CERN.MUHF.DMJ1. URL: http://cds.cern.ch/record/1082634/files/geantall_CERN-W5013.pdf.
- [86] D. Veberic, M. Roth and H. Dembinski. *Offline Reference Manual; SD Reconstruction*. Pierre Auger Observatory internal paper GAP-2005-035.
- [87] P. Assis et al. *Reference manual of fluorescence detector simulation in Offline*. Pierre Auger Observatory internal paper GAP-2008-014.
- [88] URL: <https://www.auger.unam.mx/AugerWiki/OfflineSoftware> Accessed: 30. August, 2017.
- [89] G. van Aar. ‘On the nature and origin of ultra-high-energy cosmic rays’. PhD thesis. Nijmegen Universiteit, 2016. URL: <http://repository.ubn.ru.nl/bitstream/handle/2066/160103/160103.pdf?sequence=1>.
- [90] J. Abraham, P. Abreu et al. ‘Measurement of the Depth of Maximum of Extensive Air Showers above 10^{18} eV’. In: *Physical Review Letters* 104.9 (2010). DOI: 10.1103/PhysRevLett.104.091101. arXiv: 1002.0699 [astro-ph.HE].
- [91] A. Aab et al. ‘Muons in air showers at the Pierre Auger Observatory: Mean number in highly inclined events’. In: *Phys. Rev.* D91.3 (2015). DOI: 10.1103/PhysRevD.91.059901. arXiv: 1408.1421 [astro-ph.HE].
- [92] A. Aab et al. ‘Muons in air showers at the Pierre Auger Observatory: Measurement of atmospheric production depth’. In: *Phys. Rev.* D90.1 (2014). DOI: 10.1103/PhysRevD.92.019903. arXiv: 1407.5919 [hep-ex].
- [93] E. Armengaud et al. *Fitting a variable radius of curvature*. Pierre Auger Observatory internal paper GAP-2003-108.
- [94] G. De Mauro et al. *Start time variance from non thinned CORSIKA showers and comparison with time variance models*. Pierre Auger Observatory internal paper GAP-2016-006.
- [95] A. A. Watson and J. G. Wilson. ‘Fluctuation studies of large air showers: the composition of primary cosmic ray particles of energy $E_p \approx 10^{18}$ eV’. In: *J. Phys.* A7 (1974), pp. 1199–1212. DOI: 10.1088/0305-4470/7/10/013.

-
- [96] A. Aab et al. ‘Azimuthal Asymmetry in the Risetime of the Surface Detector Signals of the Pierre Auger Observatory’. In: *Phys. Rev. D* 93.7 (2016), p. 072006. DOI: 10.1103/PhysRevD.93.072006. arXiv: 1604.00978 [astro-ph.HE].
 - [97] G. Ros et al. ‘A new composition-sensitive parameter for Ultra-High Energy Cosmic Rays’. In: *Astropart. Phys.* 35 (2011), pp. 140–151. DOI: 10.1016/j.astropartphys.2011.06.011. arXiv: 1104.3399 [astro-ph.HE].
 - [98] P. Younk. *SD Composition Indicator for Hybrid Events*. Pierre Auger Observatory internal paper GAP-2011-095.
 - [99] M. Niechciol. ‘A New Window to the Universe? Searching for Ultra-High-Energy Photons at the Pierre Auger Observatory’. PhD thesis. Universität Siegen, 2015. URL: <https://www.hep.physik.uni-siegen.de/pubs/diss/niechciol-dr.pdf>.
 - [100] F. James and M. Roos. ‘Minuit: A System for Function Minimization and Analysis of the Parameter Errors and Correlations’. In: *Comput. Phys. Commun.* 10 (1975), pp. 343–367. DOI: 10.1016/0010-4655(75)90039-9. URL: <http://citeseerx.ist.psu.edu/viewdoc/download?doi=10.1.1.158.9157&rep=rep1&type=pdf>.
 - [101] P. Billoi. *What is ageing in the tanks of the Surface Detector?* Pierre Auger Observatory internal paper GAP-2014-038.
 - [102] B. T. Stokes et al. ‘Dethinning Extensive Air Shower Simulations’. In: *Astropart. Phys.* 35 (2012), pp. 759–766. DOI: 10.1016/j.astropartphys.2012.03.004. arXiv: 1104.3182 [astro-ph.IM].
 - [103] G. J. Feldman and R. D. Cousins. ‘A Unified approach to the classical statistical analysis of small signals’. In: *Phys. Rev. D* 57 (1998), pp. 3873–3889. DOI: 10.1103/PhysRevD.57.3873. arXiv: physics/9711021 [physics.data-an].
 - [104] L. Lu. ‘A search for photons of energy above 6×10^{18} eV using data from the Water-Cherenkov detectors of the Pierre Auger Observatory’. PhD thesis. Leeds U., 2014. URL: http://etheses.whiterose.ac.uk/7354/1/Lu_Thesis.pdf.
 - [105] A. Aab et al. *The Pierre Auger Observatory Upgrade - Preliminary Design Report*. 2016. arXiv: 1604.03637 [astro-ph.IM].

- [106] J. R. Hörandel. ‘Radio detection of extensive air showers - Measuring the properties of cosmic rays with the radio technique at LOFAR and the Pierre Auger Observatory’. In: *Nuclear and Particle Physics Proceedings* 306-308 (2019), pp. 108–115. ISSN: 2405-6014. DOI: <https://doi.org/10.1016/j.nuclphysbps.2019.07.016>.

Hardware and software versions

A.1. Hardware used

- 10 nodes with 1.8 TB storage space each, additional 30 TB storage space
- 32 x86_64 AMD Opteron CPUs with 128 GB RAM in each node

A.2. Software used

- Linux Debian 3.16.36 x86_64
- CORSIKA 7.4005, 7.5600
- GNU gcc, fortran compilers 4.9.1
- ROOT framework 5.34/36
- GEANT4 4.9.4
- OpenMPI 1.6.5
- Offline framework v3r3p1
- Offline externals: aerarootio v00r11, aevread v02r00p04, aires 2.8.4a, boost 1.59.0, cdas v5r4, clhep 2.1.2.3, cmake 3.4.3, cppunit 1.12.1, eigen 3.1.2, fdeventlib 4.1.8, fftw 3.3.3, pkg-config 0.27.1, xerces-c 3.1.1

B Appendix

Steering file examples and command descriptions

Flag	Value(s)			
RUNNR	3			
PARALLEL	316000	31600000	1	F
NSHOW	1			
EVTNR	1			
PRMPAR	5626			
ERANGE	3.16e9	3.16e9		
ESLOPE	-1			
THETAP	45	45		
PHIP	0	0		
SEED	1234618	0	0	
...	...			
SEED	1234623	0	0	
OBSLEV	145200			
MAGNET	20.1	-14.2		
ECUTS	0.05	0.01	0.00005	0.00005
QGSJET	T	0		
QGSSIG	T			
MUADDI	T			
ATMOD	21			
ELMFLG	T	T		
LONGI	T	5.	T	T
DEBUG	F	6	F	1000000
USER	aab			
DIRECT	/data/simulations/Fe_E18.5_Z45_nonthin_3/output/			
EXIT				

Table B.1.: Steering file of an EAS simulation with iron nucleus primary particle, $E = 10^{18.5}$ eV, $\theta = 45^\circ$, QGSJet hadronic interaction model and without thinning (non-thinned), generated in parallel on several CPUs. FLUKA interaction model was set during the setup of CORSIKA.

Flag	Value(s)			
RUNNR	7			
NSHOW	1			
EVTNR	1			
PRMPAR	14			
ERANGE	1e9	1e9		
ESLOPE	-1			
THETAP	30	30		
PHIP	0	0		
SEED	1234642	0	0	
...	...			
SEED	1234647	0	0	
OBSLEV	145200			
MAGNET	20.1	-14.2		
ECUTS	0.05	0.01	0.00005	0.00005
THIN	1.0e-6	10000.	0	
EPOS	T	0		
EPOSIG	T			
EPOPAR	input	../epos/epos.param		
EPOPAR	fname	inics	../epos/epos.inics	
EPOPAR	fname	iniev	../epos/epos.iniev	
EPOPAR	fname	initl	../epos/epos.initl	
EPOPAR	fname	inirj	../epos/epos.inirj	
EPOPAR	fname	inihy	../epos/epos.inihy	
EPOPAR	fname	check	none	
EPOPAR	fname	histo	none	
EPOPAR	fname	data	none	
EPOPAR	fname	copy	none	
MUADDI	T			
ATMOD	21			
ELMFLG	T	T		
LONGI	T	5.	T	T
DEBUG	F	6	F	1000000
USER	aab			
DIRECT	/data/simulations/p_E18_Z0_1e-6thin_7/output/			
EXIT				

Table B.2.: Steering file of an EAS simulation with proton primary particle, $E = 10^{18}$ eV, $\theta = 30^\circ$, EPOS hadronic interaction model and thinning level of $\varepsilon_{thin} = 10^{-6}$. FLUKA interaction model was set during the setup of CORSIKA.

Flag	Function
RUNNR	Assigns the simulation run number.
PARALLEL	Provides the options for parallelization (Section 4.1.2).
NSHOW	Specifies how many EAS will be simulated in one run.
EVTNR	Defines the number of the first EAS, the next will be indicated subsequently.
PRMPAR	Defines the primary particle type.
ERANGE	Defines the energy range of the primary particle.
ESLOPE	Defines the spectral index of the differential energy spectrum in the specified range.
THETAP	Defines the zenith angle range of the primary particle.
PHIP	Defines the azimuth angle range of the primary particle.
SEED	Adjusts up to 7 seeds for random number sequences for different subroutines.
OBSLEV	Specifies the observation altitude. All particles reaching this height will be saved in the output file.
MAGNET	Specifies the magnetic field for EAS.
ECUTS	Defines the energy threshold to limit the simulation effort by sorting out low energy particles. The limits can be adjusted for hadrons (except π^0), muons, e^\pm and photons (including π^0) individually.
THIN	Enables the thinning algorithm (Section 4.1.1).
EPOS	Enables EPOS routines for high-energy hadronic interactions.
EPOSSIG	Enables EPOS high-energy hadronic cross-sections.
EPOPAR	Provides commands for subroutines of the EPOS package.
QGSJET	Enables QGSJet routines for high-energy hadronic interactions.
QGSSIG	Enables QGSJet high-energy hadronic cross-sections.
MUADDI	Enables additional muon information to be written to the output file.
ATMOD	Specifies the atmospheric model.
ELMFLG	Defines how electromagnetic interactions will be calculated.

Flag	Function
LONGI	Enables the sampling of the longitudinal profile. In this case an additional file is written, containing number of different particle types in defined steps of the slant depth.
DEBUG	Prints more information about the simulation processes.
USER	Defines the user.
DIRECT	Defines the output directory.
EXIT	Marks the end of the steering commands.

Table B.3.: Commands used for the steering files.

Module sequence files

The last capital characters of the module description (e.g. KG, OG, Xb) indicates the author or the group, who wrote the module.

```
<sequenceFile>
  <enableTiming/>
  <moduleControl>
    <loop numTimes="unbounded" pushEventToStack="yes">
      <module> EventFileReaderOG </module>
      <module> SdPMTQualityCheckerKG </module>
      <module> TriggerTimeCorrection </module>
      <module> SdCalibratorOG </module>
      <module> SdStationPositionCorrection </module>
      <module> SdBadStationRejectorKG </module>
      <module> SdSignalRecoveryKLT </module>
      <module> SdEventSelectorOG </module>
      <module> SdPlaneFitOG </module>
      <module> LDFFinderKG </module>
      <module> EnergyCalculationPG </module>
      <module> SdEventPosteriorSelectorOG </module>
      <module> RecDataWriterNG </module>
    </loop>
  </moduleControl>
</sequenceFile>
```

Table C.1.: Module sequence file used for measured air showers.

```

<sequenceFile>
  <enableTiming/>
  <moduleControl>
    <loop numTimes="1" pushEventToStack="yes">
      <module> EventFileReaderOG </module>
      <loop numTimes="1" pushEventToStack="yes">
        <module> EventGeneratorOG </module>
        <loop numTimes="unbounded" pushEventToStack="no">
          <module> CachedShowerRegeneratorOG </module>
          <module> CachedDirectInjector </module>
          <module> G4TankSimulatorOG </module>
        </loop>
        <module> SdSimulationCalibrationFillerOG </module>
        <module> SdPMTSimulatorOG </module>
        <module> SdFilterFADCSimulatorMTU </module>
        <module> SdBaselineSimulatorOG </module>
        <module> TankTriggerSimulatorOG </module>
        <module> TankGPSSimulatorOG </module>
        <module> CentralTriggerSimulatorXb </module>
        <module> CentralTriggerEventBuilderOG </module>
        <module> EventBuilderOG </module>
        <module> EventCheckerOG </module>
        <module> SdCalibratorOG </module>
        <module> SdEventSelectorOG </module>
        <module> SdMonteCarloEventSelectorOG </module>
        <module> SdPlaneFitOG </module>
        <module> LDFFinderKG </module>
        <module> SdEventPosteriorSelectorOG </module>
        <module> RecDataWriterNG </module>
      </loop>
    </loop>
  </moduleControl>
</sequenceFile>

```

Table C.2.: Model sequence file used for simulated air showers. The highlighted modules are alternatively turned on and off for thinned (ShowerRegenerator, red) and non-thinned (DirectInjector, green) simulations.

D Appendix

$\Lambda_{\gamma,p}$ histograms and graphs

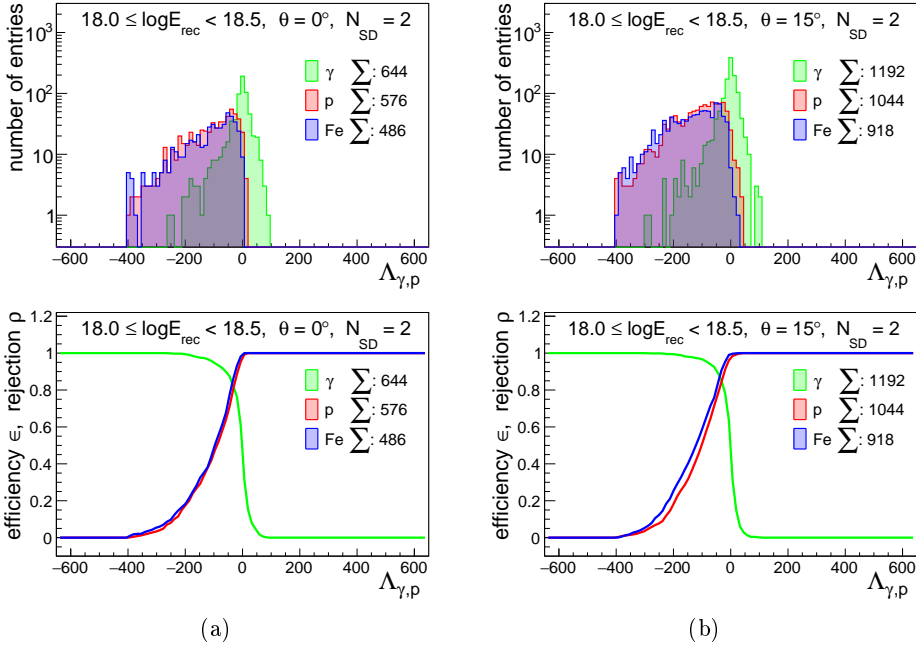


Figure D.1.: $\Lambda_{\gamma,p}$ histograms for simulated EAS with gamma rays (green), protons (red) and iron nuclei (blue) and the corresponding signal efficiency ϵ for gamma ray EAS with background rejection ρ for proton and iron nucleus induced EAS. Note that here both left and right histograms and graphs display the results with 2 SD stations. Those for 3 SD stations for nearly vertical air showers ($\theta \leq 15^\circ$) are empty due to upper limits of the distance range (Section 8.3).

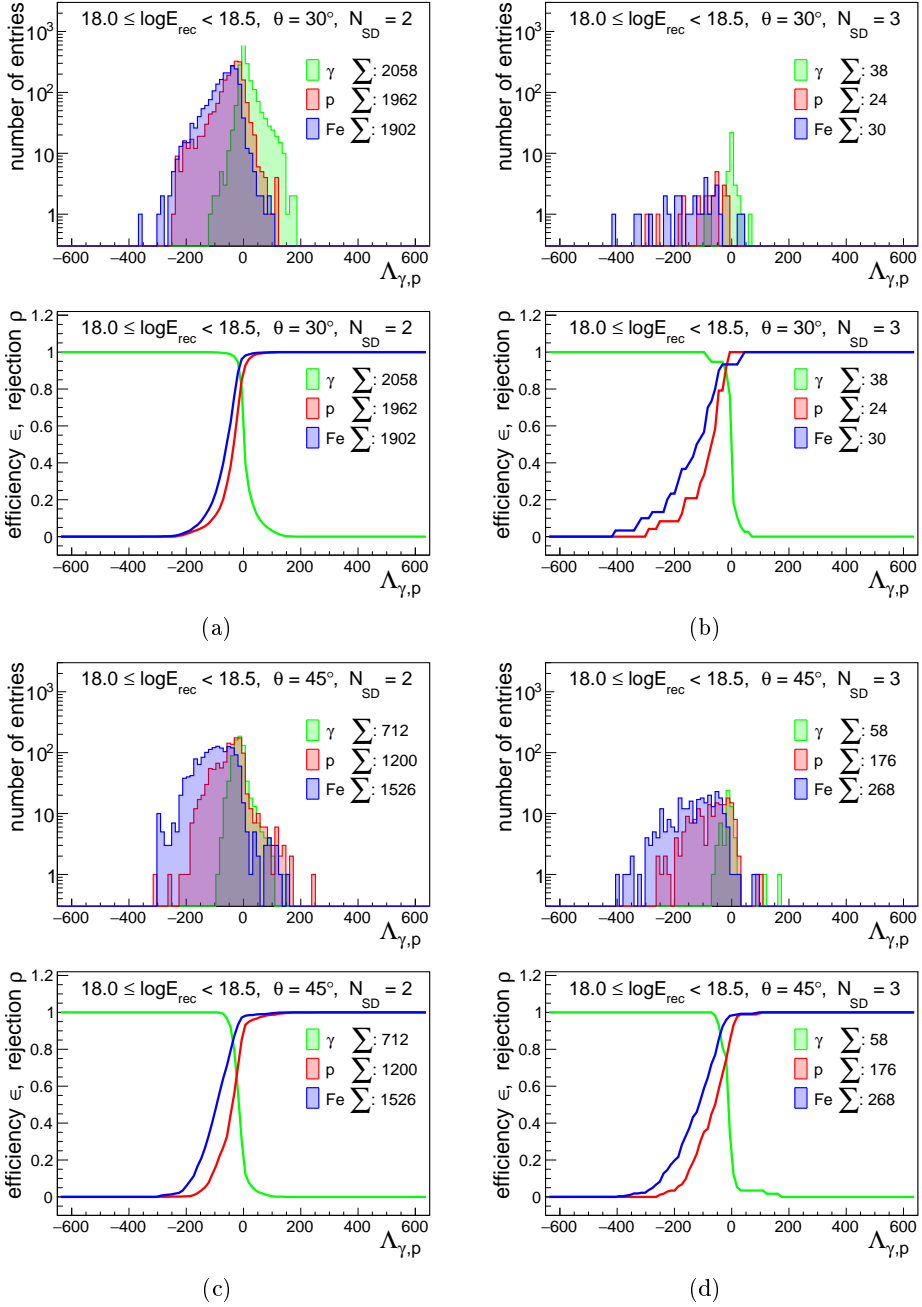


Figure D.2.: $\Lambda_{\gamma,p}$ histograms for simulated EAS with gamma rays (green), protons (red) and iron nuclei (blue) and the corresponding signal efficiency ϵ for gamma ray EAS with background rejection ρ for proton and iron nucleus induced EAS.

Appendix D

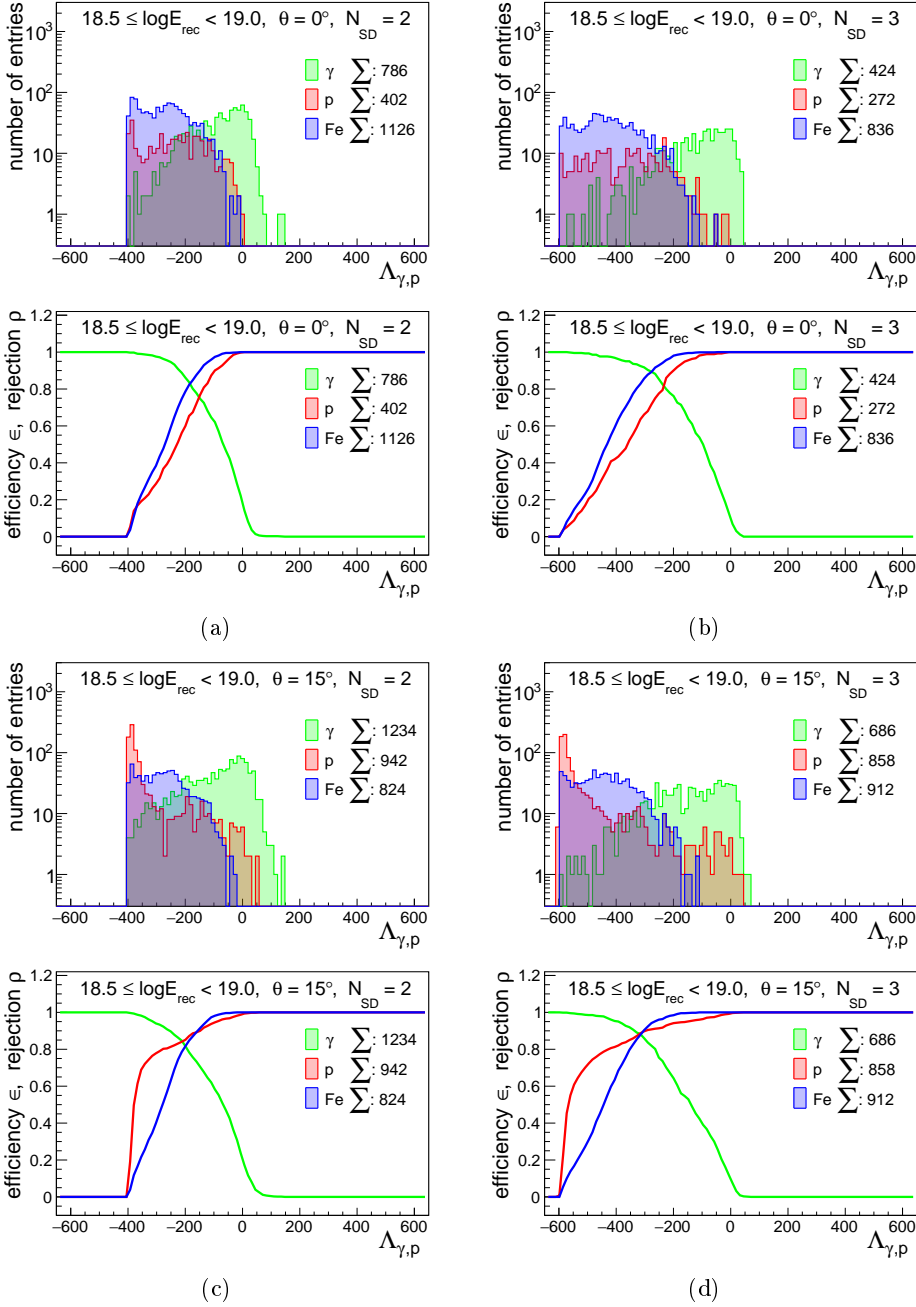


Figure D.3.: $\Lambda_{\gamma,p}$ histograms for simulated EAS with gamma rays (green), protons (red) and iron nuclei (blue) and the corresponding signal efficiency ϵ for gamma ray EAS with background rejection ρ for proton and iron nucleus induced EAS.

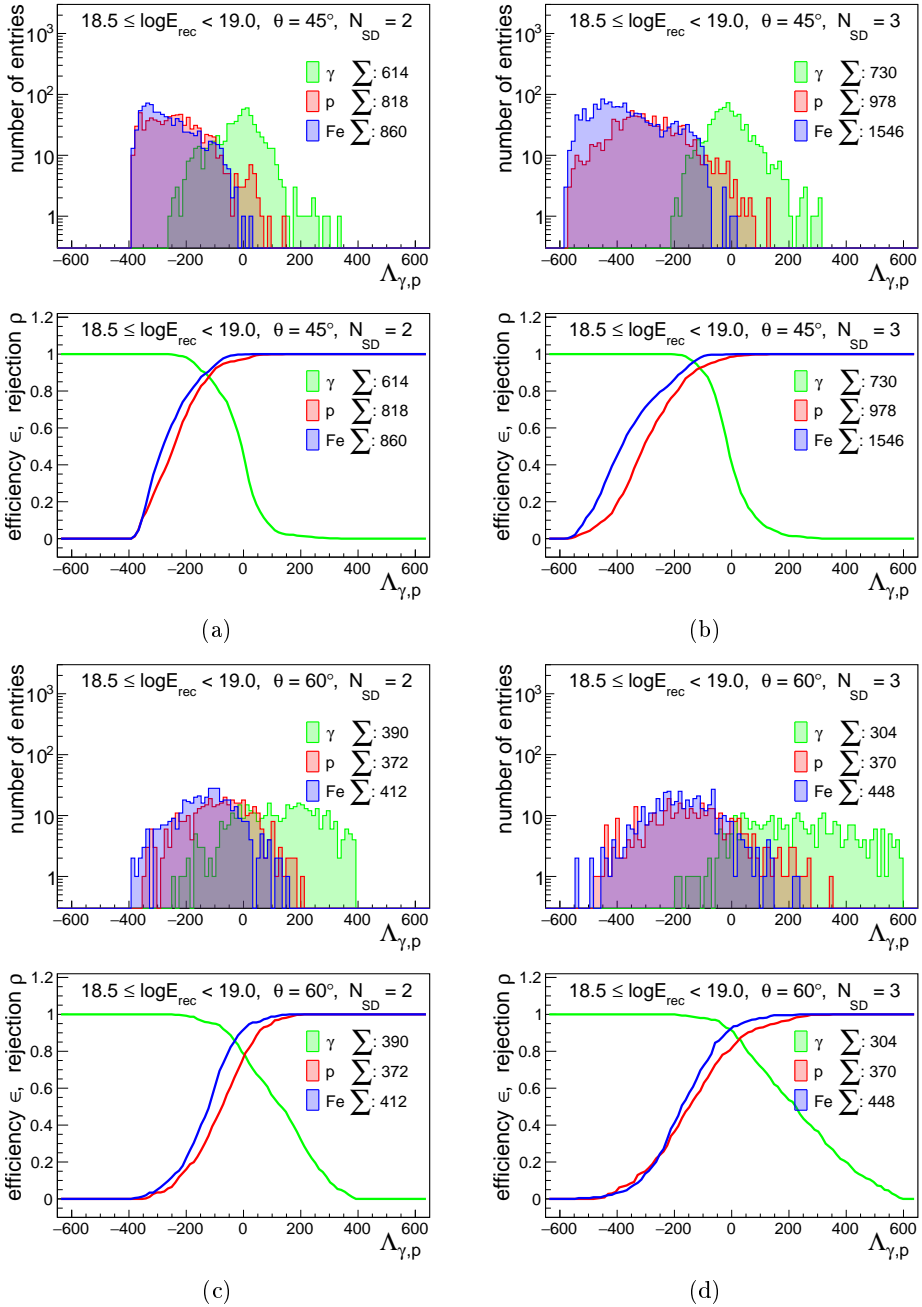
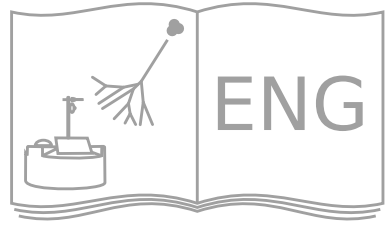


Figure D.4.: $\Lambda_{\gamma,p}$ histograms for simulated EAS with gamma rays (green), protons (red) and iron nuclei (blue) and the corresponding signal efficiency ϵ for gamma ray EAS with background rejection ρ for proton and iron nucleus induced EAS.

Glossary of abbreviations

ADST	Advanced Data Summary Tree
AERA	Auger Engineering Radio Array
AGN	Active Galactic Nuclei
AMIGA	Auger Muons and Infill for the Ground Array
CDAS	Central Data Acquisition System
CIC	Constant Intensity Cut
CMB	Cosmic Microwave Background
CORSIKA	COsmic Ray SIMulations for KASCADE
CR	Cosmic Ray(s)
EAS	Extensive Air Shower(s)
EM	Electro Magnetic
EPOS	Energy conserving quantum mechanical multi-scattering approach, based on Partons, Off-shell remnants and Splitting parton ladders
FADC	Flash Analogue to Digital Converter
FD	Fluorescence Detector
FLUKA	FLUctuationg KAscade
GDAS	Global Data Assimilation System
GPS	Global Positioning System
GZK	Greisen Zatzepin Kuzmin (limit)
HEAT	High Elevation Auger Telescope
IR	Infra Red
LDF	Longitudinal Distribution Function
LHC	Large Hadron Collider
KASCADE	KARlsruhe (Air) Shower Core And Array DETector
MC	Monte Carlo
Mpc	Mega parsec
MPI	Message Protocol Interface
MPD	Muon Production Depth
<u>Off</u> line	(Pierre) Auger (Observatory) Offline Software Framework
PAO	Pierre Auger Observatory
PMT	Photo Multiplier Tube
ROOT	Data Analysis Framework
S1000	Signal at 1000 m

S38	S1000 under 38°
SD	Surface Detector
QGSJet	Quark Gluon String model with JETs
T1-T5	Trigger 1 to 5
TA	Telescope Array
TPDF	Time Probability Density Function
UHE	Ultra-High-Energy
UHECR	Ultra-High-Energy Cosmic Ray(s)
UHEGR	Ultra-High-Energy Gamma Ray(s)
UV	Ultra Violet
VEM	Vertical Equivalent Muon
XML	Extensible Markup Language



Summary

Although outer space seems to be empty, it is filled with many kinds of particles. Several sources of these particles with galactic and extra galactic origins could be identified, first of all the stars. From our nearby star, the Sun, we receive everyday different kinds of rays like visible light, UV-radiation or the sun wind, which is deflected by the Earth's magnetic field toward the poles and gets visible as polar lights.

About 100 years ago it was discovered that besides photons also charged particles arrive at Earth from space. These are called *cosmic rays*, which mainly consist of protons. Several experiments have measured the energy, the arrival direction and the nature of these particles since then. It was found that a fraction of them are so highly energetic that they must come from outside of our solar system, some even from beyond our galaxy.

One of the big challenges is to figure out what the sources of the cosmic rays at the highest energies are. There are two main difficulties in this search. First, the flux of the cosmic rays, thus the number of particles that arrive at Earth, is rapidly decreasing with energy (Figure 2.3). Hence, the direct measurement of the cosmic rays where the primary particles interact with the detectors itself becomes unfeasible at energies above 10^{15} eV, because only a few particles per square meter per year arrive at Earth. The second difficulty originates from the charge of the cosmic rays, which induces a deflection by the galactic and extra galactic magnetic fields. The strength of the deflection depends on the charge and the energy of the particles and results in an arrival direction which does not point back to the origin. To reconstruct the origin the magnetic fields need to be precisely known but they are not.

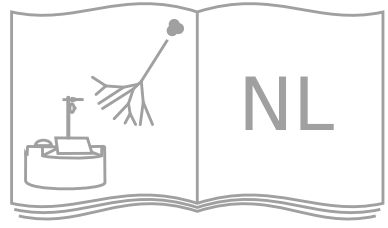
To study the cosmic rays at the highest energies above 10^{18} eV (Ultra-High-Energy Cosmic Rays, UHERC) the indirect method is used involving the Earth's atmosphere, instead of the direct method. When the high-energy particles hit the atmosphere they interact with the atomic nuclei in the air. At this process new particles are produced, which interact with further air nuclei and produce new particles again. This creates a cascade of secondary particles which moves in the same direction as the primary particle. This cascade is called the *extensive air shower* (EAS).

Its properties, like total energy and inclination angle, are obtained from the primary particle, and are used to study the cosmic rays. The advantage of using air showers is their huge cross section going up to several square kilometers. They can be analyzed with surface detectors even if only a small fraction of the secondary particles is measured. Thus, several air showers can be measured per day by many small detectors, instead of waiting for centuries for a direct hit of the cosmic ray or building a huge solid detector. The disadvantage of the indirect method is the required reconstruction of the properties of the primary particle from the measurements of a few secondary particles. In particular the identification of the nature of the primary particle is difficult, as it has only a small influence on the properties of the air shower. The knowledge of the primary particle type from the measured air showers can support different astrophysical models of the sources and the acceleration mechanisms, as they propose different *mass compositions* of the cosmic rays. Particularly the search for neutral primary particles, like photons, is of main interest, as they are not bent by the magnetic fields and point directly to their sources.

The analysis described in this thesis studies the signals of the Surface Detector (SD) of the Pierre Auger Observatory for specific signatures of different air showers with different primary particles. The SD stations are basically water tanks. When the secondary particles of an air shower are traversing through the water they produce (Vavilov-)Cherenkov light, which is captured by the Photo Multiplier Tubes (PMTs) and recorded as a function of arrival time. The time profile depends on the number of secondary particles, their individual arrival times and their energies. The route of the secondaries through the atmosphere from the first interaction of the cosmic ray until the arrival at the SD as well as the distance to the air shower axis influence the signal. To understand how the time profiles of the SD vary for different cosmic rays, air shower simulations with different primaries have been created. On the simulated SD signals the *TPDF* (Time Probability Density Function), a function with four free parameters, is fitted and their parameters are analyzed.

The parameters of the TPDF at different distances to the air shower axis are combined into models for different properties of the primary particles. The simulated and measured signals from the SD data are compared to these models to find measured air showers with characteristics of a photon (gamma ray) primary particle. The analysis with the TPDF method on the simulations revealed that it has a good separation power to distinguish

air showers induced by ultra-high-energy gamma rays from those induced by hadrons, but a very weak separation power between proton and iron nucleus induced EAS. The differences of the time profiles of photon and hadron initiated air showers are mainly due to their different fractions of electromagnetic and muonic components. The air showers initiated by a photon have almost no muons. However, the muons change the time profile significantly, as they arrive first at the SD stations. This comes mainly from the fact that they almost never interact further with the air atoms once produced. After the application on data, 152 out of 227118 tested air showers were found to fulfill the requirement to be induced by gamma rays, which is less than 0.1% of the events. This is compatible with the expected background from hadron induced air showers without evidence of the presence of gamma rays.



Samenvatting

Ondanks dat het heelal vrijwel leeg lijkt te zijn, is het gevuld met allerlei soorten deeltjes. Een aantal bronnen voor deze deeltjes met een galactische of extra-galactische oorsprong kunnen worden geïdentificeerd, op de eerste plaats: sterren. Van onze eigen ster, de zon, bereiken ons dagelijks verschillende soorten straling zoals zonlicht en uv-straling, maar ook de zonnewind die door het aardmagnetisch veld afgebogen wordt naar de polen en daar zichtbaar wordt als poollicht.

Dat niet alleen fotonen, maar ook geladen deeltjes de aarde bereiken vanuit de ruimte werd ongeveer 100 jaar geleden ontdekt. Deze deeltjes, voornamelijk protonen, worden *kosmische straling* genoemd. Verschillende experimenten hebben sindsdien de energie, aankomstrichting en aard van deze deeltjes gemeten. Sommige deeltjes zijn zo hoog-energetisch dat ze afkomstig moeten zijn van buiten ons zonnestelsel en sommige zelfs van buiten ons sterrenstelsel.

Een van de grote uitdagingen is het achterhalen van de bronnen van deze hoog-energetisch kosmische straling. De zoektocht naar de bronnen is lastig om twee redenen. Ten eerste, de flux van de kosmische straling, en daarmee ook het aantal deeltjes dat het aardoppervlak bereikt, neemt sterk af met toenemende energie (Figuur 2.3). Dit betekent dat directe detectie van kosmische straling, waarbij de primaire deeltjes direct met de detector wisselwerken, met energieën boven 10^{15} eV niet meer praktisch haalbaar is, aangezien slechts enkele deeltjes per vierkante meter per jaar de aarde bereikt. De tweede reden is dat de kosmische straling afgebogen wordt door de galactische en extra-galactische magnetische velden vanwege hun elektrische lading. De sterkte van de afbuiging is afhankelijk van de lading en de energie van de deeltjes, en het zorgt ervoor dat de richting waarin de deeltjes op aarde aankomen niet meer overeenkomt met de richting waarin de bron zich bevindt. Om de oorsprong te reconstrueren is het noodzakelijk dat de magnetische velden precies bekend zijn, wat echter niet het geval is.

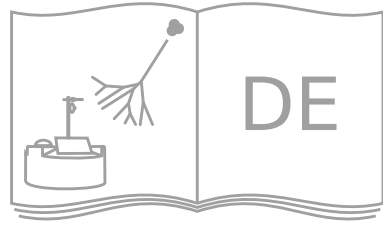
Om de kosmische straling met energieën boven 10^{18} eV (Ultra-High-Energy Cosmic Rays, UHECR) te bestuderen wordt in plaats van directe detectie een indirecte detectie methode toegepast die gebruikt maakt van

de atmosfeer. Wanneer de hoog-energetische deeltjes de atmosfeer raken, gaan ze een interactie aan met de atoomkernen in de lucht. In dit proces worden nieuwe deeltjes geproduceerd die op hun beurt weer andere atomen in de lucht raken en daarbij nog meer nieuwe deeltjes produceren. Dit resulteert in een *deeltjeslawine* (extensive air shower, EAS) van secundaire deeltjes die in dezelfde richting bewegen als de primaire deeltjes van de kosmische straling. De eigenschappen van de deeltjeslawine, zoals de energie en de invalshoek, zijn geërft van het primaire deeltje, en worden gebruikt om de kosmische straling te bestuderen. Het voordeel van het gebruik van deeltjeslawines is dat ze meerdere kilometers in diameter zijn en geanalyseerd kunnen worden met detectoren op het aardoppervlak, zelfs als slechts een fractie van de secundaire deeltjes wordt gemeten. Op deze manier is het dus mogelijk om meerdere deeltjeslawines per dag te meten, zonder dat men eeuwen hoeft te wachten op een enkele directe meting van de kosmische straling dan wel een enorme, massieve detector moet bouwen. Het nadeel van deze indirecte methode is echter dat de eigenschappen van het primaire deeltje gereconstrueerd moeten worden uit metingen van enkele secundaire deeltjes. Vooral de identificatie van de aard van het primaire deeltje is lastig, omdat dit slechts een kleine invloed heeft op de eigenschappen van de secundaire deeltjes. De kennis van de aard van het primaire deeltje van gemeten deeltjeslawines kan worden gebruikt om verschillende astrofysische modellen van bronnen en versnellingsmechanismen te toetsen, aangezien ze verschillende *samenstelling in massa* van kosmische straling veronderstellen. Vooral de zoektocht naar neutrale primaire deeltjes zoals fotonen is interessant, omdat ze niet worden afgebogen door magnetische velden en hun aankomstrichting overeenkomt met hun oorsprong.

De studie beschreven in dit proefschrift onderzoekt de signalen van de aardoppervlakdetectoren (Surface Detectors, SD) van het Pierre Auger Observatorium voor karakteristieke kenmerken van verschillende deeltjeslawines met verschillende primaire deeltjes. De SD-stations hebben elk een watertank waarin (Vavilov-)Tsjerenkof-licht wordt gegenereerd wanneer de secundaire deeltjes uit de deeltjeslawine het water passeren. Het licht wordt geregistreerd door een fotomultiplicator (Photo Multiplier Tube, PMT) als een functie van de aankomsttijd. Dit tijdprofiel hangt onder meer af van het aantal secundaire deeltjes dat de tank passeert, hun individuele aankomsttijden en hun energie. Het pad door de atmosfeer vanaf het punt van de eerste interactie tot de aankomst bij het SD-station en de

afstand tot de as van de deeltjeslawine beïnvloeden het signaal. Met behulp van gesimuleerde deeltjeslawines met verschillende soorten primaire deeltjes is onderzocht hoe de tijdprofielen van de SD-stations verschillen. Een functie met vier vrije parameters (*TPDF*, Time Probability Density Function) is gebruikt om de gesimuleerde SD-signalen te beschrijven en de best-passende parameters zijn geanalyseerd.

De parameters van de *TPDF* op verschillende afstanden tot de as van de deeltjeslawine worden gecombineerd in modellen voor verschillende eigenschappen van de primaire deeltjes. De gesimuleerde en gemeten signalen van SD-stations worden vergeleken met deze modellen om te bepalen welke van de gemeten deeltjeslawines de karakteristieke eigenschappen hebben van een foton geïnitieerde deeltjeslawine. De analyse van de *TPDF* methode op de simulaties toonde aan dat het een goed scheidingsvermogen heeft tussen deeltjeslawines geïnduceerd door ultrahoge-energie gammastralen en die geïnduceerd door hadronen, maar een zeer zwak scheidingsvermogen tussen die van protonen en ijzernuclei. De tijdprofielen van de foton en hadron geïnitieerde deeltjeslawines verschillen hoofdzakelijk vanwege hun verschillende verhoudingen in de elektromagnetische en muonische componenten. Deeltjeslawines geïnitieerd door fotonen bevatten nauwelijks muonen. Muonen beïnvloeden de tijdprofielen op significante wijze, omdat ze als eerste aankomen bij de SD-stations. Dit komt omdat muonen nauwelijks interactie hebben met de luchtatomen als ze eenmaal geproduceerd zijn. Na de toepassing op de data, bleken 152 van de 227118 geteste deeltjeslawines te voldoen aan de eis om geïnduceerd te worden door gammastralen, wat minder is dan 0,1% van de gevallen. Dit is compatibel met de verwachte achtergrond van de hadron geïnduceerde deeltjeslawines zonder bewijs van de aanwezigheid van gammastralen.



Zusammenfassung

Auch wenn das Weltall leer erscheinen mag, ist es von vielen Arten von Teilchen durchdrungen. Als Quellen dieser Teilchen konnten viele Objekte mit galaktischem und extragalaktischem Ursprung identifiziert werden, allen voran die Sterne. In der Nähe unseres Sterns, der Sonne, erreichen uns tagtäglich verschiedene Arten von Strahlung, wie Sonnenlicht, UV-Strahlung oder der Sonnenwind, der im Magnetfeld der Erde zu den Polen abgelenkt und als Polarlicht sichtbar wird.

Vor etwa 100 Jahren wurde entdeckt, dass neben Photonen auch geladene Teilchen aus dem Weltall die Erde erreichen. Diese werden als *kosmische Strahlung* bezeichnet, welche hauptsächlich aus Protonen besteht. Zahlreiche Experimente haben seitdem unter anderem die Energie, die Ankunftsrichtung und die Art der Teilchen messen können. Es konnte nachgewiesen werden, dass einige von ihnen so hochenergetisch sind, dass sie von außerhalb des Sonnensystems stammen müssen, einige sogar von außerhalb unserer Galaxie.

Eines der großen Geheimnisse der kosmischen Strahlung bei den höchsten Energien ist ihr Ursprung. Bei der Suche nach diesem gibt es zwei Schwierigkeiten. Zum einen nimmt der Fluss der Teilchen, also ihre Anzahl die auf der Erde ankommt, mit der Energie rapide ab (Bild 2.3). Dies führt dazu, dass der direkte Nachweis der kosmischen Strahlung, bei der die Primärteilchen unmittelbar mit dem Detektor interagieren, ab Energien von ca. 10^{15} eV nicht mehr praktikabel ist, da nur wenige Teilchen pro Quadratmeter pro Jahr die Erde erreichen. Die zweite Schwierigkeit besteht darin, dass die geladenen Teilchen, woraus sich die kosmische Strahlung zusammensetzt, von den galaktischen und extragalaktischen Magnetfeldern abgelenkt werden. Die Stärke der Ablenkung hängt von der Ladung und der Energie der Teilchen ab und führt dazu, dass die Ankunftsrichtung im Detektor nicht zurück zum Ursprung zeigt. Um diese zu rekonstruieren müssen die Magnetfelder genau bekannt sein, was jedoch nicht der Fall ist.

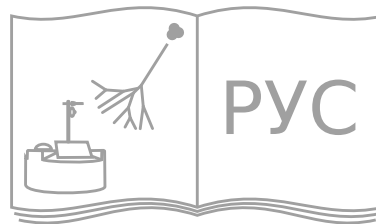
Um die kosmische Strahlung bei den höchsten Energien (Ultra-High-Energy Cosmic Rays, UHECR) ab 10^{18} eV studieren zu können wird statt der direkten Methode eine indirekte Methode genutzt, unter Zuhil-

fenahme der Erdatmosphäre. Wenn die hochenergetischen Teilchen auf die Atmosphäre treffen, wechselwirken sie mit den Atomkernen der Luftmoleküle. Bei diesem Vorgang werden neue Teilchen erzeugt, die auf weitere Atomkerne treffen und dabei weitere Teilchen erzeugen. So entsteht eine Kaskade von Sekundärteilchen, die sich in Richtung des ursprünglichen Primärteilchens der kosmischen Strahlung auf die Erdoberfläche zu bewegt. Diese Kaskade wird *Luftschauer* (extensive air shower, EAS) genannt. Sie besitzt die Eigenschaften wie Energie und Einfallswinkel des Primärteilchens und wird dazu benutzt, die kosmische Strahlung zu untersuchen. Der Vorteil der Luftschauer ist, dass sie sich über mehrere Kilometer im Durchmesser erstrecken und sich mit Detektoren auf dem Erdboden analysieren lassen, selbst wenn nur ein Bruchteil der Sekundärteilchen gemessen wird. So können mehrere Luftschauer pro Tag mit vielen kleinen Detektoren untersucht werden, anstatt Jahrhunderte auf einen direkten Treffer der kosmischen Strahlung zu warten oder einen riesigen massiven Detektor bauen zu müssen. Der Nachteil dieser indirekten Methode liegt jedoch in der erforderlichen Rekonstruktion der Eigenschaften des Primärteilchens aus den Messungen einiger weniger Sekundärteilchen. Im Besonderen ist die Identifizierung der Primärteilchenart schwierig, da diese wenig Einfluss auf die Sekundärteilcheneigenschaften hat. Mit dem Wissen der Primärteilchenart der gemessenen Luftschauer können verschiedene astrophysikalische Modelle der Quellen und Beschleunigungsmechanismen überprüft werden, da sie verschiedene *Massenzusammensetzungen* der kosmischen Strahlung voraussagen. Daher ist speziell die Suche nach neutralen Primärteilchen, wie Photonen, von Interesse, da diese nicht durch Magnetfelder abgelenkt werden und ihre Ankunftsrichtung direkt zu ihrer Quelle zeigt.

Die vorliegende Studie untersucht die Signale der Bodendetektoren (Surface Detector, SD) des Pierre Auger Observatoriums auf charakteristische Signaturen die von verschiedenen Luftschauern mit unterschiedlichen Primärteilchen stammen. Die SD-Stationen sind Wassertanks, in denen beim Durchgang von Sekundärteilchen der Luftschauer (Wawilow-)Tscherenkow-Licht erzeugt wird, welches von den Photovervielfachern (Photo Multiplier Tube, PMT) als Funktion der Ankunftszeit aufgezeichnet wird. Dieses Zeitprofil hängt unter anderem von der Anzahl der durchgehender Teilchen, ihrer Ankunftszeitverteilung und ihrer Energie ab. Auch der Weg durch die Atmosphäre von der ersten Wech-

selwirkung bis zum Auftreffen auf die SD-Stationen und der Abstand zur Achse des Luftschauers verändern das Signal. Mit Hilfe der Simulationen von Luftschauern mit verschiedenen Primärteilchenarten werden die SD-Signale auf Profilveränderungen untersucht, die auf die Art schließen lassen. Dazu wird an das Signalprofil eine Funktion mit vier freien Parametern angepasst, die *TPDF* (Time Probability Density Function), und die Werte der Parameter miteinander verglichen.

Die Parameter der TPDF für verschiedene Abstände zur Luftschauerachse werden zu Modellen für verschiedene Eigenschaften des Primärteilchens zusammengefasst. Die simulierten und die gemessenen Signale aus den Daten der SD-Stationen werden mit diesen Modellen verglichen, um zu bestimmen, welche der gemessenen Luftschauer die charakteristischen Merkmale eines Photons als Primärteilchen besitzen. Die Analyse der TPDF-Methode anhand von Simulationen hat ergeben, dass TPDF eine gute Trennkraft besitzt, um zwischen photon- und hadroninduzierten Luftschauern zu unterscheiden. Allerdings eignet sich die TPDF weniger, um die verschiedenen hadronischen Primärteilchen der Luftschauer zu unterscheiden. Die Signalprofile von Photonen- und Hadronen-Luftschauern unterscheiden sich vor allem aufgrund der unterschiedlicher Verhältnisse von elektromagnetischer und myonischer Komponenten. In Luftschauern die von Photonen gestartet werden befinden sich kaum Myonen. Dabei beeinflussen diese signifikant die SD-Signale, da sie zuerst in den SD-Stationen ankommen. Der Grund dafür ist, dass die Myonen kaum mit den Atomkernen in der Luft wechselwirken. Nach der Anwendung auf Daten wurden 152 der 227118 getesteten Luftschauern herausgefiltert, die die Eigenschaften von photoninduzierten Luftschauern aufweisen. Dies entspricht weniger als 0,1% aller analysierten Luftschauer und ist vereinbar mit dem erwarteten Untergrund aus den Luftschauern mit Hadronen als Primärteilchen, ohne einen eindeutigen Nachweis von Photonen bei den höchsten Energien.



Резюме

Несмотря на то, что космос кажется пустым, он заполнен самыми разными частицами. Были найдены многие галактические и внегалактические источники этих частиц, в первую очередь звезды. Наше Солнце излучает разные виды частиц, например солнечный свет и УФ-излучение или солнечный ветер, который в магнитном поле Земли отклоняется к полюсам и проявляется как северное сияние.

Около 100 лет тому назад было открыто, что помимо фотонов на Землю из космоса также прилетают частицы с ненулевым зарядом. Из-за их происхождения они были названы *космическими лучами*, которые состоят по большей части из протонов. С тех пор, многие проведенные эксперименты позволили измерить энергии, направления прихода и массовый состав этих частиц. Было обнаружено, что некоторые из частиц настолько высокоэнергетичны, что их источники находятся в других солнечных системах, некоторые даже за пределами нашей галактики.

До сих пор источники космических лучей при сверхвысоких энергиях не установлены. При их поиске существуют две основные сложности. Во-первых, поток частиц, то есть их количество прибывающее на Землю, резко уменьшается с увеличением энергии (рисунок 2.3). Это означает, что прямое измерение, то есть непосредственное взаимодействие космических лучей с детектором, при энергиях частиц выше 10^{15} эВ непрактично, так как их поток составляет всего несколько частиц на один квадратный метр в год. Вторая сложность состоит в том, что заряженные частицы космических лучей изменяют траекторию при воздействии галактических и внегалактических магнитных полей. Сила отклонения от изначальной траектории зависит от заряда и энергии частиц и приводит к тому, что измеренное направление прибытия не соответствует истинному направлению от источников. Чтобы понять, где возникли высокоэнергетичные частицы космических лучей с ненулевым зарядом, нужны более точные знания о магнитных полях, по сравнению с тем, что известно в настоящее время.

Для исследования космических лучей сверхвысокой энергии

выше 10^{18} эВ вместо прямого измерения используется косвенный метод где атмосфера Земли выступает в роли части детектора. Когда высокоэнергетичные частицы попадают в атмосферу они взаимодействуют с ядрами атомов воздуха. При этом порождаются новые частицы, которые в свою очередь сталкиваются с другими атомами и порождают также новые частицы. Так зарождается каскад вторичных частиц, направление которого соответствует направлению первичной частицы. Такой каскад называется *широкий атмосферный ливень (ШАЛ)*. Его свойства, такие как энергия и угол наклона оси, позволяют определить соответствующие свойства первичной частицы. Преимущество исследований ШАЛ состоит в том, что они достигают поперечных размеров в несколько километров и с помощью детекторов расположенных на земной поверхности могут быть изучены, даже если только небольшая часть вторичных частиц была измерена. Этим способом можно исследовать атмосферные ливни с помощью небольших детекторов, разнесённых на значительные расстояния, вместо того, чтобы ждать прямого попадания космических лучей столетиями или создавать огромный монолитный детектор. Недостатком такого косвенного метода является необходимость реконструкции свойств первичной частицы на основе измерений параметров немногочисленных вторичных частиц. В особенности сложна идентификация типа первичной частицы, так как он в меньшей мере влияет на свойства вторичных частиц. Зная тип первичных частиц измеренных ШАЛ можно проверить разные астрофизические модели источников и механизмов ускорения, так как они предсказывают разные *массовые составы* космических лучей. Поэтому поиск нейтральных частиц, таких как фотонов, представляет собой особый интерес, потому как они не изменяют своей траектории под воздействием магнитных полей и тем самым их направление совпадает с направлением от источников их происхождения.

Представленный в этой диссертации анализ исследует сигналы наземных детекторов (Surface Detector, SD) обсерватории имени Пьера Оже на предмет отличий разных широких атмосферных ливней с разными типами первичных частиц. Каждый из наземных детекторов в основном является баком с водой при прохождении в которой вторичные частицы атмосферных ливней порождают излучение Вавилова-Черенкова, которое в свою очередь регис-

трируется фотоумножителями как функция времени. Форма зарегистрированных сигналов зависит в том числе от количества частиц пролетевших через детектор, их временном распределении и их энергий. Так же на форму сигнала оказывают влияние: путь сквозь атмосферу начиная с первого взаимодействия до попадания в наземный детектор и расстояние от оси атмосферного ливня. С целью определения типа первичной частицы проводится анализ изменений сигналов наземных детекторов с помощью моделированных атмосферных ливней с разными первичными частицами. Для этого к временным профилям адаптируется функция с четырьмя свободными параметрами (*TPDF*, Time Probability Density Function), которые сравниваются друг с другом.

Результаты параметризаций *TPDF*-функции для разных расстояний от оси ШАЛ объединены в отдельные модели для различных свойств первичной частицы. На основе этих моделей проводится сравнительный анализ измерений наземного детектора обсерватории имени Пьера Оже с результатами компьютерного моделирования, для выявления в данных обсерватории широких атмосферных ливней с характеристиками, сходными с ожиданиями для первичных фотонов. Анализ *TPDF*-метода с использованием компьютерных моделей показал, что этот метод обладает хорошей способностью дискриминации ШАЛ инициированных фотонами от ливней, зарождённых адронами, но очень слабой способностью дискриминации протонов от ядер железа в качестве частиц космического излучения. Временные распределения сигналов от фотонных и адронных ШАЛ отличаются друг от друга в первую очередь за счет разных соотношений электромагнитных и мюонных компонент. В атмосферных ливнях инициированных фотонами практически отсутствуют мюоны. При этом мюоны вносят доминирующий вклад в раннюю часть временных распределений сигналов наземных детекторов, так как они практически не взаимодействуют с атомами воздуха после своего возникновения и имеют прямолинейные траектории. В измерениях наземного детектора были идентифицированы 152 ШАЛ, соответствующих характеристикам ливней от первичных фотонов, что составляет менее 0,1% от 227118 проверенных ШАЛ. Это значение совместимо с ожидаемым фоном от атмосферных ливней инициированных адронами, без необходимости присутствия сверхвысокоэнергичных фотонов.

Acknowledgements

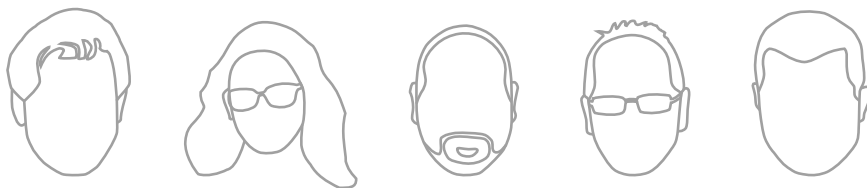
First of all I would like to thank my supervisors Charles and Sijbrand for their help, ideas and inspiring discussions. Without you it would be impossible for me to finish my thesis in Nijmegen. These have been wonderful years with nice office colleagues Guus, Stefan, Giuseppe and Fabrizia. Thank you and also Jeroen, Luca, Remco, Veronica, Anamika, Melissa, Bob and others for the events, dinners and trips we have organized together.

Many thanks to the Siegen Universität and the high-energy physics group where I've started my PhD journey with Nadine, Uwe, Sebastian, Marcus, Philip, Marek, Yuriy, Hendrik, Bertha, Sebastian, Christian, Alexey and many others. A special thanks to our administrator Wolfgang for keeping alive the whole computer cluster and workspace PCs and solving any kind of related problems.

Also thanks to the Karlsruhe group for help and discussions. Especially to Tanguy and Gevorg for solving problems with the CORSIKA simulations.

During my PhD time I've met many nice people and made new friends during DPG, AYM, Malargue and other meetings: Daniela, Martin, Christine, Florian, Ewa, Marcus, Anne, Alex, Julian, Jonas, Dima and others. Thanks to all of you for the great time. I hope we can keep our Christmas market trip tradition.

Наконец, я хочу поблагодарить моих родителей, Людмилу и Константина, за вашу поддержку и помощь. Без вас я бы не смог закончить учёбу и аспирантуру. Спасибо вам за всё.



Ultra-high-energy cosmic rays and photons (gamma rays) can be studied through the air showers they produce when interacting with the Earth's atmosphere. The sources and acceleration mechanisms of these ultra-energetic, but also very rare visitors from space are still not understood. Gamma rays have the advantage, compared to cosmic rays, that they are not deflected by the galactic and extragalactic magnetic fields. Therefore, their arrival directions point back to their origins. This makes them great candidates to analyse the mechanisms behind the creation and acceleration of particles to energies above 10^{18} eV. The identification of gamma ray induced air showers is important for such studies. The Time Probability Density Function (TPDF) introduced in this Ph.D. thesis to describe the Surface Detector data of the Pierre Auger Observatory is aimed to improve the separation of cosmic ray and gamma ray induced air showers compared to other techniques that have been used so far.



ISBN 978-94-028-1946-5



9 789402 819465